Inorganic-organic Hynrid Biomaterials for Bone Regeneration

Fan, Wei

DOI (link to publication from Publisher):
10.54337/aau510567827

Publication date:
2022

Document Version
Publisher's PDF, also known as Version of record

INORGANIC-ORGANIC HYBRID BIOMATERIALS FOR BONE REGENERATION

BY
WEI FAN

DISSERTATION SUBMITTED 2022

AALBORG UNIVERSITY
DENMARK

INORGANIC-ORGANIC HYBRID BIOMATERIALS FOR BONE REGENERATION

by

Wei FAN

AALBORG UNIVERSITY
DENMARK

Dissertation submitted 2022

Dissertation submitted: June 2022

PhD supervisor: Prof. Morten M. Smedskjær
Aalborg University

PhD co-supervisor: Associate Prof. Donghong Yu
Aalborg University

PhD committee: Associate Professor Thorbjørn T. Nielsen (chair)
Aalborg University, Denmark

Professor Delia Brauer
Friedrich Schiller University, Germany

Senior Research Associate Qiang Fu
Corning Incorporated, USA

PhD Series: Faculty of Engineering and Science, Aalborg University

Department: Department of Chemistry and Bioscience

ISSN (online): 2446-1636
ISBN (online): 978-87-7573-880-9

Published by:
Aalborg University Press
Kroghstræde 3
DK – 9220 Aalborg Ø
Phone: +45 99407140
aauf@forlag.aau.dk
forlag.aau.dk

Printed in Denmark by Stibo Complete, 2022

CV

Mr. Wei FAN was born in Dingxi, Gansu, P. R. China in April 1993. He got his bachelor's degree in Chemistry from Lanzhou University. Then, he was admitted to the University of Chinese Academy of Sciences, National Center for Nanoscience and Technology, and got his MSc. degree in Physical Chemistry in 2019. He was supported by China Scholarship Council (CSC) scholarship and started studying at the Department of Chemistry and Bioscience at Aalborg University from September 2019. His research has been focused on inorganic-organic hybrid biomaterials for bone regeneration during his 3-year Ph.D. study at AAU. He worked for 5 months with Prof. Bengang Xing at Nanyang Technological University as an exchange student for biocompatibility studies from NOV 2021 to MAR 2022.

ENGLISH SUMMARY

Bioactive glasses reveal superior advantages as bone transplant scaffolds with desirable biocompatibility and no post-operation effect compared to metal and plastic scaffolds. However, intrinsic brittleness and hardness could hardly guarantee bioglasses accommodate cyclic loadings. On this basis, bioactive hybrids are designed with the introduction of polymers, with an expectation of better flexibility and durability during cyclic loadings. However, phase separation of different phases and relatively low toughness severely restrict further practical applications. Thus, in order to overcome such issues, a more efficient design strategy could be to construct co-networks between inorganic and polymer components. In this thesis, we have designed hybrids with synergistic properties and attempted to control their mechanical properties at the molecular structure level. The main purpose of this work is to shed light on the relationship between molecular structure and mechanical performances, and prepare tough bioactive hybrids for biomedical use.

Specifically, the hybrids in this work are prepared through the sol-gel method. Inorganic components and polymer chains are covalently bonded via coupling agents. Molecular structures, mechanical performances, self-healing abilities, and biocompatibilities are characterized based on both experimental tests and molecular dynamics (MD) simulation investigations. Tough inorganic-organic hybrids for bone regeneration studied herein include i) PTHF (poly tetrahydrofuran)-SiO_2 hybrids, ii) PTHF-SiO_2-TiO_2 hybrids, iii) PTHP (poly tetrahydropyran)-SiO_2 hybrids, and iv) Alg (alginate)-Ca^{2+}-PAA (poly acrylic acid)-SiO_2 hydrogels. The structural details of hybrid materials are determined by nuclear magnetic resonance spectroscopy, Fourier-transform infrared spectroscopy, X-ray diffraction analysis, atomic force microscopy, scanning electron microscopy, and transmission electron microscopy. Moreover, mechanical performances of hybrids are investigated by tensile, compression, hardness, and DMA (dynamical mechanical analysis) tests. MD simulation is applied to investigate the deformation and fracture mechanism of hybrids at the atomic level. Finally, the biocompatibilities of hybrids are evaluated through cytotoxicity, immunohistochemistry staining, and cell proliferation tests.

Based on the aforementioned investigations, the main findings are the relations between mechanical properties and molecular structures. MD simulation indicates that the deformation and fracture behavior of hybrids are controlled by non-covalent intermolecular interactions in hybrid networks, rather than breaking of covalent bonds. Tough hybrids could be achieved by improving such intermolecular interactions in the network through constructing binary/ternary systems, controlling total inorganic-organic ratios, nanoparticle reinforcement, and ionic crosslinking. Moreover, thermal stability, self-healing ability, and cell viability could also be controlled with the adjustment of molecular structure. Finally, this work found a way to resolve the conflict between strength and toughness, which guides tailorable bioactive hybrids

design in the future. Overall these studies provide insights into structural control and mechanical properties improvement for bioactive hybrids.

DANSK RESUME

Bioaktive glasser har store fordele som knogleimplantater grundet deres høje biokompatibilitet og lave post-operationseffekt sammenlignet med metal- og plastimplantater. På trods af disse fordele gør bioglassernes sprød- og hårdhed, at disse dårligt tåler cykliske belastninger. For at løse dette er bioaktive hybrider blevet designet med tilføjelsen af polymerer, med en forventning om bedre fleksibilitet og holdbarhed under cykliske belastninger. Imidlertid begrænser faseseparation af forskellige faser og en relativt lav sejhed kraftigt praktiske anvendelser. For at overkomme disse problemer kunne en mere effektiv designstrategi være at konstruere co-netværk mellem uorganiske- og polymer-komponenter. I denne afhandling har vi designet hybrider med synergistiske egenskaber og forsøgt at kontrollere deres mekaniske egenskaber på det molekylære niveau. Hovedformålet med dette arbejde er at kaste lys over forholdet mellem molekylær struktur og mekaniske egenskaber, og producere hårde bioaktive hybrider til biomedicinsk brug.

Specifikt er hybriderne i dette arbejde fremstillet gennem sol-gel-metoden, hvor uorganiske komponenter og polymerkæder er kovalent bundet via koblingsmidler. Molekylære strukturer, mekaniske egenskaber, selvhealende evner og biokompatibilitet er dernæst karakteriseret baseret på både eksperimentelle tests og molekylær dynamiske (MD) simuleringer. Seje uorganisk-organiske hybrider til knogleregenerering, der er undersøgt i denne afhandling, omfatter i) PTHF (polytetrahydrofuran)-SiO_2-hybrider, ii) PTHF-SiO_2-TiO_2-hybrider, iii) PTHP (polytetrahydropyran)-SiO_2-hybrider og iv) Alg (alginat) Ca^{2+}-PAA (polyakrylsyre)-SiO_2 hydrogeler. Strukturen af hybridmaterialer er undersøgt vha. kernemagnetisk resonansspektrosko Fourier-transformation infrarød spektroskopi, røntgendiffraktionsanalyse, atomkraftmikroskopi, skannings elektron mikroskopi og transmissions elektron mikroskopi. Desuden er hybriders mekaniske egenskaber undersøgt ved træk-, kompressions-, hårdheds- og DMA-test (dynamisk mekanisk analyse). MD-simuleringer er anvendt til at forstå hybridernes deformation og brudmekanisme på atomart niveau. Endelig evalueres hybridernes biokompatibilitet gennem cytotoksicitet, immunohistokemi-farvning og celleproliferations tests.

Baseret på nævnte undersøgelser er hovedfundene i denne afhandling sammenhængen mellem mekaniske egenskaber og molekylære strukturer. MD-simuleringer indikerer, at hybridernes deformation og revneadfærd styres af ikke-kovalente intermolekylære interaktioner mellem polymer- og silikanetværk snarere end brud af kovalente bindinger. Hårde hybrider blev opnået ved at forbedre sådanne intermolekylære interaktioner i netværket ved at konstruere binære/ternære systemer, kontrollere forholdet mellem uorganiske og organiske delkomponenter, introducere nanopartikler som forstærkning samt ionisk krydsbinding. Derudover kunne termisk stabilitet, selvhealende evner og cellelevedygtighed også kontrolleres med justering af den molekylære struktur. Endelig blev der i dette projekt opdaget en måde at løse

konflikten mellem styrke og sejhed i disse systemer, hvilket kan guide skræddersyede design af bioaktive hybrider i fremtiden. Generelt giver denne afhandlings undersøgelser indsigt i strukturel kontrol og forbedring af mekaniske egenskaber i bioaktive hybrider.

ACKNOWLEDGEMENTS

I would like to express my sincere gratitude to numerous persons who assisted me over my three-year Ph.D. journey.

I would like to firstly thank my supervisor, Prof. Morten Mattrup Smedskjær. The story was from a skype talk 3 years ago, we applied for a CSC scholarship together and began my Ph.D. study in Denmark in 2019. Following that, with his help and support, I am able to finish my research tasks on my own. His commitment to research and scientific understanding inspired me a lot. During monthly talks and constructive discussions, he motivated me to design experiments, write high-level scientific articles, and overcome challenges in research. I am really grateful for his assistance.

Next, I would also like to give my deep thank to my co-supervisor, Associate Prof. Donghong Yu. Working with him over these three years is really memorable. His enthusiastic and meticulous attitude to research greatly inspired my own research. Monthly discussions with him are pretty valuable. He not only helped me a lot to overcome challenges in research but provided me with how to be a researcher in the future.

I would like to thank all of my collaborators, whose outstanding skills and experience made it possible for me to achieve the objective of my research. I would like to thank Dr. Randall E. Youngman from Corning Inc. Dr. Randall was very helpful and knowledgeable about the difficult method of solid-state NMR spectroscopy. In addition, he has been active in manuscript reviewing. I would like to thank Prof. Mathieu Bauchy from UCLA. He often provided me with scholarly discourse and helpful critiques on my MD simulations. I would like to thank domestic collaborators: Associate Prof. Lars R. Jensen provided ever-present helpfulness and assistance with mechanical testing and manuscript reviews. Associate Prof. Leonid. He helped me a lot with AFM measurement. Prof. Peter and Aida, thanks for their collaborations in cell *in vitro* studies. Marcel, appreciate his help in TEM measurement. I also appreciate Assoc. Prof. Deyong Wang for his scientific assistance and helpful discussions.

I also appreciate Professor Congju Li from the University of Chinese Academy of Sciences, who suggested I come to Denmark for different research and living environment. In addition, he introduced me to the world of science and assisted me a lot in applying for a CSC scholarship. I really appreciate his assistance over the last six years. And I appreciate my friends and colleagues in UCAS, Bin, Yuanyuan, Leihong, Zhenjie, Xinyuan, Ran, Xiuling, Fan, Qiang, Chunlei, Di, Tonghui, Shengming, Kaifu, Qiang, they gave me so many supports and suggestions during research and live, even though we are six time zones apart in these three years.

I would also like to thank the doctoral school and otto funding ensured I had a really fancy and unforgettable working period at Nanyang Technological University for 5 months, and experienced tropical Christmas and New Year fortunately. I am really grateful to Prof. Bengang Xing for his kindness and constructive criticism. I really want to extend my appreciation to my colleagues at NTU: Yibing, Abigail, Thang, Eve, Germain, Shonya, Ling. They taught me a lot about cell culturing experiments and bio studies. I wish all of you a fruitful academic career and a bright future.

Working with all of my colleagues in the chemical section is a wonderful experience. They were really helpful in completing my research, evaluating my paper, and engaging in leisure activities such as coffee breaks and cake sharing. I would like to thank everyone for the following: Prof. Yuanzheng Yue, Assoc. Prof. Morten Christensen, Assoc. Prof. Vittorio Boffa, Assoc. Prof. Thorbjørn Nielsen, Assoc. Prof. Mads Jørgensen, Assoc. Prof. Cejna Quist-Jensen, Asst. Prof. Aamer Ali, Dr. Martin Østergaard, Dr. Rasmus Peterson, Dr. Usuma Naknikham, Dr. Katie Kedwell, Dr. Theany To, Dr. Tao Du, Dr. Qi Zhang, Dr. Pengfei Liu, Dr. Zhencai Li, Dr. Junwei Ding, Dr. Ang Qiao, Dr. Chengwei Gao, Dr. Mikkel Bødker, Dr. Junjun Tan, Rasmus Madsen, Søren Sørensen, Johan Christensen, Rasmus Christensen, Peter Jensen, Sheng Li, Xianzheng Ma, Xiangting Ren, Wei Xu, Jiajia Yan, Xinxin Chen, Jingnan Wu, Daming Sun, Zhimin Chen, Yongbao Xiao, Elsebeth Pedersen, Annemarie Davidsen, Anne Flensborg, Lisbeth Wybrandt, Michelle Mortensen, Mohammad Shirazi, Naia H. Johannesen, Tuve Mattson, Mette Haferbier, Timo Kirwa, Camilla Hvass-Raun, Helen Kjerstein Kristensen and Sara Jellesmark.

In addition, I would like to express my sincere gratitude to my wonderful friends in Denmark and the AASI volleyball team: Hanchi, Kai, Cheng, Xueyan, Tianbao, Jiacheng, Jonas, Lars, Mikkel, Simon, Anton, Theis, Martin, Jesper. This list goes on. It is lovely to have them around in Denmark.

My heartfelt thank goes to my family. It is not easy in these Covid years and we haven't met for nearly three years. I really appreciate my parents' endless love, encouragement, and unconditional support along this way. My brother is now pursuing his medical Ph.D. in China. He is the most outstanding person I met and it is my great fortune to have him around in these 26 years. Working as a doctor is super cool but not easy, and I really hope you will enjoy and contribute to the world. I love you all forever!

TABLE OF CONTENTS

CHAPTER 1. INTRODUCTION

1.1. BACKGROUND AND CHALLENGES

After blood, bone is the second most transplanted tissue, and musculoskeletal pathology treatments comprise a significant portion of global healthcare expenditures (e.g., £10 billion per year in the UK). In 2019, the worldwide bone replacement market was valued at USD 2.91 billion and is anticipated to develop at a CAGR of 3.0% until 2030. Current therapies for skeletal defects may result in postoperative infections, and alternative implant materials are therefore being sought (1, 2). Such body implant materials should ideally be biocompatible and biodegradable and able to promote bone growth while also providing mechanical support to the tissue.

The earliest commercial glass was found thousand years ago and it was obtained by melting minerals. Theoretically, glasses are among the strongest man-made materials, which have been used extensively in several application sectors like windows, cars and mobile phones (3). However, seldom of researchers have dreamt glass applications in biomedical fields. With the emergence of the second generation biomedical materials, Dr. Hench creatively developed bioactive glass in 1969 (4-7), and the bioglass family are regarded as one of the most promising substances to be incorporated in the human body for repairing and regenerating bones (8-10). Such 45S5 bioglass reveals desirable abilities of bonding to bone and stimulating growth of bone cells (11, 12). Although bioglasses have been successfully applied into clinical fields, their inherent brittleness caused by oxide glasses compositions makes it hard to apply them in sites that are subjected to cyclic loading, such as human bones (8). Thus, more ductile and flexible bioactive glass-polymer hybrids with complementary advantages have been expected to work as scaffolds for tissue and bone.

For inorganic-polymer hybrids, phase separation and degradation of inorganic/polymer components at different rates are the main challenges since the two phases are not chemically bonded (13, 14). Thus, in order to overcome these challenges, we here consider constructing covalent bonds between two phases, and forming interpenetrating crosslinked hybrid networks at the molecular level through covalent via covalent bonds. Moreover, desirable toughness as well as strength of hybrids should be taken into consideration since their applications of implanting into body and need to bear cyclic loads. Different methods are usually applied to achieve the aim, e.g. binary/ternary systems (15-21), nanocomposite reinforcement (14, 22, 23), and ionic bondings (15, 24, 25). As to hybrid materials, improved toughness could be achieved through controlling total inorganic vs. polymer compositions, size and species of inorganic NPs, and variation on polymer networks. Meanwhile, an improved understanding of their complex synthesis is required for successful commercialization of the hybrid biomaterials, including the incorporation of calcium which is needed to promote interfacial hybrid-bone bonds (9, 10, 26, 27). Specifically, biodegradable functionalized polymers need to be synthesized to ensure that they are

suitable for a tissue scaffold and with a coupling agent to link with the inorganic glass. This also demands verifying the mechanical characteristics and congruent dissolution of the two phases, which is vital for preventing *in vivo* instability of the scaffold and phase migration. (8, 28). In summary, the aim of this project is to synthesis bioactive hybrids through organic and inorganic combination and investigate their mechanical and biological properties, with the long-term goal to enable their clinical use.

1.2. SCOPE AND OBJECTIVES

The overall purpose of this Ph.D. project is to explore the relationship between the hybrid's mechanical properties and their molecular structures by means of preparing tough inorganic-organic hybrids and investigating their biocompatibilities to bone cells. Specifically, this thesis is concerned with experimental studies together with molecular dynamic (MD) simulation that are combined to investigate deformation/fracture mechanisms of these hybrids, with the desire to pave the way for further tailorable hybrids design. Mechanical properties are improved via adjusting inorganic/organic weight ratios, silica structures/size, introducing dual nanoparticles (NPs), and binary/ternary polymer networks. Additionally, such strategies have also been applied into hydrogels with improved strength and toughness. Besides mechanical performances, multi-functions e.g. self-healing abilities, quick shape recovery, and durability of abovementioned materials have been systematically discussed. Furthermore, this thesis also attempts to research the biocompatibility of the hybrids to bone cells, including cytotoxicity, cell attachment, as well as proliferation behaviors. In conclusion, the thesis seeks to illuminate the following aspects:

- Understand the impact of SiO_2 structures and inorganic compositions on mechanical properties of hybrids.
- Understand the impact of binary/ternary interpenetrating networks on hybrid materials.
- Reveal the correlation of MD simulation with experiment results to aid the design of tailorable hybrid materials.
- Develop tough hydrogels reinforcement strategies.
- Confirm biocompatibility and proliferation of bone cells on bioactive materials.

The thesis aims to deliver ways for tough inorganic-organic bioactive hybrids and reveal the deformation and fracture mechanisms. The thesis starts with the fundamental theory and design of hybrid materials in Chapter 2, as well as molecular structures in Chapter 3. Then, the main methods for preparing tough hybrids and related mechanical tests and mechanisms are summarized in Chapter 4, and biocompatibility as well as *in vitro* studies are introduced in Chapter 5. Finally, the overall findings and results are summarized and discussed in Chapter 6.

1.3. THESIS CONTENT

The main experiments of this thesis, including syntheses, structural characterization, mechanical properties of all hybrid materials, were conducted at Aalborg University. Cell studies were completed in Nanyang Technological University, Singapore. This thesis provides a comprehensive analysis of the findings provided in three peer-reviewed scientific papers published during the project, in addition to one submitted manuscript that awaits publication. These papers comprise the primary body of the thesis and are given below with their respective roman numbers:

I. **W. Fan**, R.E. Youngman, X. Ren, D. Yu, M.M. Smedskjaer, "Structural control of self-healing silica-poly(tetrahydropyran)-poly(ε-caprolactone) hybrids". *Journal of Materials Chemistry B.* 9 (2021) 4400-4410.

II. **W. Fan**, L.R. Jensen, M. Ceccato, T.S. Quaade, L. Gurevich, D. Yu, M.M. Smedskjaer, "Flexible inorganic–organic hybrids with dual inorganic components". *Materials Today Chemistry.* 22 (2021) 100584.

III. **W. Fan**, T. Du, A. Dorce, L.R. Jensen, R.E. Youngman, X. Ren, L. Gurevich, M. Bauchy, P. Kristensen, B. Xing, D. Yu, M.M. Smedskjaer, "Resolving the conflict between strength and toughness in bioactive silica-polymer hybrid materials". *ACS Nano* (DOI: 10.1021/acsnano.2c03440).

IV. **W. Fan**, L.R. Jensen, Y. Dong, A.J. Deloria, B. Xing, D. Yu, M.M. Smedskjaer, "Super Tough, Anti-swelling, Self-healing, and Biocompatible Dual-Reinforced Binary Hydrogels". (to be submitted)

CHAPTER 2. FUNDAMENTALS OF INORGANIC-ORGANIC HYBRID MATERIALS

Bioactive glasses reveal excellent properties of bonding to bone and stimulating bone regeneration. However, because of their inert brittleness and hardness caused by inorganic oxide compositions, bioactive glasses could hardly adapt to cyclic loading during long time use. Introducing flexible polymers into the system could effectively improve these limitations. In this chapter, readers will be introduced to certain mechanisms of bioactive glasses for biomedical applications and design of inorganic-organic bioactive hybrids, which are relevant for understanding their fabrications.

2.1. BIOACTIVE GLASSES

Bone repair or regeneration because of trauma, injury, disease, and aging is a significantly important topic for tissue engineering (1). Ideal biomedical scaffolds require well-defined architectures for cell proliferation differentiation into aimed tissues and organs (see Figure 2-1) (9). Moreover, enough mechanical toughness of these scaffolds could guarantee enough support for cell growth, and synthesize new tissue with desired shape and dimensions (29). Plastic and metals have been previously applied as bone regeneration scaffolds, however, besides post-operation infections, fibrous tissue will form around materials after implantation and further restrain their further applications. Thus, alternative implant materials are being sought, which should ideally be biocompatible and biodegradable, and able to promote bone growth while also providing mechanical support to the tissue. In theory, a three-dimensional (3-D) scaffold template is employed to temporarily guide bone cell growth for bone regeneration. Therefore, cells such as bone marrow stem cells should be effectively attached on these scaffolds, and stimulate their production of new bone. Porous structures of these scaffolds are also necessary, since blood vessels could penetrate freely for new bones surviving. Moreover, the scaffold should get biodegraded over time, allowing the bone to regenerate spontaneously. Another way to look at it is that an autograft cancellous bone-like scaffold is required. Furthermore, from an engineering perspective, a desirable scaffold would be constructed of a bioactive and durable components and can be molded into a porous structure comparable to cancellous bone. In contrast, the requirements of a surgeon may not necessarily coincide with those of an engineer. Surgeons expect not only a porous structure, but better mechanical characteristics similar to tissues or bones. The prepared scaffolds can be injected into a bone defect and expanded to fill it, or shaped in the operating room and either pushed into a bone defect and expanded to fill it (28). To sum up, the requirements for an ideal scaffold must live up to five requirements:

biocompatible, desirable mechanical properties, porous 3-D architecture, ability to degrade at the same pace as the formation of new tissues, and to be processed into varied shapes and sizes.

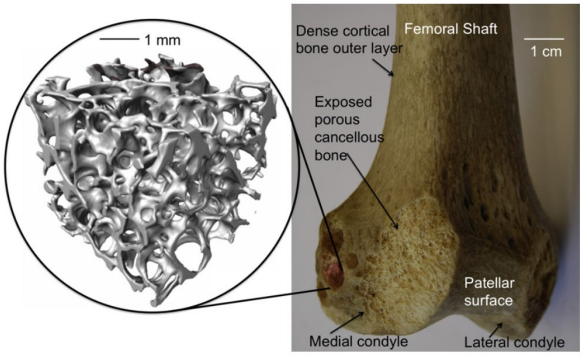

Figure 2-1 A photograph of a human femur that has been core-drilled. Figure reproduced from ref (9).

Glasses have been used by humans for several thousand years, ranging from arrowheads, and drinking vessels to decorative articles and optics. Bioglass 45S5 with a composition of 43.1 mol.% SiO_2, 2.6 mol.% P_2O_5, 24.4 mol.% Na_2O and 26.9 mol.% CaO was firstly developed by Dr. L. Hench in 1969 and applied for clinic use in 1985(4). Bioactive glasses have a high propensity to attach to bone and can be used to regenerate bone. By producing strong interfacial contacts between glass and bone *in vivo*, bioglasses enhance bone cell growth and releasing soluble silicon and calcium ions when hydrated by bodily fluids. A hydroxycarbonate apatite layer is formed on the bioglass surface, which is comparable to bone mineral and is thought to be the process for bone bonding. In contrast to standard metal implants, they may decay in the body at the same place as new bone production and without infection after surgery. As a result, they offer enormous therapeutic promise and have been studied for almost four decades. The open network and modifiers, which comprise alkali and alkaline-earth metals, increase the hydrophilicity of glass and enable water molecules to permeate glass networks considerably more easily than typical glasses. The following are the processes by which bioactive glasses function as ideal bone regeneration scaffolds (30, 31). Alkali ions on the surface of glasses, such as Na^+ and Ca^{2+}, will first be exchanged with H^+ in bodily fluids. The breakdown of SiO_2 compounds occurs as a result of this hydrolysis process, which raises the pH of the fluids. Si-O bonds break gradually as pH and OH^- group concentration rise, resulting in a hydroxycarbonate apatite layer being formed on the bioglass surface, which is similar to bone mineral. These silanol groups will re-polymerize and produce a new silica gel layer, which will attract Ca and P to the bioglass surface. These chemicals will crystallize in the presence of physiological fluids, resulting in mixed carbonated hydroxyapatite (HCA), a major component of bone (see Figure 2-2).

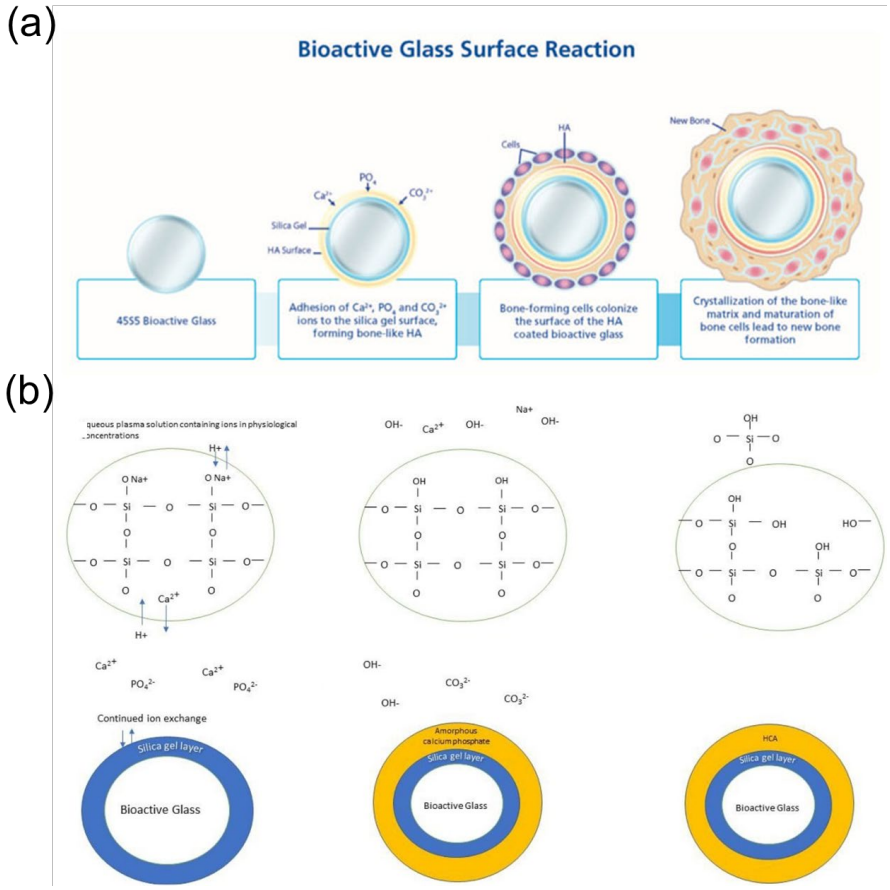

Figure 2-2. The mechanism of bioactive glass in improving bone growth. Figures reproduced from ref. (30, 31).

Thus, based on the above-mentioned mechanism, such solubility or degradability of bioactive glass are helpful to release ions and form apatite layer, further resulting in strong interfacial connections among bioactive glass and bone/tissues. Moreover, such bioactive glasses are composed of different oxides e.g. SiO_2, CaO, P_2O_5, and Na_2O, revealing to avoid foreign body reactions, and solubility or degradability of bioactive glasses could be structurally controlled through changing alkali species or amount. Moreover, bioactive glasses could control the release of active ions and further induce bone regeneration during its degradation (2, 8, 10). An apatite surface layer helpful to bone regeneration will be formed during bioactive glasses degradation and calcium and phosphate ions release. Compared with conventional glasses, bioactive glasses are more hydrophilic on the surface and allow water to penetrate glass networks much easier (see Figure 2-3).

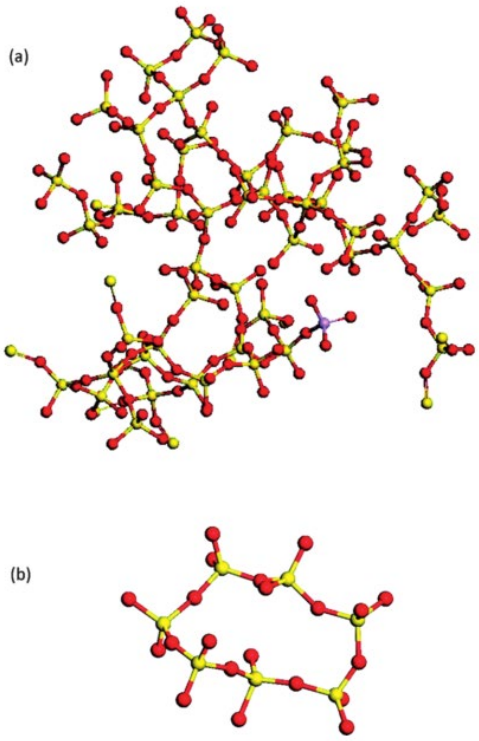

Figure 2-3 MD modeling was used to determine the structure of Bioglass 45S5. Figure adapted from ref. (10).

Based on their compositions, bioactive glasses may be divided into three categories. Silicate bioactive glass, borate bioactive glass, and phosphate bioactive glass are all examples of bioactive glass. Silicate bioactive glasses are the widest applied and investigated. Phosphate bioactive glasses are potentially used as restorable materials because of their constitution of P ions. As to the preparation method of bioactive glasses, there are three major ways: melt-quenching, sol-gel, and template. There are some limitations of melt-quenched glasses, for example, high temperatures required to provoke crystallization processes and the choice of coating is questionable for many applications.

Traditional bioactive glasses are prepared through melting inorganic oxides and carbonates precursors at high temperatures (1200-1500 °C). The sol-gel method is firstly developed by Ebelman and Graham in the mid-1880s, with the finding of hydrolysis TEOS turning to glass-like SiO_2 under acidic conditions. The benefits of the sol-gel approach include its flexibility in generating materials with diverse nano- and microstructures, getting extremely homogenous and chemically pure materials at lower temperatures, and achieving bioactive materials that may be applied in a variety of ways. (32-34). Moreover, sol-gel technology makes it feasible for investigating materials at the nanometer level and could potentially prepare covalently bonded

inorganic-organic hybrid materials with porous structures. The formation of this porous structure is essential because it enables the attachment of cells, as well as the delivery of nutrients. It has been shown that densely packed materials impede cell attaching and differentiation in addition to lowering ingrowth. (28). There are mainly seven steps accompanying the whole sol-gel process (see Figure 2-4) (35): 1) mix all the reagents with hydrolysis, and poly-condensation processes and prepare precursors at room temperature; 2) cast into different molds; 3) gelation for 3D cross-linked networks; 4) aging for decreasing porous and increasing strength; 5) drying for eliminating liquid in materials; 6) dehydration or chemical stabilization for removing silanol bonds; 7) densification under higher temperature.

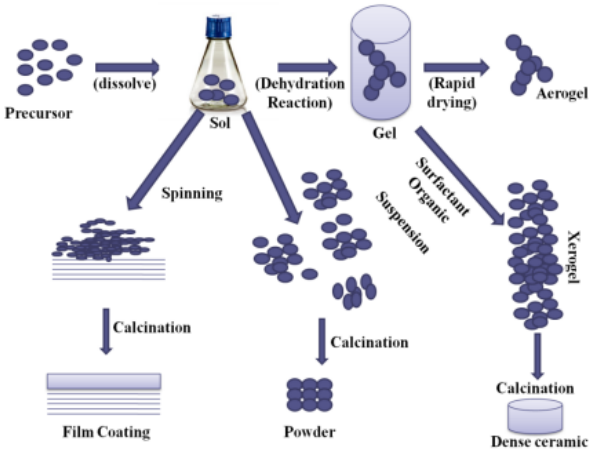

Figure 2-4. Procedures of sol-gel method. Figure reproduced from ref. (35).

2.2. DESIGN OF INORGANIC-ORGANIC HYBRID

Due to brittleness and hardness resulting from intrinsic compositions, bioactive glasses could hardly be applied in sites that are subjected to cyclic loading (such as human bones) to accommodate daily use. Ductile bioactive glass/polymer composite with introducing organic polymer chains into the system could largely improve the flexibility and toughness of bioactive glasses. According to the theory, molecular-scale interactions among polymer and inorganic networks lead the material to behave as a single phase, resulting in consistent, controlled degradation and tailor-made mechanical properties. When cells approach the hybrid's surface, they will make simultaneous contact with the inorganic and polymer constituents, and the hybrid can thus preserve the biological features of bioglasses. In accordance with macromolecular structures and phase connectivity, such composite hybrids could be divided into two main species: i) inorganic and polymer are mechanically mixed; ii) inorganic and polymer networks are covalently bonded (see Figure 2-5) (14).

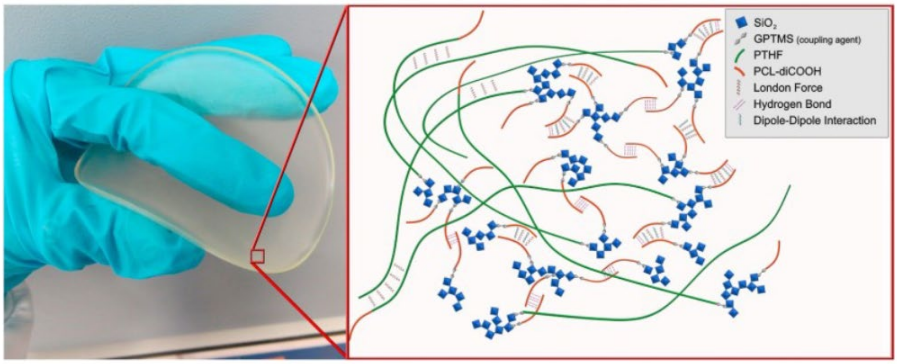

Figure 2-5. Deformation and molecular structure of silica/poly(tetrahydrofuran)/poly(ε-caprolactone) Type-II hybrid. Figure reproduced from ref. (48).

Moreover, compared with bioactive glasses prepared with high temperature melting (above 1200 ℃), which is unrealistic for incorporation with polymers. Sol-gel methods are conducted under 100 ℃ normally, which is much more mild and convenient for preparing such hybrid biomaterials. There are two elementary processes for the sol-gel method, hydrolysis, and condensation of precursors. Tetraethyl orthosilicate (TEOS) is the primary source to prepare silica-based hybrids and will form ramified, three-dimensional SiO_2 networks as solvent swollen gels (36, 37). Preformed organic polymers could be directly added to the aforementioned inorganic precursors and form interpenetrating hybrid networks after undergoing the whole sol-gel processes (see Figure 2-6). However, phase separation is a big hidden danger and could possibly affect synergistic movement and uniformity of compositions in the further.

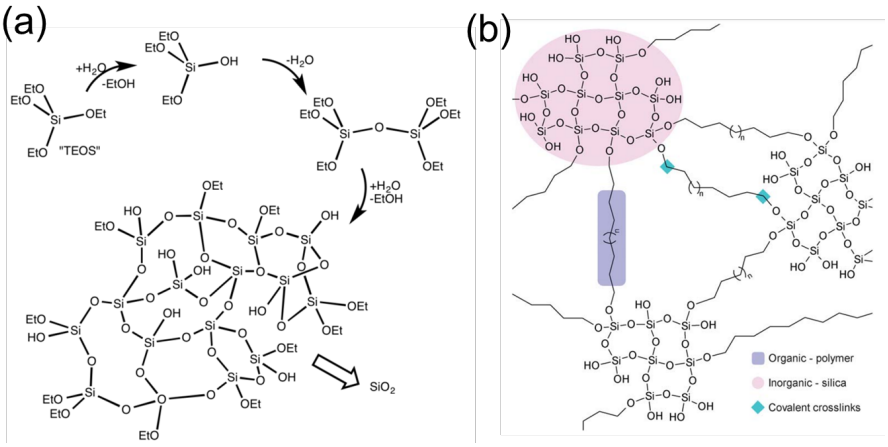

Figure 2-6. Schematic of (a) SiO_2 networks and (b) covalently bonded SiO_2/polymer Class II hybrids. Figures reproduced form ref. (28).

The hybrids can be synthesized by using a polymer with pre-existing organosilane or silanol bonds (-Si–$(OR)_3$, or -Si-$(OH)_3$) or a coupling agent to link silica and polymer. The silane coupling agents, which function as a bridge to covalently link silica networks and polymer chains together, are typically alkoxysilanes that contain reactive groups being able to react with complementary groups on polymers (such as –COOH), causing its alkoxy groups (–OR) to get hydrolyzed and then condensate with the sol-gel silicate network. As a result, the degree of cross-linking may be designed independently of the polymer's molecular weight, making a custom synthesis of organic polymers with functional groups as side groups of a chain desirable. For example, the epoxide group of glycidoxypropyl trimethoxysilane (GPTMS) can participate in a ring-opening process with suitable cyclic ether monomers (38-41), while inorganic precursors, e.g., vinyltriethoxysilane, diethoxymethylvinylsilane, and diethoxydivinylsilane with vinyl functional groups can react with other vinyl monomers via a free radical polymerization mechanism (see Figure 2-7) (42). The silyl groups could in turn react with TEOS as the inorganic precursor through the sol-gel condensation process. This allows the inorganic component to covalently link to organic polymer chains, promoting its uniform dispersion in the hybrid network and preventing further phase aggregation and separation (43). Complex hybrid networks could be formed during long-time hydrolysis and poly-condensation processes. Thus, in this way, such covalently linked inorganic-organic hybrids guarantee the synergistic movement of hybrids and avoid phase separation in the final.

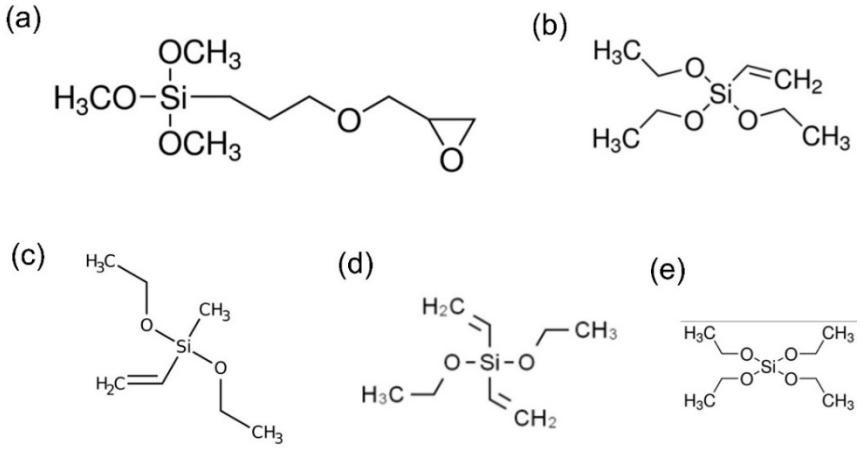

Figure 2-7. Molecular structures of typical organosilane (a) glycidoxypropyl trimethoxysilane (GPTMS); (b) vinyltriethoxysilane (VTES); (c) diethoxydivinylsilane (d) diethoxymethylvinylsilane and (e) tetraethyl orthosilicate. Figures adapted from paper III.

2.3. SUMMARY

Bioactive glass functions as an ideal candidate for tissue engineering, especially for bone repair and regeneration. During experimental research and clinic applications, its open network allows deeper penetration of water molecules and formation of apatite layer, guarantees strong interfacial bonding between scaffolds and bones. Additionally, bioactive glasses are normally prepared through high-temperature melting and are composed of SiO_2, CaO, P_2O_5, and Na_2O, the solubility and biodegradability could be controlled through the amount of different compositions. However, due to absolute oxide glasses compositions, bioactive glasses are too brittle and hard, and these drawbacks could hardly reach the requirements of cyclic loading for body use. Thus, introducing organic polymers could be an ideal option to improve the flexibility of scaffolds.

The Sol-Gel technique is an appropriate option for creating bioactive scaffolds, and it could be successfully processed under mild temperatures. Inorganic precursors (TEOS is the main precursor for preparing silica-based hybrids after hydrolysis and condensation) and organic polymers could form interpenetrating networks through sol-gel processes. Coupling agents, which could covalently link inorganic networks and polymer chains together, structurally avoid the phase separation and ensure synergistic movement and behavior of hybrid materials. In this way, we could not only improve the flexibility of original bioactive glasses but also ensures hybrids function as a whole system. These are the main concept of this chapter.

CHAPTER 3. STRUCTURE CHARACTERISTICS OF HYBRID MATERIALS

Compared with bioactive glasses, much more flexibility guarantees the durability of hybrids under cyclic loading for practical applications as biomedical scaffolds. However, in order to work synergistically and avoid phase separation/aggregations, co-networks with covalent bonds are expected. Based on the introduction in Chapter 2, covalently bonded inorganic-organic hybrids are typically prepared with sol-gel processes. Therefore, this chapter provides a fundamental description of molecular structures of both inorganic and polymer networks, confirmed by various testing methods, and investigates possible relations with their further mechanical and other functional performances.

3.1. OVERALL MOTIVATION

Compared with traditional inorganic bioglasses, introducing polymers in inorganic-organic hybrid materials will result in many property improvements. More flexible and tough materials could be expected with shape adaption abilities in practical applications. Thus, structures of inorganic NPs, polymer networks as well as co-network structures should be systematically researched. Firstly, to construct covalently bonded hybrid networks, coupling agents are usually considered based on their structures, reaction mechanism, and bridging efficiencies. Moreover, *in situ* prepared inorganic NPs are expected since they are beneficial for uniform dispersion in the matrix and further adequately reacting with polymers. Finally, T^n and Q^n structures in silica-based hybrids will primarily affect the branches and rigidity of inorganic networks (44-46). Thus, the polymer chain structures, the inorganic branched networks, and reaction efficiencies should be carefully considered before hybrid design. The abovementioned aspects could guide tailorable hybrid preparation at the atomic level and further result in subsequent functional performances.

3.2. COUPLING AGENTS IN HYBRID NETWORKS

For silica-polymer hybrids design and preparation, a silane coupling agent is usually applied to covalently link these two networks together, and thus avoiding phase separation/aggregations. Different species of silane coupling agents are chosen due to different reaction mechanisms. For example, as introduced in Chapter 2, vinyltriethoxysilane (VTES) with vinyl functional groups could effectively participate in free radical polymerization with other vinyl monomers. In contrast, the epoxide group of glycidoxypropyl trimethoxysilane (GPTMS) can react via a ring-opening

polymerization mechanism with suitable cyclic ether monomers (43) (see Figure 3-1). On the one hand, these functional groups will covalently link with polymer chains with polymer reactions, meanwhile, the silyl groups can react with other silica precursors, e.g., tetraethyl orthosilicate (TEOS) and form inorganic networks under a mild sol-gel condensation process.

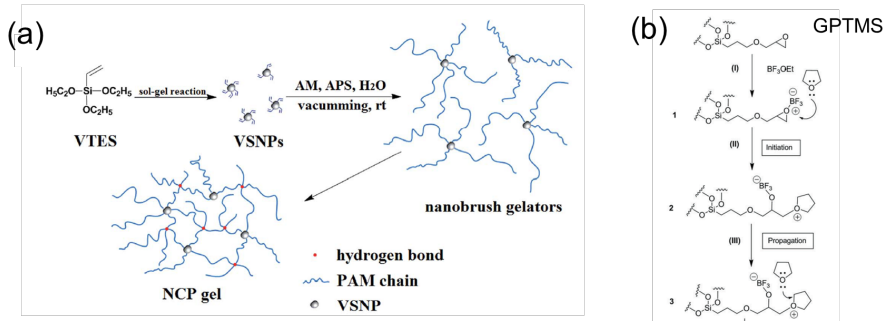

Figure 3-1. Structures of VTES and GPTMS, and corresponding reaction mechanisms. Figures reproduced from ref. (54, 48)

For PTHF-SiO_2 hybrids, ^{13}C NMR could structurally investigate the role of GPTMS and determine whether it gets reacted (see Figure 3-2). The typical signal of epoxide ring in GPTMS could be found at 44 and 51 ppm, however, with the dispersion of these peaks in hybrids, ^{13}C spectra suggests that GPTMS in hybrids are get ring opened and reacted. Furthermore, these resonances move to downfield shifts between 62 and 72 ppm also proves the ring-open process (40). Such ^{13}C NMR results confirm GPTMS functions in hybrid networks during polymerizations.

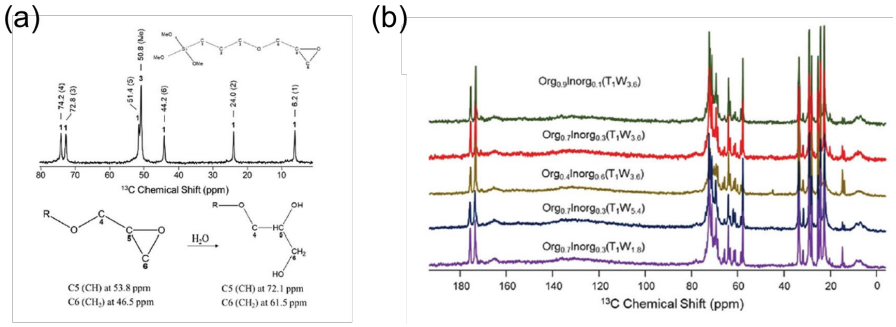

Figure 3-2. (a)^{13}C NMR of GPTMS monomer before and after ring opened; (b) ^{13}C NMR of hybrids. Figures adapted from paper I.

In comparison, for hybrids covalently linked with VTES, the results could be verified via the FTIR method. The disappearance of typical -C=C vibrations from 1610 to

1640 cm^{-1} in materials demonstrates the polymerization of AA monomers and VTES after the free radical polymerization process (see Figure 3-3).

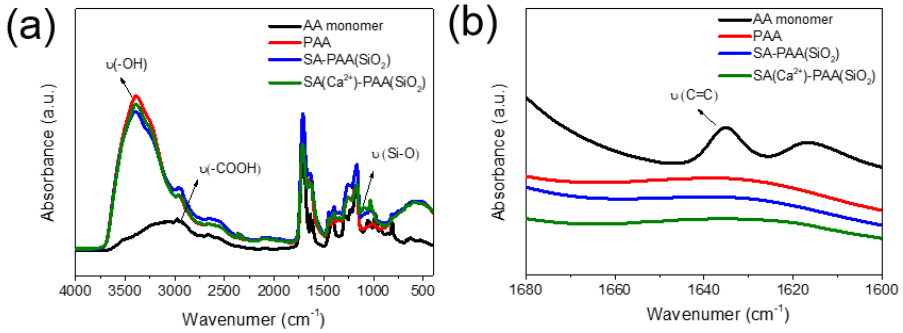

Figure 3-3. FTIR spectra of hydrogels at specific wavenumber range. Figures adapted from paper IV.

3.3. SILICA STRUCTURES AT MOLECULAR LEVEL

For the experimental part, hybrids are fabricated with the sol-gel method, with hydrolysis and condensation. Silica network structures are controlled by changing the molar ratios of H_2O and TEOS, and the final structures are determined by ^{29}Si NMR. Basically, there are four different structures for hydrolyzed TEOS. Here Q^n is distinguished based on the number of condensed -OH and/or -OEt groups in a silica molecule (41). Thus, more Q^2 structures ensure flexibility of inorganic chains, while Q^4 structures promote bulky three-dimensional networks (see Figure 3-4). Therefore, silica structures both in silica bulks and hybrids are compared for further research.

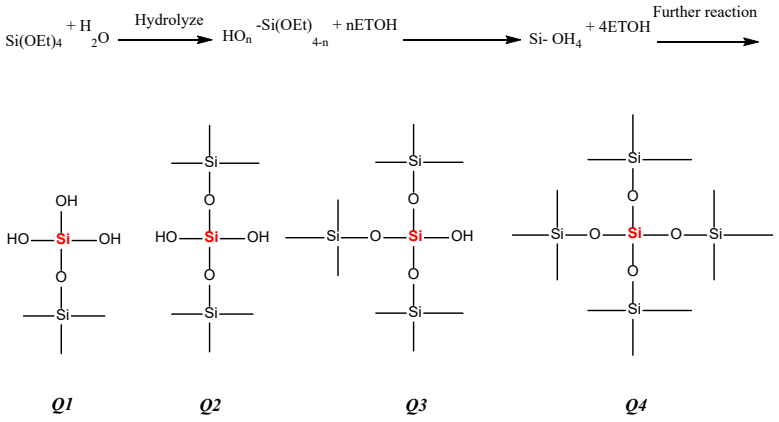

Figure 3-4. Structures of hydrolyzed TEOS with different structures. Figures adapted from paper I.

Firstly, as to pure silica bulks, which is prepared by hydrolyzing TEOS with various TEOS:H_2O molar ratios. As can be seen in Figure 3-5, typical ^{29}Si chemical shifts could be observed at 92.3, 101.7, and 110.9 ppm, which can be assigned to Q^2, Q^3, and Q^4 units, respectively (47, 48). A higher fraction of fully crosslinked (Q^4) structures was obtained for the material with less water system ($TEOS_1H_2O_{1.8}$). The differences for Q^2, Q^3, and Q^4 in each sample are relatively small, but consistent with excess water being available to shift the silanol condensation (elimination of H_2O) back towards more Si-OH (Table 3-1) (40).

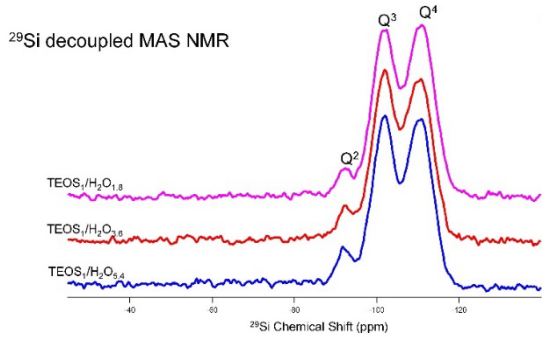

Figure 3-5. ^{29}Si NMR spectra of inorganic bulks in different TEOS/H_2O molar ratios. Figure adapted from paper I.

Table 3-1. The relative intensity (I) and position (δ) of the Q^n units in the various hydrolyzed structures. Analysis of solid-state ^{29}Si MAS-NMR spectroscopy yields the findings.

	Q^2		Q^3		Q^4	
Sample	δ [ppm]	*I* [%]	δ [ppm]	*I* [%]	δ [ppm]	*I* [%]
$TEOS_1H_2O_{1.8}$	−92.3	5	−101.7	43	−110.9	52
$TEOS_1H_2O_{3.6}$	−92.7	7	−101.7	45	−110.4	50
$TEOS_1H_2O_{5.4}$	−92.3	7	−101.7	44	−110.6	49

However, situations are different for hybrids (see Table 3-2). Due to the existence of coupling agent GPTMS, hydrolyzed TEOS could react with *T*-type silica and form final silica networks together. T^1 and T^2 structures refer to partially condensed units with two and one Si-O-Si bonds, respectively. While T^3 structure represents fully condensed with three Si-O-Si bonds (43). Structures could be referred to Figure 3-6.

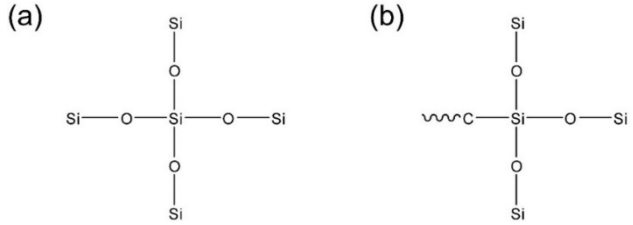

Figure 3-6. Examples of chemical structures of silica (a) Q^4 and (b) T^3 species. Figures adapted from paper III.

After adding TEOS into the organic precursors and reacting with GPTMS, silica structures changed a lot. Corresponding ^{29}Si chemical shifts at -50.5, -59.9, and -66.9 ppm could be assigned to T^1, T^2, and T^3 units, respectively. After comparison, the highest fractions of T^3 and Q^4 units were obtained in hybrids with the previous highest H_2O ratio system ($TEOS_1H_2O_{5.4}$). This result suggests that more Q^2 units in TEOS precursor ensure enough chain mobility, which is beneficial for the subsequent condensation with GPTMS, and results in more T^3 and Q^4 structures in the final hybrid materials (40).

Table 3-2. Position (δ) and relative intensity (I) of the T^n and Q^n units in hybrids with identical I/O ratios. Solid-state ^{29}Si CPMAS-NMR spectroscopy yields the findings.

	T^1		T^2		T^3		Q^3		Q^4	
Sample	δ [ppm]	I [%]	δ [ppm]	I [%]	δ [ppm]	I [%]	δ [ppm]	I [%]	δ [ppm]	I [%]
$O_{0.7}I_{0.3}(T_1W_{1.8})$	−50.9	1	−60.0	17	−67.0	60	−102.5	7	−111.8	15
$O_{0.7}I_{0.3}(T_1W_{3.6})$	−50.5	1	−60.0	17	−66.9	63	−102.2	5	−111.4	14
$O_{0.7}I_{0.3}(T_1W_{5.4})$	−51.3	2	−59.5	15	−66.9	65	−102.3	3	−111.8	15
$O_{0.9}I_{0.1}(T_1W_{3.6})$	−50.5	3	−60.0	25	−67.1	61	−102.2	4	−111.2	7
$O_{0.4}I_{0.6}(T_1W_{3.6})$	−50.4	1	−59.4	13	−66.5	47	−102.4	14	−111.6	26

Besides silica structures, silica NPs distribution and size are the other two important factors in inorganic-organic hybrids. SEM/TEM (EDX) and AFM could be ideal measurements for analyzing element distributions and confirming phase distributions in hybrids. For example, EDX images in Figures 3-7 could clearly state that elements are uniformly distributed in $Polymer_{70}/(Si_{0.6}Ti_{0.4})_{30}$ hybrid. The size of silica NPs could be controlled by reaction time, precursor vs. H_2O molar ratios, and addition of surfactant. As to the silica size in Figure 3-7, TEM could clearly determine the final size of different inorganic NPs sizes, which are approximately 30-50 nm.

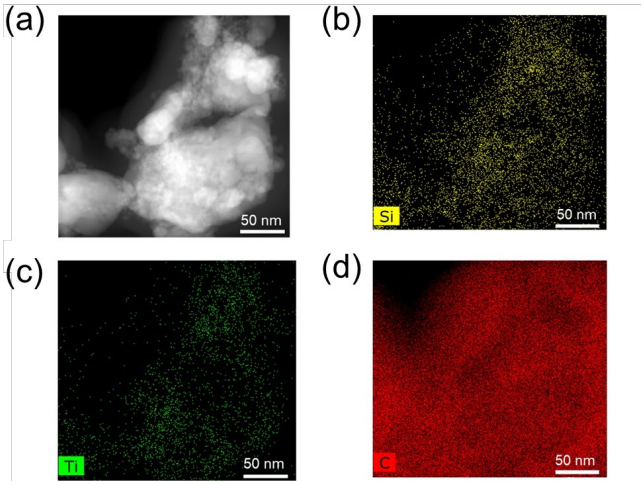

Figure 3-7. TEM morphology of hybrid $Polymer_{70}/(Si_{0.6}Ti_{0.4})_{30}$ and element distribution of Si, Ti and C. Figures adapted from Paper II.

Moreover, no phase separation/aggregation could also be confirmed by AFM results in Figures 3-8. This further proves the uniform dispersion of different phases in hybrids.

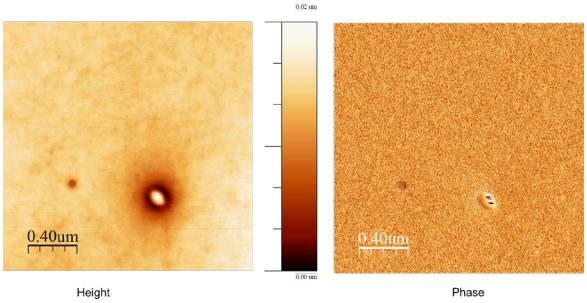

Figure 3-8. AFM topography phase images of PTHF • 8TEOS hybrid. Figures adapted from Paper III.

3.4. POLYMER STRUCTURES A MOLECULAR LEVEL

Since many hybrids are prepared with monomers, the polymerization reactions could be measured by different methods like NMR and FTIR based on reaction mechanisms. Polymers could be selected based on different coupling agents in the system. Jone's have researched a lot of PTHF-based hybrids and their properties (49), while we have investigated more detail both PTHF and PTHP based hybrids. Cationic ring-opening polymerization could be confirmed by ^{1}H NMR as can be seen in Figure 3-9. The radical polymerization process could be checked by the FTIR method, as depicted in Figure 3-3.

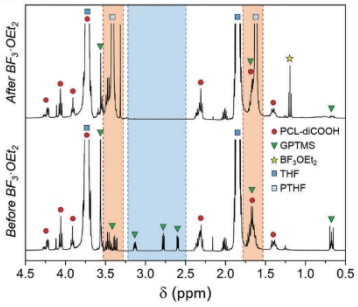

Figure 3-9. Polymerization of THF monomers measured by ^{1}H NMR. Figure reproduced by ref.(48).

Moreover, different polymer structures are also highly rated as reported by Chung et.al (50). Using the reversible addition-fragmentation chain transfer (RAFT) polymerization process, linear, randomly branched, and star-shaped polymers are produced and compared (see Figure 3-10). These hybrids possess similar functional

groups and thermal stabilities. Compared with linear hybrids, randomly branched hybrids could be regarded as various linear chains branched together in a disordered manner. Polymer chains with different lengths form a much compact spatial radius structure in the final. However, as to star shaped hybrids, silica precursors could gather around organic core surroundings, forming a relatively loose structure. At last, when compared with traditional 70S30C bioglass, these hybrid materials all show much-improved flexibility with higher flexibility while comparable strength.

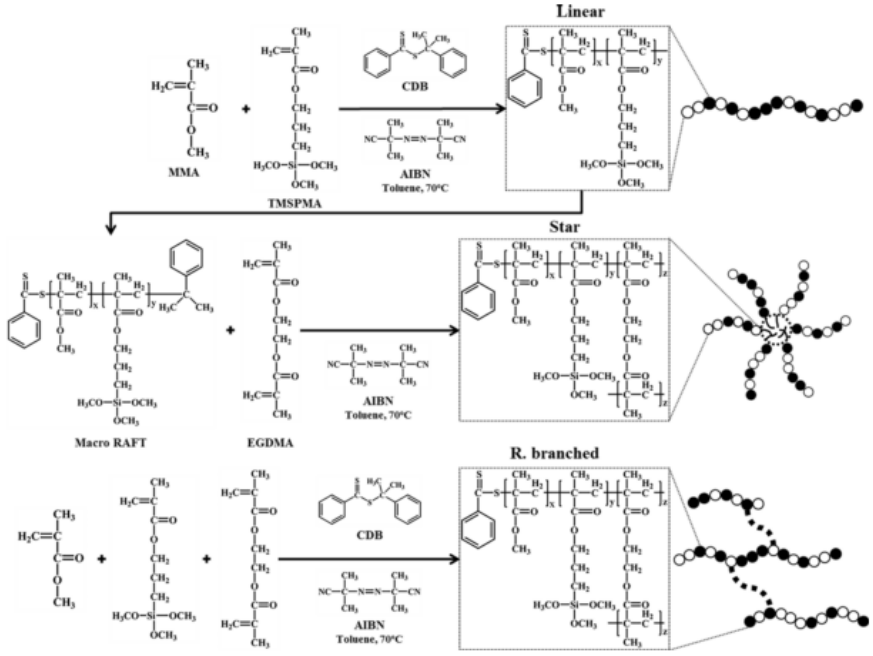

Figure 3-10. Polymerization mechanisms of different structural polymers. Figure reproduced by ref. (49).

3.5. WEAK BONDS IN HYBRID MATERIALS

Besides the abovementioned hybrid networks formed by covalent bonds, reversible weak interactions also count in these materials, especially hydrogels (51-53). These non-covalent reversible interactions, e.g. hydrogen bonds, ionic bonds, and electrostatic forces could break and reform in a short time, which enables certain hybrids with self-healing abilities and quick shape recovery performances in practical applications (see Figure 3-11).

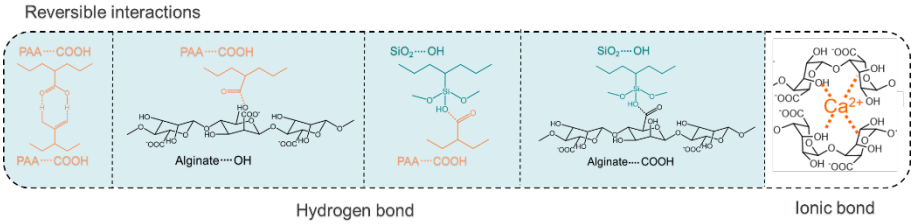

Figure 3-11. Reversible interactions of SA (Ca^{2+})-PAA (SiO_2) hydrogel. Figures adapted from Paper IV.

3.6. SUMMARY

Based on the abovementioned results and investigations, silane coupling agents could effectively bond silica and polymer networks together and reveal no phase separation or aggregation. Therefore, the molecular structures of the hybrid could be controlled via inorganic and polymer sides separately. The structure of inorganic networks may be manipulated with altering the molar ratio of silica precursor and H_2O, different inorganic NPs and total inorganic vs. polymer weight ratios, while the structure of polymer networks can be controlled by trying various monomers. Besides strong covalent bonds in hybrids, reversible non-covalent interactions are beneficial for both the mechanical and functional properties of hybrids. Structure changes by such control have been systematically illustrated in this chapter, and the influences on mechanical properties will be discussed in Chapter 4.

CHAPTER 4. MECHANICAL PROPERTIES OF HYBRID MATERIALS

Compared with bioactive glasses, the flexibility of inorganic-organic hybrids is largely improved with sacrificial strength. Thus, balancing the conflict of flexibility and hardness, toughness with strength, and preparing inorganic-organic hybrids with better mechanical performances are the main topics for further practical applications. Molecular dynamic (MD) simulation could guide tailorable hybrids design at the atomic scale. And mechanical performances could be structurally controlled both at the micro molecular structure level and macro inorganic/organic compositions. Moreover, besides traditional inorganic-organic hybrids, hydrogels combine solid-like mechanical performances and liquid-like transport properties, guarantee super good flexibility to adapt to different shape and deformation requirements. Therefore, in this chapter, the findings of tough inorganic-organic hybrids together with hydrogels will be presented and will provide methods for designing tailored hybrid materials in the future.

4.1. TOUGH HYBRID DESIGN

Usually, a series of methods have been tried to improve the toughness of materials based on previous peer research, e.g., binary/ternary systems, cross-linked networks, nanocomposite reinforcement, and ionic bonding. These methods are beneficial for effective energy dissipation and much higher toughness. Eiji et al. found silica particles in materials could serve as crosslink points, and these clusters rupture easily under external loads to dissipate energy (42, 54-56). Meanwhile, polymer networks could maintain their shapes due to rubber elasticity. Suo and his group also found similar results with hydrogen and ionic bondings with hydrogels (57, 58). Combing a brittle network and ductile polymer network is usually applied for obtaining such tough hybrid materials. Class II hybrids inherit both flexibilities of polymers and the strength of inorganic glasses, which seem hard to get balanced in hybrid materials. Thus, resolving phase separation and non-synergy, strength and toughness, flexibility and brittleness are the main conflicts in these inorganic-organic hybrids. We have tried with the inorganic and polymer aspects separately. Results are confirmed by different mechanical tests, and the mechanism is revealed via molecular dynamic (MD) simulations.

4.2. MOLECULAR DYNAMIC (MD) SIMULATIONS

Although material toughening methods are quite straightforward, the reinforcing mechanism at the atomic scale still needs further investigation. To get a deeper understanding of the deformation and fracture mechanisms of hybrids and to predict

the changing trend, molecular dynamic (MD) simulation and experimental results are combined in the project (59-61). PTHF·xSiO$_2$ hybrids are chosen to determine the mechanism of deformation and fracture behaviors of hybrids with different inorganic amounts via MD simulation. The stretching process of hybrid PTHF·*8*TEOS can be seen in Figures 4-1a, b. Here, simulated potential energy terms evolution is recognized as a function of the applied strain. Figures 4-1d, e compared influences of covalent bonds and the non-bonded term (includes Van der Waals and Coulombic terms) during stretching. These results confirm that non-bonded intermolecular interactions have more apparent influences on the deformation/fracture of hybrids. The slippage and disentanglement of the polymer chains are the main courses of the deformation and fracture of hybrids. Thus, the existence of SiO$_2$ NPs in hybrids could effectively block the motion of polymer chains and increase frictions in hybrid networks, which could be ascribed to the strengthening mechanism upon hybrid deformation/fracture (43). Thus, based on the MD simulation results, the deformation stress of hybrids is more determined by the non-covalent intermolecular interactions that existed in hybrids. Thus, more branched network structures and more polar bonds in hybrid networks could surely increase the interactions and further stress of hybrids.

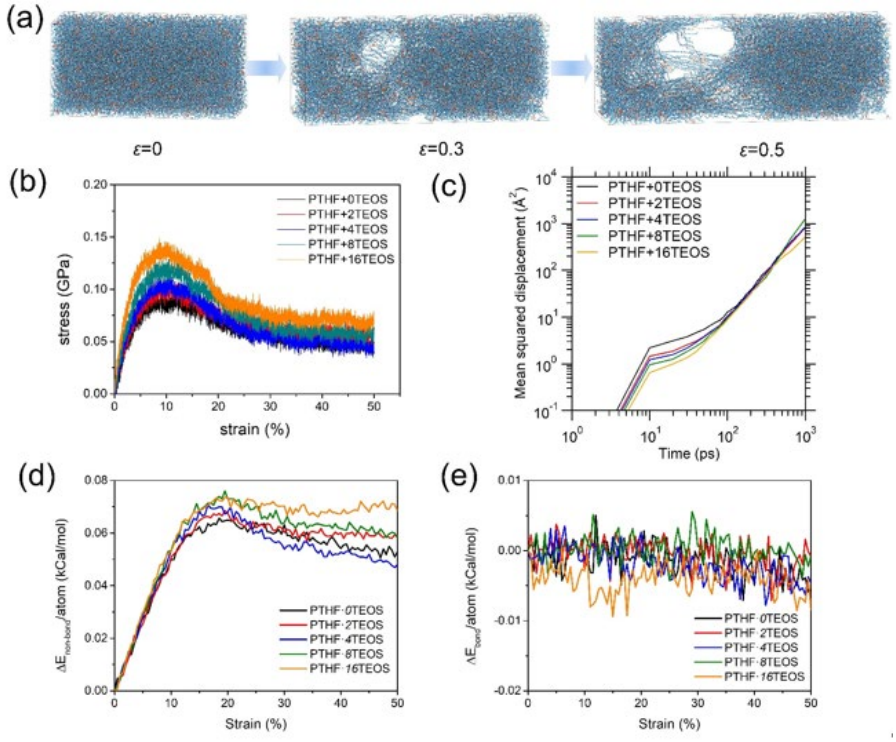

Figure 4-1. (a) Simulated fracture process of PTHF·8TEOS hybrids at the strains of ε=0, 0.3, and 0.5 using CVFF potential. (b) Simulated stress-strain curves of PTHF·xTEOS based hybrids. (c) Mean squared displacement (MSD) of Si atoms in PTHF·xTEOS hybrids as a

function of time during the tensile process. The development of simulated Potential energy terms as a function of the applied strain. (e) Non-bonded energy of PTHF·xTEOS hybrids. (f) Bonded energy of PTHF·xTEOS hybrids. Figures adapted from paper III.

4.3. MECHANICAL PERFORMANCES OF TOUGH HYBRIDS

Toughness, as well as strength, are important parameters for evaluating the mechanical performances of hybrid materials (62, 63). In many cases, we could hardly expect a balance between these two conflict parameters in a system (64, 65). Oxide glasses, for instance, may have a fracture strength of more than 10^2 MPa but are often less durable and flexible. In comparison, polymer hydrogels, which can be stretched to many times their original length but have a fracture strength only in the tens to hundreds of kPa. Strong but brittle or robust yet fragile materials are unsuitable for cyclic stress in most practical biomedical applications. Inorganic-organic hybrids, which combine advantages of both materials, reveal complementary properties and could possibly resolve toughness/strength conflict (13, 66). Based on the abovementioned MD simulation results, strategies for improving intermolecular interactions have been tried in our project. And we have systematically researched influences from the structure of polymer networks, inorganic/organic weight ratios as well as inorganic structures. Methods applied in this project include tensile test, compressive test, hardness, and modulus evaluations (see Figure 4-2).

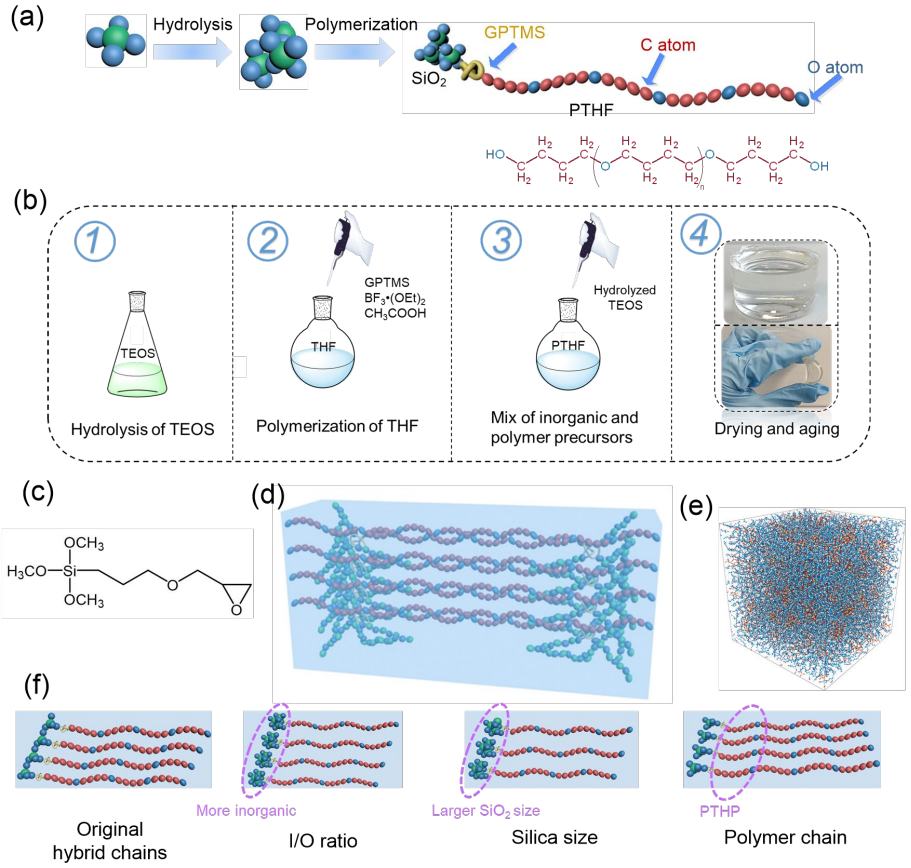

Figure 4-2. (a, b) Preparing process of Polymer-silica hybrids; (c) molecular structure of GPTMS; (d) 3D structural diagram of a Polymer-silica hybrid; (e) MD computed 3D-structure of a hybrid bulk in which the color of the atoms corresponds to that of the panel (a); and (f) structure changes with inorganic and polymer sides. Figure adapted from Paper III.

4.3.1. PTHP-SiO_2 HYBRIDS

For experiments, PTHP-SiO_2 and PTHF-SiO_2 hybrids are prepared for comparison due to their similar reaction mechanism and molecular structures. (49, 67, 68). The extra C atom in the THP monomer should allow for greater tailoring of hybrid mechanical characteristics. However, for polymerization, THP is thought to be resistant to get a six-membered ring opened due to lower ring strain. As a result, PTHP is a rare biomedical hybrid component. Thus, a series of PTHP-SiO_2 hybrids are prepared in such interest and further investigating the influences of various silica structures and inorganic/organic weight ratios. Following previous methods, with an appropriate Lewis acid (e.g., boron trifluoride diethyl etherate) as a catalyst and

GPTMS as the initiator, the cationic ring-opening process also happened and get PTHP polymers (40, 49). GPTMS is also used as the organosilane coupling agent to covalently bond silica and polymer chains together.

As already been introduced in Chapter 3, silica structures could be controlled by changing the molar ratio of TEOS/H_2O. More Q^2 structures in inorganic precursor guarantee chain mobility, while more Q^3 and Q^4 will result in bulky three-dimensional networks. Here, we applied the Archimedes principle, ultrasonic echography, and micro-indentation techniques to determine the density, Young's modulus, and hardness of prepared PTHP-SiO_2 hybrids. From the results, silica structures have very limited influence on density, while the total inorganic-organic weight ratios count. The more inorganic compositions in the system results in a higher density of materials. Moreover, higher inorganic component leads to much more compact inorganic network, which could also provide higher modulus. Furthermore, we show that the hybrid $Org_{0.7}Inorg_{0.3}(T_1W_{5.4})$ with the most T^3, and Q^4 structure has a larger Young's modulus of 1.29 GPa than the other two hybrids ($Org_{0.7}Inorg_{0.3}(T_1W_{1.8})$ and $Org_{0.7}Inorg_{0.3}(T_1W_{3.6})$) with the same inorganic/organic ratio. As a result, both silica structure and the inorganic/organic ratio have impact on hybrid elasticity. More inorganic content and more T^3, Q^4 structures result in higher Young's modulus of hybrids. The hardness of the hybrids reveals similar results, that more inorganic compositions and more T^3, and Q^4 structures improved the rigidity and hardness of hybrids (see Table 4-1) (40).

Table 4-1. Densities, modulus and hardness of hybrids with different compositions. Table adapted from Paper I.

Hybrids	Density (g cm^{-3})	Modulus (GPa)	Hardness (MPa)
$Org_{0.7}Inorg_{0.3}$ $(T_1W_{1.8})$	1.235	0.86	5.0±0.5
$Org_{0.9}Inorg_{0.1}$ $(T_1W_{3.6})$	1.216	0.54	2.6±0.7
$Org_{0.7}Inorg_{0.3}$ $(T_1W_{3.6})$	1.237	1.15	9.1±2.0
$Org_{0.4}Inorg_{0.6}$ $(T_1W_{3.6})$	1.287	1.68	58.8±7.5
$Org_{0.7}Inorg_{0.3}$ $(T_1W_{5.4})$	1.237	1.29	7.0±1.1

Finally, the rheological behaviors of hybrids with various I/O ratios were investigated. That is, the changes in storage modulus (*E'*) and loss modulus (*E''*) with time at 1 Hz for hybrids $Org_{0.9}Inorg_{0.1}(T_1W_{3.6})$, $Org_{0.7}Inorg_{0.3}(T_1W_{3.6})$, and $Org_{0.4}Inorg_{0.6}(T_1W_{3.6})$, at room temperature are evaluated. The maximum storage modulus (300 kPa) is found in $Org_{0.4}Inorg_{0.6}(T_1W_{3.6})$, whereas the lowest is found in hybrid $Org_{0.9}Inorg_{0.1}(T_1W_{3.6})$ (50 kPa). The change in *E'/E''* with I/O ratio shows that with the inorganic component increases, the hybrids reveal much more apparent glass-like behavior (69, 70). Furthermore, the storage modulus and loss modulus of all hybrids are not considerably affected by test time, indicating that the hybrids are elastically stable (see Figure 4-3). (40).

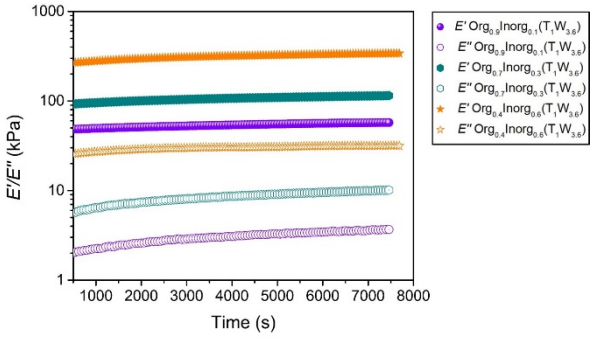

Figure 4-3. Rheology parameters of hybrid $Org_{0.9}Inorg_{0.1}$ ($T_1W_{3.6}$), $Org_{0.7}Inorg_{0.3}$ ($T_1W_{3.6}$), and $Org_{0.4}Inorg_{0.6}$ ($T_1W_{3.6}$) as a function of time storage modulus (E') and loss modulus (E''). Figure adapted from Paper I.

4.3.2. PTHF-SiO_2 HYBRIDS

Based on the above-introduced work, it seems that more inorganic components will result in higher modulus and hardness. However, for practical applications, it is of great importance to balance the strength and toughness of such hybrid materials. We then prepared a series of PTHF-SiO_2 hybrids with the same silica structure but different inorganic/organic weight ratios, expecting to resolve the conflict of strength and toughness in hybrids with such control. Polymer content in these hybrids is changing from 5.1% to 20.9% of the total mass. Figure 4-4 shows the results of uniaxial tensile testing on rectangular samples, the strain at break decreases from 50.0% to 35.2%, whereas the inorganic component of the hybrid increases from 5.1% to 20.9%. The failure stress simultaneously rises from 0.32 to 1.35 MPa. Consequently, hybrids with a greater proportion of inorganic silica have less flexibility and elastomeric deformations. These testing results are generally in accordance with previous findings. However, for PTHF·*8*TEOS hybrid, which not only displays appropriate elongation (31% for compression) and flexibility, but also has high

strength (1.75 MPa). In addition, calculating from stress-strain curves reveals that the hybrid PTHF·*8*TEOS has the maximum toughness at 219 kPa. Elongation and toughness decline dramatically as TEOS content increases after that. So, here we get the conclusion of achieving strength/toughness balance through controlling total inorganic/organic weight ratios and obtaining optimized hybrid materials (43).

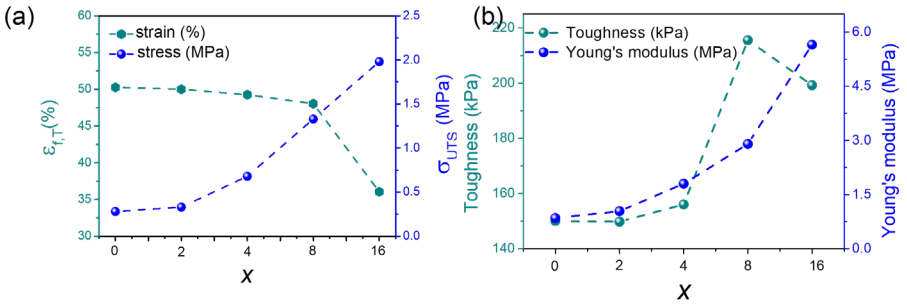

Figure 4-4. (a) Typical uniaxial tensile test, ultimate tensile stress and strain at break; (b) Toughness and Young's modulus determined with stress-strain curves. Figure adapted from Paper III.

Additionally, the size of inorganic NPs is also an important factor to affects the mechanical performance of hybrids. Except for the previous report of using surfactant during hydrolysis of inorganic precursors, we designed a way to control the size of silica NPs from the polymerization mechanism. For PTHF·*x*TEOS hybrids, GPTMS is the only bridge for covalently bond inorganic NPs and polymer chains together. Thus, the amount of GPTMS added to the system could directly control the quantity of NPs, while TEOS could control the size of covalently bonded NPs. Thus, as [GPTMS]/[TEOS] declines, larger silica NPs are created for a fixed total I/O ratio, and vice versa. Density and TGA results both confirm that these hybrids have very close I/O ratios. However, by evaluating mechanical properties via compressive tests (see Figure 4-5), we find that the stress at failure decreases when GPTMS is reduced, for example, the stress at failure is 2.34 MPa for hybrid 10GPTMS:0TEOS while 0.75 MPa for hybrid 2GPTMS:8TEOS. Meanwhile, changes in strain upon failure are minimal. (within the range of 32% to 37%). Toughness and Young's modulus, as determined by stress-strain curves, also decrease with the increment of silica NPs size. Thus, based on these results, smaller silica NPs guarantee uniform dispersion of different phases in hybrids, allowing for more intermolecular interactions between inorganic network and polymer chains, and further resulting in higher fracture stress with the deformation test.

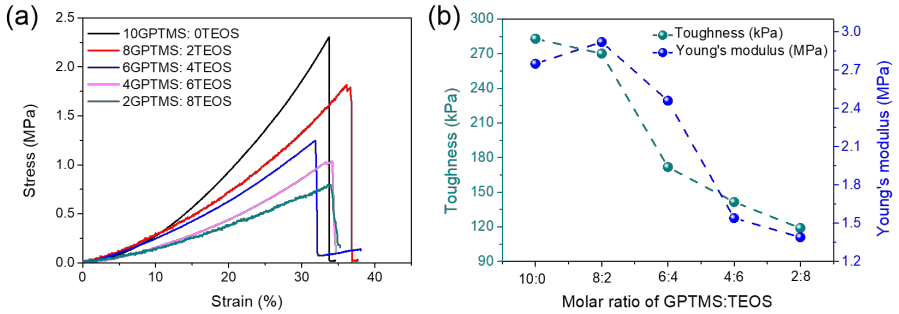

Figure 4-5. (a) Typical uniaxial compressive curves of yGPTMS:zTEOS hybrids; (b) Toughness and Young's modulus determined with stress-strain curves. Figure adapted from Paper III.

4.3.3. TIO_2/SIO_2-PTHF-PCL HYBRIDS

Besides applying SiO_2 NPs, many previous researches reported applying semiconducting NPs, e.g. TiO_2, ZrO_2, and ZnO_2 as multifunctional crosslink networks for improved mechanical performances (71-73). For instance, Du et.al. introduced both nano-SiO_2 and nano-TiO_2 particles in PAM hydrogels, which functioned as crosslinkers and nanofillers in the system via the traditional sol-gel method (74). Such hybrid hydrogel reveals improved strength and toughness in the final due to multi-intermolecular interactions in hydrogel networks. In our project, we tried to use SiO_2 and TiO_2 NPs in polymers and obtained TiO_2/SiO_2-PTHF-PCL hybrids. Because of the silane coupling agent GPTMS, SiO_2 NPs could covalently bond to polymer chains while TiO_2 NPs need to form Si-O-Ti bonds and indirectly bond with polymer networks. A series of hybrids are prepared by changing the molar ratio of TEOS: TBOT (10:0, 8:2, 6:4, 4:6, 2:8). Mechanical tests were conducted for confirming the influences of dual inorganic compositions. After comparing with other hybrids, hybrid $Poly_{70}(Si_{0.6}Ti_{0.4})_{30}$ reveals the best mechanical properties. Hybrid $Poly_{70}(Si_{0.6}Ti_{0.4})_{30}$ could be compressed to 80% of its original height and stress at a break of 1.4 MPa (see Figure 4-6). The improved mechanical performances of hybrid $Poly_{70}(Si_{0.6}Ti_{0.4})_{30}$ could be mainly ascribed to two reasons, for one thing, multi interactions in the hierarchical structures formed by dual inorganic NPs and polymers result in a more compact structure. Moreover, Ti-O bond energy (662 kJ/mol) is much higher than Si-O bond (432 kJ/mol), which results in much higher strength under deformations (41).

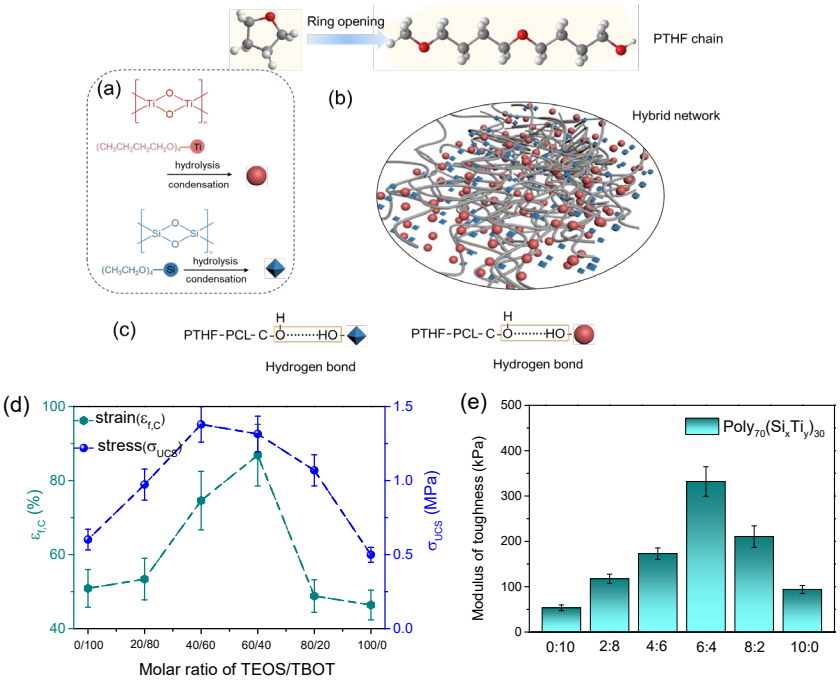

Figure 4-6. (a) Hydrolysis of TEOS and TBOT inorganic precursors; (b) schematic illustration of hybrid TiO_2/SiO_2-PTHF-PCL networks; (c) reversible interactions of nano-SiO_2 and nano-TiO_2 particles with polymer chains; (d) stress and strain of hybrids with changing molar ratio of TEOS/TBOT; (e) toughness of hybrids calculated by the compressive curves. Figure adapted from Paper II.

4.4 MECHANICAL PROPERTIES OF SOFT HYDROGELS

In practical applications, e.g. tissue engineering, drug delivery, and soft robotics require materials could adapt to a large degree of deformation without break, while normal inorganic-organic hybrids could hardly match. Thus, hydrogels become ideal candidates since they could be extended to almost over 10 times more than their original length and compressed to 70-80% of their heights without permanently deforming or breaking (75-77). Typically, hydrogels consist of 3D networks of hydrophilic polymers that are cross-linked with a substantial quantity of water and present superior mechanical flexibility and chemical properties (57, 78). Moreover, due to their propensity to soak up water, hydrogels are a suitable candidate for creating a hydrated structure that resembles native soft tissues (79, 80). However, due to low polymer compositions in the system, hydrogels inevitably lack the necessary toughness to absorb energy and deform without damage while undergoing large deformations. A variety of chemical and physical reinforcement methods have been attempted to improve their strength and toughness. The most common way is to use

reversible crosslinks, e.g. hydrogen bonds, ionic bonds, reversible covalent bonds, and metal coordination bonds. These reversible interactions could reform after breaking quickly, which are able to effectively dissipate energy, transfer center loads to neighboring networks, and get self-healed (38, 81). Reversible interactions in hydrogels greatly avoid toughness-to-fracture coupling and offer hydrogels with desirable stiffness as well as extensibility. However, replacing permanent covalent bonds with reversible bonds, will result in gradual shape changes and could restrain many practical applications. Thus, an alternative route could be to construct multi-network architectures like a double polymer network (DN) (82-84). Normally, interpenetrating crosslinked networks are formed by polymers and one of which is relatively stiffer while the other one is more stretchable. The stiffer network will firstly break and dissipate energy due to reversible bonds for high toughness while the stretchable one could hold hydrogel together and keep a good shape memory. The stronger intermolecular interactions of DN hydrogels improve toughness a lot and could result in multi-functions simultaneously (see Figure 4-7). Suo et. al tried to combine sodium alginate and acrylamide monomers and constructed an alginate-polyacrylamide double network hybrid gel. The produced PAM-Alginate hydrogels are 90% water can be stretched 20 times their original length, and have fracture energies of 9,000 J m^2. Even for samples with notches, the length may be stretched to 17 times its original length (57). NP reinforcement is also a common approach to significantly enhance the strength and toughness of such alkene polymers (57). That is, inorganic NPs could function as analogous crosslinking points (ACPs) to enable the hydrogels to withstand more external stress at a fixed strain and transfer stress to neighboring network chains and inorganic NPs incorporation. Xie *et al.* have used PAM hydrogels with size controllable SiO_2 NPs, showing an ability to be stretched over 1000% compared with their original length (42). However, the strength of the abovementioned hydrogels is only on the order of 10s of kPa and relatively low. So, we hope to find ways to improve both strength and toughness of hydrogels simultaneously.

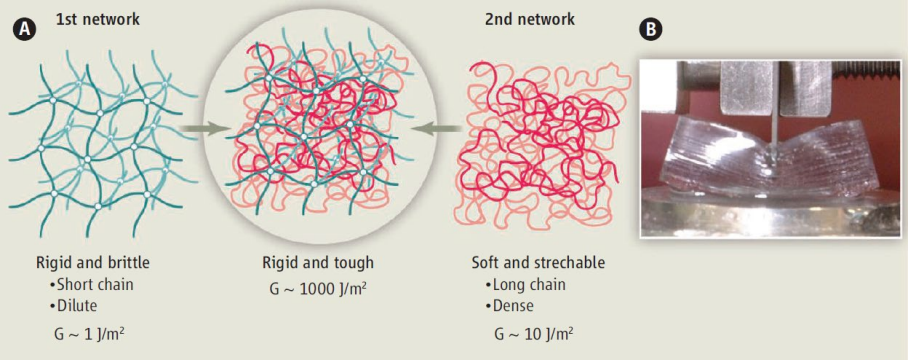

Figure 4-7 (a) By mixing multiple network materials, it is possible to develop durable double-network materials. (b) A photograph of a double-network hydrogel containing 90 percent water by weight. Adapted figures from ref (82, 83).

Sodium alginate (SA), as a natural anionic polymer with benefits such as biocompatibility, low toxicity, and cheap cost, could be potentially applied in bioengineering applications (85). The ionic crosslinking method with divalent cations (e.g., Ca^{2+}, Fe^{3+}) is the most frequent method for producing durable Alg hydrogels under mild circumstances. Hydrophilic poly-acrylic acid (PAA) is a desirable material for preparing hydrogels due to their carboxyl groups as pendants which could effectively improve intermolecular interactions among polymer networks via plenty of hydrogen bonds. Additionally, neutralized PAA could function as tissue scaffolds for wound and bone repair due to their desirable biocompatibility. Thus, we tried to construct PAA-Alginate DN hydrogels to work as a candidate for bone regeneration scaffolds. Moreover, in order to improve toughness and strength, we combined PAA and alginate together to obtain a dual reinforced double interpenetrating network (d-DIPN) hydrogel (see Figure 4-8). Extraordinary improvements in strength and toughness are achieved with simultaneous reinforcement via dual ionic crosslinking and the introduction of SiO_2 NPs.

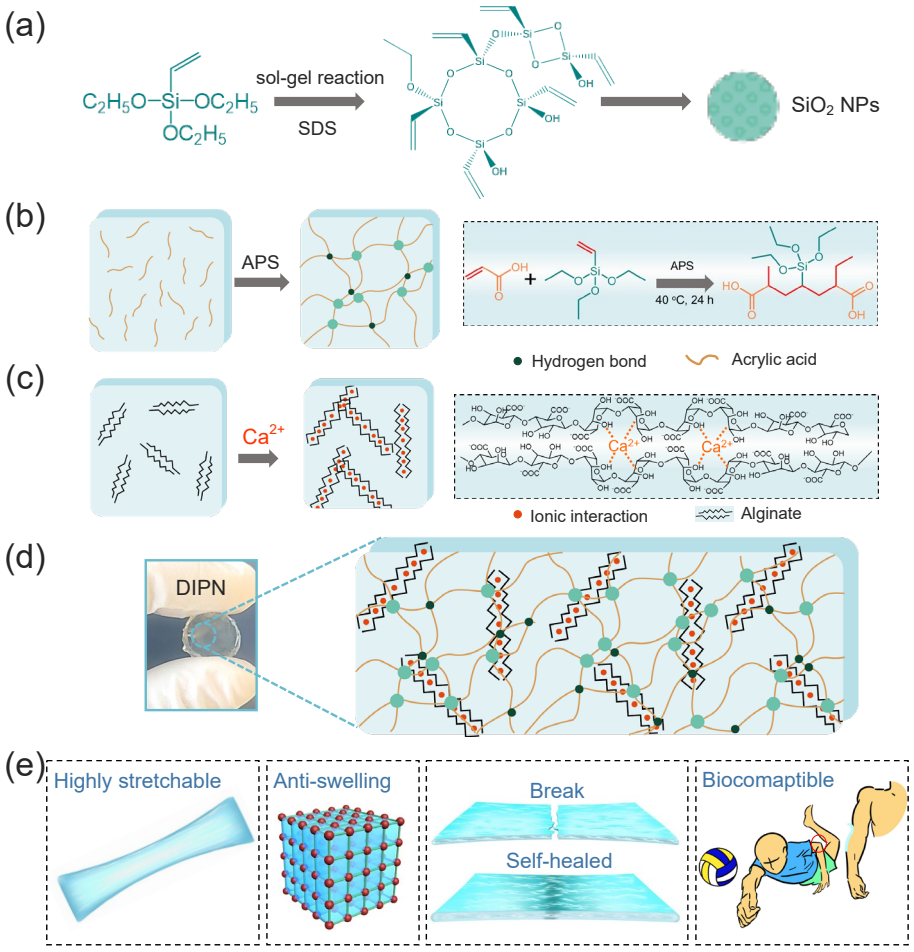

Figure 4-8. Schematic of preparing tough inorganic-polymer hydrogel. Figures adapted from Paper IV.

The addition of Ca^{2+} is quite easy and it will help to form alginate hydrogels under mild conditions. For SiO_2 NPs, in order to have stronger interactions with the polymer networks, vinyl-silica precursor VTES is hydrolyzed to form SiO_2 NPs firstly while vinyl groups could undergo further reactions. These vinyl branches on SiO_2 NPs could easily react with vinyl groups in AA monomers under free radical polymerization processes and covalently bond together. In this way, both strong covalent crosslinks and weak reversible interactions could complementarily contribute to mechanical performances and other functional properties of SA (Ca^{2+})-PAA-SiO_2 hydrogel.

With dual reinforcement, the strength and toughness of SA (Ca^{2+})-PAA-SiO_2 hydrogel improved a lot compared with non-reinforced or single-reinforced ones. The

tensile test of reinforced hydrogels was carried out and show a comparison with a single PAA hydrogel with an elongation of 240% and maximum stress of 0.03 MPa. A great improvement of both stress and elongation at breakage is achieved for the PAA-SA DIPN hydrogel. The reason appears to be that external loads are shared by the entanglements created between the PAA and SA networks. Covalent crosslinks between PAA and SA chains (reacting with carboxyl groups) have strengthened the co-networks further. Moreover, after introducing silica NPs and Ca^{2+} ions, we find that both stress and elongation of hydrogels get further improved. The hydrogel SA (Ca^{2+})-PAA-SiO_2 reveals an elongation up to 1000% compared with its original length and stress of 1.62 MPa at breakage. Moreover, the existence of Ca^{2+}greatly affects the elastic/plastic deformation region of hydrogels. Alginate network without chelating with Ca^{2+} could hardly reform after stretching, and shapes of hydrogels could also hardly get recovered. However, with introduction of Ca^{2+}, alginate networks are successfully connected together, and ionic bonds are quite reversible and could break/reform quickly. Thus, hydrogels SA (Ca^{2+})-PAA-SiO_2 and SA (Ca^{2+})-PAA-SiO_2 reveal much more apparent elastic deformation in Figure 4-9. Also, after evaluating with a typical cyclic tensile, SA (Ca^{2+})-PAA-SiO_2 hydrogel keeps a good shape recovery. Hysteresis loops exist in every loading-unloading curve, and the area between the loading and unloading curves represents the energy loss per unit volume. The curves keep a good repeat, representing good self-recoverability of SA (Ca^{2+})-PAA-SiO_2 hydrogel. Moreover, the dissipated energy maintained after the second cycle is approximately 73% compared with the first one, while the tenth dissipated energy maintains at ~61%. The reason could be ascribed to the reversible interactions, e.g., hydrogen interactions and ionic crosslinks in the hydrogels, as these reversible bonds could dissipate energy effectively during deformation. Moreover, after comparing with other similar works, our prepared SA (Ca^{2+})-PAA-SiO_2 hydrogel shows desirable mechanical properties and could certainly be applied to more practical applications.

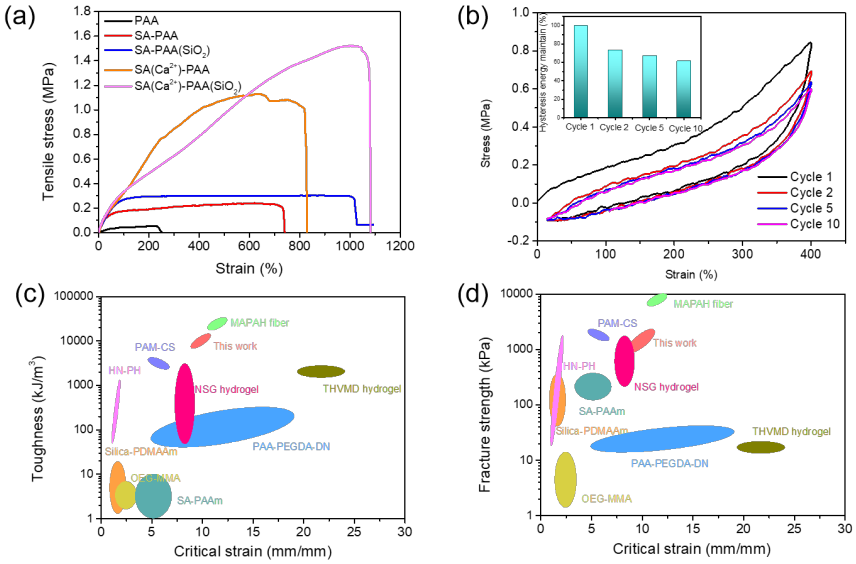

Figure 4-9. (a) Composition-dependent tensile stress-strain curves for hydrogels; (b) Hysteresis loop of cyclic tensile curves of SA (Ca^{2+})-PAA (SiO_2) hydrogel for different cycles, with the inset showing the energy maintained after each cycle; Comparison of the present hydrogels with those from the literature in terms of (c) toughness; and (f) fracture strength relative to the critical strain. Figures adapted from Paper IV.

Thus, for the mechanism of stretching under external loads, in the DIPN co-network, upon the breaking of hydrogen bonds, the Alg networks first begin to unzip and much more widely spaced ionic crosslinks unzip when the external load increases. PAA networks contribute to providing crack bridging and stabilizing deformation during this process, which in turn reduces the stress concentration and also contributes to high toughness. Hydrogen bonds and ionic crosslinks are quite reversible and could quickly reform after being broken, which further helps to heal the internal damage, leading to pronounced hysteresis resistance and limited permanent deformation. Thus, higher strength and toughness could be achieved by combining reversible weak interactions with strong crosslinks. Moreover, due to strong intermolecular interactions existed in hydrogels, multi-functions could be found in SA (Ca^{2+})-PAA-SiO_2 hydrogel. The hydrogel could be extended tenfold its initial length, and freely wrapped around a glass rod. Such behaviors give the huge potential for adapting to different shape and deformation requirements in its potential applications. The hydrogel is also strong enough and could also easily lift a 3 kg object. Reversible interactions in the hydrogel further ensured quick shape-recovery upon compression-release test. Additionally, the hydrogels reveal strong adhesion to different kinds of surfaces, including glass, plastic, metal, and finger. We ascribe this to the incorporated functional groups, e.g. hydroxide, amide, and imine bonds that exist in the system, which could effectively interact and bind with surrounding phases to enable the

adhesive properties. Moreover, the strong intermolecular interactions provide the hydrogel with very good self-healing ability. That is, the broken hydrogel could get self-healed rapidly and without cracks under stretching (see Figure 4-10).

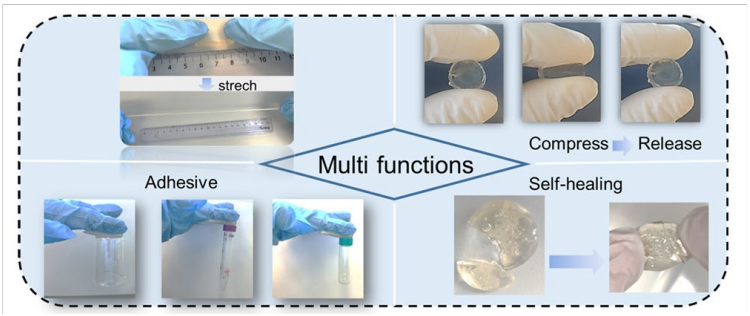

Figure 4-10. Superior extensibility, quick shape recovery, adhesive to different surfaces, and self-healing ability of SA (Ca^{2+})-PAA (SiO_2) hydrogel. Figures adapted from Paper IV.

Moreover, single polymer-based hydrogels are composed of loose networks, whose shape and volume are relatively simple to modify in solutions. In contrast, double polymer cross-linked hydrogels containing interpenetrating networks are substantially more compact, making them unchangeable in solutions. Furthermore, other reinforcement strategies e.g. nanocomposite and ionic crosslinking were able to create coordination bonds with carboxyl groups in polymer chains, considerably improving the system's cross-linked sites and resulting in a denser network. As a result, the stronger intermolecular contacts and more cross-linked structures created by dual-reinforcement in Paper IV may successfully inhibit chain disentanglement and hydrogel swelling. The mechanisms of swelling behavior with single and double reinforced hydrogels are depicted in Figure 4-11.

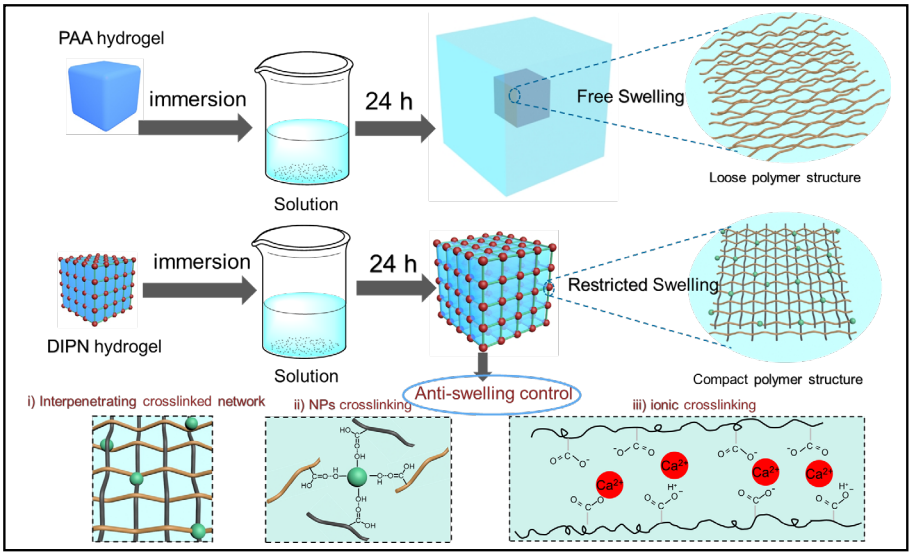

Figure 4-11. Swelling mechanism of single PAA polymer hydrogel without reinforcement and dual reinforced DIPN hydrogels. Figures adapted from Paper IV.

4.5. SUMMARY

In this chapter, we combined experimental methods and MD simulations together to investigate tough hybrid materials and their deformation/fracture mechanisms at the atomic level. After systematic research, the disentanglement of the polymer chains from the matrix upon tension is mainly controlled by non-covalent intermolecular interactions between polymer and silica networks rather than the breakage of covalent bonds, which further governs the fracture and deformation behaviors of inorganic-polymer hybrids. Thus, strategies for improving the intermolecular interactions of hybrid networks have been tried, e.g. changing the size and species of inorganic NPs, combining NPs reinforcement and ionic crosslinking together in a system, changing polymer networks, and comparing a series of hybrids with different inorganic/organic weight ratios. All in all, these attempts have all revealed improvement in toughness at different levels, and balancing strength with toughness could also be achieved in the final. Moreover, by combing strong covalent crosslinks and weak reversible interactions, tough hydrogels could be obtained not only with improved mechanical properties, but multi-functions, e.g. quick shape recovery ability, self-healing ability, adhesive to different surfaces as well as anti-swelling behaviors. All the efforts in preparing tough hybrid/hydrogels are proved to be reliable and could be potentially applied to biomedical applications as well as soft robotics.

CHAPTER 5. BIOCOMPATIBILITY AND *IN VITRO* STUDIES

Cyto-compatibility and hemo-compatibility are regarded as important factors for the materials applied into further tissue engineering and bone regenerations. Moreover, besides evaluating cytotoxicity, cell attachment and cell proliferation are also of great importance for bioactive materials. Hence, it is of great interest to report findings of correlations between molecular structures and biocompatibility. With the understanding of structures and mechanical performances of hybrids, in this chapter, the findings of related biocompatibility and cell *in vitro* studies will be presented.

5.1. CYTOTOXICITY OF HYBRIDS

Many methods could determine the cytotoxicity of materials indirectly, e.g. MTT method, CKK-8 assays and ToX-8 assays. In this thesis, cytotoxicity of materials are evaluated via ToX-8 dyes. In this test, mechanism is metabolically active and viable cells could convert blue resazurin (nonfluo-rescent dye) to pink resorufin (fluores-cent dye), proportionate fluorescence output to metabolically active and alive cells (86). (mechanism see in Figure 5-1).

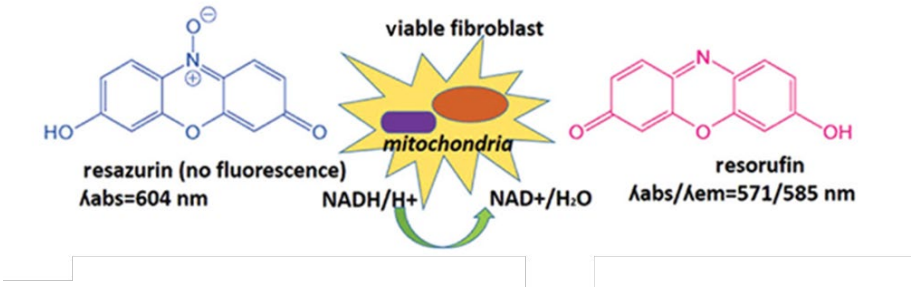

Figure 5-1 Mechanism of ToX-8 assays in evaluating cell viability.

Importantly, all the samples should be sterilized by immersing in EtOH for 30 min and place under UV light overnight before further tests. The detailed experimental processes could be found in Papers III and IV. Cell viabilities of materials are determined by the following equations:

Relative cell viability (%) = [(mean cell viability determined in sample)/ (mean cell viability determined in control)] × 100

Since our prepared materials are expected as scaffolds for bone repairing and regeneration. Thus, MC3T3-E1 bone cells are applied in our work for further *in vitro* studies. Based on ISO 10993 standard, materials are recognized as non-cytotoxic to cells with cell viability over 70% and 50% dilution viability of hydrogel extract are a little bit higher than 100% extract solutions. Thus, for our prepared bioactive materials, based on the results, PTHF-SiO_2 based hybrids and Alg-PAA hydrogels all reveal totally non-cytotoxicity with cell viability over 80%, representing potential applications as biomedical scaffolds (see Figure 5-2).

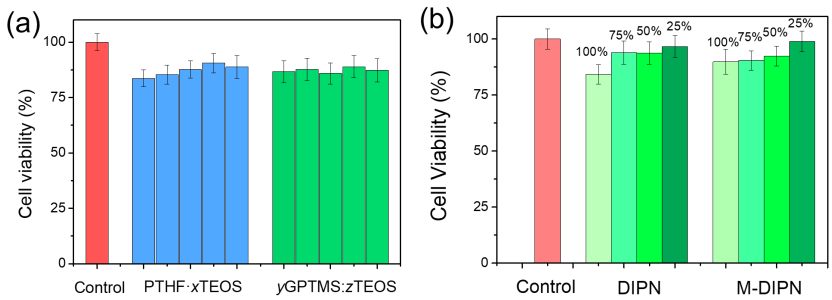

Figure 5-2. MC3T3-E1 Cell viability of (a) PTHF-SiO_2 hybrids. (b) Alg-PAA hydrogels. The dilution of the dissolution products enhanced cell viability to a level equivalent to that of the non-cytotoxic controls. Figure adapted from Paper III and IV.

5.2. CELL ATTACHMENT OF MATERIALS

After exploring the cytotoxicity of materials, cell attachment is taken into consideration by immunohistochemistry and confocal microscopy. Cells are cultured on materials for 72h before testing. Normally, alive MC3T3-E1 cells will attach on the surface of a flask or materials and grow with enough media while dead cells will float in the media. Moreover, the morphologies of alive and dead cells are totally different from their appearance. Thus, it would be a signal to determine the biocompatibility of prepared materials. The DAPI nuclear counter staining technique findings for the PTHF • *8*TEOS hybrid in Figures 5-3 show that cells are well attached to the material. Thus, materials could be suitable candidates to function as articular cartilage regeneration. Micro fractures are created in the subchondral bone to release stem cells from the bone marrow, which is used to treat sports injuries, suggesting hybrid biocompatibility and potential for bone cell development.

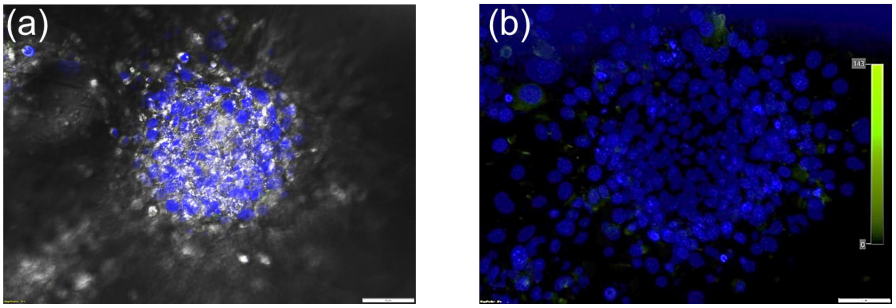

Figure 5-3. Cell attachment of MC3T3-E1 cells on hybrid PTHF·8TEOS with Immunohistochemical cell nuclei staining (DAPI, blue fluorescence). Figure adapted from Paper III.

5.3. CELL PROLIFERATION ON HYBRID MATERIALS

Based abovementioned results, hybrid materials are proved to be non-cytotoxicity to MC3T3-E1 cells and could support cell attachment. The cell proliferation onto the materials were quantitatively measured using the ToX-8 assay follow the manufacturer's instructions. Molecular structure influences to cell proliferation are discussed on the basis of PTHF·TEOS hybrids in Paper III. Cells are cultured on different hybrids for 3 and 7 days, respectively. From the experimental results, compared with control group, it is proved that nano-porous structures and inorganic NPs are benefit for cell growth, the reason could be the properties of bioactive glasses have been preserved. More inorganic NPs and much uniform dispersion of different phases are both important for cell growth. The details are depicted in Figure 5-4.

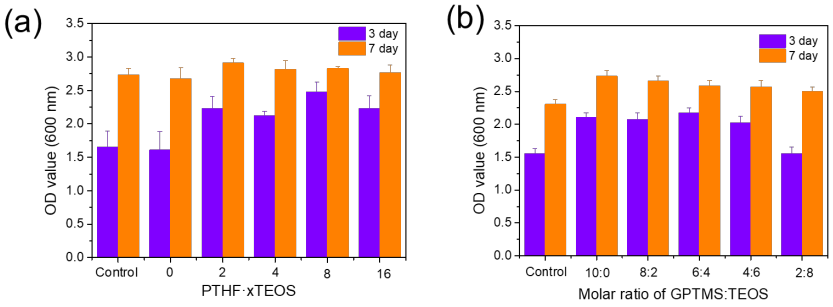

Figure 5-4. MC3T3-E1 Cell proliferation on (c) PTHF·xTEOS and (d) yGPTMS:zTEOS hybrids after incubating for 3 and 7 days. Figure adapted from Paper III.

Moreover, such polymer-SiO_2 hybrids is also proved to induce the formation of chondrogenic differentiation and hyaline cartilaginous matrix. Jone's found Sox9, Collagen Type II and Aggrecan released after culturing ATDC5 bone cells on Si80-

CL hybrids, which is importantly related with articular cartilage productions (see Figure 5-5). In order to investigate silica NPs influences, cells are cultured both on Si80-CL hybrids and PCL polymer scaffolds. The results suggest that more Sox9, Collagen Type II and Aggrecan are expressed on hybrids due to suitable surface structures, enough stiffness to support cell growth, and most importantly pore architecture results from inorganic NPs. Silica NPs could also provide improved cell recognition sites for cell attachment and growth, and such hybrids could be potentially function as tissue regeneration scaffolds with the improvement of material flexibility (49).

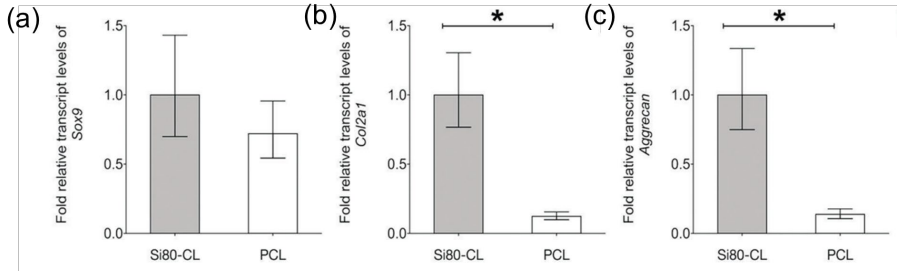

Figure 5-5. Evaluation of expression of Sox9, Col2a1 and Aggrecan on both Si80-CL hybrid and PCL polymer scaffold. Figures reproduced from ref. (48).

Besides PTHF-SiO_2 hybrids, much apparent results could be referred in SA (Ca^{2+})-PAA (SiO_2) DIPN hydrogels. In order to figure out influences of inorganic particles to cell growth, mineralized DIPN hydrogel is compared with normal hydrogels and control groups. The specific mineralization process and experimental methods could be referred in Paper IV. Normal hydrogels show nearly the same ability for cell growth compared with blank group from 1, 3 and 7 days, however, mineralized hydrogels reveal much higher optical density values and benefit for cell growth (see Figure 5-6). The mineralization process induces the production of calcium phosphate NPs, which provide a more biologically active surface, hence boosting the cell's vitality and usefulness, and could effectively improve cell growth on hydrogels (51). Thus, combing these results, inorganic NPs in hybrid networks could greatly improve biocompatibility and cell growth with *in vitro* studies.

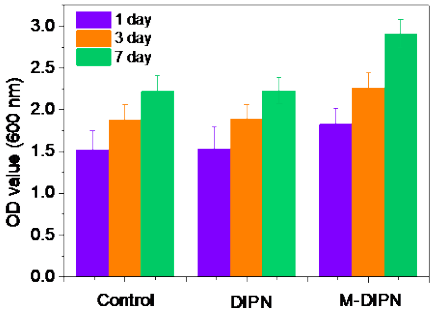

Figure 5-6. Cell proliferation of MC3T3-E1 cells on DIPN hydrogel and mineralized hydrogel after culturing for1, 3 and 7 days. Figure adapted from Paper IV.

5.4. SUMMARY

In this chapter, we have investigated the biocompatibilities of prepared hybrids and hydrogels. These materials all show non-cytotoxicity to bone cells with cell viabilities over 80%. Additionally, such materials also reveal enough support for cell attachment and proliferation. Moreover, after comparing pure polymer and hybrids, we find inorganic NPs could also provide improved cell recognition sites for cell attachment and growth due to more release of Sox9, Collagen Type II and Aggrecan. Compared with blank groups, nano-porous structures and an inorganic component could generate more biologically active sites, especially in mineralized hydrogels, which are benefit for cell growth and further enhancing the cell viability and functionality. These results, together with excellent mechanical properties, suggest these hybrids are suitable candidates function as articular cartilage scaffolds for bone regeneration.

CHAPTER 6. CONCLUSIONS AND PERSPECTIVES

In this chapter, we will highlight key results and their possible relevance based on our previous works, along with a discussion concerning perspectives and suggestions for future researches.

6.1. CONCLUSION

Bioactive inorganic-organic hybrid materials are expected to combine advantages of both components. With respect to bonding to bone and stimulating bone regenerations, and also possess improved flexibility as well as functionality. Constructing covalent bonds between inorganic and polymer networks could effectively inhibit phase aggregation, and ensure hybrids function synergistically. However, the conflict between strength of toughness should be resolved, in order to prepare materials with better mechanical properties. In this thesis, the following three topics related to inorganic-organic hybrids and mechanical performances have been systematically facilitated and developed: (i) Understanding the relations between molecular structures of both inorganic and organic aspects with mechanical performances (Chapters 3 and 4); (ii) Combining experiment and MD simulations to explore fundamental mechanisms of deformation/fracture for hybrid materials at the atomic level (Chapter 4); and (iii) Investigating biocompatibility of hybrids and their *in vitro* studies (Chapter 5). The highlights from this Ph.D. study are summarized as follows:

With the introducing of polymer chains, toughness was dramatically improved compared with bioglasses while strength decreased due to polymer component. Thus, we try to resolve the conflict between strength and toughness via controlling total inorganic vs. organic weight ratios, inorganic NPs size and polymer networks. Additionally, MD simulation is incorporated in the project for illustrating the deformation/fracture mechanism at atomic level and guiding hybrid design. On the basis of both experimental and MD simulation results, disentanglement of the polymer chains rather than their covalent bonds breakage is the main course of the deformation failure of the hybrids, which is largely determined by non-covalent intermolecular interactions among polymer and silica networks. Thus, improvements could be expected with much stronger intermolecular interactions in the hybrid networks. These findings indicate that the expected tough and strong hybrids could be prepared through the abovementioned strategies, allowing for the development of hybrids with customized features.

The findings not only inspired us in preparing abovementioned tailorable hybrids. Besides traditional hybrid materials, such strategies had been applied into preparing

tough hydrogels, with interpenetrating cross-linked structures and strong intermolecular interactions. Moreover, besides contributing to better mechanical performances of materials, reversible interactions existed in hybrid networks e.g. hydrogen bonds and ionic interactions could result in a lot of multi functions. Self-healing abilities, quick shape recovery, desirable energy dissipation as well as adhesive properties could all be ascribed to these reversible interactions.

Finally, biocompatibility and *in vitro* studies are conducted on our prepared hybrids and hydrogels. All prepared materials show non-cytotoxicity to MC3T3-E1 bone cells with cell viabilities over 80%, and could also support cell attachment as well as proliferation. Inorganic networks offer more biologically active sites for cell growth and prove to have a better ability for promoting cell proliferations.

6.2. PERSPECTIVE

In this thesis, we have successfully prepared a series of bioactive inorganic-polymer materials and investigated the relations between molecular structures and mechanical properties as well as subsequent multi-functions. Numerous strategies have been applied to improve the strength as well as toughness of such materials. However, the following research subjects deserve to be investigated further.

Although our prepared hybrids are flexible and could adapt to required shape deformation requirements. The total inorganic compositions in our prepared hybrids are still low, and strength could hardly be comparable to those bioactive glasses. Such downside may affect commercial applications in clinics. Moreover, besides silica-based hybrids, other oxides e.g. CaO, P_2O_5, and B_2O_3 should also be researched in future works since they are also important compositions of traditional bioglasses (4, 87). For the polymer side, many natural and synthetic polymers are biocompatible to cells, which should be extensively tried in the future works. Natural polymers, such as silk, chitosan, collagen, alginate, and hyaluronic acid (HA) are preferable because of their superior interactions with many cell types and absence of an immune response (88-91). In contrast to natural polymers, synthetic polymers such as poly(caprolactone) (PCL), poly(L-lactic acid) (PLLA), poly(lactic-co-glycolic) acid (PLGA) and poly(glycolic acid) (PGA) reveal advantages of less expensive and more functional (92-95). Additionally, in order to mimic morphologies of human bones, porous materials and their mechanical properties deserve to be thoroughly researched in the future. 3D printing scaffolds and electrospinning nanofiber membranes could be ideal options to achieve such purposes (96-99).

Finally, although we have tested biocompatibility and cell *in vitro* studies of hybrid materials, further *in vivo* research is significantly important for the final clinical applications (11, 26, 29, 85). By incorporating metal ions/NPs, surface nanostructures design and modifications, antibacterial effects are expected to hybrid biomaterials (100). These processes could effectively prevent implant-related infections in clinics,

while preserving their biocompatibility. Lastly, as the materials will be implanted into human bodies, evaluating the degradation rate of hybrid to match that of bone growth will be another very important topic for the next step of research (12, 85, 87, 101, 102).

BIOGRAPHY

1. Shegarfi H, Reikeras O. Review article: bone transplantation and immune response. J Orthop Surg. 2009;17(2):206-11.

2. Izquierdo-Barba I, Salinas AJ, Vallet-Regí M. Bioactive Glasses: From Macro to Nano. Int J Appl Glass Sci. 2013;4(2):149-61.

3. Axinte E. Glasses as engineering materials: A review. Mater Des. 2011;32(4):1717-32.

4. Hench LL. The story of Bioglass. J Mater Sci Mater Med. 2006;17(11):967-78.

5. Hench LL. Biomaterials: a forecast for the future. Biomaterials. 1998;19(16):1419-23.

6. Hench LL. Bioceramics: From Concept to Clinic. J Am Ceram Soc. 1991;74(7):1487-510.

7. Hench LL. Bioceramics. J Am Ceram Soc. 2005;81(7):1705-28.

8. Fu Q, Saiz E, Rahaman MN, Tomsia AP. Bioactive glass scaffolds for bone tissue engineering: state of the art and future perspectives. Mater Sci Eng, C. 2011;31(7):1245-56.

9. Jones JR. Review of bioactive glass: from Hench to hybrids. Acta Biomater. 2013;9(1):4457-86.

10. Brauer DS. Bioactive glasses-structure and properties. Angew Chem. 2015;54(14):4160-81.

11. Rahaman MN, Day DE, Bal BS, Fu Q, Jung SB, Bonewald LF, et al. Bioactive glass in tissue engineering. Acta Biomater. 2011;7(6):2355-73.

12. Brauer DS, Karpukhina N, O'Donnell MD, Law RV, Hill RG. Fluoride-containing bioactive glasses: effect of glass design and structure on degradation, pH and apatite formation in simulated body fluid. Acta Biomater. 2010;6(8):3275-82.

13. Munch E, Launey ME, Alsem DH, Saiz E, Tomsia AP, Ritchie RO. Tough, bio-inspired hybrid materials. Science. 2008;322(5907):1516-20.

14. Novak BM. Hybrid Nanocomposite Materials?between inorganic glasses and organic polymers. Adv Mater. 1993;5(6):422-33.

15. Kamio E, Yasui T, Iida Y, Gong JP, Matsuyama H. Inorganic/Organic Double-Network Gels Containing Ionic Liquids. Adv Mater. 2017;29(47).

16. Yang Y, Wang X, Yang F, Shen H, Wu D. A Universal Soaking Strategy to Convert Composite Hydrogels into Extremely Tough and Rapidly Recoverable Double-Network Hydrogels. Adv Mater. 2016;28(33):7178-84.

17. Xu X, Jerca VV, Hoogenboom R. Bioinspired double network hydrogels: from covalent double network hydrogels via hybrid double network hydrogels to physical double network hydrogels. Mater Horiz. 2021;8(4):1173-88.

18. Ou K, Dong X, Qin C, Ji X, He J. Properties and toughening mechanisms of PVA/PAM double-network hydrogels prepared by freeze-thawing and anneal-swelling. Mater Sci Eng, C. 2017;77:1017-26.

19. Arno MC, Inam M, Weems AC, Li Z, Binch ALA, Platt CI, et al. Exploiting the role of nanoparticle shape in enhancing hydrogel adhesive and mechanical properties. Nat Commun. 2020;11(1):1420.

20. Erol-Taygun M, Zheng K, Boccaccini AR. Nanoscale Bioactive Glasses in Medical Applications. Int J Appl Glass Sci. 2013;4(2):136-48.

21. Hooper JB, Schweizer KS. Theory of Phase Separation in Polymer Nanocomposites. Macromolecules. 2006;39(15):5133-42.

22. Xia LW, Xie R, Ju XJ, Wang W, Chen Q, Chu LY. Nano-structured smart hydrogels with rapid response and high elasticity. Nat Commun. 2013;4:2226.

23. Fiorini F, Prasetyanto EA, Taraballi F, Pandolfi L, Monroy F, Lopez-Montero I, et al. Nanocomposite Hydrogels as Platform for Cells Growth, Proliferation, and Chemotaxis. Small. 2016;12(35):4881-93.

24. Kuo CK, Ma PX. Ionically crosslinked alginate hydrogels as scaffolds for tissue engineering: Part 1. Structure, gelation rate and mechanical properties. Biomaterials. 2001;22(6):511-21.

25. Bin Imran A, Esaki K, Gotoh H, Seki T, Ito K, Sakai Y, et al. Extremely stretchable thermosensitive hydrogels by introducing slide-ring polyrotaxane cross-linkers and ionic groups into the polymer network. Nat Commun. 2014;5:5124.

26. Kumar A, Rao KM, Han SS. Synthesis of mechanically stiff and bioactive hybrid hydrogels for bone tissue engineering applications. Chem Eng J. 2017;317:119-31.

27. Jones JR, Brauer DS, Hupa L, Greenspan DC. Bioglass and Bioactive Glasses and Their Impact on Healthcare. Int J Appl Glass Sci. 2016;7(4):423-34.

28. Valliant EM, Jones JR. Softening bioactive glass for bone regeneration: sol–gel hybrid materials. Soft matter. 2011;7(11):5083.

29. Fu Q, Rahaman MN, Fu H, Liu X. Silicate, borosilicate, and borate bioactive glass scaffolds with controllable degradation rate for bone tissue engineering applications. I. Preparation and in vitro degradation. J Biomed Mater Res, Part A. 2010;95(1):164-71.

30. Hench LL, Jones JR. Bioactive Glasses: Frontiers and Challenges. Front Bioeng Biotechnol. 2015;3:194.

31. Crush J, Hussain A, Seah KTM, Khan WS. Bioactive Glass: Methods for Assessing Angiogenesis and Osteogenesis. Front Cell Dev Biol. 2021;9:643781.

32. Hench LL, West JK. The sol-gel process. Chem Rev. 1990;90(1):33-72.

33. Ogoshi T, Chujo Y. Organic–inorganic polymer hybrids prepared by the sol-gel method. Compos Interfaces. 2012;11(8-9):539-66.

34. Baino F, Fiume E, Miola M, Verné E. Bioactive sol-gel glasses: Processing, properties, and applications. Int J Appl Ceram Technol. 2018;15(4):841-60.

35. Tripathi SK, Kaur R, Rani M. Oxide Nanomaterials and their Applications as a Memristor. Solid State Phenom. 2014;222:67-97.

36. Matos MC, Ilharco LM, Almeida RM. The evolution of TEOS to silica gel and glass by vibrational spectroscopy. J Non-Cryst Solids. 1992;147-148:232-7.

37. Peña-Alonso R, Téllez L, Rubio J, Rubio F. Surface chemical and physical properties of TEOS-TBOT-PDMS hybrid materials. J Sol-Gel Sci Technol. 2006;38(2):133-45.

38. Li M, Li W, Cai W, Zhang X, Wang Z, Street J, et al. A self-healing hydrogel with pressure sensitive photoluminescence for remote force measurement and healing assessment. Mater Horiz. 2019;6(4):703-10.

39. Gabrielli L, Connell L, Russo L, Jiménez-Barbero J, Nicotra F, Cipolla L, et al. Exploring GPTMS reactivity against simple nucleophiles: chemistry beyond hybrid materials fabrication. RSC Adv. 2014;4(4):1841-8.

40. Fan W, Youngman RE, Ren X, Yu D, Smedskjaer MM. Structural control of self-healing silica-poly(tetrahydropyran)-poly(epsilon-caprolactone) hybrids. J Mater Chem B. 2021.

41. Fan W, Jensen LR, Ceccato M, Quaade TS, Gurevich L, Yu D, et al. Flexible inorganic–organic hybrids with dual inorganic components. Mater Today Chem. 2021;22:100584.

42. Zhong M, Liu XY, Shi FK, Zhang LQ, Wang XP, Cheetham AG, et al. Self-healable, tough and highly stretchable ionic nanocomposite physical hydrogels. Soft matter. 2015;11(21):4235-41.

43. Fan W, Du T, Droce A, Jensen LR, Youngman RE, Ren X, et al. Resolving the Conflict between Strength and Toughness in Bioactive Silica-Polymer Hybrid Materials. ACS Nano. 2022.

44. Lee DW, Yoo BR. Advanced silica/polymer composites: Materials and applications. J Ind Eng Chem. 2016;38:1-12.

45. Macon ALB, Li S, Chung JJ, Nommeots-Nomm A, Solanki AK, Stevens MM, et al. Ductile silica/methacrylate hybrids for bone regeneration. J Mater Chem B. 2016;4(36):6032-42.

46. Poologasundarampillai G, Yu B, Tsigkou O, Wang D, Romer F, Bhakhri V, et al. Poly(gamma-glutamic acid)/silica hybrids with calcium incorporated in the silica network by use of a calcium alkoxide precursor. Chemistry. 2014;20(26):8149-60.

47. Glaser RH, Wilkes GL, Bronnimann CE. Solid-state 29Si NMR of TEOS-based multifunctional sol-gel materials. J Non-Cryst Solids. 1989;113(1):73-87.

48. Artaki I, Bradley M, Zerda TW, Jonas J. NMR and Raman study of the hydrolysis reaction in sol-gel processes. J Phys Chem. 2002;89(20):4399-404.

49. Tallia F, Russo L, Li S, Orrin ALH, Shi X, Chen S, et al. Bouncing and 3D printable hybrids with self-healing properties. Mater Horiz. 2018;5(5):849-60.

50. Chung JJ, Li S, Stevens MM, Georgiou TK, Jones JR. Tailoring Mechanical Properties of Sol–Gel Hybrids for Bone Regeneration through Polymer Structure. Chem Mater. 2016;28(17):6127-35.

51. Teng L, Chen Y, Jin M, Jia Y, Wang Y, Ren L. Weak Hydrogen Bonds Lead to Self-Healable and Bioadhesive Hybrid Polymeric Hydrogels with Mineralization-Active Functions. Biomacromolecules. 2018;19(6):1939-49.

52. Bajomo M, Robb I, Steinke JHG, Bismarck A. Fully Reversible pH-Triggered Network Formation of Amphoteric Polyelectrolyte Hydrogels. Adv Funct Mater. 2011;21(1):172-6.

53. Imai Y, Naka K, Chujo Y. Reversible Formation of Interpenetrating Polymer Network Structure in Organic-Inorganic Polymer Hybrids. Polym J. 1998;30(12):990-5.

54. Shi FK, Zhong M, Zhang LQ, Liu XY, Xie XM. Robust and self-healable nanocomposite physical hydrogel facilitated by the synergy of ternary crosslinking points in a single network. J Mater Chem B. 2016;4(37):6221-7.

55. Shi FK, Wang XP, Guo RH, Zhong M, Xie XM. Highly stretchable and super tough nanocomposite physical hydrogels facilitated by the coupling of intermolecular hydrogen bonds and analogous chemical crosslinking of nanoparticles. J Mater Chem B. 2015;3(7):1187-92.

56. Ducrot E, Chen Y, Bulters M, Sijbesma RP, Creton C. Toughening elastomers with sacrificial bonds and watching them break. Science. 2014;344(6180):186-9.

57. Sun JY, Zhao X, Illeperuma WR, Chaudhuri O, Oh KH, Mooney DJ, et al. Highly stretchable and tough hydrogels. Nature. 2012;489(7414):133-6.

58. Morelle XP, Illeperuma WR, Tian K, Bai R, Suo Z, Vlassak JJ. Highly Stretchable and Tough Hydrogels below Water Freezing Temperature. Adv Mater. 2018;30(35):e1801541.

59. Lin J, Li Y, Yang W, Liu X, Huang W, Wang Y, et al. Molecular dynamics simulation study on the structure and properties of polyimide/silica hybrid materials. J Appl Polym Sci. 2019;136(16):47335.

60. Yu C, Yang L, Chen H, Qin Y, Wang T, Sun W, et al. Microscale investigations of mechanical responses of TKX-50 based polymer bonded explosives using MD simulations. Comput Mater Sci. 2020;172:109287.

61. Liu C, Ning W, Tam LH, Yu Z. Understanding fracture behavior of epoxy-based polymer using molecular dynamics simulation. J Mol Graphics Modell. 2020;101:107757.

62. Ritchie RO. The conflicts between strength and toughness. Nat Mater. 2011;10(11):817-22.

63. Yuk H, Zhang T, Lin S, Parada GA, Zhao X. Tough bonding of hydrogels to diverse non-porous surfaces. Nat Mater. 2016;15(2):190-6.

64. To T, Jensen LR, Smedskjaer MM. On the relation between fracture toughness and crack resistance in oxide glasses. J Non-Cryst Solids. 2020;534:119946.

65. To T, Sorensen SS, Christensen JFS, Christensen R, Jensen LR, Bockowski M, et al. Bond Switching in Densified Oxide Glass Enables Record-High Fracture Toughness. ACS Appl Mater Interfaces. 2021;13(15):17753-65.

66. Zhao X. Designing toughness and strength for soft materials. Proc Natl Acad Sci U S A. 2017;114(31):8138-40.

67. Pan J, Hanna I, Lallemand J-Y. Synthesis of chiral cyclobutane derivatives by tetrahydropyran ring-opening. Tetrahedron Lett. 1991;32(51):7543-4.

68. Watanabe N, Uemura S, Okano M. Ring-opening Reaction of Oxiranes, Oxetanes, and Tetrahydropyran by Mercury(II) Salts and Alkyl Halides. Bull Chem Soc Jpn. 1979;52(12):3611-4.

69. Her SC, Lin KY. Dynamic mechanical analysis of carbon nanotube-reinforced nanocomposites. J Appl Biomater Funct Mater. 2017;15(Suppl. 1):e13-e8.

70. Pillai KV, Renneckar S. Dynamic mechanical analysis of layer-by-layer cellulose nanocomposites. Ind Crops Prod. 2016;93:267-75.

71. Mokhtarifar M, Kaveh R, Bagherzadeh M, Lucotti A, Pedeferri M, Diamanti MV. Heterostructured TiO2/SiO2/gamma-Fe2O3/rGO Coating with Highly Efficient Visible-Light-Induced Self-Cleaning Properties for Metallic Artifacts. ACS Appl Mater Interfaces. 2020;12(26):29671-83.

72. Hu J, Gao Q, Xu L, Zhang M, Xing Z, Guo X, et al. Significant Improvement in Thermal and UV Resistances of UHMWPE Fabric through in Situ Formation of Polysiloxane-TiO2 Hybrid Layers. ACS Appl Mater Interfaces. 2016;8(35):23311-20.

73. Zhang D, Yang J, Bao S, Wu Q, Wang Q. Semiconductor nanoparticle-based hydrogels prepared via self-initiated polymerization under sunlight, even visible light. Sci Rep. 2013;3:1399.

74. Du J, She X, Zhu W, Yang Q, Zhang H, Tsou C. Super-tough, anti-fatigue, self-healable, anti-fogging, and UV shielding hybrid hydrogel prepared via simultaneous dual in situ sol-gel technique and radical polymerization. J Mater Chem B. 2019;7(45):7162-75.

75. Miao Y, Xu M, Zhang L. Electrochemistry-Induced Improvements of Mechanical Strength, Self-Healing, and Interfacial Adhesion of Hydrogels. Adv Mater. 2021;33(40):e2102308.

76. Si Y, Wang L, Wang X, Tang N, Yu J, Ding B. Ultrahigh-Water-Content, Superelastic, and Shape-Memory Nanofiber-Assembled Hydrogels Exhibiting Pressure-Responsive Conductivity. Adv Mater. 2017;29(24).

77. Sun G, Li Z, Liang R, Weng LT, Zhang L. Super stretchable hydrogel achieved by non-aggregated spherulites with diameters <5 nm. Nat Commun. 2016;7:12095.

78. Liu C, Morimoto N, Jiang L, Kawahara S, Noritomi T, Yokoyama H, et al. Tough hydrogels with rapid self-reinforcement. Science. 2021;372(6546):1078-81.

79. Zhao W, Jin X, Cong Y, Liu Y, Fu J. Degradable natural polymer hydrogels for articular cartilage tissue engineering. J Chem Technol Biotechnol. 2013;88(3):327-39.

80. Freedman BR, Uzun O, Luna NMM, Rock A, Clifford C, Stoler E, et al. Degradable and Removable Tough Adhesive Hydrogels. Adv Mater. 2021;33(17):e2008553.

81. Phadke A, Zhang C, Arman B, Hsu CC, Mashelkar RA, Lele AK, et al. Rapid self-healing hydrogels. Proc Natl Acad Sci U S A. 2012;109(12):4383-8.

82. Li X, Wang H, Li D, Long S, Zhang G, Wu Z. Dual Ionically Cross-linked Double-Network Hydrogels with High Strength, Toughness, Swelling Resistance, and Improved 3D Printing Processability. ACS Appl Mater Interfaces. 2018;10(37):31198-207.

83. Gong JP. Materials both Tough and Soft. Science. 2014;344(6180):161-2.

84. Gong JP, Katsuyama Y, Kurokawa T, Osada Y. Double-Network Hydrogels with Extremely High Mechanical Strength. Adv Mater. 2003;15(14):1155-8.

85. Mahony O, Tsigkou O, Ionescu C, Minelli C, Ling L, Hanly R, et al. Silica-Gelatin Hybrids with Tailorable Degradation and Mechanical Properties for Tissue Regeneration. Adv Funct Mater. 2010;20(22):3835-45.

86. Csepregi R, Lemli B, Kunsagi-Mate S, Szente L, Koszegi T, Nemeti B, et al. Complex Formation of Resorufin and Resazurin with Beta-Cyclodextrins: Can Cyclodextrins Interfere with a Resazurin Cell Viability Assay? Molecules. 2018;23(2).

87. Blaker JJ, Bismarck A, Boccaccini AR, Young AM, Nazhat SN. Premature degradation of poly(alpha-hydroxyesters) during thermal processing of Bioglass-containing composites. Acta Biomater. 2010;6(3):756-62.

88. Necas J, Bartosikova L, Brauner P, Kolar J. Hyaluronic acid (hyaluronan): a review. Vet Med. 2008;53(No. 8):397-411.

89. Parenteau-Bareil R, Gauvin R, Berthod F. Collagen-Based Biomaterials for Tissue Engineering Applications. Materials. 2010;3(3):1863-87.

90. Chopra S, Mahdi S, Kaur J, Iqbal Z, Talegaonkar S, Ahmad FJ. Advances and potential applications of chitosan derivatives as mucoadhesive biomaterials in modern drug delivery. J Pharm Pharmacol. 2006;58(8):1021-32.

91. Muller FA, Muller L, Hofmann I, Greil P, Wenzel MM, Staudenmaier R. Cellulose-based scaffold materials for cartilage tissue engineering. Biomaterials. 2006;27(21):3955-63.

92. Lee P, Tran K, Chang W, Fang Y-L, Zhou G, Junka R, et al. Bioactive polymeric scaffolds for osteochondral tissue engineering: in vitro evaluation of the effect of culture media on bone marrow stromal cells. Polym Adv Technol. 2015;26(12):1476-85.

93. Dhandayuthapani B, Yoshida Y, Maekawa T, Kumar DS. Polymeric Scaffolds in Tissue Engineering Application: A Review. Int J Polym Sci. 2011;2011:1-19.

94. Narayanan G, Gupta BS, Tonelli AE. Poly(epsilon-caprolactone) nanowebs functionalized with alpha- and gamma-cyclodextrins. Biomacromolecules. 2014;15(11):4122-33.

95. Stratton S, Shelke NB, Hoshino K, Rudraiah S, Kumbar SG. Bioactive polymeric scaffolds for tissue engineering. Bioact Mater. 2016;1(2):93-108.

96. Norris E, Ramos-Rivera C, Poologasundarampillai G, Clark JP, Ju Q, Obata A, et al. Electrospinning 3D bioactive glasses for wound healing. Biomed Mater. 2020;15(1):015014.

97. Fan W, Zhang X, Li C. Functional fibrous compositions: Applications and perspectives. Compos Commun. 2019;15:68-75.

98. Che L, Lei Z, Wu P, Song D. A 3D Printable and Bioactive Hydrogel Scaffold to Treat Traumatic Brain Injury. Adv Funct Mater. 2019;29(39):1904450.

99. Fu Q, Saiz E, Tomsia AP. Bioinspired Strong and Highly Porous Glass Scaffolds. Adv Funct Mater. 2011;21(6):1058-63.

100. Chen ZY, Gao S, Zhang YW, Zhou RB, Zhou F. Antibacterial biomaterials in bone tissue engineering. J Mater Chem B. 2021;9(11):2594-612.

101. Tian D, Dubois P, Grandfils C, Jérôme R, Viville P, Lazzaroni R, et al. A Novel Biodegradable and Biocompatible Ceramer Prepared by the Sol−Gel Process. Chem Mater. 1997;9(4):871-4.

102. Lueckgen A, Garske DS, Ellinghaus A, Desai RM, Stafford AG, Mooney DJ, et al. Hydrolytically-degradable click-crosslinked alginate hydrogels. Biomaterials. 2018;181:189-98.

LIST OF PUBLICATIONS

PUBLICATIONS IN PEER-REVIEW JOURNALS

Contributed as the first author:

I. **W. Fan**, R.E. Youngman, X. Ren, D. Yu, M.M. Smedskjaer, "Structural control of self-healing silica-poly(tetrahydropyran)-poly(ε-caprolactone) hybrids". *Journal of Materials Chemistry B.* 9 (2021) 4400-4410.

II. **W. Fan**, L.R. Jensen, M. Ceccato, T.S. Quaade, L. Gurevich, D. Yu, M.M. Smedskjaer, "Flexible inorganic–organic hybrids with dual inorganic components". *Materials Today Chemistry.* 22 (2021) 100584.

III. **W. Fan**, T. Du, A. Dorce, L.R. Jensen, R.E. Youngman, X. Ren, L. Gurevich, M. Bauchy, P. Kristensen, B. Xing, D. Yu, M.M. Smedskjaer, "Resolving the conflict between strength and toughness in bioactive silica-polymer hybrid materials". *ACS Nano* (DOI: 10.1021/acsnano.2c03440).

IV. **W. Fan**, L.R. Jensen, Y. Dong, A.J. Deloria, B. Xing, D. Yu, M.M. Smedskjaer, "Super Tough, Anti-swelling, Self-healing, and Biocompatible dual-Reinforced Binary Hydrogels". (to be submitted)

ORAL AND POSTER PRESENTATIONS AT CONFERENCES

W. Fan, R.E. Youngman, X. Ren, D. Yu, M.M. Smedskjaer, "Structural Control of Self-healing Silica-Poly(tetrahydropyran)-Poly(ε-caprolactone) Hybrids". **Oral:** *14th Pacific Rim Conference on Ceramic and Glass Technology including Glass&Optical Materials Division Meeting (PACRIM 14/ GOMD 21)*, December 14, online 2021.

W. Fan, L.R. Jensen, D. Yu, M.M. Smedskjaer, "Tough Double Interpenetrating Network Hydrogel with Dual Reinforcement Mechanism". **Poster:** *14th Pacific Rim Conference on Ceramic and Glass Technology including Glass&Optical Materials Division Meeting (PACRIM 14/ GOMD 21)*, December 14, online 2021.

W. Fan, L.R. Jensen, B. Xing, D. Yu, M.M. Smedskjaer, "Toughening and strengthening of bioactive hydrogels based on double interpenetrating networks". **Poster:** *International Year of Glass Symposium*, May 18-19, 2022

Paper I

Journal of Materials Chemistry B

ROYAL SOCIETY OF CHEMISTRY

PAPER

Cite this: J. Mater. Chem. B, 2021, 9, 4400

Structural control of self-healing silica–poly(tetrahydropyran)–poly(ε-caprolactone) hybrids†

Wei Fan,[a] Randall E. Youngman,[b] Xiangting Ren,[a] Donghong Yu *[a] and Morten M. Smedskjaer *[a]

Received 14th March 2021,
Accepted 14th May 2021

DOI: 10.1039/d1tb00555c

rsc.li/materials-b

In some biomaterial applications, the device needs to resist cyclic loading. Recently, self-healing hybrid systems with interpenetrating network of organic and inorganic components have been discovered. In this work, we clarify the structure–mechanical property relations in a new series of silica–poly(tetrahydropyran)–poly(ε-caprolactone) (SiO_2–PTHP–PCL) materials, which were prepared through a three-step synthesis, including one-pot cationic ring-opening polymerization, sol–gel reaction, and polymer–silica cross condensation. We applied THP as the main constituent of the organic phase and achieved successful polymerization under mild conditions, while the hybrid structures were controlled by the degree of silica-crosslinking and the organic/inorganic ratio. The thermal stabilities, densities, Young's modulus as well as hardness could also be regulated through such control. Notably, we find that the hybrid materials with organic polymer content above 73% are able to self-heal induced damages, including under body temperature conditions and the mechanical properties of the self-healed material are similar to those of the fresh samples. We ascribe this primarily to the reversible intermolecular interactions and hydrogen bonding among the polymer chains. Finally, we discover that the PTHP–SiO_2 networks are stable in a simulated bio-environment although PCL underwent biodegradation. The present structural control approach could lead to the design of tailored functional hybrid materials, with potential applications within areas such as soft robotics and bone regeneration.

1. Introduction

Bioactive glasses for tissue engineering and bone regeneration have received widespread attention due to their potential in bonding to bones and stimulating bone regeneration.[1–7] However, as they are made from amorphous oxides, they feature an intrinsic disadvantage, namely high brittleness, which makes them unable to withstand sustained cyclic loading as needed for use in the human body.[8] Such bioactive hybrids are mostly applied into the transplanted articular cartilage and tissues, and in order to accommodate the motions of the human body, materials with much better flexibility and strength are needed.[9,10] Organic–inorganic amorphous hybrids with stiff inorganic contents and soft polymers can potentially overcome this problem by offering improved functional and mechanical properties.[11–14] Distinct from a simple mixture of organic and inorganic phases, these hybrids possess inorganic–organic interpenetrating networks (IO-IPNs) at the molecular scale by having covalent bonds between the two networks. Generally, this approach has the advantage of avoiding aggregation of the different phases and enabling synergistic functions of organic polymer matrix and inorganic glass components.[13,15–18]

To enable the covalent bonding between the inorganic phase and the polymeric chains, and thus obtain an IO-IPN, a coupling agent is needed, which also leads to improved mechanical performance.[18,19] The one-pot sol–gel process has for years been the most common and successful method for preparing nano-scale networks,[20–23] although more recent alternative methods such as 3D printing and electrospinning exist.[24–26] Long time condensation and low gelation rate ensure hybrids with homogeneous structures. The formed interpenetrating inorganic–organic networks achieve synergistic functions of hybrids. Silica (SiO_2) is the typical inorganic component in hybrids with IO-IPNs due to various reasons, such as its availability, low cost, simple synthesis, stability, and bio-compatibility.[1,2] It is usually obtained through hydrolysis of tetraethyl orthosilicate (TEOS), with the mechanical properties of silica based hybrids being affected by the formed SiO_2 structures.[27,28]

[a] Department of Chemistry and Bioscience, Aalborg University, 9220 Aalborg, Denmark. E-mail: yu@bio.aau.dk, mos@bio.aau.dk
[b] Science and Technology Division, Corning Incorporated, Corning, New York 14831, USA

† Electronic supplementary information (ESI) available. See DOI: 10.1039/d1tb00555c

Regarding the organic component of hybrids, polycaprolactone (PCL) has shown excellent rheological and viscoelastic properties, as well as biodegradation *in vivo*.[29,30] This makes PCL a strong candidate for biomedical hybrid fabrication. Based on the work of Jones *et al.*,[31] we here propose that tetrahydropyran (THP) has the potential to be used as the main polymer source in such hybrids. Compared to tetrahydrofuran (THF) that was adopted in the work of Jones *et al.*, the additional C atom in the THP monomer could be expected to enable better tuning of the mechanical properties of hybrids. Considering its stable six-membered cyclic structure with low ring-strain, THP is generally considered to be resistant against ring-opening and thus polymerization under mild conditions.[32] As such, polyTHP (PTHP) is a very uncommon component in biomedical hybrids.[33] However, the cationic ring-opening process can possibly solve this in the presence of an epoxide ring with higher ring strain and a suitable Lewis acid (*e.g.*, boron trifluoride diethyletherate) as a catalyst.[31,34] In order to obtain PTHP as the main organic component and SiO_2 as the inorganic one, we selected glycidoxypropyl trimethoxysilane (GPTMS) as the organosilane coupling agent. The epoxide group in GPTMS is structurally similar to THP monomer and could therefore act as an initiator for the polymerization of THP, while the silyl group in GPTMS would simultaneously participate in the sol–gel condensation to link with the silica network, and therefore further construct the IO-IPNs as the final product. In this way, inorganic/organic composition ratio and their corresponding structures could directly determine the structure and mechanical properties of hybrids.[14]

In this work, *via* applying PTHP and PCL as the polymer component and silica as the inorganic one for IO-IPN hybrids, we successfully controlled their structure by varying the total silica/polymer composition ratio, as well as the exact chemical structure of both of the two phases, and investigated the thermal stability, mechanical properties, and biodegradation for exploring their structure–mechanical property relationship. Herein, we have also systematically studied how the inorganic/organic (I/O) ratio and silica structures (by different TEOS/water ratios) affect the hybrids' structure, mechanical properties, and self-healing abilities. These results show how mechanical properties including self-healing ability can be controlled bottom-up from the molecular level. Compared with pure inorganic samples, the hybrids offered improved flexibility and self-healing properties, suggesting the potential design strategy in the future for applications of tailored IO-IPN hybrids in soft matter and biomedical fields. We envision that our findings will be important for the rational design of hybrid materials.

2. Experimental section

2.1. Materials

All chemicals, polycaprolactone diol (HO–PCL–OH) (average M_n of 530 Da), $NaHCO_3$, KBr, 2,2,6,6-tetramethyl-1-piperidinyloxy (TEMPO), CH_3CN, tetrahydropyran (THP), (3-glycidoxypropyl) trimethoxysilane (GPTMS), boron trifluoride-diethyl ether ($BF_3{\cdot}OEt_2$), tetraethylorthosilicate (TEOS), HCl, phosphate buffered saline (PBS) solution were purchased from Sigma-Aldrich, and used as received.

2.2. Synthesis of organic sol precursor

HOOC–PCL–COOH was prepared *via* following the existing method of oxidation of HO–PCL–OH by using TEMPO.[31]

2.3. Synthesis of organic sol

The prepared HOOC–PCL–COOH (0.5 mol) was dissolved in anhydrous tetrahydropyran (THP) at a concentration of 50 mg mL^{-1}. Then, 1 mol GPTMS was added. After continuous stirring for 30 minutes, 0.25 mol $BF_3{\cdot}OEt_2$ was added into the mixture in order to catalyze the epoxide ring-opening polymerization. In our preliminary work, we added PCL–COOH as terminating agents both at the start and end of the THF and THP organic-sol processes. We found that the reaction rate was too high to remain control when adding HOOC–PCL–COOH at the end, and TEOS precursor will not mix with polymer precursor uniformly in very high viscosity solution. Consequently, we added HOOC–PCL–COOH from the beginning of the organic-sol preparation for the consistency of the experiment. This solution was stirred for 1.5 h for reaction. The high strain of the oxirane ring gave GPTMS much higher reactivity towards catalytic ring-opening than THP. Then the carboxylic acid groups in HOOC–PCL–COOH terminated the chain growth and form the structure of GPTMS–PTHP–PCL.

2.4. Synthesis of inorganic sol

TEOS, deionized water and 36 wt% hydrochloric acid (12 M HCl) were added with the molar ratio of 1 : 1.8 : 0.01, 1 : 3.6 : 0.01, and 1 : 5.4 : 0.01. These three mixtures were stirred vigorously to ensure that TEOS became hydrolyzed. The completion of the reaction was directly confirmed when the mixtures turned from cloudy to clear.

2.5. Synthesis of hybrids

After preparing the organic sol, the inorganic precursors (TEOS/H_2O at the molar ratio of 1/1.8, 1/3.6, 1/5.4) were mixed with the organic sol using five different ratios (in wt%) of TEOS/HOOC–PCL–COOH, namely 10/90, 20/80, 30/70, 40/60, and 60/40. The inorganic sol was poured drop-wise into the organic sol and stirred for at least 30 minutes at room temperature to obtain a homogeneous solution. Then, the mixed sols were transferred into a cylindrical polytetrafluoroethylene (PTFE) mold and sealed for aging for 1 week at 40 °C. Afterwards, the molds were partially opened to allow for drying over the following three weeks at 40 °C in the furnace. When all of these processes were finished, disc-shaped samples were peeled off from the containers and used for the characterization experiments. Hence, we obtained a total of 15 samples with different compositions and thus different structures. The used TEOS/water molar ratios and TEOS/PTHP–PCL mass ratios are summarized in Table S1 (ESI†). All of these prepared hybrids were classified into two groups (the same silica structure with different inorganic/organic (I/O) ratio and a constant I/O ratio with various silica structure). This was done to independently evaluate the effects

of SiO_2 structure and I/O ratio on the hybrid structure and mechanical properties.

2.6. Infrared spectroscopy

Fourier-transform infrared (FTIR) spectroscopy was performed by using a Bruker TENSOR II along with a Bruker Platinum ATR attachment, in the range of 4000 to 400 cm^{-1}. All spectra were compiled from 64 consecutive scans and were baseline corrected using the vendor supplied software OPUS.

2.7. Solid state NMR spectroscopy

^{29}Si magic-angle spinning (MAS) NMR data were collected with an Agilent DD2 spectrometer in conjunction with an Oxford 4.7 T widebore superconducting magnet, with a ^{29}Si resonance frequency of 39.70 MHz. Samples were powdered and loaded into 5 mm zirconia rotors with sample spinning of 5.0 kHz. Spectra were acquired using a $\pi/6$ tip angle of 2.7 μs, a recycle delay of 180 s, averaging of 400 to 1900 scans and with high-power ^{1}H decoupling during signal acquisition.

$^{1}H \rightarrow {}^{29}Si$ cross-polarization magic-angle spinning (CPMAS) NMR measurements were made on the same instrument with a 4 ms contact time between the spins, recycle delay of 5 s and signal averaging of 5500 to 33 000 scans. All ^{29}Si NMR data were processed with 25 Hz apodization, referenced to tetramethylsilane at 0.0 ppm, using the GRAMS Spectroscopy Software Suite (Thermo Fisher Scientific) to plot and fit the spectra.

^{13}C MAS NMR measurements were made at 11.7 T (125.67 MHz resonance frequency) using an Agilent DD2 spectrometer and Oxford wide-bore superconducting magnet. Powdered samples were packed into 3.2 mm zirconia rotors, with sample spinning of 20.0 kHz. ^{1}H decoupled MAS NMR data were acquired by the combination of a $\pi/4$ tip angle (2.4 μs), a 90 s delay between scans and signal averaging of 800 to 2800 scans. ^{13}C NMR data were processed with 10 Hz line broadening and referenced to tetramethylsilane at 0.0 ppm. Plotting and spectral analyses were done in the GRAMS software package.

2.8. Thin layer chromatography and liquid NMR

The oxidation of HO–PCL–OH into HOOC–PCL–COOH reaction was monitored through thin-layer chromatography (TLC) on Silica Gel 60 F254 plates. The mobile phase was a mixture of acetonitrile and ethanol in a volume ratio of 9 : 1 and visualization was done using I_2. The oxidation of HO–PCL–OH into HOOC–PCL–COOH was confirmed by liquid-state ^{1}H NMR spectroscopy performed on a 600 MHz Bruker spectrometer. 10 mg of polymer was dissolved in 0.5 mL deuterated chloroform ($CDCl_3$). The experimental parameters were set to acquire 16 scans in the range of chemical shift from 0 to 12 ppm.

2.9. Thermal gravimetric analysis (TGA)

The final inorganic *vs.* organic weight ratio was determined by thermal gravimetric analysis (TGA) (DSC 449C; Netzsch, Selb, Germany). The samples were run under a flow of air at the rate of 10 °C min^{-1}, from room temperature to 800 °C. Weight loss could be ascribed to the burning-out of the organic phase.

2.10. X-Ray diffraction (XRD) analysis

X-Ray diffraction (XRD) analysis was carried out on pulverized samples at $2\theta = 5^{\circ}$ to 80° using a Panalytical Empyrean diffractometer with a Cu-Kα radiation source (λ = 1.54 Å) with a Ni-filter.

2.11. Densities and the Young's modulus

Densities and the Young's modulus were conducted through Archimedes principle and ultrasonic echography, respectively.[35]

Densities of hybrids were firstly calculated here according to the eqn (1)

$$\rho_{sample} = \frac{\rho_{ethanol} \times m_{sample}^{air}}{m_{sample}^{air} - m_{sample}^{ethanol}} \quad (1)$$

Then, the Young's modulus (E) was obtained with the eqn (2)

$$E = \rho \frac{3V_L^2 - 4V_T^2}{(V_L/V_T)^2 - 1} \quad (2)$$

2.12. Hardness

Micro-indentation measurements were performed using a Nanovea CB500 hardness tester to determine the hardness (H). On each sample, 20 indentations with a maximum load of 0.07 N were generated to determine H, with a loading duration and dwell time of both 10 seconds. The loading and unloading rate were both 0.7 N min^{-1}. Measurements were performed under laboratory conditions (temperature: 23 °C; relative humidity: 23.5%). Then hardness was calculated from the force–displacement curves using the Oliver–Pharr model as follows,

$$H = \frac{P_{max}}{A_{pml}} \quad (3)$$

$$A_{pml} = F(h_c) \quad (4)$$

$$h_c = h_{max} - h_s \quad (5)$$

$$h_s = \varepsilon \frac{P_{max}}{S} \quad (6)$$

Here, P_{max} is the peak load, h_{max} is the depth at peak load, A_{pml} is the projected contact area, h_c is the contact depth, ε is a constant depending on the indenter, and S is the contact stiffness.

2.13. Dynamic mechanical analysis (DMA)

Dynamic mechanical analysis (DMA) was carried out using TA Instruments DMA 850. The frequency was set at 1 Hz at room temperature.

2.14. Self-healing process

Cracks were created by a sharp knife and all samples were self-healed without any external stimuli. The temperature was 23 °C and the relative humidity was 23.5%. We also performed the same experiment at body temperature conditions (37 °C).

3. Results and discussion

3.1. Hybrid synthesis

The schematic structures of pure inorganic SiO_2, physically mixed inorganic–organic hybrids (image of non-uniform dispersion of two phases), and covalently bonded hybrids are compared in Fig. 1. Compared with the pure bulk SiO_2 that has many cracks (Fig. 1a), hybrids without visible cracks (Fig. 1c) can be obtained upon introducing the organic polymers into the inorganic sol. A traditional mechanically mixed hybrid material easily suffers from aggregation of nanoparticles, which would inevitably affect the uniformity and decrease the mechanical reliability. In that case, inorganic network with covalently link polymer chains is an effective way to avoid aforementioned issues. The coupling agent, GPTMS applied in this experiment, due to its oxirane group, participates in the ring-opening process with THP monomers. Additionally, the –Si–OCH_3 was also hydrolyzed and bonded to silica networks through condensation process, bridging polymer chains. Thus further uniform dispersion of inorganic nanoparticles were achieved within the polymer chains, improving the mechanical properties (Fig. 1d and e). Consequently, we prepared the hybrids through a two-pot synthesis, combining cationic ring-opening method and sol–gel process, as shown in Scheme 1.

HO–PCL–OH had firstly been oxidized into HOOC–PCL–COOH for further reaction with PTHP and functioned as a quencher of the oxonium ion intermediates, with structure confirmed in Fig. S1 and S2 (ESI†).[31] ^{1}H NMR- and FTIR-spectroscopy (Fig. S1 and S2, ESI†), and TLC analysis were performed to confirm its molecular structure. The peaks at 3300 cm^{-1} of FTIR and broad peak from 8.0–9.5 ppm of ^{1}H NMR both confirm the conversion of HO–PCL–OH into HOOC–PCL–COOH. THP is relatively stable due to its six-membered cyclic structure, while the ring strain of oxirane in GPTMS is much higher, and as such, the epoxide ring in GPTMS is opened firstly by $BF_3{\cdot}OEt_2$ initiation.[32,34] Then, a nucleophilic attack of the oxygen of THP by BF_3 initiated the cationic ring opening polymerization and further chain elongation steps. In this way, covalent bonds were formed between GPTMS and PTHP polymer chains, thus constructing the organic copolymer with HOOC–PCL–COOH (Fig. S3a, ESI†). We noted that GPTMS not only participated in the THP ring-opening reaction, but also acted as an organosilane coupling agent for connecting silica network and polymer chains. For the inorganic sol, TEOS could be hydrolyzed into Q^1, Q^2, Q^3, and Q^4 units. Here Q^n refers to a unit with n number of –O–Si neighboring groups, and Q^1 to Q^4 are thus distinguished based on the degree of condensation of –OH and/or –OEt groups,[11,24] as schematically illustrated in Fig. S3b (ESI†).[27,28] More Q^2 structures helps to ensure flexibility, while bulky three-dimensional networks are promoted by Q^4 structures. It is generally challenging to prepare crack-free class II hybrids[13,36] with high inorganic content, but the introduction of polymer chains and crosslinkers make it possible.

3.2. Structure of hybrids

The silica molecular structures and the polymer architectures were investigated by Fourier-transform infrared (FTIR) spectroscopy, including comparisons of the FT-IR spectra of pure inorganic samples with the hybrids. The effect of varying the molar ratio of TEOS to H_2O on the silica structure is illustrated in Fig. S4 (ESI†). We could roughly investigate the amount of different Q^n structures.[27,37] The band at 1038 cm^{-1} is assigned as the Si–O–Si asymmetric stretching vibration, while the peak at 946 cm^{-1} represents vibration of Si–OH groups.[27] Moreover, the peaks at 1160 and 794 cm^{-1} are ascribed to (Si–O) Q^n structures (peaks at 1200, 970, and 820 cm^{-1} could be ascribed to ν(Si–O)Q^3, ν(Si–O)Q^2, and ν(Si–O)Q^1).[37,38] Upon incorporation of the organic precursor and GPTMS, more complicated structures were formed (Fig. 2a). The bands at 2930 and 1710 cm^{-1} are ascribed to the characteristic –CH_2 stretching and C═O stretching, respectively.[12]

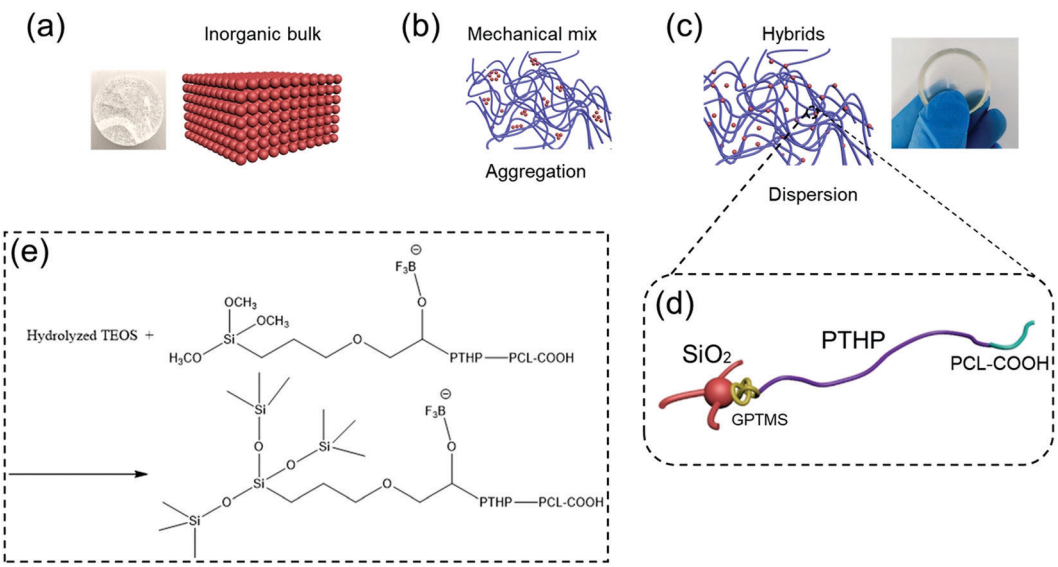

Fig. 1 Structural schemes of (a) inorganic bulk, (b) physically mixed hybrids, (c) covalently bonded hybrids, (d) covalent bonds between inorganic and organic parts, and (e) reaction process of precursors into hybrids.

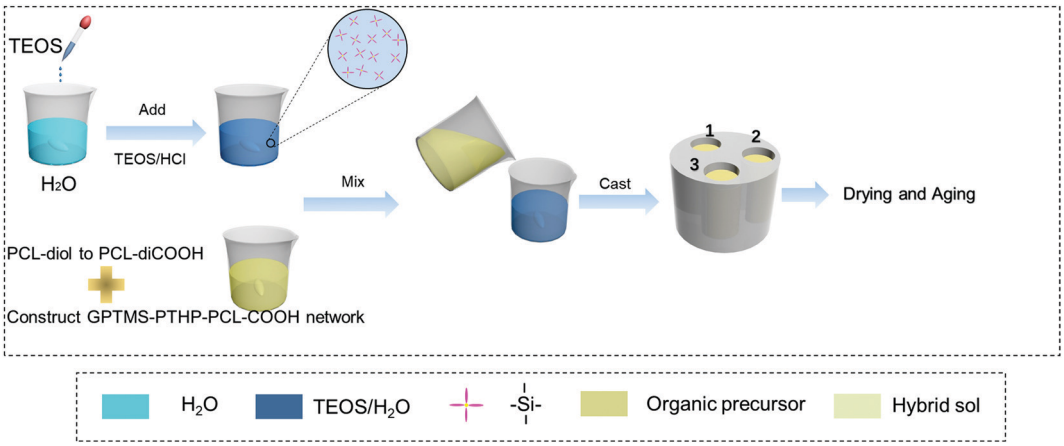

Scheme 1 The synthetic set-up and procedures of hybrids: casting, gelation, and aging and drying of merged sols from two pots of reactions for formation of silica-sol *via* hydrolysis of TEOS and organic sol by means of oxidation of HOOC–PCL–COOH and follow-up end-capping of GPTMS–PTHP (ring-opening polymerization of THP initiated by GPTMS).

These peaks appear very similar in the three hybrids, since they were kept at a constant composite ratio of PCL : TEOS = 7 : 3. The bands at 3300 cm^{-1} can be assigned to –OH stretching. Considering the silica network, the absorption peak at 1166 cm^{-1} could be identified as the Si–O–Si asymmetric stretching vibration like in the pure inorganic system. There are also new bands in the hybrids that can be ascribed to T-type –Si–O (where T-type refers to a Si atom with one $–CH_2–$ neighbor, while the other three are –O–Si).[24,34] The peaks around 1230 cm^{-1} are due to $–Si–CH_2$ in GPTMS. Considering the Si–O vibration range, peaks around 1099 cm^{-1} could also be ascribed to –(C═O)–O– groups in the organic polymer structures. As to the specific amount of different Q-type (Si–O– for all four bonds) and T-type SiO_2 structures, we next consider the solid-state ^{29}Si NMR spectroscopy analysis.

Focusing on the samples with different degree of hydrolysis in both pure inorganic and hybrid samples, we have used ^{29}Si NMR to evaluate differences in the SiO_2 structures (*e.g.*, extent of hydrolysis and condensation) (Fig. 2b). Three different hydrolyzed pure silica structures were observed in Fig. S5 (ESI†), with typical ^{29}Si chemical shifts at −92.3, −101.7, and −110.9 ppm that can be assigned to Q^2, Q^3, and Q^4 units, respectively.[11,24,28,39,40] As seen from Fig. S5 (ESI†) and Table 1, a higher fraction of fully cross-linked (Q^4) structures was obtained for the material with less water available for hydrolysis of the TEOS. The population differences for Q^2, Q^3 and Q^4 in each sample are small, but consistent with excess water being available to shift the silanol condensation (elimination of H_2O) back towards more Si–OH (*i.e.* more Q^2 and Q^3 species).

However, when mixed with the organic precursor and reacted with GPTMS, the resulting silicate network is substantially affected, as illustrated in Fig. 2b. Namely, T-type SiO_2 structures are present, due to GPTMS, as reflected in the more intense ^{29}Si resonances around −60 ppm.[34] Corresponding ^{29}Si chemical shifts at −50.5, −59.9, and −66.9 ppm are assigned to T^1, T^2, and T^3 units, respectively, where T^3 are fully-crosslinked polyhedra with three siloxane bonds (Si–O–Si) and one Si–C bond.[19] The partially condensed species, T^1 and T^2, contain two and one silanol group, respectively. As shown in Fig. 2b and Table 2, after condensation the highest fractions of T^3 and Q^4 units were obtained in hybrids with the ratio as $TEOS_1H_2O_{5.4}$. This interesting result suggests that more Q^2 units in the inorganic precursors, with more chain mobility, is beneficial for the subsequent condensation with GPTMS, and results in more T^3 and Q^4 structures in the final hybrid materials. The data in Fig. 1c, measured with CPMAS NMR, are not strictly quantitative due to the nature of cross-polarization (*i.e.* enhancement of signal due to nearby protons), which is an issue in precise measurement of Q^4 populations. The other resonances all have sufficient organic or silanol groups, and have been shown to give fairly equal responses under these measurement conditions (data not shown). The other trend in Fig. 2b is that the general ratio of T-type to Q-type species is consistent with the intended ratio of organic to inorganic precursors. The top spectrum ($Org_{0.9}Inorg_{0.1}$) has the lowest Q-type signal level, while the middle spectrum ($Org_{0.4}Inorg_{0.6}$) has the highest. The other three spectra in Fig. 2b are very similar to one another due to their identical I/O ratios. For these data, the differences in synthesis are due to water content and this appears to have only a minor impact on the extent of condensation for both the T- and Q-type silanes.

The other structural feature of these hybrid materials is the nature of the organic components, which are reflected in their ^{13}C NMR spectra. Fig. 2c contains the ^{13}C decoupled MAS NMR data for all five hybrids listed above in Table 2. While highly complex due to the different organic functional groups, including those from GPTMS, PCL and PTHP, the data have several features which support the hydrolysis and condensation reactions outlined in the aforementioned treatment of the silanes, and also the polymerization schemes of THP and CL (Fig. S3, ESI†). Unreacted alkoxide functional groups, due to incomplete hydrolysis of TEOS and GPTMS, would be reflected by ethoxy peaks at 18 ($–CH_3$) and 60 ($OCH_2–$) ppm for TEOS, and a methoxy peak around 51 ppm in GPTMS. The latter peak from methoxy groups is completely absent in all spectra, informing that all hydrolysis of methoxy groups on GPTMS was accomplished during fabrication of these hybrid materials. The other source of alkoxide peaks, ethoxy groups of TEOS, are also noticeably absent, so again very

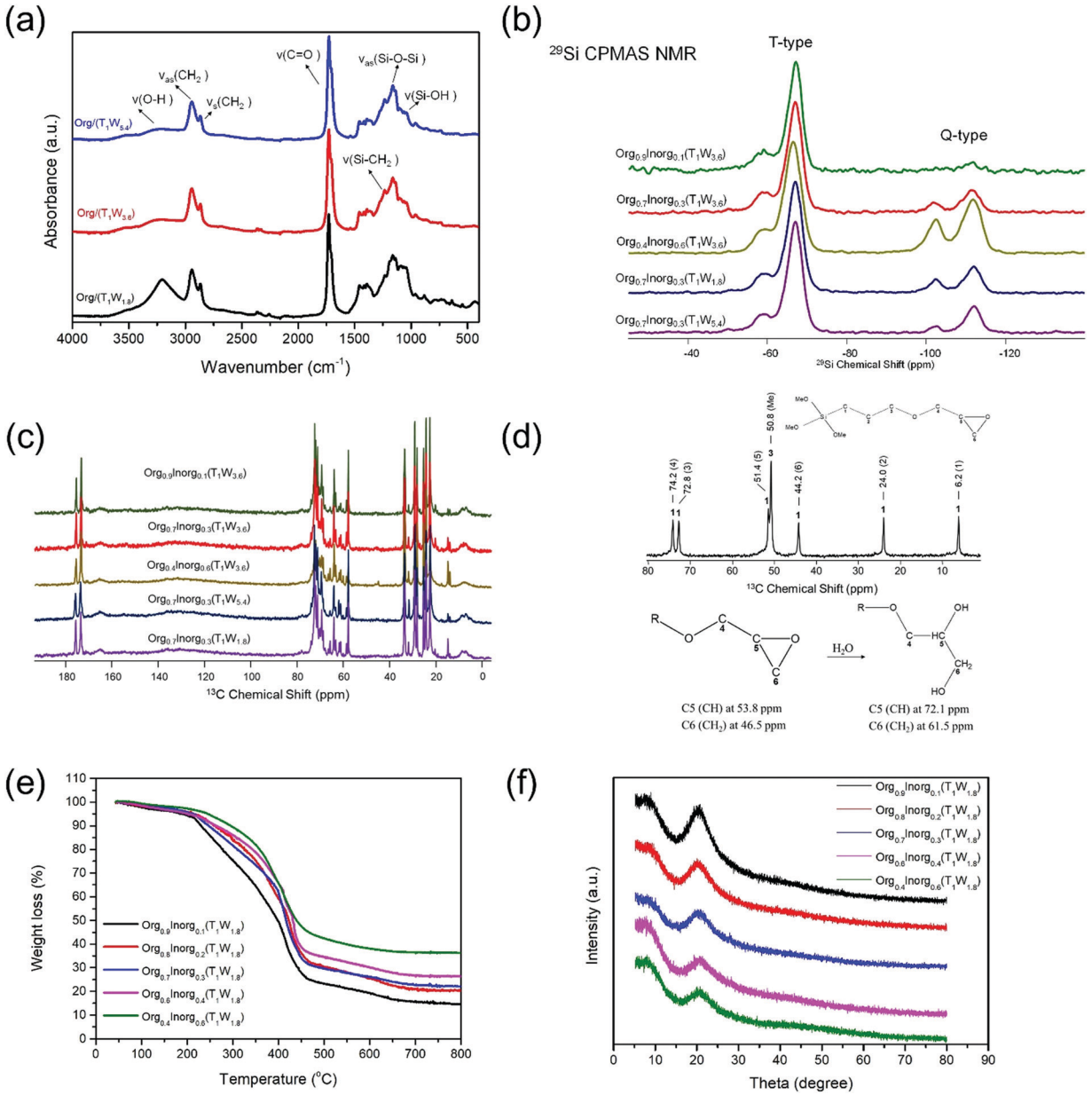

Fig. 2 (a) FT-IR spectra of hybrids with the same inorganic/organic (I/O) ratio but different TEOS/water (T/W) ratio. Solid state (b) ^{29}Si and (c) ^{13}C NMR spectra of hybrids with different compositions. (d) Hydrolysis of GPTMS and corresponding peak assignment of ^{13}C NMR spectrum. (e) TGA and (f) XRD spectra of hybrids with different I/O ratio.

Table 1 Position (δ) and relative intensity (I) of the Q^n units in the different hydrolyzed structures. The results are obtained from the solid-state ^{29}Si MAS-NMR spectroscopy analysis

	Q^2		Q^3		Q^4	
Sample	δ [ppm]	I [%]	δ [ppm]	I [%]	δ [ppm]	I [%]
$TEOS_1H_2O_{1.8}$	−92.3	5	−101.7	43	−110.9	52
$TEOS_1H_2O_{3.6}$	−92.7	7	−101.7	45	−110.4	50
$TEOS_1H_2O_{5.4}$	−92.3	7	−101.7	44	−110.6	49

efficient hydrolysis of the alkoxysilanes must have occurred. Only the $Org_{0.4}Inorg_{0.6}$ ($T_1W_{3.6}$) material shows much signal at 60 ppm, which suggests the possibility of incomplete TEOS hydrolysis in the most inorganic-rich hybrid. The lack of any appreciable signal around 18 ppm indicates that such residual ethoxide functionality is very low in all samples.

Another finding from the ^{13}C NMR data is the confirmation that GPTMS has undergone complete epoxide ring opening during the polymerization of the organic fraction in these hybrids (Fig. 2d). ^{13}C resonances in the original epoxide ring of GPTMS are found at 44 and 51 ppm, and Fig. 2c indicates that none of the five hybrid materials contain any evidence of these cyclic carbon peaks. Furthermore, once open and reacted with the caprolactone, these resonances move to very downfield shifts of around 62 and

Table 2 Position and relative intensity of the T^n and Q^n units in the different hybrids with the same I/O ratio. The results are obtained from the solid-state ^{29}Si CPMAS-NMR spectroscopy analysis

	T^1		T^2		T^3		Q^3		Q^4	
Sample	δ [ppm]	I [%]	δ [ppm]	I [%]	δ [ppm]	I [%]	δ [ppm]	I [%]	δ [ppm]	I [%]
$O_{0.7}I_{0.3}(T_1W_{1.8})$	−50.9	1	−60.0	17	−67.0	60	−102.5	7	−111.8	15
$O_{0.7}I_{0.3}(T_1W_{3.6})$	−50.5	1	−60.0	17	−66.9	63	−102.2	5	−111.4	14
$O_{0.7}I_{0.3}(T_1W_{5.4})$	−51.3	2	−59.5	15	−66.9	65	−102.3	3	−111.8	15
$O_{0.9}I_{0.1}(T_1W_{3.6})$	−50.5	3	−60.0	25	−67.1	61	−102.2	4	−111.2	7
$O_{0.4}I_{0.6}(T_1W_{3.6})$	−50.4	1	−59.4	13	−66.5	47	−102.4	14	−111.6	26

72 ppm, consistent with the large number of peaks in this region and the corresponding large fraction of different ether linkages in the organic polymers.

Thermal gravimetric analysis (TGA) has been applied to measure the inorganic *vs.* organic weight ratios in the hybrids. Initially, we distinguish hybrids by the weight ratio of PCL to TEOS. However, the total organic content is composed of PCL, PTHP, and the organic part of GPTMS, while the SiO_2 nanoparticles and the inorganic part of GPTMS constitute the total inorganic content. The results in Fig. 2e show that the weight begins to decrease at around 230 °C for all hybrids, which was higher than 170 °C of PTHF based hybrids in the work of Jones *et al.*[31] It represents more thermal stable hybrid materials obtained with PTHP than those with PTHF, which resulted from one more C atom in each repeat unit in the polymer backbone. The steric hindrance for the rotation of C–O bond is less than that of C–C. Thus, the rigidity of PTHP polymer chains is higher than that of PTHF polymer, which is the main reason for improved thermal stability of PTHP based hybrids.[41,42] Fig. 2e shows a comparison of weight loss *vs.* temperature profiles for hybrids with the same SiO_2 structure but varying PCL/TEOS weight ratio. We find that the remaining inorganic weight found at high temperature after thermal decomposition of the organic components constitute 15.0 wt%, 20.5 wt%, 22.3 wt%, 26.7 wt%, and 36.5 wt% of hybrid $Org_{0.9}Inorg_{0.1}$ to hybrid $Org_{0.4}Inorg_{0.6}$, respectively. The results are also summarized in Table 3. Additionally, hybrids with the same PCL/TEOS weight ratio feature almost identical TGA curves (Fig. S6, ESI†), which should be because the organic part is the same and decomposes, while the remaining SiO_2 particles constitute 22.3 wt%.

Finally, the non-crystallinity of the hybrid materials has been tested by X-ray diffraction (XRD). Hybrids were also compared according to various silica structures (Fig. S7, ESI†) and different I/O composition ratio (Fig. 2f). As depicted in Fig. 2b, no sharp diffraction peaks typical of crystalline SiO_2 are found in the hybrids, meaning no crystalline structures in the hybrids. This is due to the hydrolysis and condensation of TEOS and GPTMS, effectively preventing the crystallization of SiO_2 nanoparticles. It is also supported by the formation of covalent bonds between silica and polymer chains during reaction and sol–gel processes, resulting in the final amorphous state. Similarly, the hybrids with different SiO_2 structures but the constant organic content are also revealed to be completely amorphous. All of these XRD results are also consistent with the ^{29}Si NMR data (Fig. 1c and Fig. S7, ESI†), which showed linewidths for all peaks that reflected amorphous silicate groups.

Table 3 The weight ratios of PCL/TEOS in the starting sol–gel reaction and the actual O/I wt% values measured from TGA processes

Samples	PCL–diCOOH/TEOS wt%	Organic/inorganic wt%
Org_1Inorg_0	100/0	86.7/13.3
$Org_{0.9}Inorg_{0.1}$	90/10	84.9/15.1
$Org_{0.8}Inorg_{0.2}$	80/20	79.6/20.4
$Org_{0.7}Inorg_{0.3}$	70/30	77.7/22.3
$Org_{0.6}Inorg_{0.4}$	60/40	73.3/26.7
$Org_{0.4}Inorg_{0.6}$	40/60	63.5/36.5

3.3. Density, elasticity and rheology

We next evaluated the density, Young's modulus, and hardness for the five hybrids through Archimedes principle, ultrasonic echography, and micro-indentation methods, respectively.[37] Results are summarized in Tables 4 and 5. We find that the mechanical properties (modulus, hardness) of the five hybrids are affected by the silica structure (from TEOS/water (T/W) ratio) and I/O composition ratio. On the other hand, the densities of the hybrids $Org_{0.7}Inorg_{0.3}(T_1W_{1.8})$, $Org_{0.7}Inorg_{0.3}(T_1W_{3.6})$, and $Org_{0.7}Inorg_{0.3}(T_1W_{5.4})$ are very similar, being attributed to the same organic/inorganic ratio in these hybrids. Higher silica content in the hybrids resulted in higher density, with $Org_{0.4}Inorg_{0.6}(T_1W_{3.6})$ showing the highest density among the hybrids with the same TEOS to water molar ratio. This can be understood based on the relatively higher density of pure amorphous silica (2.2 g cm^{-3}) than those of polymers. However, we note that the type of silica structure has a negligible influence on hybrid density.

Considering the variation in Young's modulus, we find that the hybrids with higher inorganic content but the same silica structures, *i.e.*, $Org_{0.9}Inorg_{0.1}(T_1W_{3.6})$, $Org_{0.7}Inorg_{0.3}(T_1W_{3.6})$, and $Org_{0.4}Inorg_{0.6}(T_1W_{3.6})$ reveals higher Young's modulus, up to 1.68 GPa for the hybrid $Org_{0.4}Inorg_{0.6}(T_1W_{3.6})$. This is ascribed to the high network connectivity and bond strength of amorphous silica. Moreover, based on the silica structure analysis (^{29}Si NMR data), we find that the hybrid $Org_{0.7}Inorg_{0.3}(T_1W_{5.4})$ with the most T^3, Q^4 structural feature has a higher Young's modulus of 1.29 GPa compared with those of the other two hybrids ($Org_{0.7}Inorg_{0.3}(T_1W_{1.8})$ and $Org_{0.7}Inorg_{0.3}(T_1W_{3.6})$) with the same inorganic/organic ratio. As such, the elasticity of hybrids is found to be affected by both silica structure and inorganic/organic ratio, with higher inorganic content and more T^3, Q^4 structures resulting in hybrids with higher Young's modulus.

Table 4 Densities and Young's modulus of hybrids

	$Org_{0.7}Inorg_{0.3}(T_1W_{1.8})$	$Org_{0.9}Inorg_{0.1}(T_1W_{3.6})$	$Org_{0.7}Inorg_{0.3}(T_1W_{3.6})$	$Org_{0.4}Inorg_{0.6}(T_1W_{3.6})$	$Org_{0.7}Inorg_{0.3}(T_1W_{5.4})$
Density (g cm^{-3})	1.235	1.216	1.237	1.287	1.237
Modulus (GPa)	0.86	0.54	1.15	1.68	1.29

Table 5 Hardness of hybrids from micro-indentation measurements

	$Org_{0.7}Inorg_{0.3}(T_1W_{1.8})$	$Org_{0.9}Inorg_{0.1}(T_1W_{3.6})$	$Org_{0.7}Inorg_{0.3}(T_1W_{3.6})$	$Org_{0.4}Inorg_{0.6}(T_1W_{3.6})$	$Org_{0.7}Inorg_{0.3}(T_1W_{5.4})$
H (MPa)	5.0	2.6	9.1	58.8	7.0
Error	0.5	0.7	2.0	7.5	1.1

Considering the variation in hardness (*H*),[43,44] the results are shown in Fig. S8–S10 (ESI†) and Table 5. The hybrid $Org_{0.9}Inorg_{0.1}(T_1W_{3.6})$ is the softest among all hybrids as it has the highest organic content, while the hardness of $Org_{0.4}Inorg_{0.6}(T_1W_{3.6})$ reaches 58 MPa because of its high inorganic content (36.5%). By comparing the results for hybrids $Org_{0.9}Inorg_{0.1}(T_1W_{3.6})$, $Org_{0.7}Inorg_{0.3}(T_1W_{3.6})$, and $Org_{0.4}Inorg_{0.6}(T_1W_{3.6})$, we conclude that the hardness increases rapidly with the increase in the inorganic content. Additionally, the results also demonstrate that hybrids with the same I/O ratio but different silica structure (as controlled by the T/W ratio) also show variation in hardness. That is, hybrid $Org_{0.7}Inorg_{0.3}(T_1W_{1.8})$ shows relatively lower hardness than $Org_{0.7}Inorg_{0.3}(T_1W_{3.6})$ and $Org_{0.7}Inorg_{0.3}(T_1W_{5.4})$. This can mainly be ascribed to the lowest amount of T^3 structures in $Org_{0.7}Inorg_{0.3}(T_1W_{1.8})$ compared with the other two. The hybrid with higher rigidity to the network reveals much higher hardness structurally. Therefore, the higher T/W ratio induces more polymerized and branched silica structures, which in turn give higher hardness.

To test the cycling loading resistance of the hybrids, we performed up to 20 cycles of indentation load–unloading experiments to the same maximum load (Fig. S9, ESI†). The curves are generally well repeated and samples avoiding cracking even after 20 cycles, although there is a minor increase in the penetration depth after multiple cycles. This generally proves the stability and durability of the prepared hybrids, confirming their potential applications within, *e.g.* soft robots and tissue engineering.

Finally, we also tested the rheological properties of hybrids with different I/O ratios. That is, the change in storage modulus (*E′*) and loss modulus (*E″*) with time for hybrids $Org_{0.9}Inorg_{0.1}(T_1W_{3.6})$, $Org_{0.7}Inorg_{0.3}(T_1W_{3.6})$, and $Org_{0.4}Inorg_{0.6}(T_1W_{3.6})$ at 1 Hz under room temperature. As shown in Fig. 3, $Org_{0.4}Inorg_{0.6}(T_1W_{3.6})$ possesses the highest storage modulus (~300 kPa), while hybrid $Org_{0.9}Inorg_{0.1}(T_1W_{3.6})$ has the lowest (~50 kPa). The change of *E′*/*E″* with I/O ratio demonstrates that the hybrids transform from rubber-like to glass-like behavior with the increase in inorganic fraction. Additionally, with the increment of time, both storage modulus and loss modulus of all hybrids do not change considerably, confirming the elastic stability of the hybrids.[45]

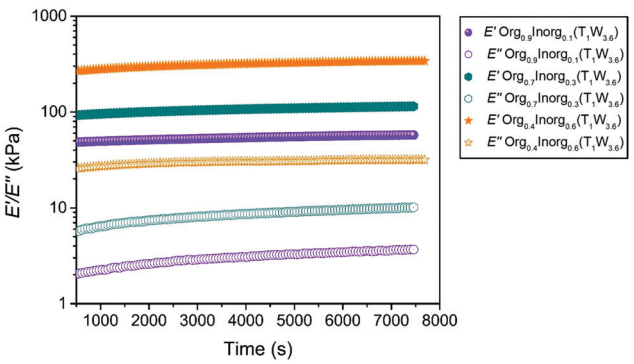

Fig. 3 Rheology properties: storage modulus (*E′*) and loss modulus (*E″*) as a function of time for hybrid $Org_{0.9}Inorg_{0.1}(T_1W_{3.6})$, $Org_{0.7}Inorg_{0.3}(T_1W_{3.6})$, and $Org_{0.4}Inorg_{0.6}(T_1W_{3.6})$.

3.4. Self-healing

With good reproducibility from all six different samples based on different PCL–diCOOH/TEOS compositions (100/0, 90/10, 80/20, 70/30, 60/40, and 40/60), we found that the hybrids with certain organic contents are able to autonomously self-heal after mechanical damage. Autonomous self-healing materials means that no heat, artificial light or other stimulus and materials has been used to induce repair of the damage. Here, we introduced defects by a sharp cut on the top surface of the hybrids, as shown in the optical microscopy images in Fig. 4a–d. Then samples were held at room temperature without any other stimulus for 24 h. The hybrids revealed self-healing ability to varying degree, which could also be proven by the optical microscopy images in Fig. 4e–h. The samples without SiO_2 nanoparticles (Org_1Inorg_0) and the hybrid with the smallest inorganic content $Org_{0.9}Inorg_{0.1}(T_1W_{1.8})$ were perfectly re-joined and self-healed after 24 h. Moreover, we compare self-healing abilities of hybrids $Org_{0.9}Inorg_{0.1}(T_1W_{3.6})$ and $Org_{0.9}Inorg_{0.1}(T_1W_{5.4})$ in Fig. S11 (ESI†), which reveal well recovery after storage for 24 hours under the same conditions. Afterwards, in order to test if the mechanical properties are fully recovered after cracking and self-healing, Fig. S12 (ESI†) shows a typical indentation test of the fresh sample and self-healed after 24 h. The maximum indentation depth of fresh sample is 62 μm, while that of the self-healed sample is 70 μm. However, both samples show complete load–unload curves, and the slopes of the loading and unloading curves are also similar. We thus conclude that the mechanical properties of the self-healed hybrid $Org_{0.9}Inorg_{0.1}(T_1W_{1.8})$ are only slightly impacted.

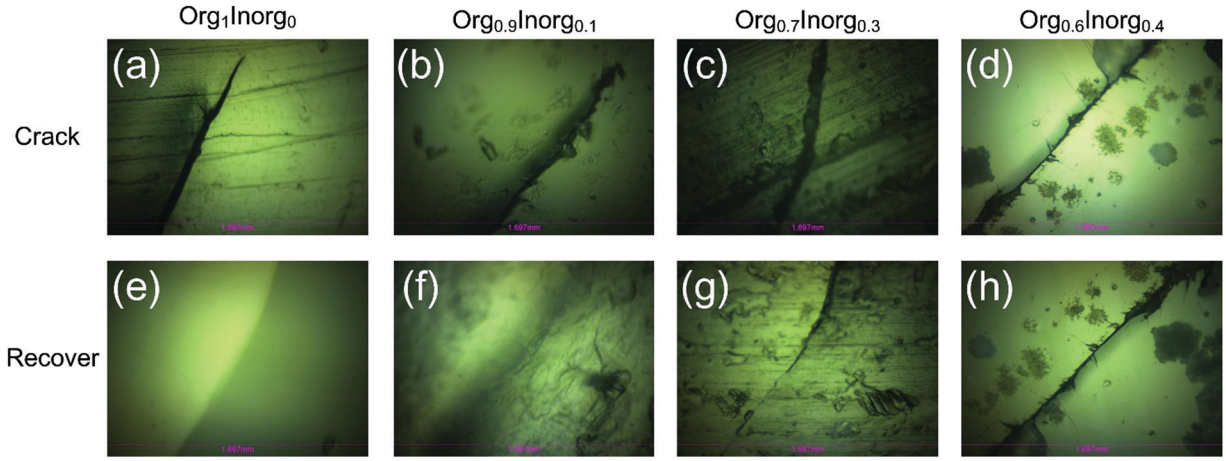

Fig. 4 Optical microscope images of four hybrid compositions after creation of a defect (top view) (a) Org_1Inorg_0; (b) $Org_{0.9}Inorg_{0.1}(T_1W_{1.8})$; (c) $Org_{0.7}Inorg_{0.3}(T_1W_{1.8})$; (d) $Org_{0.6}Inorg_{0.4}(T_1W_{1.8})$ and after self-healing for 24 hours (e) Org_1Inorg_0; (f) $Org_{0.9}Inorg_{0.1}(T_1W_{1.8})$; (g) $Org_{0.7}Inorg_{0.3}(T_1W_{1.8})$; (h) $Org_{0.6}Inorg_{0.4}(T_1W_{1.8})$.

The hybrid $Org_{0.7}Inorg_{0.3}$ also underwent recovery during the same time period, although not as much pronounced as the two hybrids with lower silica content. No apparent self-healing could be observed in $Org_{0.6}Inorg_{0.4}$, as the decreasing content of organic polymer leads to weaker intermolecular forces (London dispersive forces together with dipole–dipole interactions among PTHP and PCL polymer chains) and hydrogen bonds (formed among the carboxyl groups of PCL–COOH ending groups and hydroxyl groups in silanol in SiO_2), resulted in unfavorable self-healing properties. Thus, the driving force for the autonomous self-healing is largely triggered by the above-described supramolecular interactions in the polymer phases, and the polymer fraction therefore largely controls the self-healing ability in the present hybrid system, especially in terms of the hydrogen bonds in PCL–COOH.[31]

We have also confirmed that the self-healing is possible under body temperature by storing the cracked hybrid $Org_{0.9}Inorg_{0.1}(T_1W_{1.8})$ over 8 hours at 37 °C (Fig. S13, ESI†). The hybrid begins to self-heal quickly as the large crack becomes narrower after 2 hours. The cracks are almost rejoined after 4 hours and totally disappeared after 8 hours.

3.5. Biodegradability

We tested the biodegradation properties of the hybrids in order to investigate their stability in a bio-like environment since PCL has been well-recognized as a biodegradable polyester in the

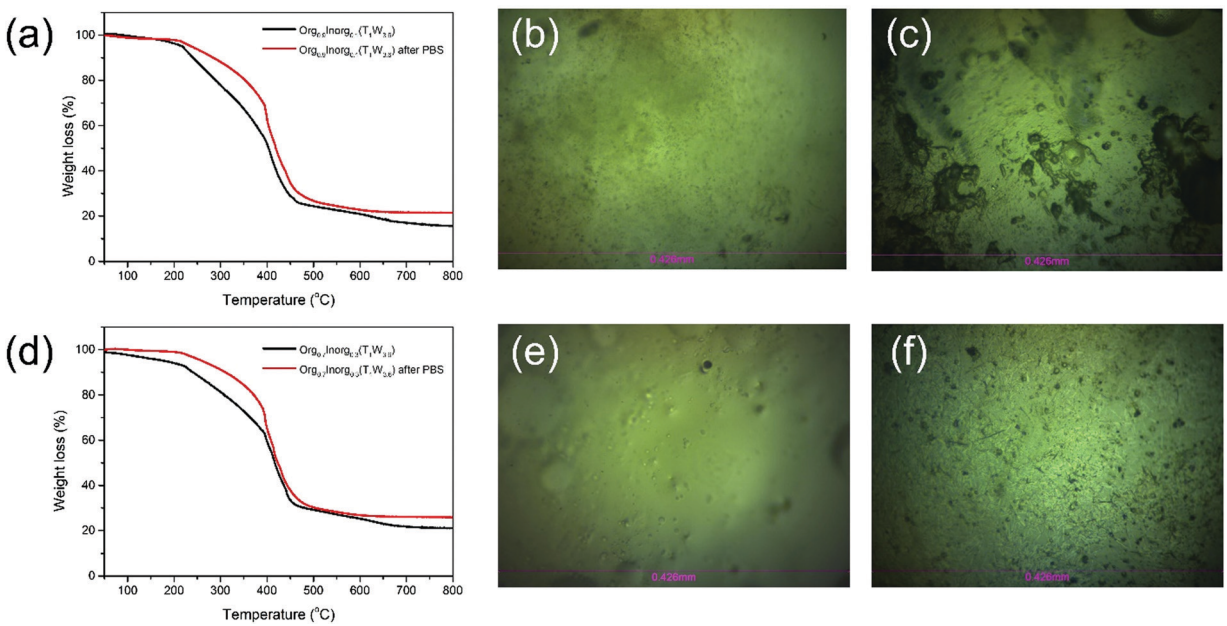

Fig. 5 (a) TGA of hybrid $Org_{0.9}Inorg_{0.1}(T_1W_{3.6})$ before and after immersed in PBS solution; optical microscope images of hybrid $Org_{0.9}Inorg_{0.1}(T_1W_{3.6})$, (b) before and (c) after immersed in PBS solution; (d) TGA of hybrid $Org_{0.7}Inorg_{0.3}(T_1W_{3.6})$ before and after immersed in PBS solution; optical microscope images of hybrid $Org_{0.7}Inorg_{0.3}(T_1W_{3.6})$, (e) before and (f) after immersed in PBS solution.

system.[18,29,30] To this end, choosing hybrids representatively like mentioned above, five hybrid samples are immersed into phosphate buffered saline (PBS) solution with pH = 7.4 (a buffer solution which is widely used in biological experiments and possesses similar osmotic pressure and pH to human body fluids) for 7 days at 37 °C (Fig. S14a, ESI†). The original weight of the five hybrids ($Org_{0.7}Inorg_{0.3}(T_1W_{1.8})$; $Org_{0.9}Inorg_{0.1}(T_1W_{3.6})$; $Org_{0.7}Inorg_{0.3}(T_1W_{3.6})$; $Org_{0.4}Inorg_{0.6}(T_1W_{3.6})$; $Org_{0.7}Inorg_{0.3}(T_1W_{5.4})$) was 192.1, 330.7, 319.9, 286.7, and 205 mg, respectively. No apparent visual damage was formed after 7 days immersion and the weight of hybrids became 151.7, 251.4, 253.2, 251.6, and 162.6 mg, respectively. After immersion, the weight of the hybrids thus declined slightly, which we mainly ascribe to hydrolytic scission of the ester linkage of PCL in such aqueous situation.[9,22] However, the bulk samples kept their original shape after immersion and avoided swelling or cracking after soaking in PBS, revealing good stability of the PTHF–SiO_2 networks in the aqueous solution. The weight loss in the samples is exclusively due to PCL, which constituted 21.03%, 23.98%, 20.85%, 12.24%, and 20.69% of total weight mass in the five samples, respectively. In order to determine any change in total inorganic/organic ratio upon immersion, the five hybrids were tested by TGA (see, Fig. 5a, d and Fig. S14b–d, ESI†). The inorganic weight fraction before immersion was 22.2%, 16.2%, 20.8%, 29.4%, and 20.9%, respectively, while it changed to 27.7%, 21.4%, 26.5%, 33.3%, and 25.8%, respectively, after immersion and drying. With the increment of 20.2%, 24.4%, 21.5%, 11.7% and 19.0%, respectively (calculated through TGA changes). These calculated changing results through TGA and mass loss of bulk samples are also in good accordance. Optical microscope images of the hybrids before and after immersion are shown in Fig. 5b, c, e, f and Fig. S14, S15 (ESI†). The surfaces of the hybrids were relatively smooth before immersion, but defects appeared after 7 days of immersion, with the appearance of small cracks in hybrids with higher inorganic content (especially in the brittle pure inorganic sample). This provides additional strong indication that PCL degraded and entered the PBS solution. Hence, shapes and volumes of samples are maintained under such circumstance but with the degradation of PCL, which is important in biomedical applications.

4. Conclusions

In summary, we have successfully prepared a novel series of SiO_2–PTHP–PCL ternary inorganic–organic hybrids through one-pot cationic ring-opening polymerization and sol–gel method. In this work, THP was successfully polymerized under a mild condition, as inspired by related synthesis processes. Such an extended monomer repeat unit, *i.e.*, THP-based hybrids, improved their thermal stability and Young's modulus compared with THF-based ones. In this work, we focused on systematically exploring structural and mechanical influences of silica structures together with I/O compositions, finding that silica structures determined the molecular structures and mechanical properties of hybrids, while I/O compositions controlled densities, mechanical properties, and self-healing abilities. Moreover, the constructed PTHP–SiO_2 networks maintained desirable bio-stability, without dissolving or swelling in PBS solution although with PCL being biodegraded. Our work has revealed potential in guaranteeing enough mechanical support with reasonable bio-degradability as biomedical materials applied in tissue engineering, bone regeneration, and soft robotics.

Conflicts of interest

There are no conflicts to declare.

Acknowledgements

This work was supported by the China Scholarship Council (CSC No. 201904910782).

References

1 M. Colilla, A. J. Salinas and M. Vallet-Regí, Amino-Polysiloxane, *Chem. Mater.*, 2006, **18**, 5676–5683.
2 P. Saravanapavan, J. R. Jones, R. S. Pryce and L. L. Hench, *J. Biomed. Mater. Res., Part A*, 2003, **66**, 110–119.
3 D. S. Brauer, *Angew. Chem., Int. Ed.*, 2015, **54**, 4160–4181.
4 U. G. Wegst, H. Bai, E. Saiz, A. P. Tomsia and R. O. Ritchie, *Nat. Mater.*, 2015, **14**, 23–36.
5 H. Shegarfi and O. Reikeras, *J. Orthop. Surg.*, 2009, **17**, 206–211.
6 Q. Fu, E. Saiz, M. N. Rahaman and A. P. Tomsia, *Adv. Funct. Mater.*, 2013, **23**, 5461–5476.
7 M. Vallet-Regi and E. Ruiz-Hernandez, *Adv. Mater.*, 2011, **23**, 5177–5218.
8 M. N. Rahaman, D. E. Day, B. S. Bal, Q. Fu, S. B. Jung, L. F. Bonewald and A. P. Tomsia, *Acta Biomater.*, 2011, **7**, 2355–2373.
9 I. Izquierdo-Barba, A. J. Salinas and M. Vallet-Regí, *Int. J. Appl. Glass Sci.*, 2013, **4**, 149–161.
10 Q. Fu, E. Saiz and A. P. Tomsia, *Adv. Funct. Mater.*, 2011, **21**, 1058–1063.
11 E. M. Valliant, F. Romer, D. Wang, D. S. McPhail, M. E. Smith, J. V. Hanna and J. R. Jones, *Acta Biomater.*, 2013, **9**, 7662–7671.
12 J. J. Chung, S. Li, M. M. Stevens, T. K. Georgiou and J. R. Jones, *Chem. Mater.*, 2016, **28**, 6127–6135.
13 B. M. Novak, *Adv. Mater.*, 1993, **5**, 422–433.
14 J. R. Jones, *Acta Biomater.*, 2013, **9**, 4457–4486.
15 L. S. Connell, L. Gabrielli, O. Mahony, L. Russo, L. Cipolla and J. R. Jones, *Polym. Chem.*, 2017, **8**, 1095–1103.
16 A. Kumar, K. M. Rao and S. S. Han, *Chem. Eng. J.*, 2017, **317**, 119–131.
17 J. J. Blaker, A. Bismarck, A. R. Boccaccini, A. M. Young and S. N. Nazhat, *Acta Biomater.*, 2010, **6**, 756–762.
18 D. Wang, W. Liu, Q. Feng, C. Dong, Q. Liu, L. Duan, J. Huang, W. Zhu, Z. Li, J. Xiong, Y. Liang, J. Chen, R. Sun, L. Bian and D. Wang, *Mater. Sci. Eng., C*, 2017, **70**, 969–975.

19 O. Mahony, O. Tsigkou, C. Ionescu, C. Minelli, L. Ling, R. Hanly, M. E. Smith, M. M. Stevens and J. R. Jones, *Adv. Funct. Mater.*, 2010, **20**, 3835–3845.
20 G. J. Owens, R. K. Singh, F. Foroutan, M. Alqaysi, C.-M. Han, C. Mahapatra, H.-W. Kim and J. C. Knowles, *Prog. Mater. Sci.*, 2016, **77**, 1–79.
21 L. L. Hench and J. K. West, *Chem. Rev.*, 1990, **90**, 33–72.
22 D. Tian, P. Dubois, C. Grandfils, R. Jérôme, P. Viville, R. Lazzaroni, J.-L. Brédas and P. Leprince, *Chem. Mater.*, 1997, **9**, 871–874.
23 F. Baino, E. Fiume, M. Miola and E. Verné, *Int. J. Appl. Ceram. Technol.*, 2018, **15**, 841–860.
24 E. Norris, C. Ramos-Rivera, G. Poologasundarampillai, J. P. Clark, Q. Ju, A. Obata, J. V. Hanna, T. Kasuga, C. A. Mitchell, G. Jell and J. R. Jones, *Biomed. Mater.*, 2020, **15**, 015014.
25 W. Fan, X. Zhang and C. Li, *Compos. Commun.*, 2019, **15**, 68–75.
26 L. Che, Z. Lei, P. Wu and D. Song, *Adv. Funct. Mater.*, 2019, **29**, 1904450.
27 M. C. Matos, L. M. Ilharco and R. M. Almeida, *J. Non-Cryst. Solids*, 1992, **147–148**, 232–237.
28 R. H. Glaser, G. L. Wilkes and C. E. Bronnimann, *J. Non-Cryst. Solids*, 1989, **113**, 73–87.
29 M. A. Woodruff and D. W. Hutmacher, *Prog. Polym. Sci.*, 2010, **35**, 1217–1256.
30 S.-H. Rhee, *Biomaterials*, 2003, **24**, 1721–1727.
31 F. Tallia, L. Russo, S. Li, A. L. H. Orrin, X. Shi, S. Chen, J. A. M. Steele, S. Meille, J. Chevalier, P. D. Lee, M. M. Stevens, L. Cipolla and J. R. Jones, *Mater. Horiz.*, 2018, **5**, 849–860.
32 N. Watanabe, S. Uemura and M. Okano, *Bull. Chem. Soc. Jpn.*, 1979, **52**, 3611–3614.
33 J. Pan, I. Hanna and J.-Y. Lallemand, *Tetrahedron Lett.*, 1991, **32**, 7543–7544.
34 L. Gabrielli, L. Connell, L. Russo, J. Jiménez-Barbero, F. Nicotra, L. Cipolla and J. R. Jones, *RSC Adv.*, 2014, **4**, 1841–1848.
35 T. To, L. R. Jensen and M. M. Smedskjaer, *J. Non-Cryst. Solids*, 2020, **534**, 119946.
36 M. Erol-Taygun, K. Zheng and A. R. Boccaccini, *Int. J. Appl. Glass Sci.*, 2013, **4**, 136–148.
37 F. Rubio, J. Rubio and J. L. Oteo, *Spectrosc. Lett.*, 1998, **31**, 199–219.
38 P. Yu, R. J. Kirkpatrick, B. Poe, P. F. McMillan and X. Cong, *J. Am. Ceram. Soc.*, 2004, **82**, 742–748.
39 I. Artaki, M. Bradley, T. W. Zerda and J. Jonas, *J. Phys. Chem.*, 1985, **89**, 4399–4404.
40 L. S. Connell, F. Romer, M. Suarez, E. M. Valliant, Z. Zhang, P. D. Lee, M. E. Smith, J. V. Hanna and J. R. Jones, *J. Mater. Chem. B*, 2014, **2**, 668–680.
41 L. Abate, I. Blanco, G. Cicala, A. Mamo, G. Recca and A. Scamporrino, *Polym. Degrad. Stab.*, 2010, **95**, 798.
42 M. Tanimoto, T. Yamagata, K. Miyata and S. Ando, *ACS Appl. Mater. Interfaces*, 2013, **5**, 4374.
43 W. C. Oliver and G. M. Pharr, *J. Mater. Res.*, 2011, **7**, 1564–1583.
44 E. Broitman, *Tribol. Lett.*, 2016, **65**, 23.
45 R. Arrigo and G. Malucelli, *Materials*, 2020, **13**, 2771.

Electronic Supplementary Information

Structural Control of Self-Healing Silica-Poly(Tetrahydropyran)-Poly(ε-caprolactone) Hybrids

Wei Fan[1], Randall E. Youngman[2], Xiangting Ren[1], Donghong Yu[1,*], Morten M. Smedskjaer[1,*]

[1] *Department of Chemistry and Bioscience, Aalborg University, 9220 Aalborg, Denmark*

[2] *Science and Technology Division, Corning Incorporated, Corning, New York 14831, USA*

[*] *Corresponding authors. email: yu@bio.aau.dk (D.Y.), mos@bio.aau.dk (M.M.S.)*

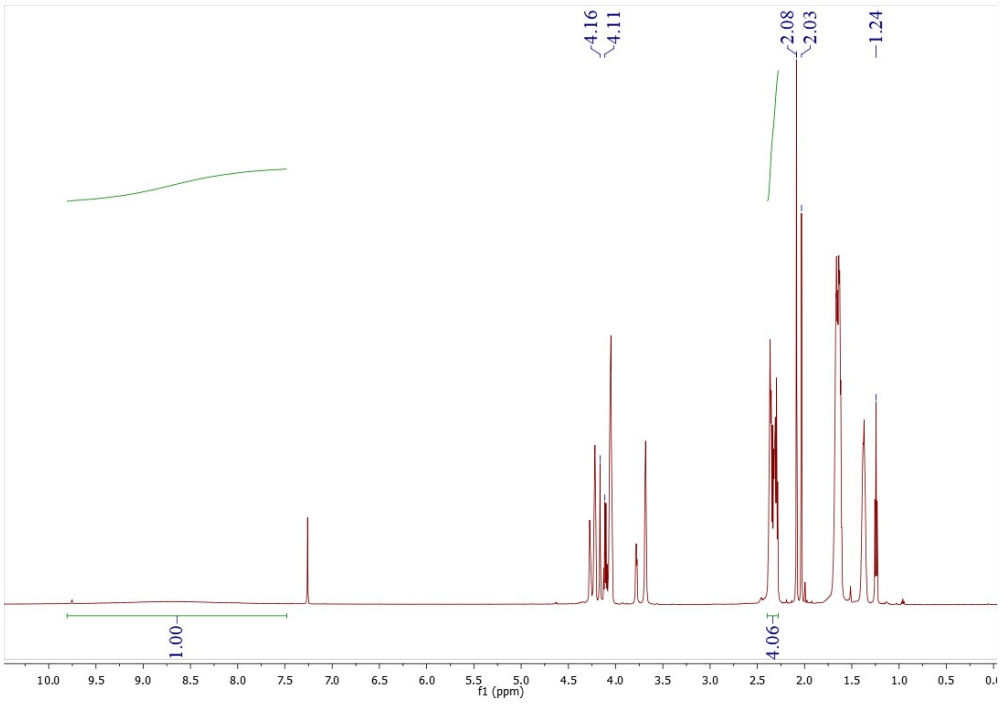

Fig. S1 ^{1}H-NMR spectrum of HOOC-PCL-COOH in $CDCl_3$.

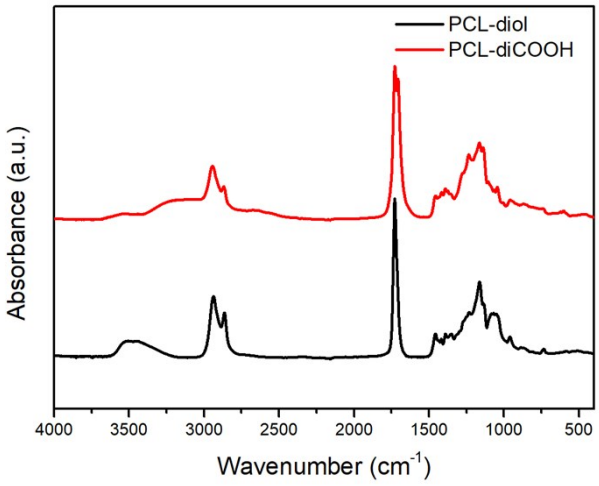

Fig. S2 FT-IR spectra HO-PCL-OH and HOOC-PCL-COOH.

(a) Step 1

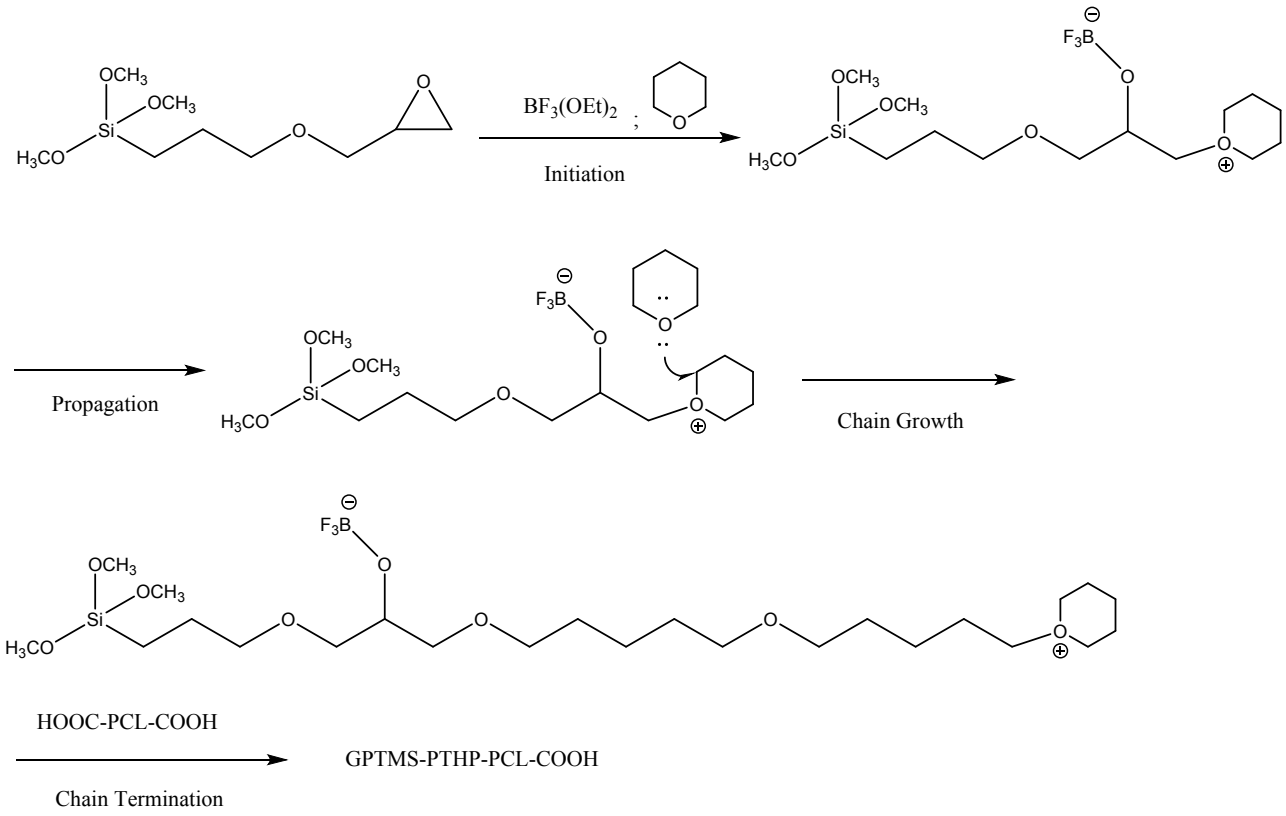

(b) Step 2

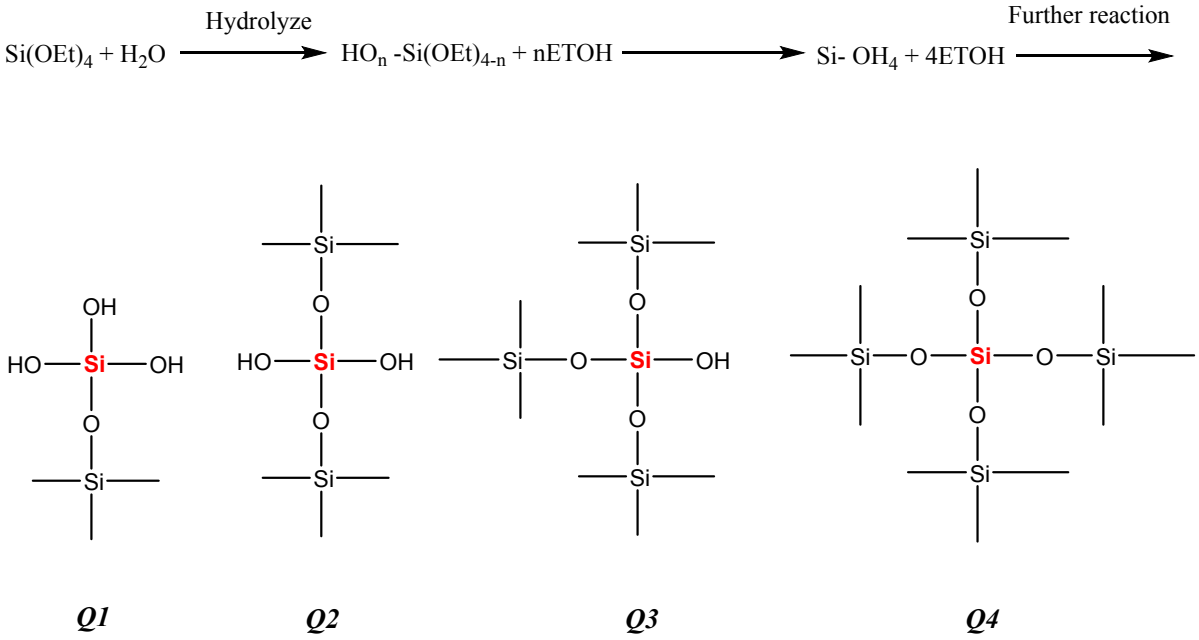

Fig. S3 Reaction mechanism of (a) THP cationic ring-opening polymerization; (b) hydrolysis of TEOS.

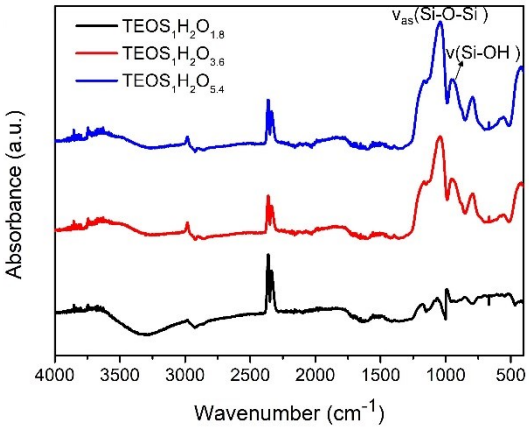

Fig. S4 Molecular structures of pure inorganic bulks compared through FTIR.

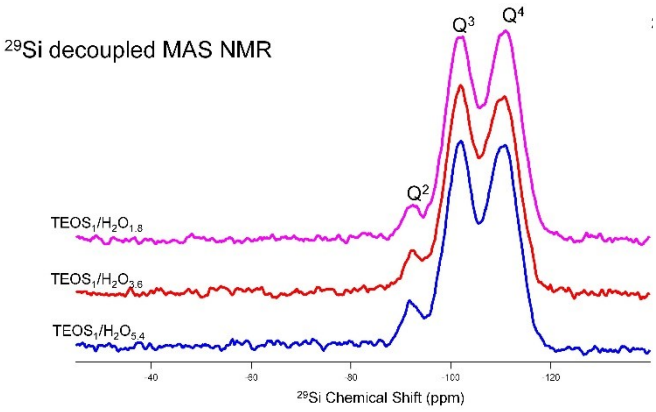

Fig. S5 ^{29}Si NMR spectra of inorganic bulks in different TEOS/H_2O molar ratios.

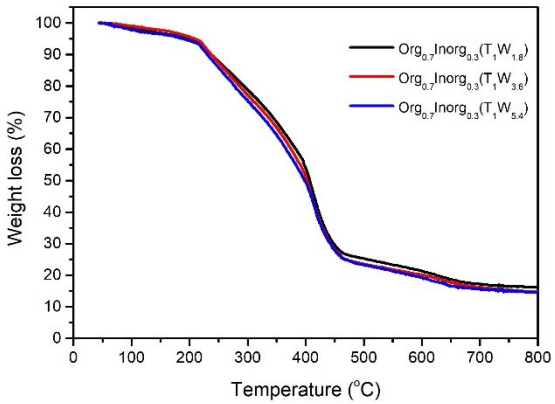

Fig. S6 TGA of hybrids with the same organic/inorganic compositions $Org_{0.7}Inorg_{0.3}$ with different silica structures.

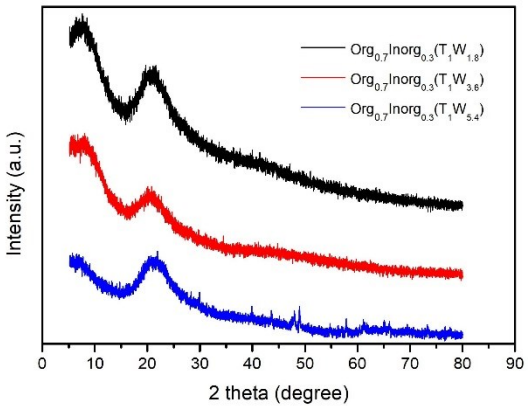

Fig. S7 XRD of hybrids with the same organic/inorganic compositions but different silica structures.

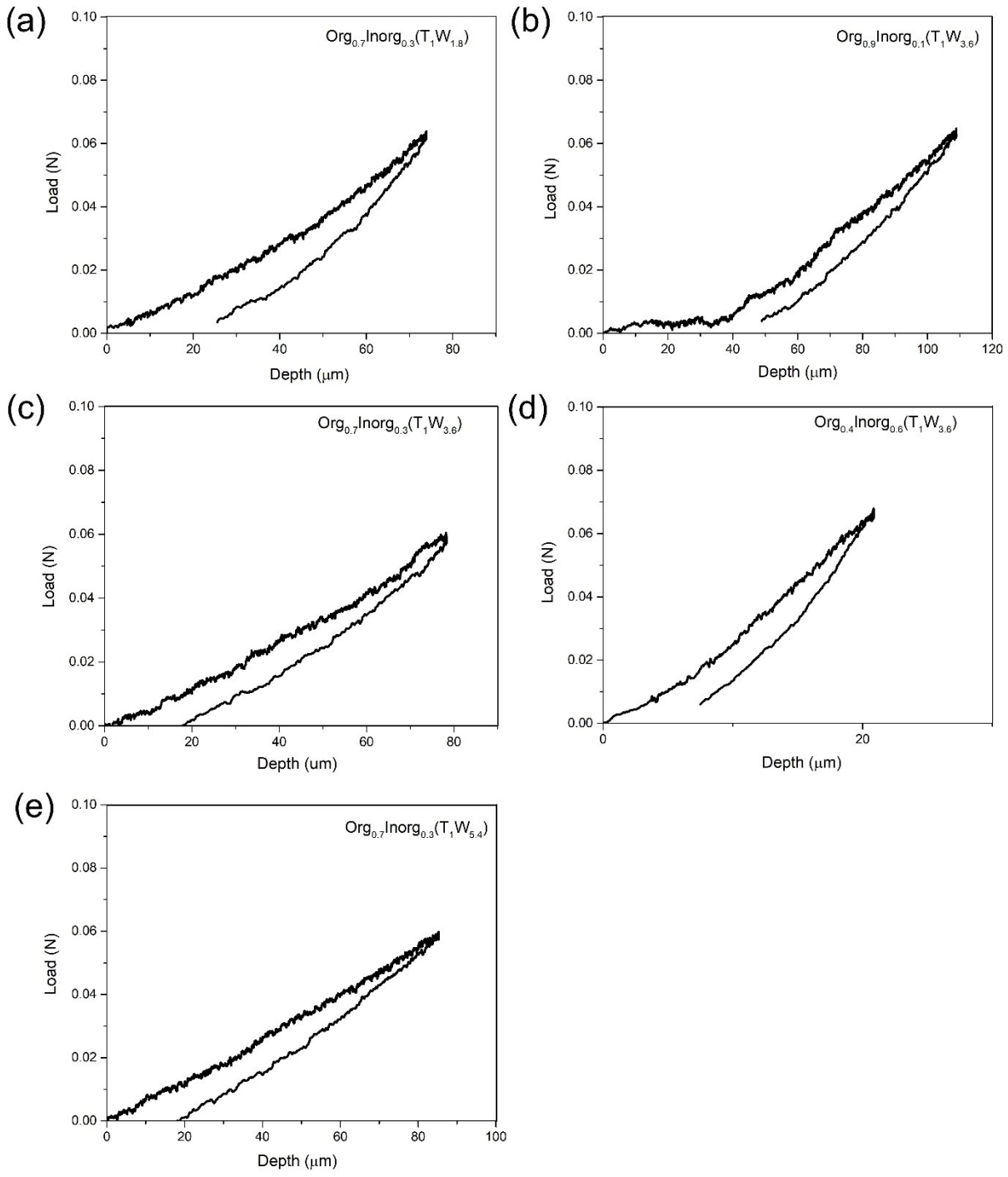

Fig. S8 Load-depth curves for the loading-unloading of the five hybrids as measured by micro-indentation.

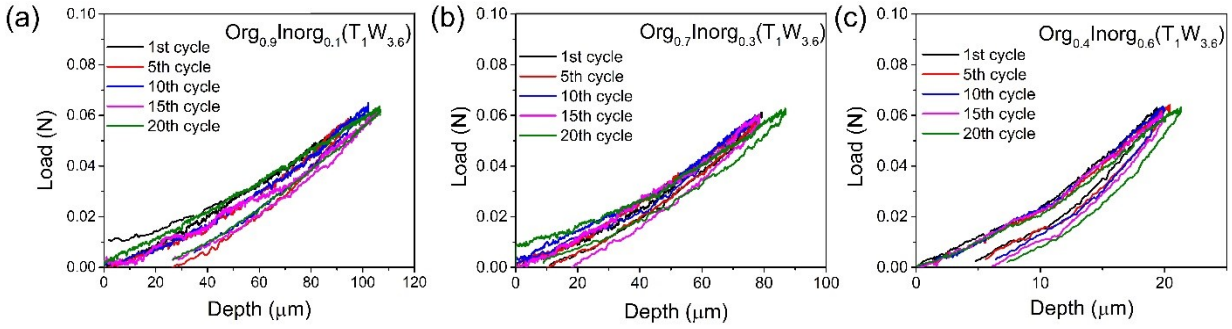

Figure S9. Indentation loading-unloading experiment of hybrids with different I/O ratios ($Org_{0.9}Inorg_{0.1}(T_1W_{3.6})$; $Org_{0.7}Inorg_{0.3}(T_1W_{3.6})$; $Org_{0.4}Inorg_{0.6}(T_1W_{3.6})$) for up to 20 cycles.

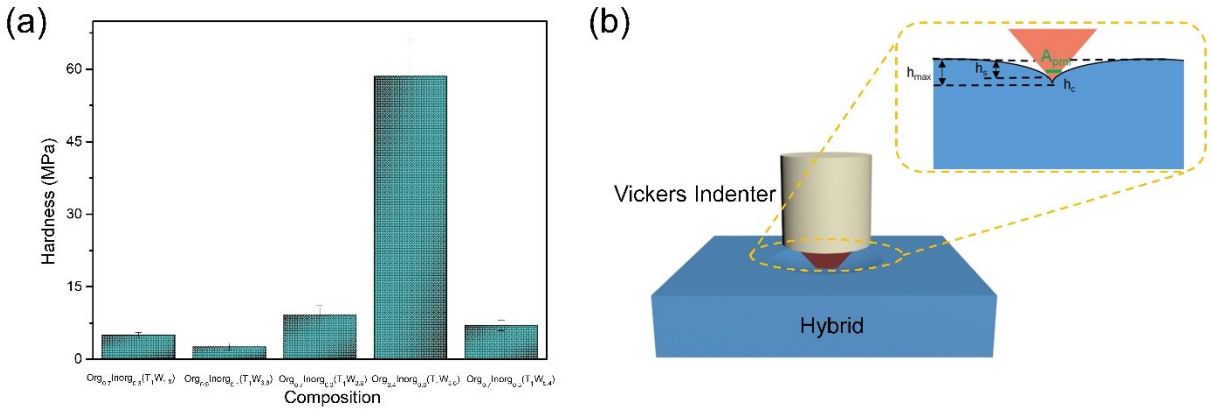

Fig. S10 (a) The hardness of five hybrids tested by micro-indentation method; (b) Elasto-plastic deformation of hybrids at the maximum load.

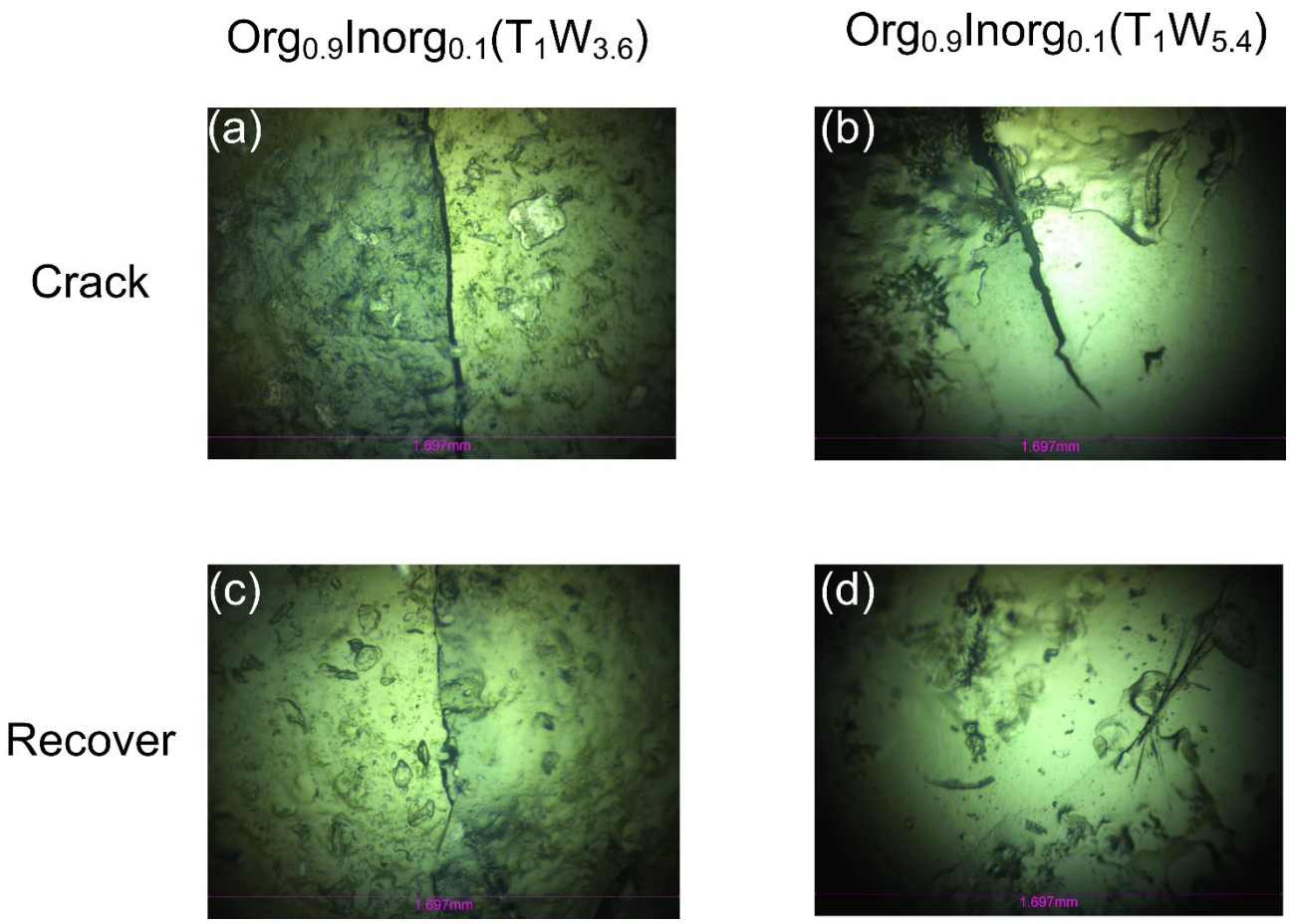

Fig. S11 Optical microscope images of four hybrid compositions after creation of a defect (top view): (a) $Org_{0.9}Inorg_{0.1}(T_1W_{3.6})$; (b) $Org_{0.9}Inorg_{0.1}(T_1W_{5.4})$. After self-healing for 24 hours: (c) $Org_{0.9}Inorg_{0.1}(T_1W_{3.6})$; (d) $Org_{0.9}Inorg_{0.1}(T_1W_{5.4})$.

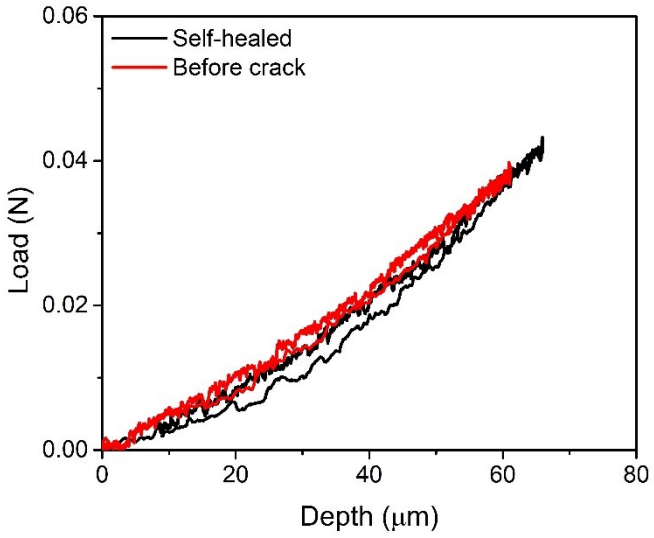

Fig. S12 Indentation test of hybrid $Org_{0.9}Inorg_{0.1}(T_1W_{1.8})$ before the induced crack (fresh samples) and after cracking and self-healing.

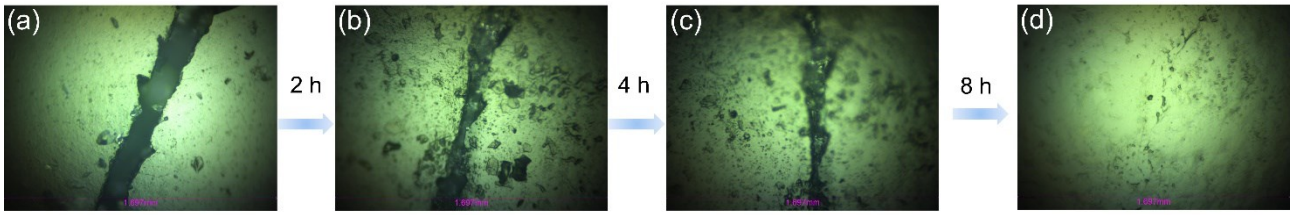

Fig. S13 Monitoring self-healing ability of hybrid $Org_{0.9}Inorg_{0.1}(T_1W_{1.8})$ at 37 ℃.

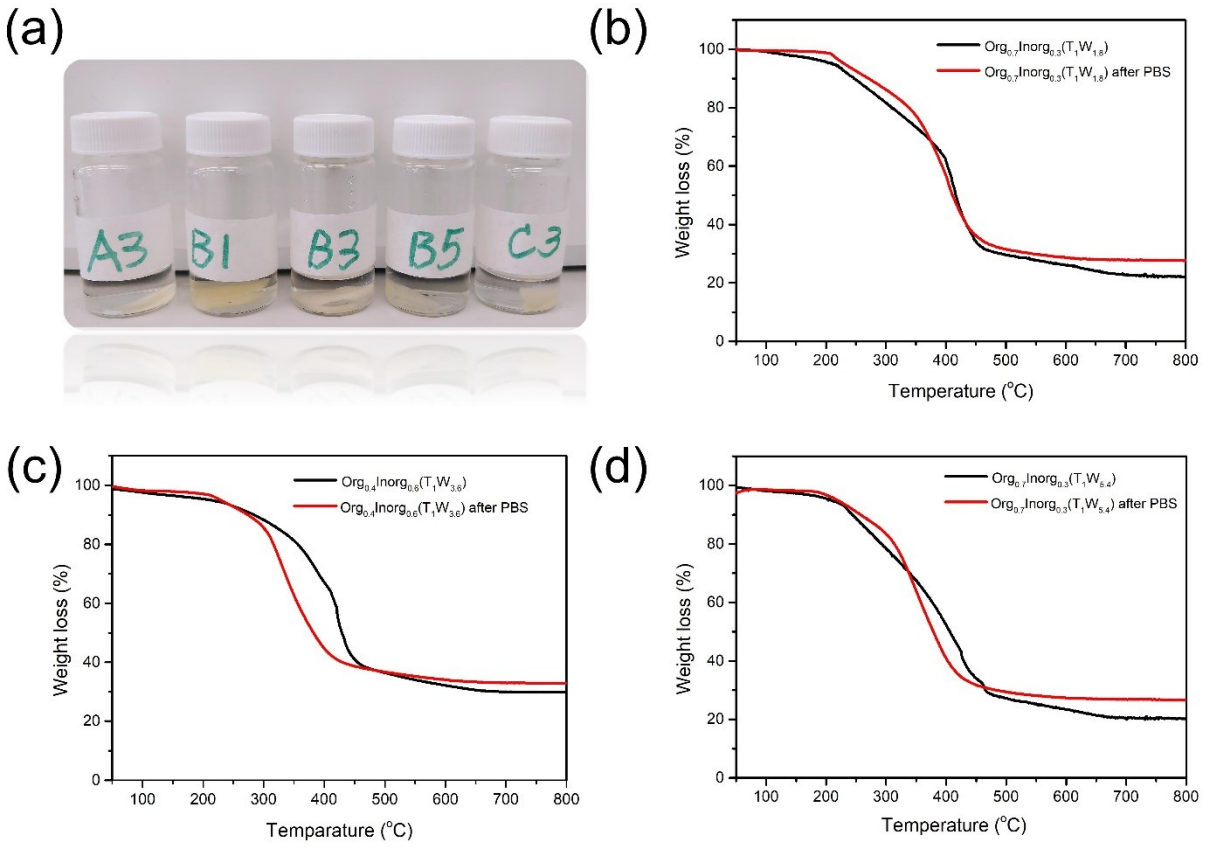

Fig. S14 (a) Pictures of hybrids after immersion (A3-C3 respresent hybrids $Org_{0.7}Inorg_{0.3}(T_1W_{1.8})$; (b) $Org_{0.9}Inorg_{0.1}(T_1W_{3.6})$; $Org_{0.7}Inorg_{0.3}(T_1W_{3.6})$; $Org_{0.4}Inorg_{0.6}(T_1W_{3.6})$; and $Org_{0.7}Inorg_{0.3}(T_1W_{5.4})$, respectively); TGA curves of hybrids (b) $Org_{0.7}Inorg_{0.3}(T_1W_{1.8})$; (c) $Org_{0.4}Inorg_{0.6}(T_1W_{3.6})$; (d $Org_{0.7}Inorg_{0.3}(T_1W_{5.4})$ before and after immersed in PBS solution.

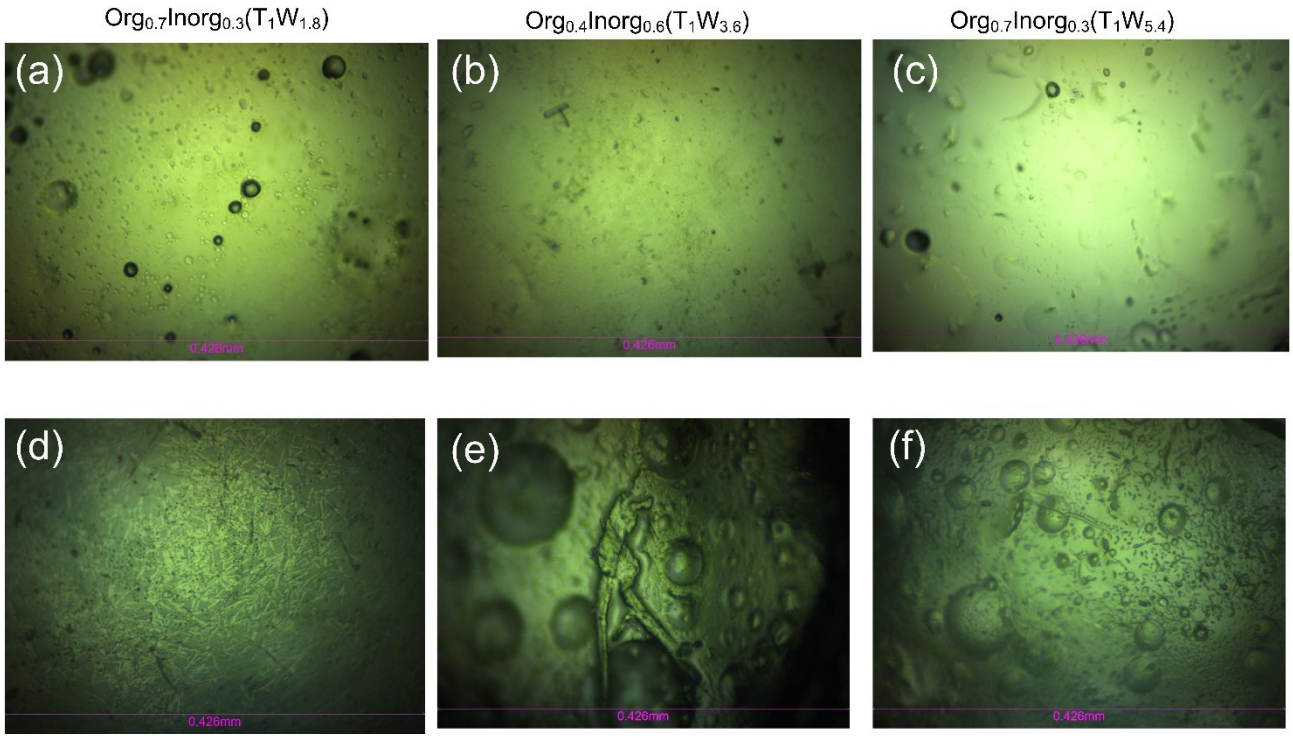

Fig. S15 Optical microscope images of hybrids before immersed in PBS (a) $Org_{0.7}Inorg_{0.3}(T_1W_{1.8})$; (b) $Org_{0.4}Inorg_{0.6}(T_1W_{3.6})$; (c) $Org_{0.7}Inorg_{0.3}(T_1W_{5.4})$; after immersed in PBS (d) $Org_{0.7}Inorg_{0.3}(T_1W_{1.8})$; (e) $Org_{0.4}Inorg_{0.6}(T_1W_{3.6})$; (f) $Org_{0.7}Inorg_{0.3}(T_1W_{5.4})$.

Table S1. Compositions of different hybrids.

Types	TEOS (mol)	H_2O (mol)	TEOS (wt %)	PCL-diCOOH (wt%)
$Org_{0.9}Inorg_{0.1}(T_1W_{1.8})$	1	1.8	10	90
$Org_{0.8}Inorg_{0.2}(T_1W_{1.8})$	1	1.8	20	80
$Org_{0.7}Inorg_{0.3}(T_1W_{1.8})$	1	1.8	30	70
$Org_{0.6}Inorg_{0.4}(T_1W_{1.8})$	1	1.8	40	60
$Org_{0.4}Inorg_{0.6}(T_1W_{1.8})$	1	1.8	60	40
$Org_{0.9}Inorg_{0.1}(T_1W_{3.6})$	1	3.6	10	90
$Org_{0.8}Inorg_{0.2}(T_1W_{3.6})$	1	3.6	20	80
$Org_{0.7}Inorg_{0.3}(T_1W_{3.6})$	1	3.6	30	70
$Org_{0.6}Inorg_{0.4}(T_1W_{3.6})$	1	3.6	40	60
$Org_{0.4}Inorg_{0.6}(T_1W_{3.6})$	1	3.6	60	40
$Org_{0.9}Inorg_{0.1}(T_1W_{5.4})$	1	5.4	10	90
$Org_{0.8}Inorg_{0.2}(T_1W_{5.4})$	1	5.4	20	80
$Org_{0.7}Inorg_{0.3}(T_1W_{5.4})$	1	5.4	30	70
$Org_{0.6}Inorg_{0.4}(T_1W_{5.4})$	1	5.4	40	60
$Org_{0.4}Inorg_{0.6}(T_1W_{5.4})$	1	5.4	60	40

Paper II

Materials Today Chemistry 22 (2021) 100584

Contents lists available at ScienceDirect

Materials Today Chemistry

journal homepage: www.journals.elsevier.com/materials-today-chemistry/

Flexible inorganic–organic hybrids with dual inorganic components

W. Fan [a], L.R. Jensen [b], M. Ceccato [c], T.S. Quaade [b], L. Gurevich [b], D. Yu [a, **], M.M. Smedskjaer [a, *]

[a] Department of Chemistry and Bioscience, Aalborg University, 9220 Aalborg, Denmark
[b] Department of Materials and Production, Aalborg University, 9220 Aalborg, Denmark
[c] Interdisciplinary Nanoscience Center (iNANO) and Department of Biological and Chemical Engineering, Aarhus University, 8200 Aarhus N, Denmark

ARTICLE INFO

Article history:
Received 3 June 2021
Received in revised form
18 August 2021
Accepted 6 September 2021
Available online xxx

Keywords:
Hybrid materials
Interpenetrating networks
Mechanical properties
Structure–property relations

ABSTRACT

Combining multiple inorganic components is an effective approach to improve the mechanical properties of inorganic–organic hybrid materials. The inorganic components can form interactions with the organic polymer matrix, and there is thus a need to understand the reinforcement mechanism under the optimal combination of organic polymer and inorganic particles. In this work, we prepared a series of dual inorganic particle–based titania/silica–poly(tetrahydrofuran)–poly(ε-caprolactone) (TiO_2/SiO_2–PTHF–PCL) hybrids by means of simultaneous cationic ring-opening polymerization and sol–gel reaction. In addition to constructing hybrid networks, the SiO_2 and TiO_2 components play important roles in multiple toughening mechanisms. The prepared dual inorganic hybrids feature enhanced thermal stability and mechanical properties when compared with the ones with a single inorganic component. The optimized mixing of such two inorganic components is identified through mechanical tests, revealing that the hybrid polymer$_{70}$/$(Si_{0.6}Ti_{0.4})_{30}$ (70/18/12 mass ratio) has the highest compressive failure strain (80%) and compressive ultimate strength (1.3 MPa) as well as storage modulus (120 kPa), enabling elongation of up to 37% when compared with its original length. We thus find that the dual inorganic component approach is an effective strategy to enhance the mechanical properties of hybrid materials, suggesting potential applications as scaffolds for tissue engineering and soft robotics.

1. Introduction

Designing and preparing mechanically tough, strong, and flexible materials is of great interest because such materials can find a broad range of applications from cartilage replacement and tissue engineering to soft robotics [1–3]. To this end, a potential strategy is to combine—at a nanometer scale—stiff inorganic glass networks with flexible organic polymer chains, which has been found as an effective strategy for enabling materials with both high strength and desirable flexibility [4–7]. We refer to such covalently linked inorganic–organic networks as hybrid materials, which could potentially inherit the advantages of both material families, including improved mechanical properties [7,8]. To enable this, the formation of covalent bonds between the inorganic and organic components is required, for further avoiding inorganic particle aggregation and improving the mechanical properties of such hybrid materials [8–12]. Hybrids with inorganic/organic interpenetrating networks (IPNs) have shown both high toughness and flexibility [12–17].

To ensure that covalent bonds between the inorganic and organic constituents are formed at the molecular level, synthesis routes based on *in situ* polymerization of organic monomers with a coupling agent have been applied. Monomers and coupling agents should be chosen based on their polymerization mechanism. For example, Jones et al. [12,18,19] applied a tetrahydrofuran (THF) monomer with a (3-glycidoxypropyl)trimethoxysilane (GPTMS) coupling agent as they undergo similar ring-opening processes. Xie et al. [20–23] chose to combine the acrylamide monomer with vinyltriethoxysilane as a coupling agent and thus take advantage of the common free-radical reactions of their vinyl groups. For constructing hybrid networks, the sol–gel method has been the most successful one as it forms hybrid IPNs during a long-time condensation process. Recent studies have shown that both density and Young's modulus of such hybrids can be controlled by changing the weight ratio of inorganic and polymer components [24].

* Corresponding author.
** Corresponding author.
E-mail addresses: yu@bio.aau.dk (D. Yu), mos@bio.aau.dk (M.M. Smedskjaer).

https://doi.org/10.1016/j.mtchem.2021.100584

Methods based on nanocomposite reinforcement [25,26], ionic bonding [27], and hydrogen bonding [28] have previously been explored to tailor the mechanical properties of hybrids. Among these, nanoparticle reinforcement could efficiently promote mechanical properties of materials, becoming the most commonly used method [27,28]. Insulating silica (SiO_2) nanoparticles [29] as well as semiconducting nanoparticles such as TiO_2 [25,26,30], SnO_2 [31], and ZrO_2 [32] have been applied as multifunctional cross-linkers in hybrids with improved mechanical properties in previous reports. Under the deformation process, intermolecular interactions (such as hydrogen bonds, London forces, and dipole−dipole interactions among polymer chains) dynamically break and recombine to homogenize hybrids. Polymer chains, which function as a transfer center, could dissipate energy and homogenize stress distribution during the stretching and compression process [20]. Inorganic particles, formed during the sol−gel process, not only function as an important component in constructing the IPN but also act as chemical/physical cross-linkers. Based on research of dual nanocomposites, multihierarchical inorganic nanoparticles could greatly improve the toughness of hybrids [33,34], which is achieved through multi-interactions of dual inorganic hierarchical nanoparticles with the polymer matrix [33–35] opposite to single-nanoparticle−based hybrids.

In this work, we designed and prepared a series of dual inorganic particle−based hybrids (DIHs), namely, titania/silica−poly(tetrahydrofuran)−poly(ε-caprolactone) (TiO_2/SiO_2−PTHF−PCL), to prepare inorganic−organic hybrids with improved fracture resistance and to further investigate the role of different inorganic components on the mechanical properties. The TiO_2/SiO_2−PTHF−PCL−based hybrids exhibited higher thermal stability and improved ultimate strength and failure strain than the single-nanoparticle−based hybrids. We performed *in situ* initiation of THF polymerization by GPTMS to ensure covalent linkage between the inorganic component and organic chains at the molecular level, whereas the IPN structure was controlled by adjusting the molar ratio between the two inorganic particles of SiO_2 and TiO_2. We found optimized mechanical properties of the DIH with its composition of 70/18/12 (mass ratio) for polymer/TiO_2/SiO_2. The obtained flexible hybrids could possibly find applications for soft devices as substitutes for load-bearing tissue.

2. Materials and methods

2.1. Materials

Polycaprolactone diol (HO−PCL−OH, Mn of 530 Da), $NaHCO_3$, KBr, 2,2,6,6-tetramethyl-1-piperidinyloxy (TEMPO), CH_3CN, THF, GPTMS, boron trifluoride−diethyl ether ($BF_3{\cdot}OEt_2$), tetraethylorthosilicate (TEOS), tetrabutyl orthotitanate (TBOT), triethanolamine (TEOA), and HCl (36 wt%) were all purchased from Sigma-Aldrich and used as received.

2.2. Synthesis of inorganic sol

For the silica-based sol, we initially prepared a solution of TEOS, deionized water, and 36 wt% hydrochloric acid (12 M HCl) with the molar ratio of 1:3.6:0.01. Then, the mixture was stirred vigorously to induce hydrolysis of TEOS. The completion of the reaction was confirmed when the mixture turned from cloudy to clear. The structure of silica is illustrated in Fig. S1. For the titanium-based sol, we firstly mixed TBOT and TEOA for 30 min at the molar ratio of 1:2. Then, an appropriate amount of deionized water was added into the TBOT/TEOA solution for achieving a Ti concentration of 1.25 mol/L, and finally, it was stirred for 2 h to achieve its sol.

2.3. Synthesis of organic sol

The method for synthesizing the organic precursor was based on the work of Jones and Tallia et al. [18]. To this end, HOOC−PCL−COOH was firstly prepared via following the existing method of oxidation of HO−PCL−OH by using TEMPO [17]. Second, 0.5 mol of the product was dissolved in anhydrous THF (at a concentration of 50 mg/mL). Third, 1 mol GPTMS was added. After continuously stirring for 30 min, 0.25 mol $BF_3{\cdot}OEt_2$ was added into the mixture to catalyze the epoxide ring-opening polymerization. This solution was stirred for 1.5 h for reaction. Then, the carboxylic acid groups in HOOC−PCL−COOH terminated the chain growth and formed the structure of GPTMS−PTHF−PCL.

2.4 Synthesis of hybrids

The inorganic silica-based sol and titania-based sol were added dropwise into the organic sol under different ratios as shown in Table S1 and stirred for 30 min at room temperature to obtain a homogeneous solution. Here, all the hybrids followed the weight ratio of (TEOS + TBOT)/PCL = 3/7, the molar ratio of TEOS: H_2O = 3.6:1 (the Si^{4+} concentration was 1.17 mol/L, and the hydrolyzed Ti^{4+} concentration was maintained at 1.25 mol/L), and the molar ratios of TEOS to TBOT were varied from 100/0, 80/20, 60/40, 40/60, 20/80, and 0/100, respectively (Table S1). Then, the mixed sol was transferred into cylindrical polytetrafluoroethylene molds, which were sealed for aging for 1 week at 40 °C. The lids were opened gradually to allow drying for the following three weeks at this temperature, and disc-shaped samples could then be recovered from the molds and used for characterization. The dimensions of the mold and the samples were $\Phi = 4.5$ and 4 cm, respectively, with an observed shrinkage of the sample on drying of about 21%. All samples are immersed in distilled water for 5 min to remove by-products and non-covalently bonded inorganic particles.

2.5. Structure characterization

Fourier-transform infrared (FTIR) spectroscopy was performed to determine the functional groups in inorganic bulks and hybrids by using a Bruker TENSOR II spectrometer along with Bruker Platinum attenuated total reflectance attachment, in the range of 4,000 to 400 cm^{-1}. All spectra were compiled from 64 consecutive scans and were baseline corrected using the vendor-supplied software OPUS. The surface morphology and element distribution in hybrids were tested by scanning electron microscopy (SEM) using a Zeiss Gemini SEM 500 instrument at 5 kV/10 μA. The size of TEOS and TBOT precursors was determined based on dynamic light scattering (DLS) measurements using a Zetasizer nano series (Malvern). Transmission electron microscopy (TEM) and high-angle annular dark-field scanning electron transmission microscopy (HAADF-STEM) images were obtained using a transmission electron microscope (TALOS F200X, FEI Company, USA) equipped with a TWIN lens system, an X-FEG electron source, and a CETA 16 M camera. The accelerating voltage was set to 200 kV. Elemental analysis was performed by energy-dispersive X-ray spectroscopy mapping recorded in STEM mode, whereas bright-field images were collected in TEM mode. The hybrid materials were carefully scraped off with a scalpel and then uniformly dispersed in absolute acetone using ultrasonication for 30 min.

The final inorganic vs. organic (I/O) weight ratio in the hybrids was determined by thermal gravimetric analysis (TGA) on an STA 449C (Netzsch) instrument. The samples were cut into small pieces and heated under a flow of air at the rate of 10 °C/min, from room temperature to 800 °C. The recorded weight loss could be ascribed to the combustion of the organic phase. To confirm the non-

crystalline structure of the hybrid materials, X-ray diffraction (XRD) analysis was carried out on pulverized samples at 2θ angles from 5° to 80° using a Panalytical Empyrean diffractometer with the Cu-Kα radiation source and Ni-filter. Atomic force microscopy (AFM) measurements were performed with an NTEGRA Aura AFM (NT-MDT, Russia) operating in tapping mode using HA_HR (ScanSens, Germany) cantilevers.

2.6. Mechanical tests of hybrids

Compression tests were performed using a Zwick Z100 universal testing machine equipped with a 100 kN load cell at room temperature. Samples were punched into cylinders with a diameter of 10 mm and a height of 5 mm. The crosshead speed was set to 1 mm/min. Tensile tests were performed using a Linkam TST350 tensile testing stage equipped with a 200 N load cell at room temperature. The hybrid samples were cut into rectangular shapes with a length of 30 mm, a width of 10 mm, and a thickness of 2 mm, and the crosshead speed was set to 2 mm/min. Dynamic mechanical analysis (DMA) was carried out using TA Instruments DMA 850. The DMA experiments were performed at room temperature in compression mode with an amplitude of 20 μm and a frequency in the range of 0.01–100 Hz.

3. Results and discussion

3.1. Hybrid synthesis and structure

Based on the previous work [18,35], the expected structures of the prepared DIHs (TiO_2/SiO_2–PTHF–PCL) are schematically illustrated in Fig. 1. GPTMS initiated the ring-opening process of THF and then covalently linked the polymer chains and inorganic components after adding inorganic precursors. The reaction mechanism is shown in Fig. S2 [18]. In addition, HOOC–PCL–COOH controlled the THF ring-opening reaction rate, ended the chain growth, and also formed strong intermolecular interactions, e.g. hydrogen bonds, with TiO_2/SiO_2 inorganic particles [18,35]. Experimentally we have found that the polymerization rate would be very fast and out of control when adding HOOC–PCL–COOH in the late stage of the chain propagation. Combining literature reports, we speculate that the rate of initiation of GPTMS by $BF_3 \cdot OEt_2$ would be strongly retarded by HOOC–PCL–COOH because of Lewis acid–base reactions between them [18], whereas the termination of the propagating chain would occur when boric-acid salts (formed between $BF_3 \cdot OEt_2$ and HOOC–PCL–COOH) would have been accumulated at a sufficiently high concentration, i.e. after a certain time of polymerization. Such a design achieves both covalent bonding between inorganic particles and polymer chains and non-covalent interactions (such as hydrogen bonds and London forces) in the hybrid system, which contributes to the improved mechanical properties in multiple ways. Covalent Si–O–Ti bonds are formed between TiO_2 and SiO_2 inorganic particles during the sol–gel condensation [35]. For the deformation processes, the intermolecular interactions, e.g. hydrogen bonds, are expected to break first, and then, covalent bonds break irreversibly at the final stage. In addition, it is known that the hydrogen bonds of PCL–COOH can trigger the self-healing ability of such hybrid materials [20,35], which is not expected to be affected by the titania incorporation in the present study. Multiple strengthening mechanisms in this system by dual inorganic components could effectively enhance the interactions among the various components in the hybrid networks and efficiently impede the fracture process during the material deformation. To systematically investigate how different inorganic components affect structures and mechanical properties of hybrids, we have compared six hybrids with different TiO_2 and SiO_2 compositions (see Table S1).

3.2. Structure confirmation of hybrids

An image of the hybrid polymer$_{70}$/(Si$_{0.6}$Ti$_{0.4}$)$_{30}$ sample is shown in Fig. 2a, revealing that this hybrid material possesses observable flexibility and can be bent to a large extent without breaking or permanently deforming. One may notice the lack of transparency for this hybrid sample (polymer$_{70}$/(Si$_{0.6}$Ti$_{0.4}$)$_{30}$), which could be ascribed to the TiO_2 nanoparticles (as further discussed in the following), because hybrid polymer$_{70}$/(Si$_1$Ti$_0$)$_{30}$ is relatively transparent. Distinct from stiff inorganic bulks on the one hand and completely soft polymer on the other hand, the well-balanced ductility and stiffness could reasonably ensure supporting scaffolds for applications within biomedical fields. To evaluate the size of SiO_2 and TiO_2 particles after sol-formation, we have performed

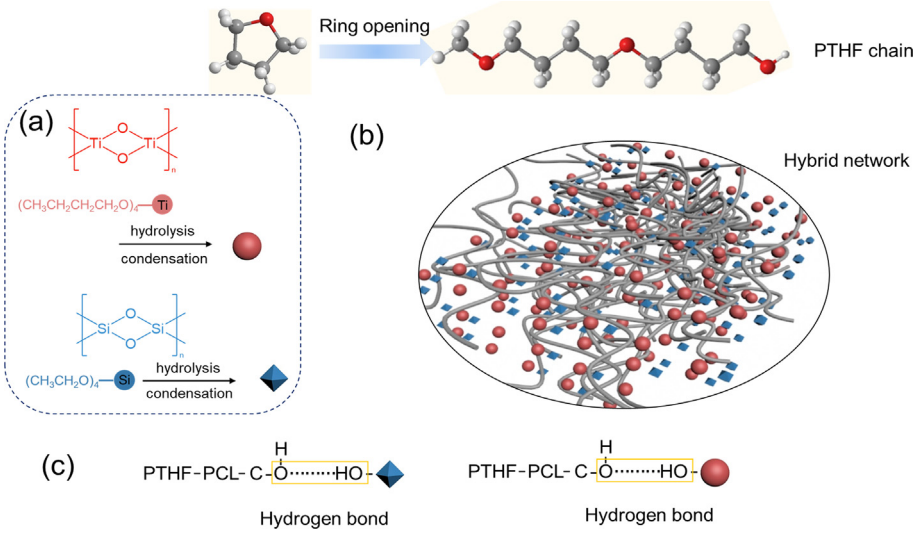

Fig. 1. Schematic illustration of the polymer–SiO_2/TiO_2 hybrid structure. (a) Hydrolysis and condensation processes of inorganic precursors; (b) structure of hybrids with the PTHF–PCL–COOH–SiO_2/TiO_2 network; (c) hydrogen bonds among inorganic particles and polymer chains.

DLS measurements using a Zetasizer Range [37,38] (Fig. 2b) before further reacting with the organic precursor of PCL–PTHF–GPTMS. The most typical size of SiO_2-sol was found to be 9 nm with a relatively narrow size distribution, whereas the size of TiO_2 was in a range of 10–20 nm with broader distribution. The nanoscale size of these components is beneficial for their uniformed reaction with every reactive terminal trimethoxysilane group of GPTMS–PTHF–PCL and thus controls the structure of the hybrids at the nanoscale [35]. Co-networks formed by inorganic composites and polymers could be formed during the long-time polycondensation process.

Then, for the prepared samples, the spatial distribution of inorganic particles and polymer chains can also be detected through element mapping by means of scanning electron microscopy–energy dispersive X-ray (SEM-EDX) analysis. As is shown in Fig. S3, the surface of the hybrid polymer$_{70}$/(Si$_{0.6}$Ti$_{0.4}$)$_{30}$ is relatively uniform. That is, the main elements C, O, Si, and Ti are all evenly distributed across the surface. Because polymer chains are the main component in the hybrids, C is easily detected. The analysis also shows that inorganic composites are well integrated in the hybrids. Furthermore, to determine the morphology and dispersion of SiO_2 and TiO_2 composites, we have performed TEM and HAADF-STEM analyses on the hybrids polymer$_{70}$/(Si$_0$Ti$_1$)$_{30}$, polymer$_{70}$/(Si$_1$Ti$_0$)$_{30}$, and polymer$_{70}$/(Si$_{0.6}$Ti$_{0.4}$)$_{30}$. As shown in Fig. 2c, the inorganic nanoparticles of SiO_2 and TiO_2 are irregular with a size of around 10–30 nm in the hybrid polymer$_{70}$/(Si$_{0.6}$Ti$_{0.4}$)$_{30}$. The elemental mapping images of Si, Ti, and C presented in Fig. 2d–f reveal that the inorganic components are homogeneously dispersed in the hybrid material, without aggregation of separate SiO_2 or TiO_2 clusters. The reason for this could be the Si–O–Ti bonds that are formed between these two inorganic composites as a result of the long-term sol–gel processes [35,39]. Moreover, the element mapping images of hybrid polymer$_{70}$/(Si$_0$Ti$_1$)$_{30}$ in Fig. S4a show that the size of TiO_2 nanoparticles is around 10 nm. The detection of small amounts of the Si element is ascribed to the coupling agent GPTMS, which functions as a bridge between polymer and inorganic composites. When TiO_2 dominates the hybrid polymer$_{70}$/(Si$_0$Ti$_1$)$_{30}$, TiO_2 could easily get agglomerated as shown in Fig. S4c. However, Si elements in the hybrid polymer$_{70}$/(Si$_1$Ti$_0$)$_{30}$ (see Fig. S5b) are uniformly dispersed in the hybrid material, without aggregation or apparent inorganic clusters. Thus, we infer that TiO_2 is covalently linked to the polymers by forming covalent bonds with SiO_2 during the sol–gel process. Excess TiO_2 nanoparticles might easily aggregate, whereas this is not the case for SiO_2 nanoparticles.

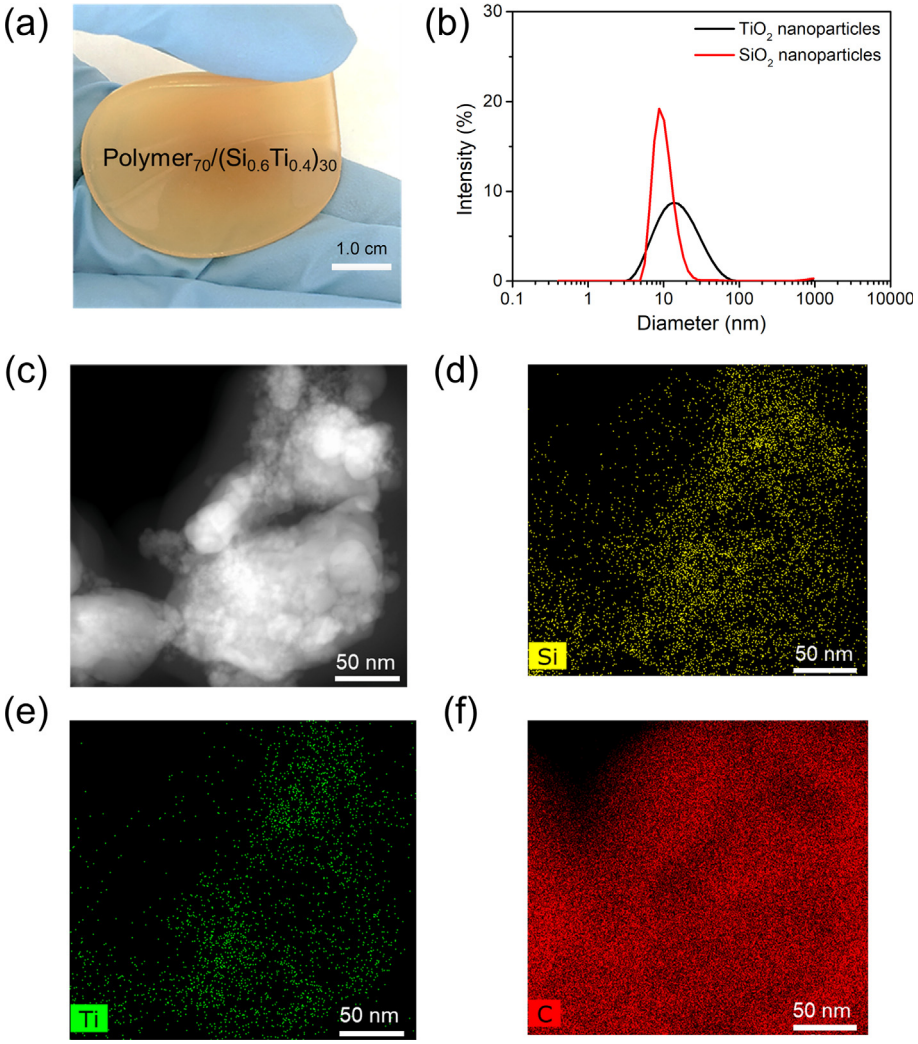

Fig. 2. (a) Image illustrating the flexibility of the hybrid polymer$_{70}$/(Si$_{0.6}$Ti$_{0.4}$)$_{30}$; (b) size distribution of SiO_2 and TiO_2 nanoparticles as tested by DLS; (c) the HAADF-STEM image of the bulk of the polymer$_{70}$/(Si$_{0.6}$Ti$_{0.4}$)$_{30}$ hybrid and STEM images with corresponding element distribution of (d) Si, (e) Ti, and (f) C.

Next, we have performed FTIR spectroscopy measurements to characterize the molecular structures of the different hybrids (Fig. 3a). The bands at 568 cm^{-1} and 1,090 cm^{-1} can be assigned to typical stretching vibration of Ti–O–Ti bonds and asymmetric stretching vibration of Si–O–Si bonds, respectively [40]. The intensity of these bands varies in the different hybrids as a result of the varying fraction of inorganic particles [40,41]. Notably, we further ascribe the weak band at 920 cm^{-1} to stretching vibration of Si–O–Ti bonds, thus providing evidence for covalent linkage of SiO_2 and TiO_2 inorganic particles during the condensation reactions [31]. Considering the organic polymer chains, the observed peaks could also be assigned to PCL and PTHF. That is, the bands at 2,900, 1,730, and 1,200 cm^{-1} could be assigned to the characteristic stretching of $-CH_2-$, C=O, and –C–O–C– groups, respectively [18]. We have also performed XRD analysis and confirmed the amorphous structure of the hybrids (Fig. 3b). As expected, all the synthesized hybrids are fully amorphous, without any sharp diffracted peaks caused by crystals. The non-crystalline state is formed mainly because of the hydrolysis and condensation process of inorganic precursors, but also due to the Si–O–Ti bonds formed during the sol–gel process [28,35]. In accordance with the EDX results, the reason for the inorganic particles being uniformly dispersed in the system can likely be ascribed to the following factors: (i) the SiO_2 and TiO_2 particles are covalently bonded to PTHF polymer chains via the coupling agent GPTMS, (ii) SiO_2 and TiO_2 particles are bonded with each other through condensation, and (iii) non-covalent interactions, e.g. hydrogen bonds are formed between PCL–COOH and TiO_2/SiO_2.

The thermal stability of the six hybrids has been evaluated via TGA, as shown in Fig. 3c. The hybrids with both silica and titania feature improved their thermal stability in comparison with those containing only one type of inorganic component. It could be seen from the first order derivative of weight loss (inset of Fig. 3c) that the decomposition temperature of all hybrids is very close, mainly because polymer components begin to degrade in that temperature range. We further analyzed them via differential scanning calorimetry (DSC) as presented in Fig. 3d. Small peaks at around 220 °C are observed for single inorganic particle–based hybrids (SIHs). However, the exothermic peak area (around 400 °C) of DIHs is much larger than that of SIHs, representing higher enthalpy of decomposition of the polymer degradation process for DIHs. Based on aforementioned findings, we conclude that the hierarchical dual inorganic-composite structure forms a compact structure and multiple interactions between polymers and inorganic components, which improve the thermal stability of the hybrids. Another possible reason is that O_2 diffusion is reduced because of the addition of dual inorganic particles [42], and hence, the thermo-oxidative degradation takes longer time at the interior of the

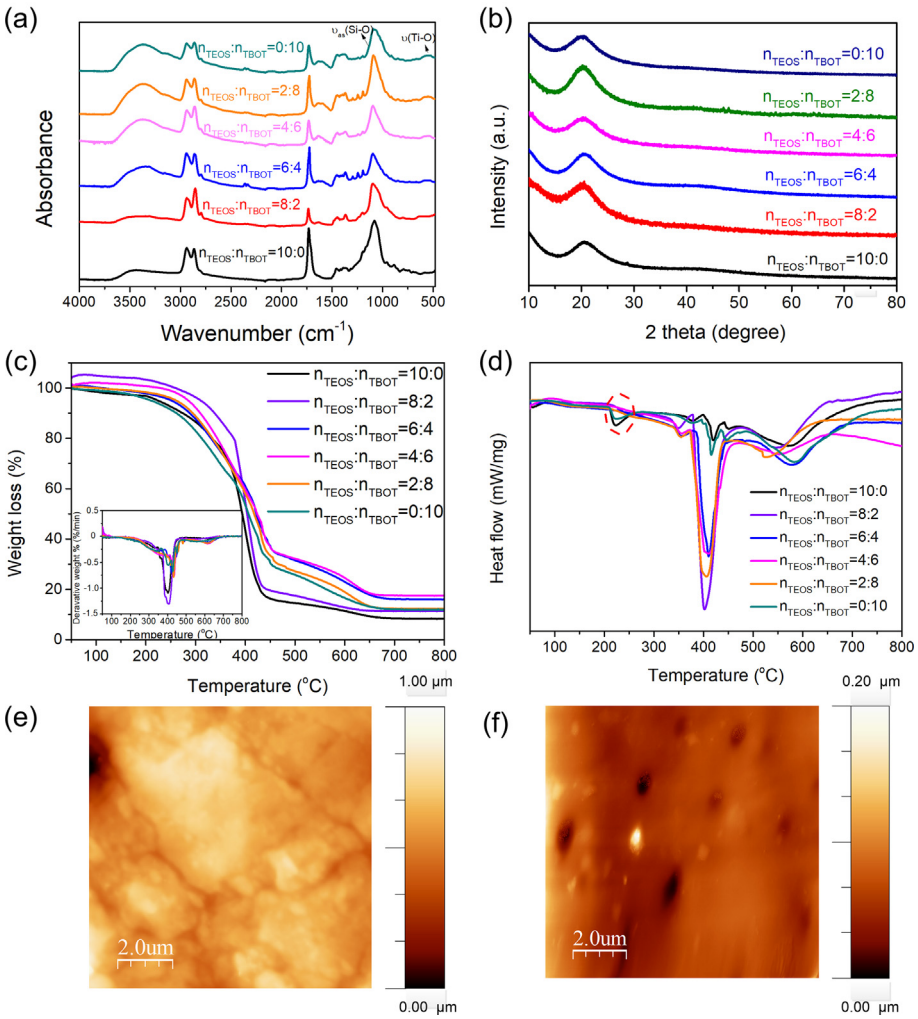

Fig. 3. Studies of (a) FT-IR, (b) XRD, (c) TGA, and (d) DSC on hybrids with different SiO_2/TiO_2 ratios (as reflected by the TEOS-to-TBOT ratio); (e, f) AFM topography phase images of hybrids polymer$_{70}$/(Si$_{0.6}$Ti$_{0.4}$)$_{30}$ and polymer$_{70}$/(Si$_0$Ti$_1$)$_{30}$, respectively.

samples. Moreover, the bond energy of Si–C, Si–O, and Ti–O is 290, 432, and 662 kJ/mol, respectively [36], and therefore, the higher bond energy of Ti–O could also help to explain the observed behavior.

The actual total I/O weight ratios in the hybrids vary with composition, i.e. it firstly increases and then decreases with increasing titania content (Table 1). First, we note that TiO_2 could only bond to hybrid materials with SiO_2, and the amount of TiO_2 bonded to the hybrid networks is positively correlated with that of SiO_2. The molecular weight of TiO_2 is 76.87 g/mol, whereas that of SiO_2 is 60.08 g/mol. Thus, we believe that the I/O ratio increases slightly when the amount of SiO_2 dominates the hybrid. That is, all TiO_2 could bond with the hybrid and contributes to final I/O ratios. However, when TiO_2 becomes prevalent, the number of reactive sites is reduced simultaneously and excessive TiO_2 could not effectively bond to the hybrid. TiO_2 aggregates may thus form that are not connected to anything and likely washed away in the rinsing stage. The fact that TiO_2 is not as good a glass network former as SiO_2 might be another reason why less Ti is incorporated into the hybrids as the TEOS content decreases.

The morphology of the surface of the hybrids was further investigated through AFM analyses. Specifically, we have compared the topography and phase images of polymer$_{70}$/(Si$_{0.6}$Ti$_{0.4}$)$_{30}$ (Fig. 3e) and polymer$_{70}$/(Si$_0$Ti$_1$)$_{30}$ (Fig. 3f). In accordance with TEM and XRD results, components are dispersed uniformly and phase aggregation is avoided with the hybrid polymer$_{70}$/(Si$_{0.6}$Ti$_{0.4}$)$_{30}$ (Fig. S6). On the contrary, porous microstructures (black pores in Fig. 3f) and phase aggregations are observed in the hybrid polymer$_{70}$/(Si$_0$Ti$_1$)$_{30}$. This is likely due to the drying and aging process, after which the hybrids are washed with distilled water to remove by-products and non-covalently bonded inorganic particles. Thus, we believe that the micropores should be ascribed to the washed TiO_2 nanoparticles. It could also be observed that the cross-linking density of polymer$_{70}$/(Si$_{0.6}$Ti$_{0.4}$)$_{30}$ is much higher than that of the others (Fig. S7). Dual inorganic–based hybrids with multiple interactions among inorganic particles and polymer chains achieve uniformed dispersion of inorganic particles and largely enhance the cross-linking density and further contribute to mechanical enhancement of hybrids. SiO_2 and TiO_2 inorganic components bond together and form hybrid networks together with the hybrid polymer$_{70}$/(Si$_{0.6}$Ti$_{0.4}$)$_{30}$, whereas there will be fewer inorganic particles covalently bonded to polymer chains for the hybrid polymer$_{70}$/(Si$_0$Ti$_1$)$_{30}$. The results are also in accordance with the TGA analysis (Fig. 3c).

3.3. Mechanical tests of hybrids

Tensile [43] and compression tests [44] as well as DMA [45] were performed, aiming to understand the influence of the inorganic components on the mechanical response to identify the optimal hybrid composition and microstructure. The results are all recorded based on conventional strain and stress.

First, we consider the tensile test results in Fig. 4a. The DIHs with multimolecular interactions (covalent bonds, non-covalent interactions, physical cross-linking) generally possess higher strains at failure and ultimate tensile strengths than the SIHs. Among all the hybrids, the hybrid polymer$_{70}$/(Si$_{0.6}$Ti$_{0.4}$)$_{30}$ reveals the largest strain at failure of 39.2% and tensile strength of 68 kPa, whereas the hybrid polymer$_{70}$/(Si$_1$Ti$_0$)$_{30}$ exhibits the smallest ability to be stretched without fracturing ($\varepsilon_{f,T}$ = 4.8%), likely because the large fraction of the stiff and brittle silica network prevents plastic deformation during the stretching process. Nevertheless, the hybrid polymer$_{70}$/(Si$_0$Ti$_1$)$_{30}$ exhibits the lowest tensile strength (8.8 kPa). TiO_2 dominates in this system, and the decrease of total inorganic particles with fewer covalent bonds to polymer chains is the main reason for its low fracture strength.

Next, we consider DMA to obtain the storage modulus (E'), loss modulus (E''), and damping coefficient tan (δ) of the hybrids [46–50]. The storage and loss moduli represent the elastic and viscous portion, respectively, of the viscoelastic response of the hybrids. The change in the two moduli with the hybrid composition is depicted in Fig. 4b (for 1 Hz) and Fig. S8 (for 0.01–100 Hz). Results of E' and E'' of all hybrids at 1 Hz are summarized in Table S2. We observe that the storage modulus is almost ten times higher than the loss modulus for all six hybrids. Among the hybrids, all four DIHs reveal higher storage modulus than the two SIHs, among which polymer$_{70}$/(Si$_{0.6}$Ti$_{0.4}$)$_{30}$ exhibits the highest (160 kPa). Thus, stiffer hybrids are obtained through dual inorganic particle regulating. Moreover, the damping coefficient tan (δ), which is defined as the ratio of E'' to E', represents the relative contribution of the dissipative to elastic contribution and is considered as an indicator of how efficiently hybrids release energy to molecular rearrangement and internal friction [46,49,50] (Fig. S9). We note that the hybrid polymer$_{70}$/(Si$_{0.6}$Ti$_{0.4}$)$_{30}$ reveals relatively higher tan (δ) than other hybrids. This might be due to its higher cross-linking density and resulting stiffness. The internal frictions of polymer chains with SiO_2 restrain its elasticity and make it release energy more efficiently.

Finally, we also compared the mechanical properties of the hybrids via uniaxial compression tests of cylindrical monolith bulks. As is shown in Fig. 4c and S6, the representative stress–strain curves clearly illustrate that SiO_2-rich hybrids have higher compressive strength than TiO_2-rich ones. This suggests that the SiO_2 particles are easily covalently linked to the hybrid system compared with TiO_2 particles, and loss of inorganic particles reduces the compressive strength of TiO_2-rich hybrids. Of all the studied hybrids, polymer$_{70}$/(Si$_{0.6}$Ti$_{0.4}$)$_{30}$ features the best flexibility, as it could be compressed to a strain of 80% (at 1.4 MPa). For comparison, the conventional stress to failure of our prepared polymer$_{70}$/(Si$_{0.6}$Ti$_{0.4}$)$_{30}$ thus reaches 1.4 MPa, whereas the true stress to failure for the materials of Tallia et al. [18] is only 1.2 MPa, even though the inorganic composite content in their system is higher (24.7%) than that in ours (17.5%). The reason is due to its more compact structure and multistrengthening mechanism of dual inorganic particles. Thus, flexible DIHs are achieved by utilizing mixed SiO_2/TiO_2 as the multifunctional inorganic constituent of hybrids. The modulus of toughness of hybrids, which represents how much energy our prepared hybrids can absorb before rupturing, obtained as the total area under the stress–strain curve, is shown in Fig. 4d. It could be seen that DIHs maintain higher strength than SIHs, which indicates DIHs reveal the property of strength and ductility. Among the hybrids, polymer$_{70}$/(Si$_{0.6}$Ti$_{0.4}$)$_{30}$ has the highest modulus of toughness. The tangent modulus of the hybrids under certain strains is shown in Fig. S10 and Table S3 (strains at 20% can be compared). Polymer$_{70}$/(Si$_{0.4}$Ti$_{0.6}$)$_{30}$ and polymer$_{70}$/(Si$_{0.6}$Ti$_{0.4}$)$_{30}$ have low tangent modulus for a strain of 20%, namely, 0.21 and 0.59 MPa, respectively. Compared with other hybrids, polymer$_{70}$/(Si$_{0.4}$Ti$_{0.6}$)$_{30}$ and polymer$_{70}$/(Si$_{0.6}$Ti$_{0.4}$)$_{30}$ thus exhibit easier deformation. Tough materials are urgently needed in

Table 1
Actual values of I/O (wt%) as measured from TGA in the final hybrid samples.

Hybrid	I/O wt%
Polymer$_{70}$/(Si$_1$Ti$_0$)$_{30}$	11.9/88.1
Polymer$_{70}$/(Si$_{0.8}$Ti$_{0.2}$)$_{30}$	12.3/87.7
Polymer$_{70}$/(Si$_{0.6}$Ti$_{0.4}$)$_{30}$	17.5/82.5
Polymer$_{70}$/(Si$_{0.4}$Ti$_{0.6}$)$_{30}$	16.1/83.9
Polymer$_{70}$/(Si$_{0.2}$Ti$_{0.8}$)$_{30}$	11.3/88.7
Polymer$_{70}$/(Si$_0$Ti$_1$)$_{30}$	8.3/91.7

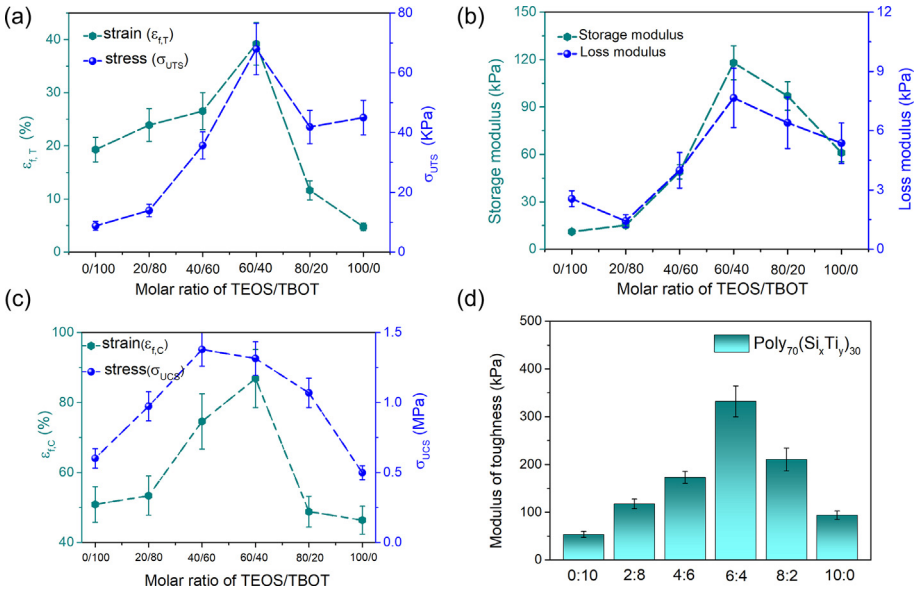

Fig. 4. Mechanical performance of the hybrids. (a) Composition dependence of ultimate tensile strength (σ_{UTS}) and tensile strain at failure ($\varepsilon_{f,T}$) as obtained from uniaxial tensile testing. (b) composition dependence of storage modulus (E') and loss modulus (E'') as obtained from DMA in compression at 1 Hz; (c) composition dependence of ultimate compressive strength (σ_{UCS}) and compressive strain at failure ($\varepsilon_{f,C}$) as obtained from compression testing; (d) modulus of toughness of hybrids with different SiO_2/TiO_2 compositions from the compression test.

many practical application fields such as tissue engineering and soft robotics, for example, native human articular cartilage has a compression modulus of about 0.4–2.0 MPa [51,52]. Our results show that the hybrid polymer$_{70}$/(Si$_{0.6}$Ti$_{0.4}$)$_{30}$ has the highest compressive ultimate strength (1.3 MPa), modulus of toughness (332 kPa), up to 37% tensile elongation, and compression modulus of 0.59 MPa, thus falling within the needed property range. Such an inorganic–polymer hybrid design with optimized mechanical properties therefore offers good prospects for future applications.

4. Conclusion

In summary, we have prepared flexible inorganic–organic hybrids by controlling the compositions of dual inorganic components. Covalent bonds in polymer–polymer, polymer–SiO_2 network, and TiO_2–SiO_2 inorganic particles as well as reversible intermolecular interactions (e.g. London forces and hydrogen bonds) all play important roles in synergistically promoting the improved fracture stress and strain in the mixed hybrid materials. The hybrid polymer$_{70}$/(Si$_{0.6}$Ti$_{0.4}$)$_{30}$ reveals optimal mechanical properties compared with the other hybrids. For the DIHs, the multiple interactions existing among polymer chains and inorganic components prevent the fracture propagation during the tensile deformation and compression processes, which reveals the potential in obtaining hybrids that can be deformed without fracture. This work refines the roles of different inorganic particles on the mechanical properties of organic–inorganic hybrid materials, and we believe such findings will be important for the design of ductile hybrids that can be applied in soft robotics and biomedical fields.

Credit author statement

W.F., M.M.S., and D.Y. conceived the study and designed the experiments. M.M.S. and D.Y. supervised the project. W.F. prepared the samples and performed the basic structure characterization. W.F. and L.R.J. performed the mechanical characterization. M.C. performed the TEM experiments. T.S.Q. performed the DMA experiments. L.G. performed the AFM experiments. W.F., M.M.S., and D.Y. wrote the manuscript with inputs from other co-authors. All authors contributed to analyzing and discussing the data.

Declaration of competing interest

The authors declare that they have no known competing financial interests or personal relationships that could have appeared to influence the work reported in this article.

Acknowledgments

This work was supported by the China Scholarship Council (CSC No. 201904910782).

Appendix A. Supplementary data

Supplementary data to this article can be found online at https://doi.org/10.1016/j.mtchem.2021.100584.

References

[1] Q. Fu, E. Saiz, M.N. Rahaman, A.P. Tomsia, Toward strong and tough glass and ceramic scaffolds for bone repair, Adv. Funct. Mater. 23 (2013) 5461–5476.
[2] L. Che, Z. Lei, P. Wu, D. Song, A 3D printable and bioactive hydrogel scaffold to treat traumatic brain injury, Adv. Funct. Mater. 29 (2019) 1904450.
[3] F. Baino, E. Fiume, M. Miola, E. Verné, Bioactive sol-gel glasses: processing, properties, and applications, Int. J. Appl. Ceram. Technol. 15 (2018) 841–860.
[4] J.R. Jones, Review of bioactive glass: from Hench to hybrids, Acta Biomater. 9 (2013) 4457–4486.
[5] G.J. Owens, R.K. Singh, F. Foroutan, M. Alqaysi, C.-M. Han, C. Mahapatra, H.-W. Kim, J.C. Knowles, Sol–gel based materials for biomedical applications, Prog. Mater. Sci. 77 (2016) 1–79.
[6] J.Y. Sun, X. Zhao, W.R. Illeperuma, O. Chaudhuri, K.H. Oh, D.J. Mooney, J.J. Vlassak, Z. Suo, Highly stretchable and tough hydrogels, Nature 489 (2012) 133–136.
[7] B.M. Novak, Hybrid nanocomposite materials? Between inorganic glasses and organic polymers, Adv. Mater. 5 (1993) 422–433.
[8] Y. Vueva, L.S. Connell, S. Chayanun, D. Wang, D.S. McPhail, F. Romer, J.V. Hanna, J.R. Jones, Silica/alginate hybrid biomaterials and assessment of their covalent coupling, Appl. Mater. Today 11 (2018) (2018) 1–12.
[9] O. Mahony, O. Tsigkou, C. Ionescu, C. Minelli, L. Ling, R. Hanly, M.E. Smith, M.M. Stevens, J.R. Jones, Silica-gelatin hybrids with tailorable degradation and mechanical properties for tissue regeneration, Adv. Funct. Mater. 20 (2010) 3835–3845.

[10] A. Kumar, K.M. Rao, S.S. Han, Synthesis of mechanically stiff and bioactive hybrid hydrogels for bone tissue engineering applications, Chem. Eng. J. 317 (2017) 119–131.
[11] J.J. Chung, S. Li, M.M. Stevens, T.K. GePolyiou, J.R. Jones, Tailoring mechanical properties of sol–gel hybrids for bone regeneration through polymer structure, Chem. Mater. 28 (2016) 6127–6135.
[12] L.S. Connell, L. Gabrielli, O. Mahony, L. Russo, L. Cipolla, J.R. Jones, Functionalizing natural polymers with alkoxysilane coupling agents: reacting 3-glycidoxypropyl trimethoxysilane with poly(γ-glutamic acid) and gelatin, Polym. Chem. 8 (2017) 1095–1103.
[13] E.M. Valliant, F. Romer, D. Wang, D.S. McPhail, M.E. Smith, J.V. Hanna, J.R. Jones, Bioactivity in silica/poly(gamma-glutamic acid) sol-gel hybrids through calcium chelation, Acta Biomater. 9 (2013) 7662–7671.
[14] L.L. Hench, I. Thompson, Twenty-first century challenges for biomaterials, J. R. Soc. Interface 7 (2010) S379–S391.
[15] U.G. Wegst, H. Bai, E. Saiz, A.P. Tomsia, R.O. Ritchie, Bioinspired structural materials, Nat. Mater. 14 (2015) 23–36.
[16] L.S. Connell, F. Romer, M. Suarez, E.M. Valliant, Z. Zhang, P.D. Lee, M.E. Smith, J.V. Hanna, J.R. Jones, Chemical characterisation and fabrication of chitosan-silica hybrid scaffolds with 3-glycidoxypropyl trimethoxysilane, J. Mater. Chem. B 2 (2014) (2014) 668–680.
[17] W. Fan, R.E. Youngman, X. Ren, D. Yu, M.M. Smedskjaer, J. Mater. Chem. B 9 (2021) 4400–4410.
[18] F. Tallia, L. Russo, S. Li, A.L.H. Orrin, X. Shi, S. Chen, J.A.M. Steele, S. Meille, J. Chevalier, P.D. Lee, M.M. Stevens, L. Cipolla, J.R. Jones, Bouncing and 3D printable hybrids with self-healing properties, Mater. Horiz 5 (2018) 849–860.
[19] L. Gabrielli, L. Connell, L. Russo, J. Jiménez-Barbero, F. Nicotra, L. Cipolla, J.R. Jones, Exploring GPTMS reactivity against simple nucleophiles: chemistry beyond hybrid materials fabrication, RSC Adv. 4 (2014) 1841–1848.
[20] F.K. Shi, X.P. Wang, R.H. Guo, M. Zhong, X.M. Xie, Highly stretchable and super tough nanocomposite physical hydrogels facilitated by the coupling of intermolecular hydrogen bonds and analogous chemical crosslinking of inorganic particles, J. Mater. Chem. B 3 (2015) 1187–1192.
[21] L.-q. Zhang, L.-w. Chen, M. Zhong, F.-k. Shi, X.-y. Liu, X.-m. Xie, Phase transition temperature controllable poly(acrylamide-co-acrylic acid) nanocomposite physical hydrogels with high strength, Chin. J. Polym. Sci. 34 (2016) 1261–1269.
[22] F.K. Shi, M. Zhong, L.Q. Zhang, X.Y. Liu, X.M. Xie, Robust and self-healable nanocomposite physical hydrogel facilitated by the synergy of ternary crosslinking points in a single network, J. Mater. Chem. B 4 (2016) 6221–6227.
[23] M. Zhong, X.Y. Liu, F.K. Shi, L.Q. Zhang, X.P. Wang, A.G. Cheetham, H. Cui, X.M. Xie, Self-healable, tough and highly stretchable ionic nanocomposite physical hydrogels, Soft Matter 11 (2015) (2015) 4235–4241.
[24] D. Wang, W. Liu, Q. Feng, C. Dong, Q. Liu, L. Duan, J. Huang, W. Zhu, Z. Li, J. Xiong, Y. Liang, J. Chen, R. Sun, L. Bian, D. Wang, Effect of inorganic/organic ratio and chemical coupling on the performance of porous silica/chitosan hybrid scaffolds, Mater. Sci. Eng. C 70 (2017) 969–975.
[25] M. Mokhtarifar, R. Kaveh, M. Bagherzadeh, A. Lucotti, M. Pedeferri, M.V. Diamanti, Heterostructured TiO_2/SiO_2/gamma-Fe_2O_3/rGO coating with highly efficient visible-light-induced self-cleaning properties for metallic artifacts, ACS Appl. Mater. Interfaces 12 (2020) 29671–29683.
[26] J. Hu, Q. Gao, L. Xu, M. Zhang, Z. Xing, X. Guo, K. Zhang, G. Wu, Significant improvement in thermal and UV resistances of UHMWPE fabric through in situ formation of polysiloxane-TiO_2 hybrid layers, ACS Appl. Mater. Interfaces 8 (2016) 23311–23320.
[27] P. Yu, R.J. Kirkpatrick, B. Poe, P.F. McMillan, X. Cong, Structure of calcium silicate hydrate (C-S-H): near-, mid-, and far-infrared spectroscopy, J. Am. Ceram. Soc. 82 (2004) 742–748.27.
[28] D. Wang, Y. Tan, L. Yu, Z. Xiao, J. Du, J. Ling, N. Li, J. Wang, S. Xu, J. Huang, Tuning morphology and mechanical property of polyacrylamide/laponite/titania dual nanocomposite hydrogels by titania, Polym. Compos. 40 (2019) (2019) E466–E475.
[29] L.L. Hench, J.K. West, The sol-gel process, Chem. Rev. 90 (1990) 33–72.
[30] D. Zhang, J. Yang, S. Bao, Q. Wu, Q. Wang, Semiconductor nanoparticle-based hydrogels prepared via self-initiated polymerization under sunlight, even visible light, Sci. Rep. 3 (2013) 1399.
[31] F.H. Aragón, I. Gonzalez, J.A.H. Coaquira, P. Hidalgo, H.F. Brito, J.D. Ardisson, W.A.A. Macedo, P.C. Morais, Structural and surface study of praseodymium-doped SnO_2 nanoparticles prepared by the polymeric precursor method, J. Phys. Chem. C 119 (2015) 8711–8717.
[32] F. Fan, Z. Xia, Q. Li, Z. Li, H. Chen, ZrO2/PMMA nanocomposites: preparation and its dispersion in polymer matrix, Chin. J. Chem. Eng. 21 (2013) 113–120.
[33] H. Li, C.P. Tripp, Infrared study of the interaction of charged silica particles with TiO_2 particles containing adsorbed cationic and anionic polyelectrolytes, Langmuir 21 (2005) 2585–2590.
[34] R. Peña-Alonso, L. Téllez, J. Rubio, F. Rubio, Surface chemical and physical properties of TEOS-TBOT-PDMS hybrid materials, J. Sol Gel Sci. Technol. 38 (2006) 133–145.
[35] J. Du, X. She, W. Zhu, Q. Yang, H. Zhang, C. Tsou, Super-tough, anti-fatigue, self-healable, anti-fogging, and UV shielding hybrid hydrogel prepared via simultaneous dual in situ sol-gel technique and radical polymerization, J. Mater. Chem. B 7 (2019) 7162–7175.
[36] R.T. Sanderson, Chemical Bonds and Bond Energy, second ed., 1976.
[37] M. Lehmann, W. Tabaka, T. Moller, A. Oppermann, D. Woll, D. Volodkin, S. Wellert, R.V. Klitzing, DLS setup for in situ measurements of photoinduced size changes of microgel-based hybrid particles, Langmuir 34 (2018) 3597–3603.
[38] S. Bhattacharjee, DLS and zeta potential – what they are and what they are not? J. Controlled Release 235 (2016) 337–351.
[39] M. Liu, Y. Qing, Y. Wu, J. Liang, S. Luo, Facile fabrication of superhydrophobic surfaces on wood substrates via a one-step hydrothermal process, Appl. Surf. Sci. 330 (2015) 332–338.
[40] F. Rubio, J. Rubio, J.L. Oteo, A FT-IR study of the hydrolysis of tetraethylorthosilicate (TEOS), Spectrosc. Lett. 31 (1998) 199–219.
[41] E. Norris, C. Ramos-Rivera, G. Poologasundarampillai, J.P. Clark, Q. Ju, A. Obata, J.V. Hanna, T. Kasuga, C.A. Mitchell, G. Jell, J.R. Jones, Electrospinning 3D bioactive glasses for wound healing, Biomed. Mater. 15 (2020), 015014.
[42] K. Chrissafis, D. Bikiaris, Can nanoparticles really enhance thermal stability of polymers? Part I: an overview on thermal decomposition of addition polymers, Thermochim. Acta 523 (2011) 1–24.
[43] W. Wu, Q. Wang, W. Li, Comparison of tensile and compressive properties of carbon/glass interlayer and intralayer hybrid composites, Materials 11 (2018) 1105.
[44] G. Czél, M. Jalalvand, M.R. Wisnom, Hybrid specimens eliminating stress concentrations in tensile and compressive testing of unidirectional composites, Compos. A 91 (2016) 436–447.
[45] S.C. Her, K.Y. Lin, Dynamic mechanical analysis of carbon nanotube-reinforced nanocomposites, J. Appl. Biomater. Funct. Mater. 15 (2017) e13–e18.
[46] C.S.M.F. Costa, A.C. Fonseca, A.C. Serra, J.F.J. Coelho, Dynamic mechanical thermal analysis of polymer composites reinforced with natural fibers, Polym. Rev. 56 (2016) 362–383.
[47] L. Chen, X. Zhang, G. Liu, Analysis of dynamic mechanical properties of sprayed fiber-reinforced concrete based on the energy conversion principle, Constr. Build. Mater. 254 (2020) 119167.
[48] K.V. Pillai, S. Renneckar, Dynamic mechanical analysis of layer-by-layer cellulose nanocomposites, Ind. Crops Prod. 93 (2016) 267–275.
[49] Z. Deng, X. Liu, X. Yang, N. Liang, R. Yan, P. Chen, Q. Miao, Y. Xu, A study of tensile and compressive properties of hybrid basalt-polypropylene fiber-reinforced concrete under uniaxial loads, Struct. Concr. 22 (2020) 396–409.
[50] M.S. Islam, S. Hamdan, Z.A. Talib, A.S. Ahmed, M.R. Rahman, Tropical wood polymer nanocomposite (WPNC): the impact of nanoclay on dynamic mechanical thermal properties, Compos. Sci. Technol. 72 (2012) 1995–2001.
[51] W. Zhao, X. Jin, Y. Cong, Y. Liu, J. Fu, Degradable natural polymer hydrogels for articular cartilage tissue engineering, J. Chem. Technol. Biotechnol. 88 (2013) 327–339.
[52] L.A. Setton, D.M. Elliott, V.C. Mow, Altered mechanics of cartilage with osteoarthritis: human osteoarthritis and an experimental model of joint degeneration, Osteoarthr. Cartil. 7 (1999) 2–14.

Supporting Information

Flexible Inorganic-Organic Hybrids with Dual Inorganic Components

Wei Fan[1], Lars R. Jensen[2], Marcel Ceccato[3], Thomas S. Quaade[2], Leonid Gurevich[2], Donghong Yu[1,*], Morten M. Smedskjaer[1,*]

[1] *Department of Chemistry and Bioscience, Aalborg University, 9220 Aalborg, Denmark*

[2] *Department of Materials and Production, Aalborg University, 9220 Aalborg, Denmark*

[3] *Interdisciplinary Nanoscience Center (iNANO) and Department of Biological and Chemical Engineering, Aarhus University, 8200 Aarhus N, Denmark*

[*] *Corresponding authors. e-mail: yu@bio.aau.dk (D.Y.), mos@bio.aau.dk (M.M.S.)*

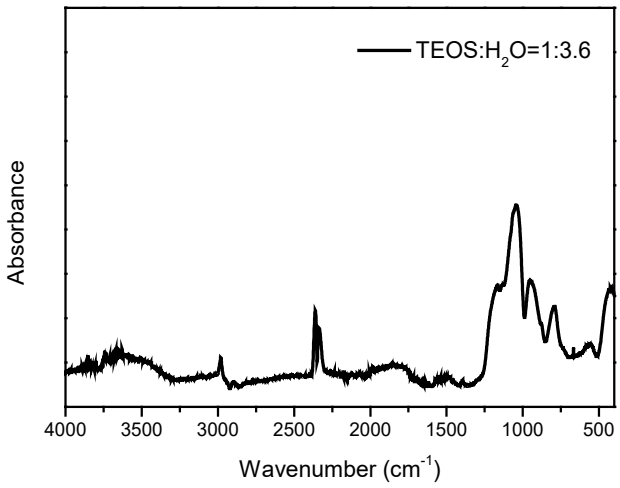

Fig. S1 FTIR absorbance spectrum of the pure silica structure at the molar ratio of TEOS:H_2O=1:3.6.

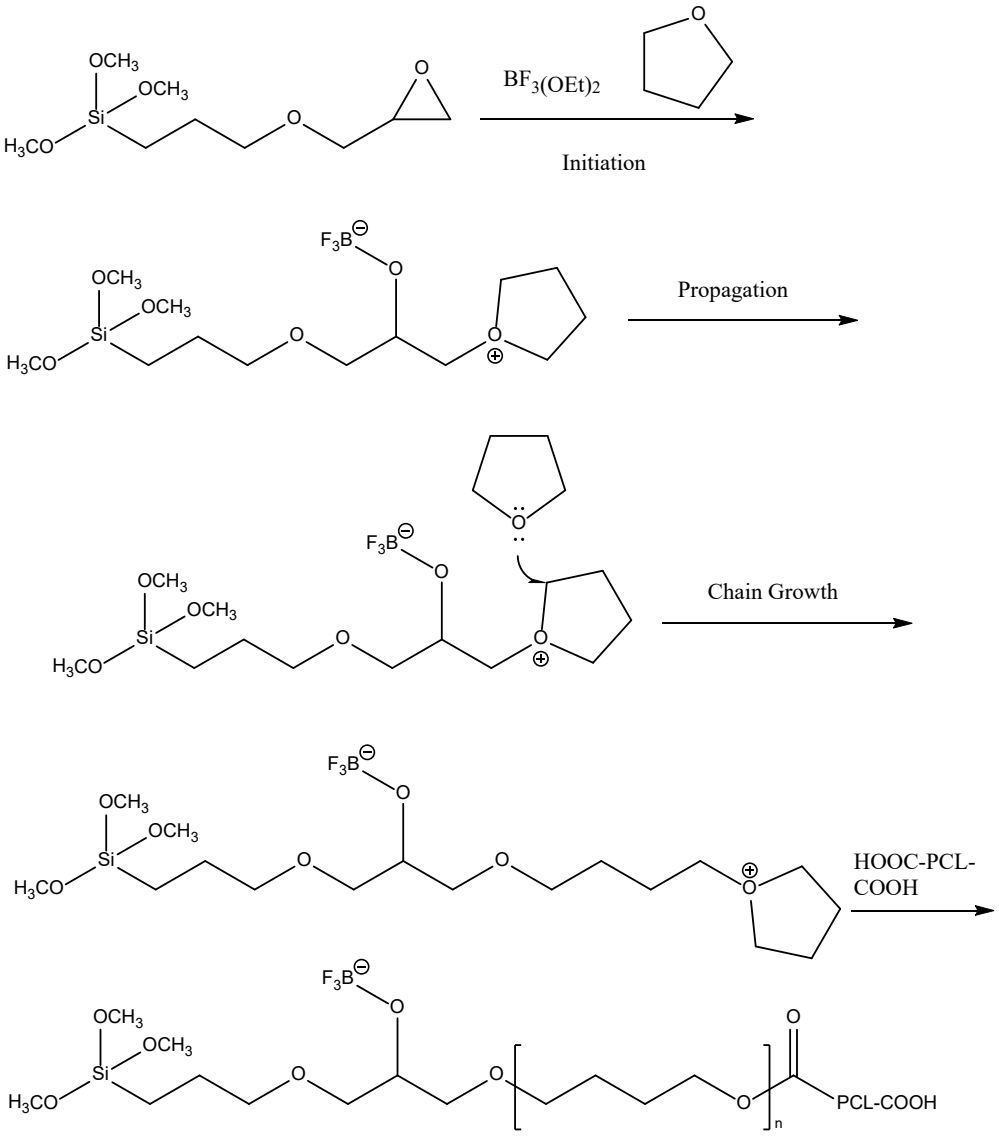

Fig.S2. Synthesis mechanism of GPTMS-PTHF-PCL.

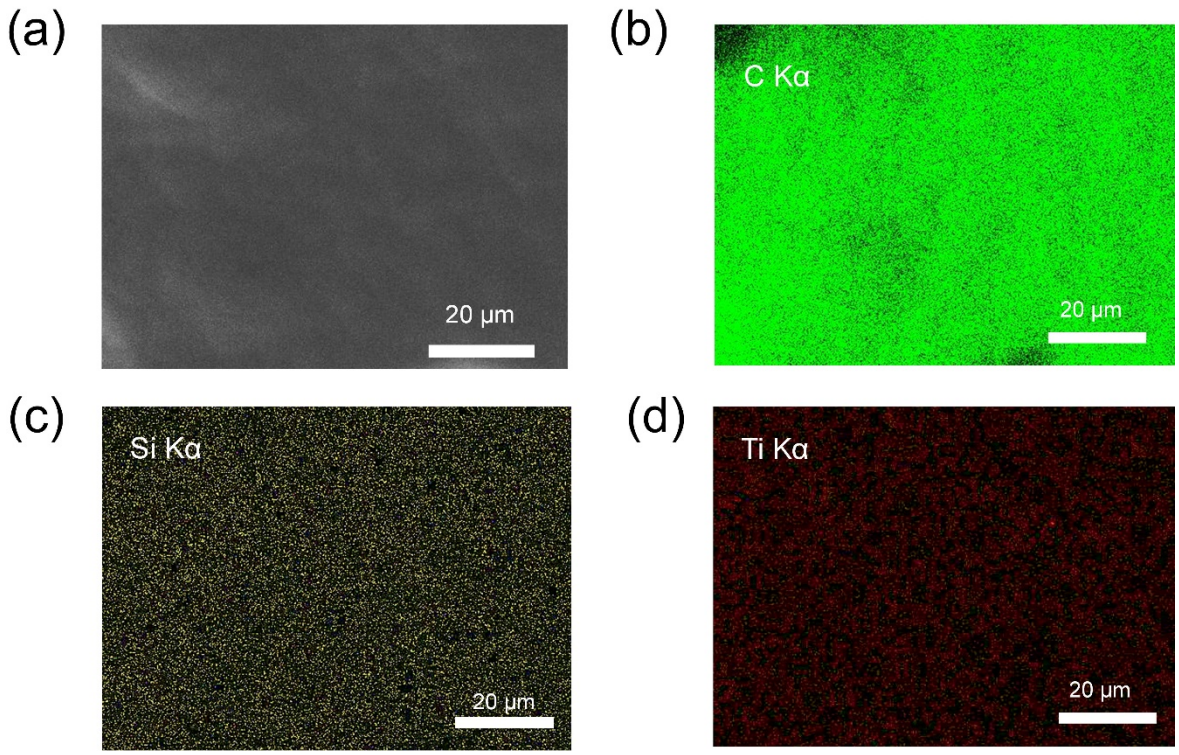

Fig. S3. (a) Scanning electron microscope (SEM) image of the surface of $Polymer_{70}/(Si_{0.6}Ti_{0.4})_{30}$ hybrid, with the corresponding element distribution of (b) C, (c) Si, and (d) Ti as detected by the energy dispersive X-ray (EDX) analyzer.

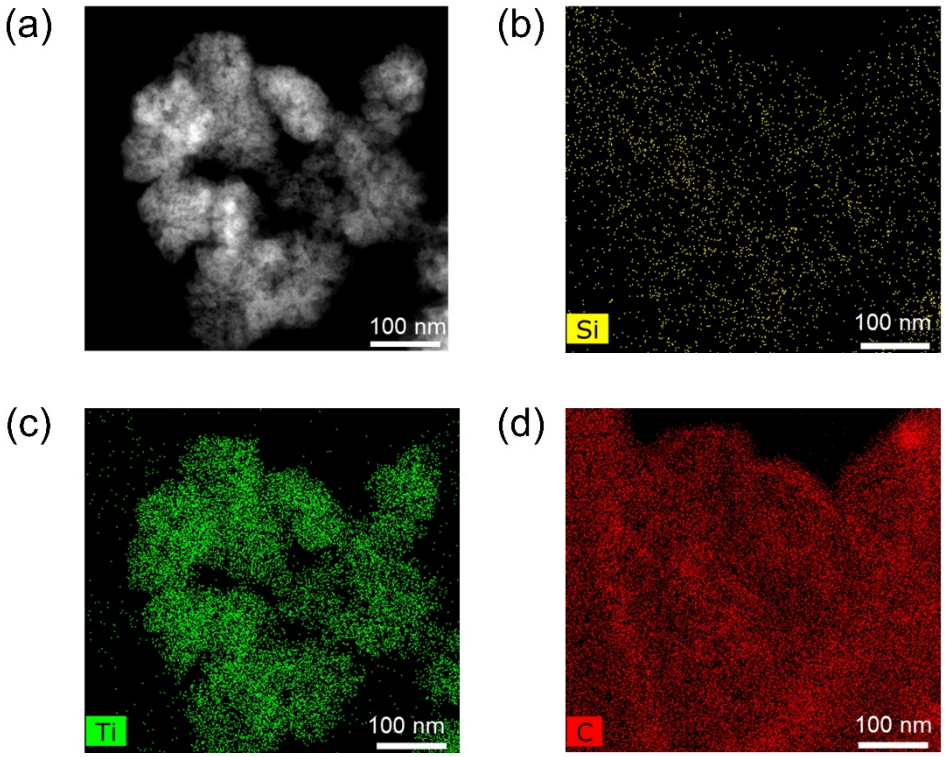

Fig. S4. (a) HAADF-STEM image of the bulk of hybrid Polymer$_{70}$/(Si$_0$Ti$_1$)$_{30}$; and the corresponding element mapping of (b) Si; (c) Ti; (d) C.

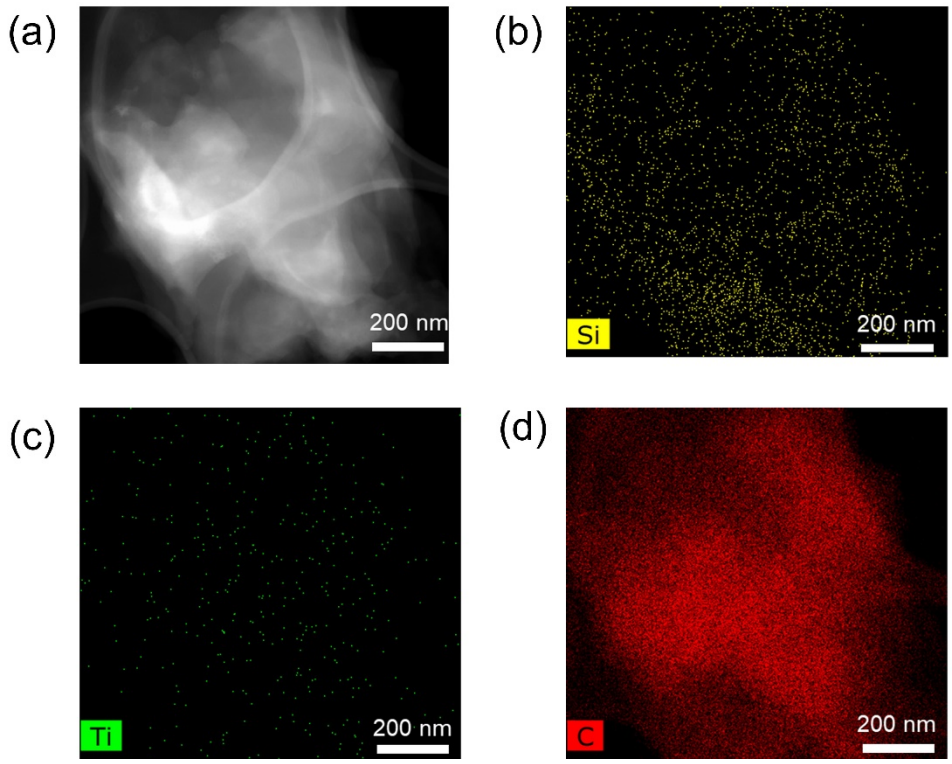

Fig. S5. (a) HAADF-STEM image of the bulk of hybrid Polymer$_{70}$/(Si$_1$Ti$_0$)$_{30}$; and the corresponding element mapping of (b) Si; (c) Ti; (d) C.

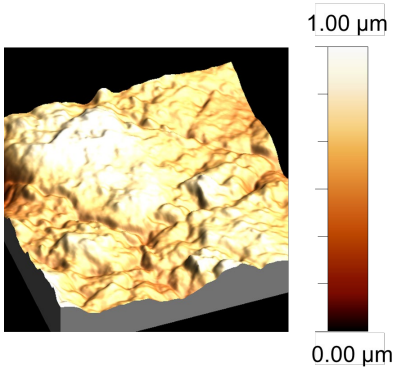

Fig. S6. AFM topography of hybrid Polymer$_{70}$/(Si$_{0.6}$Ti$_{0.4}$)$_{30}$.

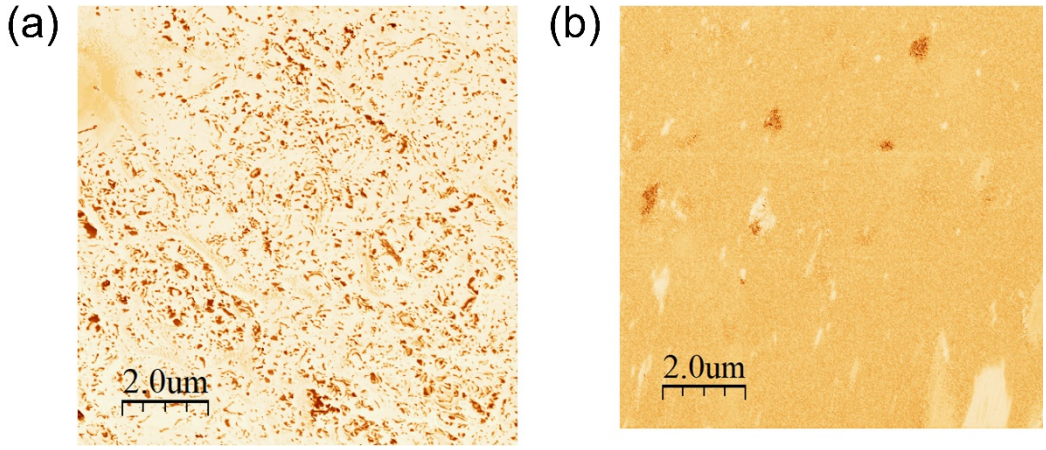

Fig. S7. AFM phase images of hybrid Polymer$_{70}$/(Si$_{0.6}$Ti$_{0.4}$)$_{30}$ and Polymer$_{70}$/(Si$_0$Ti$_1$)$_{30}$.

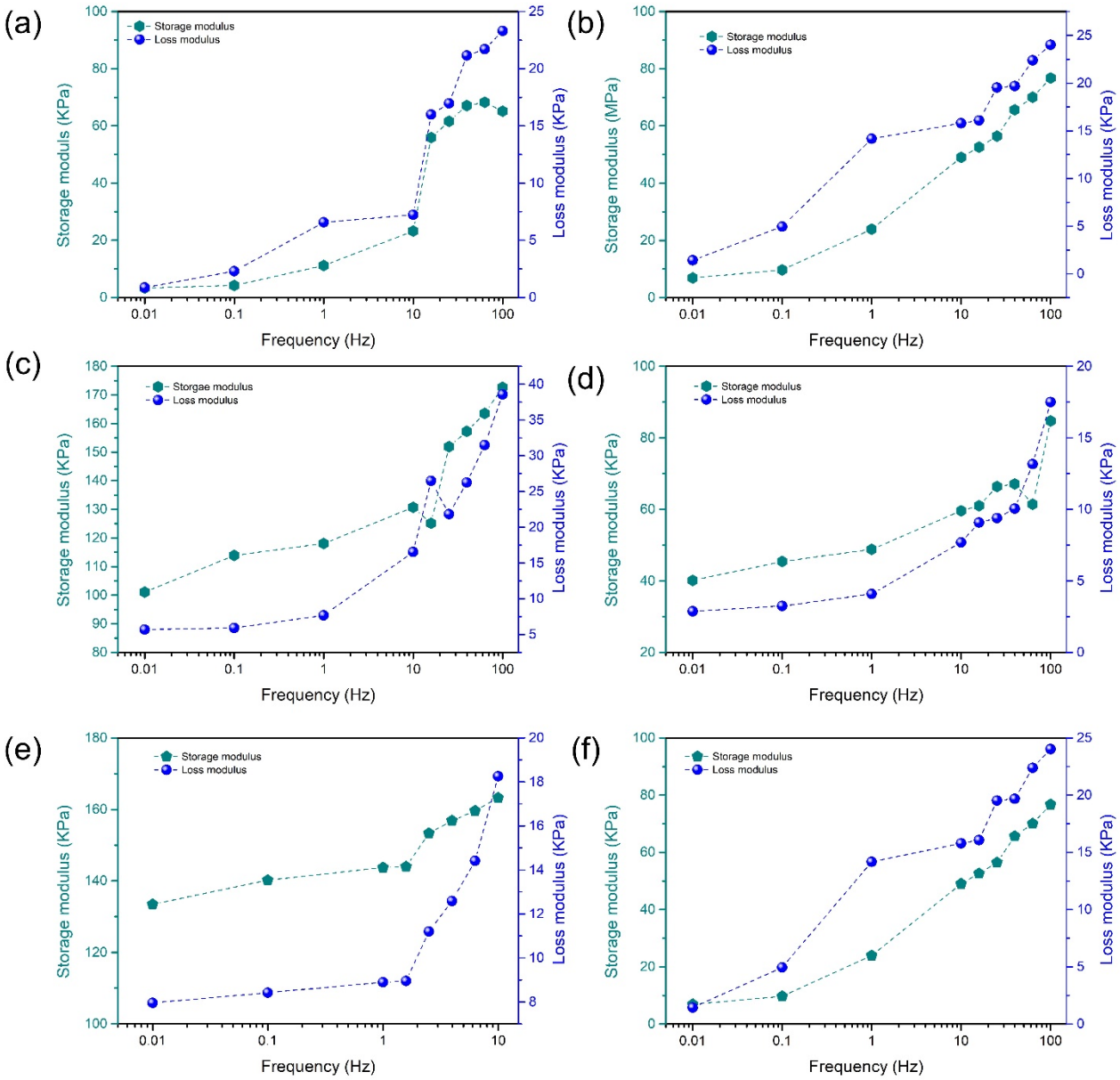

Fig. S8 Frequency dependence of storage modulus (*E'*) and loss modulus (*E''*) of hybrid (a) $Polymer_{70}/(Si_1Ti_0)_{30}$, (b) $Polymer_{70}/(Si_{0.8}Ti_{0.2})_{30}$,(c) $Polymer_{70}/(Si_{0.6}Ti_{0.4})_{30}$, (d) $Polymer_{70}/(Si_{0.4}Ti_{0.6})_{30}$, (e) $Polymer_{70}/(Si_{0.2}Ti_{0.8})_{30}$, and (f) $Polymer_{70}/(Si_0Ti_1)_{30}$.

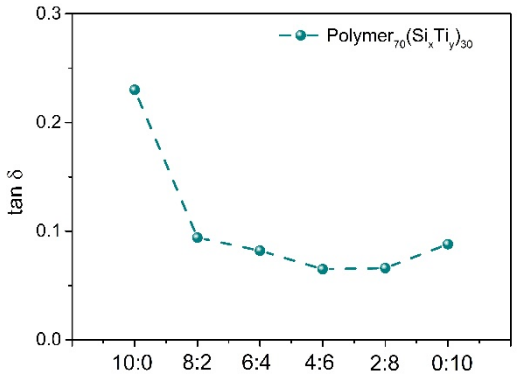

Fig. S9 Composition dependence of the damping coefficient tan (δ) of hybrids at 1 Hz as obtained from the DMA analysis.

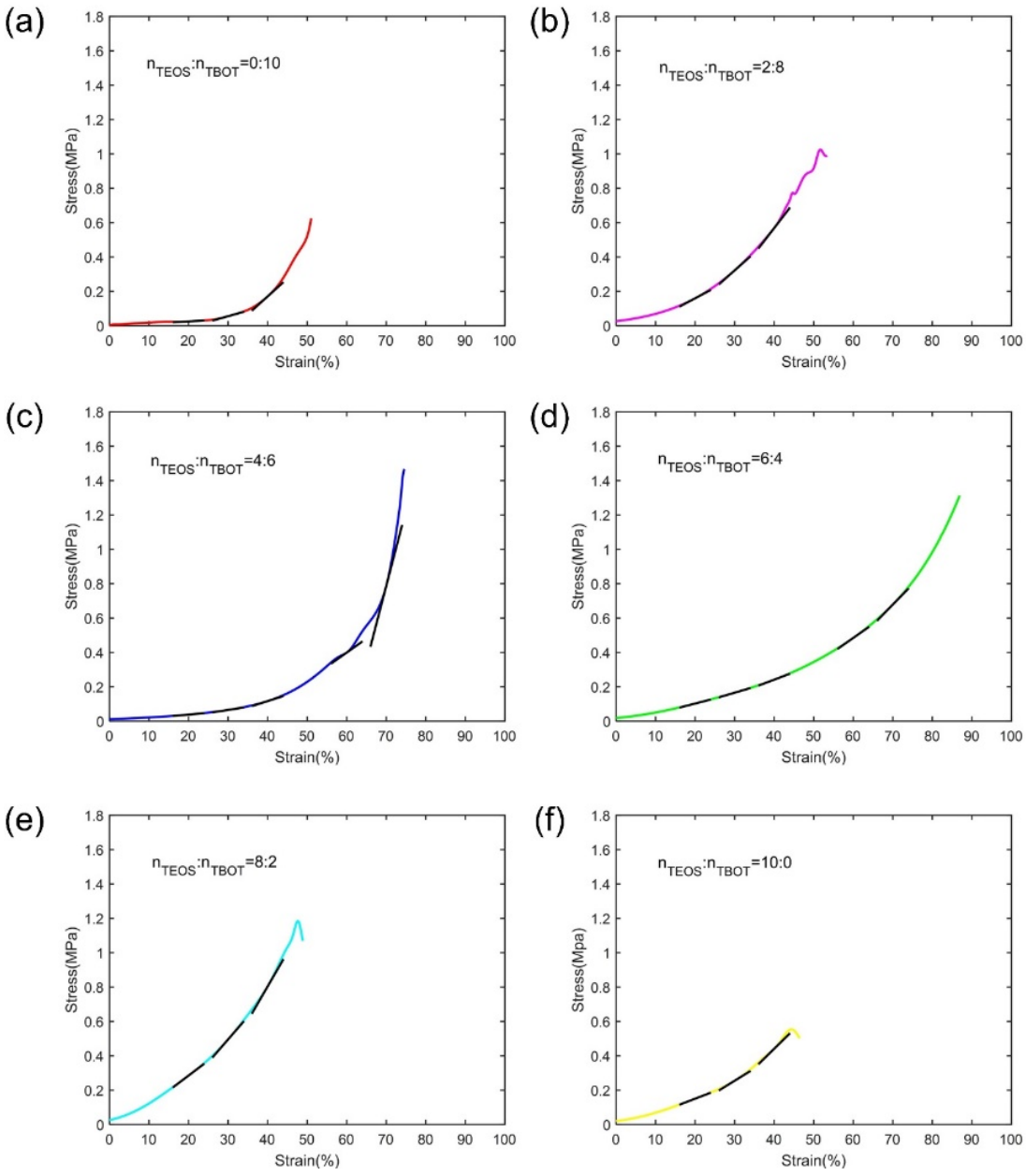

Fig. S10 Stress-strain curves used to determine the tangent modulus of the six hybrids at a selected strain of 20%. This strain value is selected as some of the hybrids break during compression.

Table S1. Amount of THF monomer, HOOC-PCL-COOH, TEOS and TBOT in different hybrids.

Hybrid	n(TEOS):n(TBOT) a total of 0.86 g	THF	HOOC-PCL-COOH
$Polymer_{70}/(Si_1Ti_0)_{30}$	10:0	40 mL	2 g
$Polymer_{70}/(Si_{0.8}Ti_{0.2})_{30}$	8:2	40 mL	2 g
$Polymer_{70}/(Si_{0.6}Ti_{0.4})_{30}$	6:4	40 mL	2 g
$Polymer_{70}/(Si_{0.4}Ti_{0.6})_{30}$	4:6	40 mL	2 g
$Polymer_{70}/(Si_{0.2}Ti_{0.8})_{30}$	2:8	40 mL	2 g
$Polymer_{70}/(Si_0Ti_1)_{30}$	0:10	40 mL	2 g

Table S2. Storage modulus and loss modulus of hybrids at 1 Hz.

Sample	Frequency (Hz)	Storage modulus (KPa)	Loss modulus (KPa)
$Polymer_{70}/(Si_1Ti_0)_{30}$	1	11.11	2.56
$Polymer_{70}/(Si_{0.8}Ti_{0.2})_{30}$	1	15.25	1.43
$Polymer_{70}/(Si_{0.6}Ti_{0.4})_{30}$	1	49	4
$Polymer_{70}/(Si_{0.4}Ti_{0.6})_{30}$	1	118	7.66
$Polymer_{70}/(Si_{0.2}Ti_{0.8})_{30}$	1	97	6.4
$Polymer_{70}/(Si_0Ti_1)_{30}$	1	61	5.37

Table S3. Tangent modulus (MPa) of the six different hybrids at five different strain values.

Strain(%) / Sample	20	30	40
$Polymer_{70}/(Si_1Ti_0)_{30}$	0.1242	0.6484	2.0801
$Polymer_{70}/(Si_{0.8}Ti_{0.2})_{30}$	1.2286	2.0441	2.9832
$Polymer_{70}/(Si_{0.6}Ti_{0.4})_{30}$	0.2073	0.3555	0.7361
$Polymer_{70}/(Si_{0.4}Ti_{0.6})_{30}$	0.5909	0.6746	0.8713
$Polymer_{70}/(Si_{0.2}Ti_{0.8})_{30}$	1.7424	2.6541	3.9697
$Polymer_{70}/(Si_0Ti_1)_{30}$	0.8821	1.424	2.2582

Paper III

ACS NANO

www.acsnano.org

ARTICLE

Resolving the Conflict between Strength and Toughness in Bioactive Silica–Polymer Hybrid Materials

Wei Fan, Tao Du, Aida Droce, Lars R. Jensen, Randall E. Youngman, Xiangting Ren, Leonid Gurevich, Mathieu Bauchy, Peter Kristensen, Bengang Xing, Donghong Yu,* and Morten M. Smedskjaer*

Cite This: https://doi.org/10.1021/acsnano.2c03440

ABSTRACT: **Simultaneously improving the strength and toughness of materials is a major challenge. Inorganic–polymer hybrids offer the potential to combine mechanical properties of a stiff inorganic glass with a flexible organic polymer. However, the toughening mechanism at the atomic scale remains largely unknown. Based on combined experimental and molecular dynamics simulation results, we find that the deformation and fracture behavior of hybrids are governed by noncovalent intermolecular interactions between polymer and silica networks rather than the breakage of covalent bonds. We then attempt three methods to improve the balance between strength and toughness of hybrids, namely the total inorganic/organic (I/O) weight ratio, the size of silica nanoparticles, and the ratio of −C−O *vs* −C−C bonds in the polymer chains. Specifically, for a hybrid with matched silica size and I/O ratio, we demonstrate optimized mechanical properties in terms of strength (1.75 MPa at breakage), degree of elongation at the fracture point (31%), toughness (219 kPa), hardness (1.08 MPa), as well as Young's modulus (3.0 MPa). We also demonstrate that this hybrid material shows excellent biocompatibility and ability to support cell attachment as well as proliferation. This supports the possible application of this material as a strong yet tough bone scaffold material.**

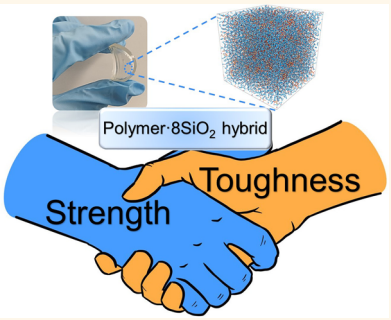

KEYWORDS: *silica–polymer hybrid, strength toughness balance, atomic-scale predicting, simulation, bioactive materials*

INTRODUCTION

The conflict between strength and toughness in materials continues to have important consequences for various structural and functional applications, despite the progress that has been made.[1,2] Strength represents the largest achievable stress in the material, whereas toughness is the material's resistance to fracture when a crack is present.[3] Materials that can dissipate high local stresses by undergoing limited deformation are tough, which explains why strong materials, *i.e.*, those that deform less readily, tend to be brittle.[1] For instance, oxide glasses can reveal high fracture strength above 10^2 MPa but typically are less tough and flexibile,[4] while polymer hydrogel materials can be stretched to several times their original length but at the same time exhibit low fracture strength in the range of tens to hundreds of kPa.[5] Such strong-but-brittle or tough-but-weak materials are unsuitable for accommodating cyclic loading in a wide range of applications, including those within soft robotics and tissue regeneration. Balancing strength and toughness is thus urgently needed to satisfy the aforementioned requirements. Strategies based on, for instance, double-network polymers[6] and binary/ternary systems[7] have been attempted. However, all-polymer systems with desirable flexibility could hardly reach the strength requirements for applications *in vivo*, since native human articular cartilage has a compression modulus of about 0.4–2.0 MPa.[8,9] On the other hand, binary or ternary systems usually suffer from phase separation and undesirable synergetic properties, which hinder many possible applications.[10]

To overcome the conflict of strength *vs* toughness and avoid issues with phase separation, a promising method would be the synthesis of covalently linked inorganic–polymer hybrid materials[11−13] since such hybrid materials can synergistically combine the advantages of flexible polymers and rigid inorganic glass networks.[14−16] In some cases, such inorganic–polymer hybrids have been reported to feature excellent

Received: April 8, 2022
Accepted: June 6, 2022

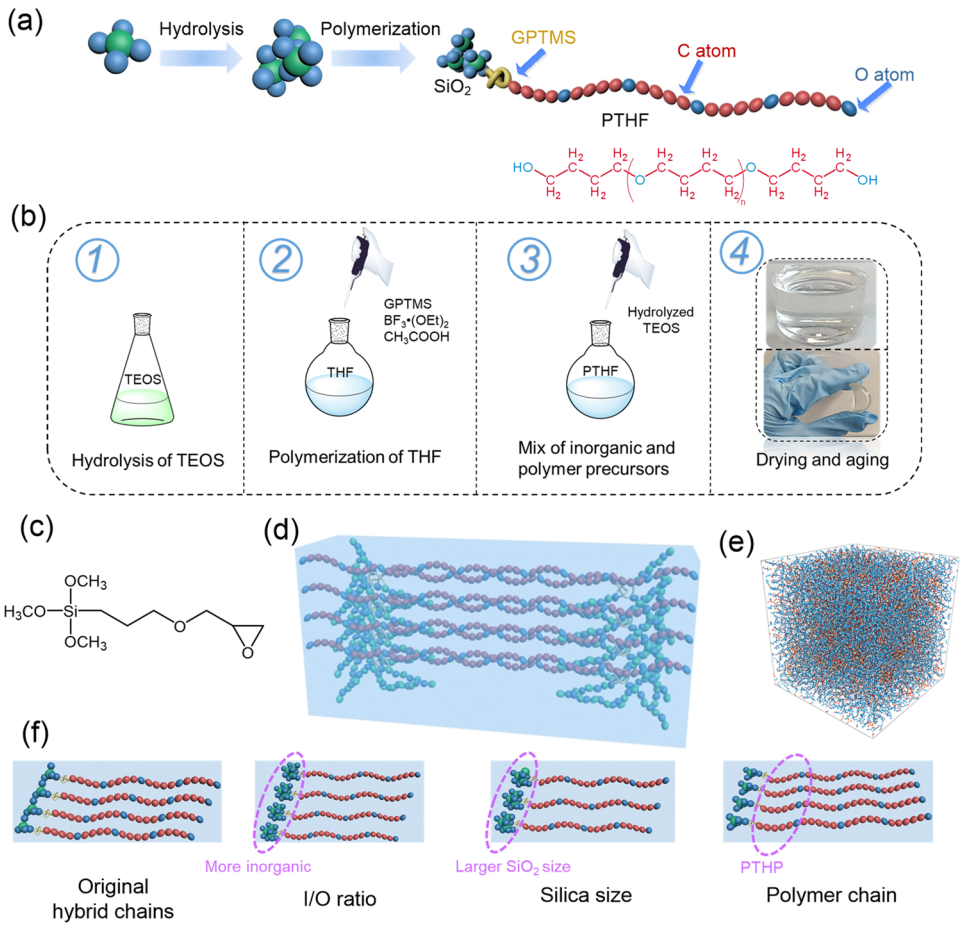

Figure 1. (a) Schematic structure of hybrid: the silica network is covalently bonded to polymer chains *via* coupling agents and the molecular structure of PTHF; (b) synthesis process and obtained flexible and optically transparent PTHF·*x*TEOS hybrids; (c) molecular structure of coupling agent GPTMS; (d) schematic 3D-structure of a hybrid bulk; (e) MD simulated 3D-structure of a hybrid bulk where the color of the atoms matches that of panel (a); and (f) schematic structures of hybrids with different I/O weight ratio, silica size, and polymer repeating unit.

functional and mechanical properties, making them suitable for bio-related applications as mentioned above.[17−19] To ensure the integrity of the hybrids at the atomic scale, covalent bonding between the two phases to form interpenetrating hybrid co-networks is usually achieved *via* organic−inorganic coupling agents.[20] Different organic silane coupling agents are widely applied as they can adapt to various reaction mechanisms for constructing covalent bonds between silica and polymers.[21−23] For example, coupling agents such as vinyltriethoxysilane, diethoxydivinylsilane, and diethoxymethylvinylsilane with vinyl functional groups can react with other vinyl monomers *via* a free-radical polymerization mechanism,[24,25] while the epoxide group of glycidoxypropyl trimethoxysilane (GPTMS) can participate in a ring-opening process with suitable cyclic ether monomers.[26−29] In turn, the silyl group on the latter can react with tetraethyl orthosilicate (TEOS) as the inorganic precursor through sol−gel condensation process. This enables the inorganic component to bond to organic polymer chains and thus promote its uniform dispersion in the hybrid network to avoid phase aggregation and separation.[29,30] As such, the amount of silane coupling agent determines the number of covalent links between the silica sub-network and the polymer chains.[27,28]

Hydrolyzed TEOS bonds to polymer chains in such systems and can be used to control the size of the silica nanoparticles and total inorganic-to-organic (I/O) ratio.[27] In addition, varying the structure of the polymer backbone is another path to adjust the mechanical properties of hybrids.[28] Due to their controllable structures and polymerization mechanism, epoxides and other cyclic ether monomers are good candidates for forming the polymer backbone.[29] As a thermoplastic, polytetrahydrofuran (PTHF) is commonly applied for biomedical applications due to its desirable anticoagulant abilities when incorporating polyurethane[30,31] *via* cationic ring opening approach, giving rise to bulk materials with bouncy and tough mechanical performance.[25] Similar monomers such as ethylene oxide and tetrahydropyran undergo the same polymerization mechanisms,[27] but with different ratio of C−O to C−C bonds, thus enabling further control of the hybrid structure and mechanical properties at the molecular level.[29,32]

To understand the changes in the structure of such hybrid materials at the atomic scale *in situ* during deformation and fracture, molecular dynamics (MD) simulations are needed. This is necessary since *in situ* mapping of atomic rearrangements during fracture is still out of reach experimentally. MD simulations have previously been used to understand the fracture behavior of various materials, including epoxy resins,[33] oxide glasses,[34] nanocomposites,[35] *etc.* However, such simulations have not yet been applied to understand the mechanical properties of hybrids with systematically varying components.

https://doi.org/10.1021/acsnano.2c03440
ACS Nano XXXX, XXX, XXX−XXX

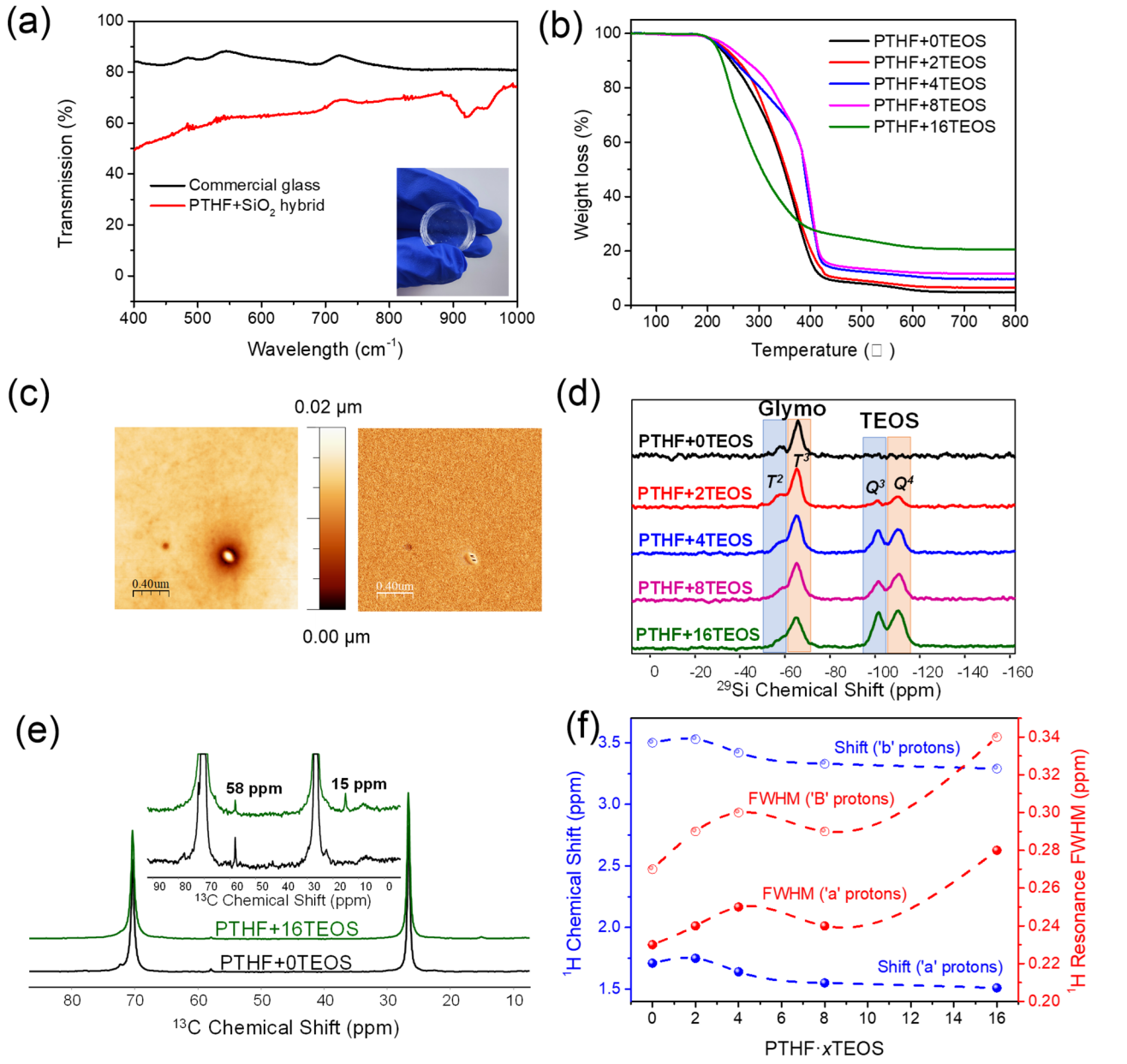

Figure 2. (a) UV−vis transmission spectra of the PTHF·8TEOS hybrid sample as well as commercial soda−lime−silica glass, both with a thickness of 5 mm. (b) TGA heating curves of hybrids with varying I/O ratios, *i.e.*, the series of PTHF·*x*TEOS hybrids. (c) Height (left) and phase (right) AFM images of the hybrid PTHF·16TEOS. (d) ^{29}Si and (e) ^{13}C spectra of PTHF·*x*TEOS hybrids. (f) FWHM (full width at half-maximum) and chemical shift for ^{1}H peaks in PTHF structures. The names and compositions of these hybrid samples are given in Table 1.

In this work, we systematically investigate the mechanism of deformation and fracture of inorganic−polymer hybrid materials at the atomic scale using a combination of experiments and MD simulations. Specifically, we attempt to control the noncovalent intermolecular interactions in the hybrids by varying the size of silica nanoparticles (NPs), fraction of C−O bonds in hybrids, and total organic−inorganic weight ratios. Based on these systematic studies, we successfully achieved an improved balance of toughness and strength (or flexibility and hardness) in a hybrid PTHF·8TEOS that can be compressed to 31% compared with its original height for a strength of 1.75 MPa at breakage and toughness of 219 kPa. Importantly, we show that these hybrids reveal excellent biocompatibility, including noncytotoxicity and the ability to support cell attachment as well as further cell proliferations. Overall, our study shows that by understanding the hybrid deformation and fracture mechanism it is possible to control the hybrids' mechanical properties. These findings could enable applications of such tailorable inorganic−polymer hybrids within tissue engineering and soft robotics.

RESULTS AND DISCUSSION

Synthesis of Hybrid Materials. As shown schematically in Figure 1a, silica and PTHF backbones were covalently linked through the silane coupling agent GPTMS.[25,27] The synthesis combines a sol−gel method for preparation of the SiO_2 precursor with cationic ring-opening processes for the organic monomers (Figure 1b). Specifically, TEOS was first hydrolyzed, generating −OH groups (see steps 1 and 2 in

https://doi.org/10.1021/acsnano.2c03440
ACS Nano XXXX, XXX, XXX−XXX

Figure 1b), and second co-condensed, leading to covalent links between SiO_2 and organic polymers (see step 3 in Figure 1b). Then, upon initiation by the Lewis acid $BF_3{\cdot}(OEt)_2$, the oxirane group of GPTMS (Figure 1c) started the ring-opening polymerization of THF monomers, resulting in covalent links between the phases in the hybrid after prolonged condensation and drying (see step 4 in Figure 1b).[25,36] The hydrolysis process, polymerization mechanism, and molecular structures of such PTHF−SiO_2 hybrids are presented in Figure S1.[27] As we will show in this study, the obtained hybrids inherit the advantages of flexible polymers and hard inorganic components but also exhibit good transparency (Figure 1b). We combine experimental methods and MD simulations (Figure 1d,e) and perform systematic investigations of three compositional effects on the hybrid structure and mechanical properties, namely (Figure 1e): (i) varying amount of TEOS for the same content of GPTMS and PTHF (leading to different I/O weight ratios, in PTHF·$x$$SiO_2$ series of hybrids) in experiments and MD simulations; (ii) varying molar ratios of TEOS-to-GPTMS under a constant I/O weight ratio (resulting in differences in the silica size, in y·GPTMS:z·TEOS series of hybrids) in experiments; and (iii) varying polymer chain repeating unit (PTHF *vs* PTHP (poly tetrahydropyran)) in MD simulations. Regarding the TEOS-to-GPTMS variation for series ii, we note that since GPTMS is the only compound herein that can form covalent links between the organic and inorganic components the amount of GPTMS determines the number of covalently linked silica particles in the system and thus their size. We also note that hybrid series iii is only done in simulations due to the difficulty in polymerizing PTHP, but it allows us to gain fundamental understanding of the role of varyiation on the C−O to C−C bond ratio on the hybrids' mechanical properties.

Experimentally Produced Hybrids with Different I/O Ratio. Considering first the PTHF·xTEOS (x = 0, 2, 4, 8, 16) hybrids, we find that after drying and aging processes the hybrids possess high visual transparency (see inset of Figure 2a). Ultraviolet−visible (UV−vis) spectroscopy measurements are performed to quantify the optical transparency of the hybrid PTHF·8TEOS and make a comparison with a commercial soda−lime−silica glass.[37] Both hybrid and glass samples have a thickness of 5 mm. As shown in Figure 2a, the transparency of the hybrid is up to around 70% over a wide wavelength range of 400 to 1000 nm. Next, to understand the molecular structures of the PTHF·xTEOS series of hybrids, Fourier transform infrared (FT-IR) absorption spectra were recorded, as shown in Figure S2. The bands at 490 and 1090 cm^{-1} correspond to characteristic Si−O−Si asymmetric stretching vibrations.[38−40] Peaks at around 1365 cm^{-1} could be ascribed to ν(C−O−C), while typical $-CH_2$ stretching vibration bands could be observed at 2845 and 2930 cm^{-1}.[27] Hydroxyl (−OH) groups formed during the process of TEOS hydrolysis appear at 3200 cm^{-1}.[38,39] The composition-induced changes in the bands around 3200 cm^{-1} indicate that the silica subnetwork becomes increasingly cross-linked with the increase of TEOS content and consumed excessive −OH groups in GPTMS. Overall, the FT-IR results suggest the formation of PTHF-SiO_2 conetworks.

The final I/O ratio in the hybrids was determined by thermogravimetric analysis (TGA) (Figure. 2b). The total inorganic weight fraction varies from 5.1% to 20.9% in the studied samples (Table 1). As observed during the TGA heating process, the organic polymers begin to degrade at ~210 °C and are fully decomposed at 390 °C in all hybrids. X-ray diffraction (XRD) measurements are also conducted, showing that all of the hybrids are completely amorphous, as seen from the absence of any characteristic sharp diffraction peaks (Figure S3). Such noncrystallinity is in agreement with expectations, since hydrolysis, extended condensation, and covalent linkage processes effectively lead to uniform dispersion of SiO_2, which strongly hinders the effective ordering among either inorganic "SiO_4" tetrahedral or organic macromolecules into crystalline structures.[41] Furthermore, atomic force microscopy (AFM) images of the PTHF·16TEOS hybrid demonstrate a relatively uniform morphology and phase distribution on the nanoscale (see height and phase AFM images in Figure 2c).

Table 1. Compositions of PTHF·xTEOS Hybrids with Different I/O Ratios, including the Amounts of THF Monomer, Coupling Agent GPTMS, Inorganic Precursor (Hydrolyzed TEOS), and Final I/O Weight Ratio

Sample	THF monomer (mL)	GPTMS (mL)	TEOS precursor aqueous (mL)	Final I/O wt%[a]
PTHF·0TEOS	20	1.24	0	5.1/94.9
PTHF·2TEOS	20	1.24	0.60	6.8/93.2
PTHF·4TEOS	20	1.24	1.20	10.0/90.0
PTHF·8TEOS	20	1.24	2.40	12.8/87.2
PTHF·16TEOS	20	1.24	4.80	20.9/79.1

[a]Determined from TGA data (see Figure 2b).

Considering the structure of the silica subnetwork, we have investigated the differences induced by I/O ratio variations through solid state ^1H, ^{13}C, and ^{29}Si nuclear magnetic resonance (NMR) spectroscopy measurements (Figure 2d−f, S6). First, regarding the coupling agent (GPTMS) used in the experiment, the T^3 structure represents fully condensed −C−Si−(O−Si−)$_3$ moieties.[42] In comparison, T^1 and T^2 structures refer to partially condensed units with two and one −O−Si bonds connected to Si, respectively.[43] For the silica structure hydrolyzed from TEOS, the fully cross-linked structure is defined as Q^4 with four siloxane bonds.[16,42] The molecular structures of T^3 and Q^4 are illustrated in Figure S4. As depicted in Figure 2d, with the increase in the content of TEOS, the fraction of Q-type structures increases while the fraction of T^2 decreases, indicating the presence of more branched structures.

Regarding the organic polymer subnetwork, we consider ^{13}C NMR spectra, which are dominated by the PTHF-related peaks at 26.5 and 70.4 ppm (Figure 2e). This is consistent with literature data for poly(tetramethylene oxide), which is a structural analogue of PTHF.[44−46] Almost undetectable peaks (at 58 and 15 ppm in Figure 2e) indicate a very low fraction of alkoxide functionality as ending groups, suggesting a small fraction of unhydrolyzed GPTMS and/or TEOS. Moreover, through analysis of the ^1H NMR data, we find that with the increase in the content of TEOS a slight increase in the shielding of both the methylene protons (H_a and H_b in Figure S5) in the PTHF segment is observed (see Figures 2f and S6). Such a smaller deshielding effect from the oxygen atom in oxymethylene moiety on both H_a and H_b nuclei indicates enhanced intermolecular interactions between the silanol and oxymethylene moieties in the hybrids with higher TEOS

https://doi.org/10.1021/acsnano.2c03440
ACS Nano XXXX, XXX, XXX−XXX

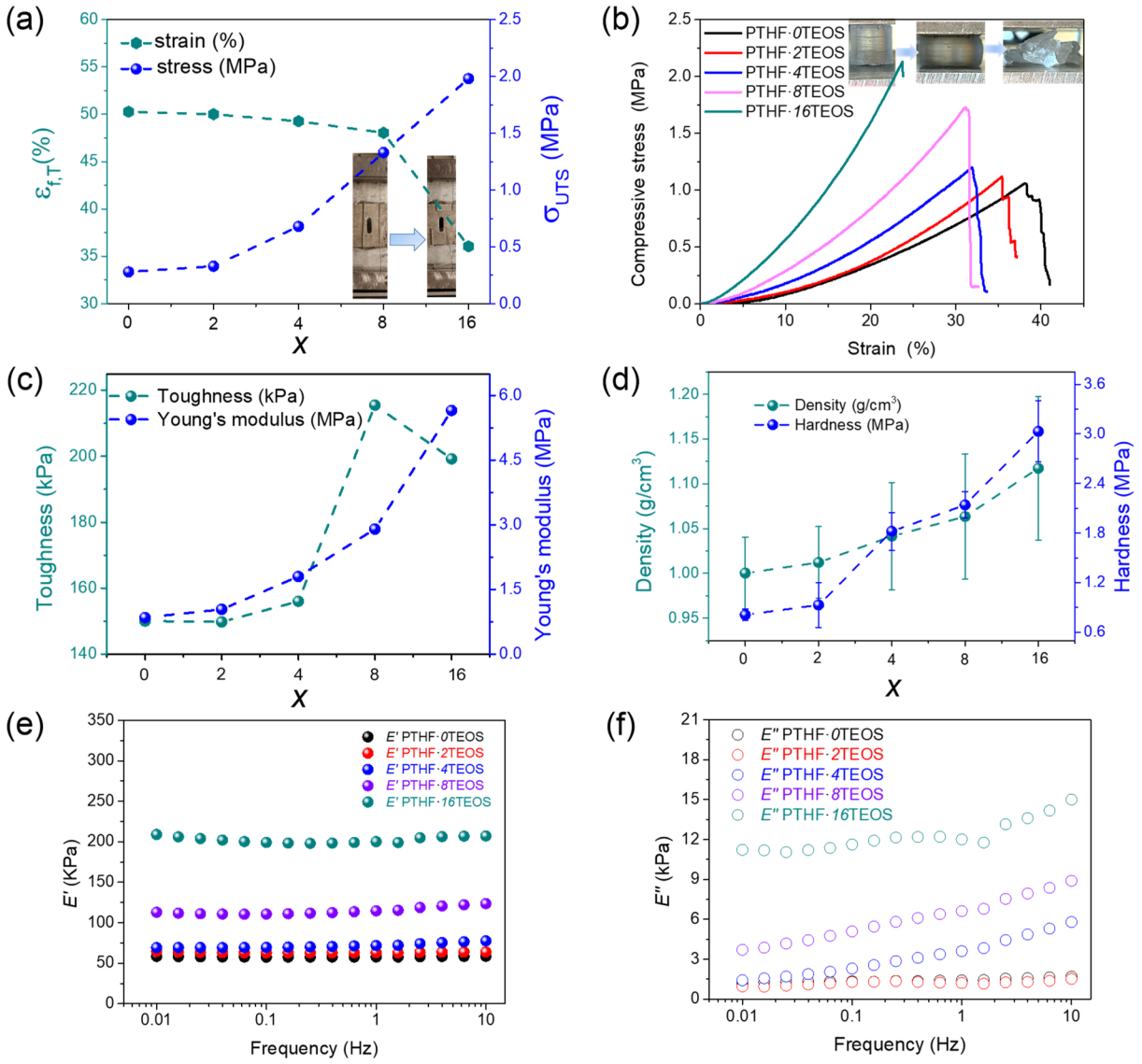

Figure 3. Mechanical properties of PTHF·*x*TEOS hybrids with different I/O weight ratios. (a) Ultimate tensile strength (σ_{UTS}) and tensile strain at failure ($\varepsilon_{f,T}$) as obtained from uniaxial tensile measurement as a function of TEOS content. (b) Stress–strain curves from compression test. (c) Modulus of toughness and Young's modulus as a function of TEOS content. (d) Density and hardness from microindentation test as a function of TEOS content. (e) Storage modulus (E') and (f) loss modulus (E'') as a function of frequency.

content. Moreover, we find a well-pronounced increase in the FWHM (full width at half-maximum) of both resonance peaks of H_a and H_b with higher TEOS content. This behavior reveals pronounced noncovalent interactions among organic/organic and organic/inorganic phases, restricting the "free-rotation" of methylene C–C bonds, and therefore leads to broader peaks related to these two methylene hydrogen atoms.

The variations in the protons' chemical shifts with hybrid composition could be attributed to (i) higher TEOS content, resulting in higher degree of cross-linking of the silica subnetwork; (ii) organic PTHF becomes more entangled within the silica subnetwork; (iii) intermolecular H-bonding between silanols and H-nuclei becomes more pronounced; and/or (iv) H-nuclei become more deshielded, having lower electron density. In other words, the peaks are shifted to lower fields based on how dense the network is, *i.e.*, how much TEOS has been added.

Based on the apparent flexibility of the samples observed during their handling (see step 4 in Figure 1b), we expect the hybrids to be able to undergo significant permanent deformation without fracturing. To quantify such mechanical properties of the hybrids, we have performed systematic studies of the influence of I/O ratio on the mechanical performances. Uniaxial tensile tests performed on rectangular specimens are compared in Figure 3a, with the extent of ultimate strain decreasing from 50.0% to 35.2% with the increase of the inorganic content in the hybrid from 5.1% to 20.9%. Simultaneously, the failure strength increases from 0.32 to 1.35 MPa. Thus, the hybrids with a higher content of inorganic silica exhibit less flexibility and elastomeric deformation behavior.

Stress–strain curves from uniaxial compression tests on cylindrical monolith bulk PTHF·*x*TEOS hybrids are shown in Figure 3b. A larger polymer content in the hybrids results in larger deformation and a lower level of ultimate stress, showing that such hybrids are more ductile compared with the inorganic-rich hybrids. The hybrid PTHF·0TEOS can be compressed to 38.3% of its original height at a stress of 1.06

https://doi.org/10.1021/acsnano.2c03440
ACS Nano XXXX, XXX, XXX–XXX

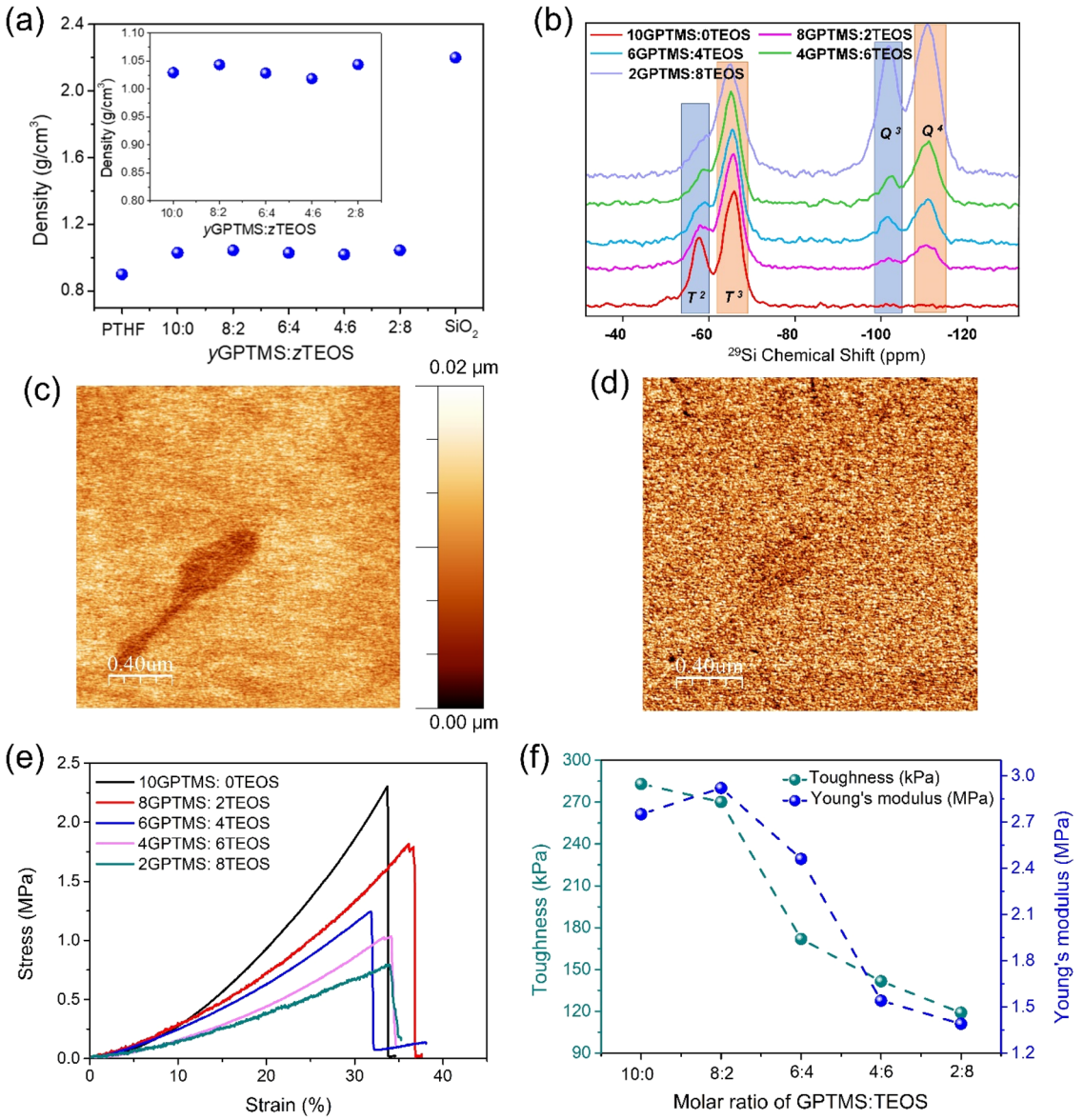

Figure 4. (a) Composition dependence of density of *y*GPTMS:*z*TEOS hybrids, pure PTHF, and pure silica glass. (b) Solid-state ^{29}Si CPMAS NMR spectra of *y*GPTMS:*z*TEOS hybrids. (c) Height and (d) phase AFM images of the 2GPTMS:8TEOS hybrid. (e) Stress−strain curves of *y*GPTMS:*z*TEOS hybrids from compression test. (f) Composition dependence of modulus of toughness and Young's modulus for *y*GPTMS:*z*TEOS hybrids.

MPa and then fractures, while PTHF·16TEOS ruptures at 23.7% of its original height at a stress of 2.14 MPa under the same loading conditions. The compression processes are illustrated in the insets of Figure 3b.

Achieving a good balance between strength and toughness is a major challenge. As seen from Figure 3a,b, with the increase of TEOS content, the failure strain of hybrids decreases while the strength increases. However, in order to function as tissue scaffolds and accommodate cyclic loading, hybrids with both desirable strength and toughness are required. We here achieve such balance in the PTHF·8TEOS hybrid, which not only reveals desirable elongation (31% for compression) and good flexibility but also high strength at 1.75 MPa. It also features the highest compressive toughness as can be seen in Figure 3c. At higher TEOS content, the elongation and toughness sharply drop. Such balancing of strength and toughness by controlling the I/O weight ratios is achieved through size of the inorganic nanoparticles, intermolecular interactions, and chain frictions.

We have further evaluated the modulus of toughness (U) and Young's modulus (E) through the area under the compression stress−strain curves and the slopes of the initial linear elastic portion of the stress−strain curve in Figure 3b, respectively.[47] The results are summarized in Figure 3c, showing that U and E are positively correlated to the SiO_2 content in the hybrids. For the hybrid PTHF·0TEOS, U and E are 150.0 kPa and 0.85 MPa, respectively, while they are 199.2 kPa and 5.65 MPa, respectively, for hybrid PTHF·16TEOS. Considering the five hybrids in the PTHF·*x*TEOS series, PTHF·8TEOS reveals the highest U of 219 kPa, again highlighting the good mechanical properties of this material.

Such balance of strength and toughness through controlling the I/O weight ratio of hybrid materials could guide further materials designing. As to the improvement in mechanical

https://doi.org/10.1021/acsnano.2c03440
ACS Nano XXXX, XXX, XXX−XXX

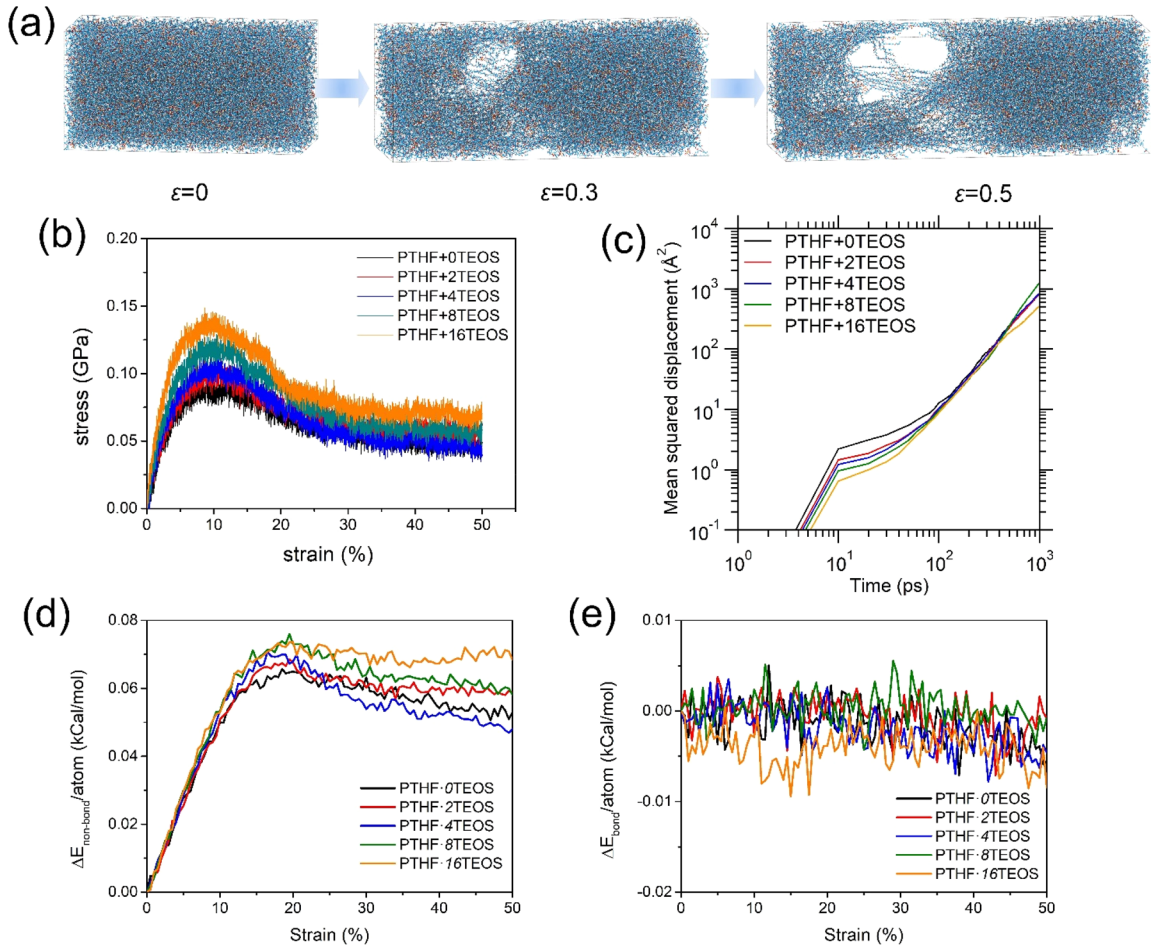

Figure 5. (a) Simulated fracture evolutions of PTHF·8TEOS hybrids by means of CVFF potential under the elongation at the strains of ε = 0, 0.3, and 0.5. The simulation box has dimensions of around 200 × 100 × 100 Å. (b) Simulated stress−strain curves of PTHF·*x*TEOS-based hybrids. (c) Time-dependence of the mean squared displacement of Si atoms in PTHF·*x*TEOS-based hybrids during the tensile process. Variation in the simulated potential energy of PTHF·*x*TEOS hybrids as a function of the applied strain, as decomposed into (d) nonbonded and (f) bonded energy.

properties, it can be explained by the formation of more cross-linked $-SiO_2-$ units as the I/O ratio increases. The hybrids show less elongation at fracture but at a higher stress, transforming from a rubber-like (polymer dominated) to a glass-like state (silica dominated). These changes in mechanical performance are supported by the ^{29}Si CPMAS NMR results (Figure 2d), showing that the silica subnetwork becomes more cross-linked and condensed with the increase of TEOS content, resulting in higher stress needed for deformation. The density (ρ) of the hybrids also increases with the addition of more silica, namely from 1.00 g/cm^3 for hybrid PTHF·0TEOS to 1.12 g/cm^3 for hybrid PTHF·16TEOS, *i.e.*, an increase of 12% (Figure 3d). Vickers microhardness (H_V) also increases with higher silica content from 0.8 MPa for PTHF·0TEOS to 3.0 MPa for PTHF·16TEOS (Figure 3d).

In order to investigate the dependence of I/O weight ratio on the hybrids' viscoelastic properties, dynamic mechanical analysis (DMA) measurements were performed.[48] The results of sweep frequency show that the storage modulus (E') (Figure 3e) of the five hybrids is 15 to 30 times higher than the corresponding loss modulus (E'') (Figure 3f), confirming the formation of elastic solid hybrids.[25,49] We also note that no significant changes in E' and E'' values could be observed in any of the hybrids over the tested frequency range (0.01−10 Hz), indicating a rubber plateau like behavior and cross-linked structures of the hybrid networks.[50] The values of tan (δ) equal to E''/E' are ≤0.06 for all five hybrids at 1 Hz (Figure S7), representing elastic properties of the hybrid materials.

Experimentally Produced Hybrids with Different Silica Size. To investigate the role of the silica domain size on the mechanical properties, we have prepared PTHF-based hybrids with different molar ratios of GPTMS to TEOS. GPTMS as the coupling agent is the only bridge to link PTHF polymer chains and hydrolyze TEOS, and therefore, the [GPTMS]/[TEOS] ratio controls the size of silica particles in the system. Namely, for a constant total I/O ratio, fewer but larger silica nanoparticles are obtained as [GPTMS]/[TEOS] decreases and *vice versa*.

TGA measurements are performed to determine the final I/O weight ratio of *y*GPTMS:*z*TEOS (10:0, 8:2, 6:4, 4:6, 2:8) hybrids, as shown in Figure S8. The results confirm very similar I/O values for the five hybrids. The density data of the *y*GPTMS:*z*TEOS hybrids are shown in Figure 4a, which also show limited variation. Thus, the size of silica particles has only a minor impact on density compared to the variation in the total I/O ratios (Figure 3d). The molecular structures of the *y*GPTMS:*z*TEOS hybrids are probed by FT-IR spectroscopy

https://doi.org/10.1021/acsnano.2c03440
ACS Nano XXXX, XXX, XXX−XXX

(Figure S9). Typical signals of these five *y*GPTMS:*z*TEOS hybrids for Si−O (at 490 and 1090 cm^{-1}) and C−O (at 1365 cm^{-1}) are observed due to their similar chemical compositions. ^{29}Si CPMAS NMR spectroscopy is also performed on these samples to confirm the silica structures (Figure 4b). For the 10GPTMS·0TEOS hybrid, *Q*-type silane signals are not observed at any significant fraction, while T^3-type structure is dominant, since no TEOS exists in this hybrid. With the increase in content of TEOS, the intensity of the *Q*-type signals increases, indicating that the silica network becomes more cross-linked. AFM height and phase images of hybrid 2GPTMS:8TEOS are shown in parts c and d, respectively, of Figure 4, revealing the uniformity of the two phases and surface morphology of the sample at the nanoscale. All hybrids in this series are also fully X-ray amorphous as expected (Figure S10), since they also undergo sol−gel condensation process.

To confirm that we can control the size of silica particles, SEM and EDX studies have been conducted as shown in Figure S11. As observed, the representative size of single silica NPs (not their aggregates) in hybrid 2GPTMS:8TEOS and 4GPTMS:6TEOS reaches 300−400 nm, while those in hybrid 6GPTMS:4TEOS and 8GPTMS:2TEOS are around 100 nm. For the hybrid 10GPTMS:0TEOS, the silica NPs are much smaller and uniformly dispersed in the material.

As to the mechanical properties, we first consider the results of the compression tests. As shown in Figure 4e, the stress at failure of the hybrids decreases with the decrease of GPTMS, for example, 2.34 MPa for 10GPTMS:0TEOS and 0.75 MPa for 2GPTMS:8TEOS. On the other hand, the conventional strain to failure features only minor differences (within the range of 32−37%). Toughness and Young's modulus, as calculated from these stress−strain curves, follow the same trend as stress with the change in composition (Figure 4f). Thus, stress at failure, toughness, and Young's modulus highly depend on the size of the silica nanoparticles in the hybrid, while the deformation ability (ultimate strain) appears to be largely related to the polymer content. Smaller silica nanoparticles give rise to more uniform dispersion in the system, which increases the possibility of sufficient intermolecular interactions between Si−O bond in the inorganic network and C−O−C bond of polymer chains. In this way, stronger hybrids can be obtained for much smaller silica nanoparticles in the system, while hybrids with more ductile deformation can be obtained for higher polymer content. Such strategy involving control on both inorganic *vs* organic weight ratios and NP sizes reveal improved properties with breakage strain of 34% and stress of 2.32 MPa. This is an improvement compared to previous work on similar compositions, exhibiting breakage strain and stress of 26% and 1.24 MPa, respectively.[27]

MD Simulation and Predicting. The above experimental results were combined with MD simulations to better understand the deformation and fracture mechanisms of the hybrids. We focused on hybrids with different I/O ratio (PTHF·*x*TEOS series) from the experiments, as they exhibited a good balance of strength and toughness. The simulations are done using a classical Consistent Valence Force-Field (CVFF) potential (see the Methods in the Supporting Information). As shown in Figure 5a, the simulated PTHF·8TEOS hybrid with a good strength-toughness balance in experiments exhibits a fairly ductile response upon deformation at the nanoscale, which manifests itself by the continuous stretching and disentanglement of the polymer chain from the matrix upon tension. The basic structural units of hybrids with different I/O ratios are depicted in Figure S12, and the corresponding fracture simulations of the different hybrids are shown in Figure S13.

As the utilized CVFF potential does not allow for explicit bond-breaking processes, we have validated this approach through a similar tensile fracture simulation of the PTHF·8TEOS hybrid using a reactive (ReaxFF) potential, which accounts for bond-breakage and bond-formation processes. Overall, this reactive simulation confirms the tensile simulation of the CVFF simulation (see Figure S14). In detail, due to the higher computational cost of the ReaxFF simulation, we have reduced the simulated system size by 20% compared to that of CVFF; *i.e.*, it consists of 20 structural units. Interestingly, despite the reactive nature of ReaxFF, the structural units of the hybrids persist during the tensile process, indicating that the failure of the hybrids is indeed attributed to the disentanglement of the polymer chains rather than their breakage (see Figure S14a). When comparing the stress−strain responses based on these two types of simulation potentials, we find that both predict the nanoductile features of the hybrids. Additionally, good agreement between the predicted maximum stress and corresponding strain by the two potentials is observed (Figure S14). Therefore, we adopt the CVFF potential for the following simulations as it allows for larger system size and longer time scales.

To further understand the effect of the I/O ratio on mechanical properties and also investigate the role of the polymer repeating unit, we include comparison of PTHF·*x*TEOS and PTHP·*x*TEOS hybrid series in the MD simulations. Peaks in the simulated pair distribution functions of the PTHF−SiO_2 and PTHP−SiO_2 hybrids at intramolecular−atomic distances of 0.95, 1.10, 1.45, 1.53, and 1.60 Å are attributed to the O−H, C−H, C−O, C−C, and Si−O pairs, respectively, corresponding to those of covalent bonds (Figure S15). Therefore, the short-range structures (first coordination shell) of the different hybrids are fairly similar. The simulated stress−strain curves of PTHF·*x*TEOS and PTHP·*x*TEOS hybrid series are presented in Figure 5b and Figure S17, respectively. We observe that all of the hybrids exhibit a ductile response upon tension at the nanoscale, which is attributed to the high covalent bond strengths and possibility for structural rearrangements. The maximum stress increases with an increase in the content of the SiO_2 nanoparticles for both PTHF·*x*TEOS (Figure 5b) and PTHP·*x*TEOS (Figure S17) hybrids, which echoes the experimental observations of SiO_2 strengthening shown in Figure 3b. Interestingly, the strain at the maximum stress (yield stress) is constantly around 10% for all samples. As shown in Figures 5c and S16, the averaged mean squared displacement of Si atoms decreases at the early stage of tension (*i.e.*, for strain <20%) with an increase of the TEOS amount, indicating that the hybrids are more rigid when they are constructed as higher SiO_2 content. We also notice that the evolution of potential energy terms (*i.e.*, bonded term and nonbonded term) exhibit different trends upon tension (see Figures 5d,e and S18). That is, the nonbonded term consisting of van der Waals and Coulombic terms exhibits much larger changes compared to the bonded term, which further confirms that the deformation and fracture of the hybrids is controlled by the intermolecular interaction, *i.e.*, the slippage and disentanglement of the polymer chains. The strengthening mechanism can be attributed to the fact that the

https://doi.org/10.1021/acsnano.2c03440
ACS Nano XXXX, XXX, XXX−XXX

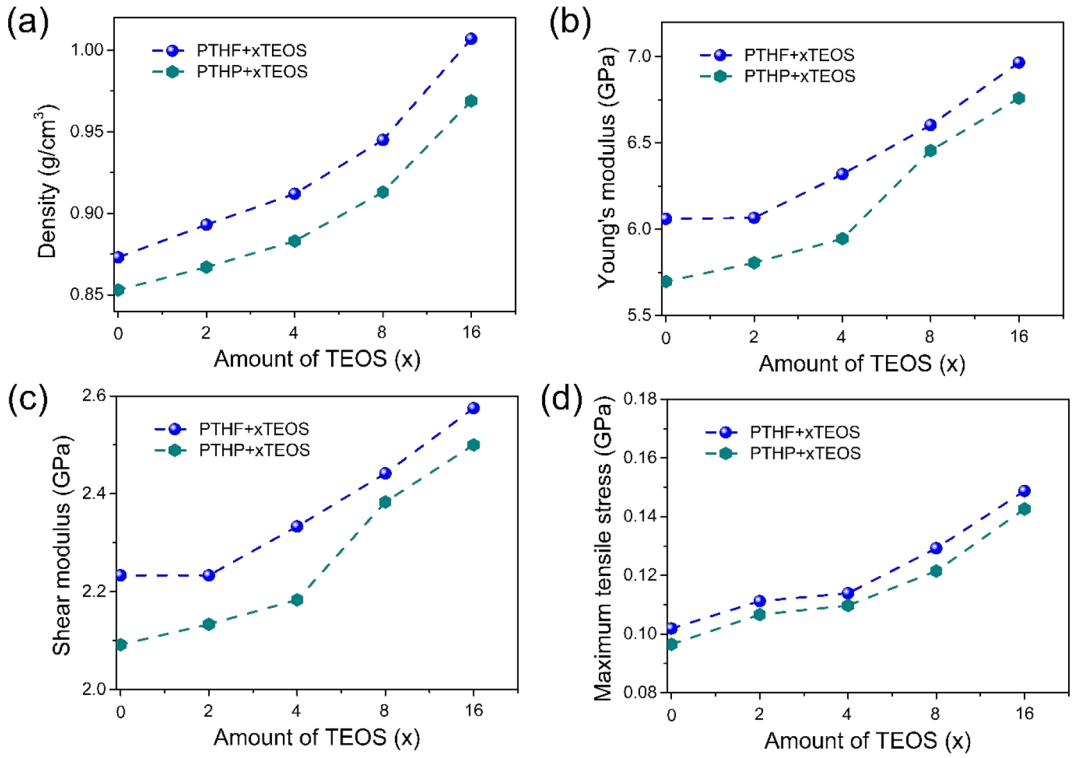

Figure 6. Composition dependence of simulated (a) density, (b) Young's modulus, (c) shear modulus, and (d) maximum tensile stress for PTHF·*x*TEOS and PTHP·*x*TEOS series of hybrids.

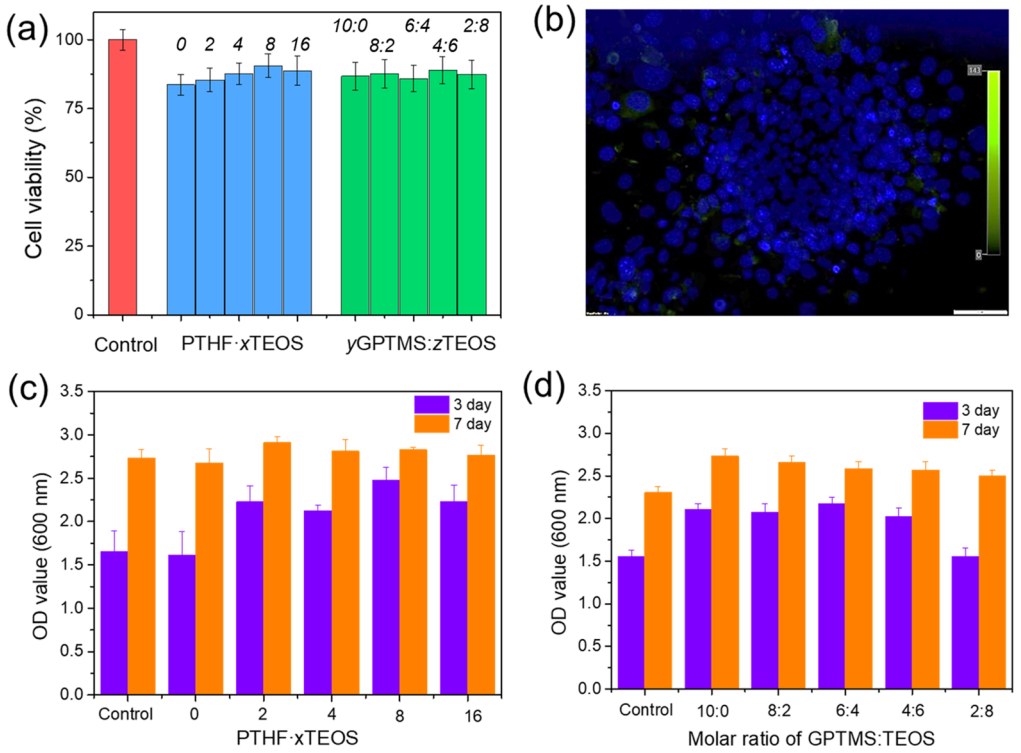

Figure 7. (a) Assessment of cell viability of hybrids by ToX8 metabolic activity assay following ISO 10993 standards. (b) Immunohistochemical staining of the nuclei of MC3T3-E1 cells cultured on PTHF·8TEOS hybrid. (c, d) Cell proliferation of MC3T3-E1 cells on (c) PTHF·*x*TEOS and (d) *y*GPTMS:*z*TEOS hybrids after culturing for 3 and 7 days.

existence of SiO_2 nanoparticles in the hybrids can effectively block the motion of polymer chains upon deformation.

The effects of TEOS content (*i.e.*, I/O ratio) for the two different repeating unit of polymer chains (PTHF *vs* PTHP) on the mechanical properties of the simulated hybrids are summarized in Figure 6. As shown in Figure 6a, density increases with an increase in the TEOS amount for both hybrid series, but the density of the PTHF·*x*TEOS hybrid series is

https://doi.org/10.1021/acsnano.2c03440
ACS Nano XXXX, XXX, XXX−XXX

always higher than that of the PTHP·xTEOS for each value of x. That is, density decreases with the ratio of C−O− to C−C bonds. This trend agrees well with the experimental results shown in Figure 3d. The simulated Young's modulus, shear modulus, and maximum (yield) strength also exhibit the same trend as the experimental results (see Figure 6b−d), indicating the transition from rubber-like to glass-like behavior with increasing size and fraction of SiO_2. Despite reproducing the qualitative trends, we also note that the simulated strength and modulus values are systematically higher than the experimental ones, which can be attributed to the following reasons: (i) the polymer chain lengths in the experimental samples exhibit a broad distribution, but they are simplified as a monodispersed length in the simulations; (ii) defects exist in the experimental specimens, while the simulated structures are ideally flawless; and (iii) the strain rate in the loading simulation is much higher than that in the experiments. In the meantime, it is noted that the mechanical performances of both Young's modulus and tensile strength for the PTHF−SiO_2 hybrid are better than those for the PTHP−SiO_2 hybrid. This can be attributed to the improved intermolecular interactions of PTHF−SiO_2 relative to PTHP−SiO_2 due to the higher amount of the more polar C−O functional groups (with stronger dipole moments) relative to C−C groups. Moreover, the MD simulations also reveal that van der Waals interactions are found to be the main contribution of noncovalent interactions in the hybrids compared with Coulombic interactions (Figure S19). Given the comparable stress−strain curves obtained from CVFF and ReaxFF potentials, the simulated values are also in agreement with the existing literature data for similar systems.[33,35,51] Overall, the simulations thus confirm that the content of SiO_2 nanoparticles plays an important role in controlling the mechanical properties.

Biocompatibility and Cell Growth. In addition to showing promising mechanical properties for applications within bone regeneration and tissue repairing, such hybrid materials also need to exhibit cyto-compatibility for promoting osteogenic cell attachment.[8,13] First, we have investigated the cytotoxicity of the two experimental series of hybrids. Based on the ISO 10993 standard, the materials are considered noncytotoxic if the cell viability is higher than 70% compared with the blank.[14,52] As can be seen in Figure 7a for the PTHF·xTEOS (x increases from left to right) and yGPTMS:zTEOS (y:z decreases from left to right) experimentally produced hybrids, the cell viabilities are all above 70%, ranging from 83 to 90% compared with the control group, demonstrating the noncytotoxicity of these hybrids. They are thus promising candidates for further cell attachment, proliferation, and even *in vivo* studies. To this end, we next determined the bone cell (MC3T3-E1) attachment of the hybrid materials by immunohistochemistry and confocal microscopy measurements after culturing the cells for 72 h.[22,27] As seen from the DAPI nuclear counter staining method results in Figure 7b for the PTHF·8TEOS hybrid, cells are well attached on the material, demonstrating biocompatibility of hybrids and potential for growth of bone cells. Finally, we studied the cell proliferation possibility on the hybrids *via* the ToX8 method. Bone cells cultured on PTHF·xTEOS and yGPTMS:zTEOS hybrids are compared with control groups in Figure 7c,d, respectively, by determining optical density (OD) values.[53] The cells seem to have better growth on hybrids relative to the control, demonstrating that these biocompatible hybrids possess excellent performance for promoting MC3T3-E1 cell growth. This could be because the silica networks can offer enhanced cell recognition sites and further improve the cell attachment and growth.[27] After culturing for 3 days, the cell number increases in samples with higher content of inorganic component, which might be because the uniform dispersion of inorganic−organic phases and adequate cross-linking networks help promote cell proliferation. Thus, based on these results, the PTHF-SiO_2 based hybrids reveal the necessary mechanical and biomedical properties for acting as desirable bone repair scaffolds.

CONCLUSIONS

Based on the experiments and MD simulations performed in this study, noncovalent intermolecular interactions are found to play an important role in controlling the deformation and fracture of inorganic−polymer hybrid materials. By decreasing the silica nanoparticle size and increasing the fraction of C−O bonds in polymer chains, the interactions between polymer chains and silica networks can be enhanced. Importantly, by further controlling the total I/O ratio the important balance of the toughness and strength can be tailored. Namely, the hybrid PTHF·8TEOS achieves a balance between these otherwise conflicting performances, showing 31% of compressive deformation, 1.75 MPa of stress at breakage, and 219 kPa of toughness. Moreover, the prepared hybrids all show non-cytotoxicity and the ability to support cell attachment as well as cell proliferation in the *in vitro* studies. These insights suggest the potential use of especially the PTHF·8TEOS hybrid material for engineering applications such as tissue scaffolds and soft robotics.

EXPERIMENTAL METHODS

Materials. Tetrahydropyfuran (THF), (3-glycidoxypropyl) trimethoxysilane (GPTMS), boron trifluoride-diethyl ether (BF_3·OEt_2), tetraethyl orthosilicate (TEOS), acetic acid glacial ≥99.7%, and HCl (36 wt %) were all purchased from Sigma-Aldrich and used as received. Cell culture reagents were purchased from Invitrogen and Sigma-Aldrich UK. The MC3T3-E1 preosteoblast cell line (ATCC, UK) was cultured in basal α-MEM supplemented with 10% (v/v) FCS (fetal calf serum) and 1% (v/v) penicillin. Cultures were maintained in a humidified atmosphere at 37 °C, 5% CO_2, and 21% O_2. Cells were passaged upon confluence using 500 μg/mL trypsin-EDTA (ethylene diamine tetraacetic acid).

Synthesis of Inorganic sol. SiO_2 was prepared *via* hydrolysis process. TEOS, deionized water, and 36 wt % hydrochloric acid (12 M HCl) were mixed with a molar ratio of 1:3.6:0.01. The completion of the reaction was confirmed when the mixture turned from cloudy to clear.

Synthesis of Hybrids. The organic precursors were prepared based on an established procedure using HAc as a terminator[15] and then mixed with the inorganic sols based on the precalculated THF, GPTMS, and TEOS compositions. The mixtures were transferred into polytetrafluoroethylene molds and sealed for aging for 1 week at 40 °C. Afterward, the lids were removed gradually to allow drying for the following 3 weeks at the same temperature. Finally, disc-shaped samples were recovered from the molds and used for characterization. All samples were immersed in distilled water for 5 min and followed by filtration to remove any unreacted monomers and water-soluble byproducts.

Structure Characterization. Fourier-transform infrared (FT-IR) spectroscopy was performed to determine the functional groups in the inorganic bulk samples as well as the final hybrids by using a Bruker TENSOR II spectrometer with a Bruker Platinum attenuated total reflectance attachment in the range of 4000 to 400 cm^{-1}. All spectra

https://doi.org/10.1021/acsnano.2c03440
ACS Nano XXXX, XXX, XXX−XXX

were compiled from 64 consecutive scans and were baseline corrected using the vendor-supplied software OPUS.

To determine the final inorganic *vs* organic (I/O) weight ratio in the hybrids, thermal gravimetric analysis (TGA) was performed on a STA 449C (Netzsch) instrument. The hybrid samples were cut into small pieces and heated under a flow of air at the rate of 10 °C min^{-1}, from room temperature to 800 °C. The recorded weight loss could be ascribed to the combustion of the organic phase. The silica nanoparticles' size and element distribution in the hybrids were tested by scanning electron microscopy (SEM) using a Zeiss Gemini SEM 500 instrument at 5 kV/10 μA.

To confirm the noncrystalline structure of the hybrid materials, X-ray diffraction (XRD) analysis was carried out on pulverized samples at 2θ angles from 5° to 80° using a Panalytical Empyrean diffractometer with Cu−Kα-1 radiation source and Ni-filter.

Atomic force microscopy (AFM) measurements were carried out to determine surface morphology and phase images of hybrids. The measurements were performed with an NTEGRA Aura AFM (NT-MDT, Russia) instrument, operating in tapping mode using HA_HR (ScanSens, Germany) cantilevers.

^{29}Si magic-angle spinning (MAS) NMR was conducted to confirm the silica structures in the hybrid materials. The data were collected with an Agilent DD2 spectrometer in conjunction with an Oxford 4.7 T widebore superconducting magnet with a ^{29}Si resonance frequency of 39.70 MHz. Samples were powdered and loaded into 5 mm zirconia rotors with sample spinning of 5.0 kHz. Spectra were acquired using a $\pi/6$ tip angle of 2.7 μs, a recycle delay of 180 s, averaging of 400−1900 scans, and with high-power ^{1}H decoupling during signal acquisition. ^{1}H → ^{29}Si cross-polarization magic-angle spinning (CPMAS) NMR measurements were made on the same instrument with a contact time of 3 ms between the spins, recycle delay of 5 s, and signal averaging of 40000−80000 scans. All ^{29}Si NMR data were processed with 25 Hz apodization, referenced to tetramethylsilane (TMS) at 0.0 ppm, using the GRAMS Spectroscopy Software Suite (Thermo Fisher Scientific) to plot and fit the spectra. ^{13}C MAS NMR measurements were made at 47 T (50.25 MHz resonance frequency) using an Agilent DD2 spectrometer and Oxford wide-bore superconducting magnet. Powdered samples were packed into 5 mm zirconia rotors, with sample spinning of 7.0 kHz. ^{1}H-decoupled ^{13}C MAS NMR data were acquired by the combination of a $\pi/6$ tip angle (2.0 μs), with a delay of 60 s between scans and signal averaging of 1000 to 2000 scans. ^{13}C NMR data were processed with 10 Hz line broadening and referenced to TMS at 0.0 ppm. Plotting and spectral analyses were done in the GRAMS software package. ^{1}H MAS NMR data were collected at 4.7T (199.82 MHz resonance frequency) using a 5 mm MAS NMR probe and a background suppression pulse sequence. A calibrated $\pi/2$ pulse width of 4 μs was immediately follow by two π pulses (8.0 μs each), and 64 acquisitions were made using a 5s recycle delay. ^{1}H MAS NMR data were referenced to TMS at 0.0 ppm and processed without any additional line broadening.

Property Characterization. Density measurements on the hybrid samples were conducted through the Archimedes principle using the following equation:

$$\rho_{sample} = \frac{\rho_{ethanol} \times m_{sample}^{air}}{m_{sample}^{air} - m_{sample}^{ethanol}} \quad (1)$$

Here,$\rho_{ethanol}$ is the density of absolute ethanol, m_{sample}^{air} is the weight of sample in air, and $m_{sample}^{ethanol}$ is the weight of the sample upon immersion in ethanol.

Compression tests were performed using a Zwick Z100 universal testing machine equipped with a 100 kN load cell at room temperature. Samples were punched into cylinders with a diameter of 10 mm and a length of 5 mm. The crosshead speed was set to 1 mm min^{-1}. Tensile tests were performed using a Linkam TST350 tensile testing stage equipped with a 200 N load cell at room temperature. For these measurements, the hybrid samples were cut into rectangular shapes with a length of 30 mm, a width of 10 mm, and a thickness of 2 mm, and the crosshead speed was set to 2 mm min^{-1}. Modulus of toughness (U) and Young's modulus (E) were evaluated through the area under the stress−strain curves and the slopes of the initial linear elastic portion of the stress−strain curve, respectively. Finally, dynamic mechanical analysis (DMA) was carried out using TA Instruments DMA 850. The experiments were performed in compression mode with an amplitude of 20 μm, with the frequency varied in the range from 0.01 to 10 Hz at room temperature.

Microindentation measurements were performed using a Nanovea CB500 hardness tester to determine the hardness (H). Vickers indentations with a maximum load of 0.02 N were generated to determine H, with a loading duration and dwell time of both 10 s. The loading and unloading rate were both 0.2 N min^{-1}. Measurements were performed under laboratory conditions (temperature: 23 °C; relative humidity: ∼36%). Then hardness was calculated from the force−displacement curves using the Oliver−Pharr model.[54,55]

Cytotoxicity Test. *In vitro* cytotoxicity of the hybrids was evaluated based on the ISO 10993 standard. Hybrids were immersed in α-MEM (0.2 g/mL) and stored in n incubator for over 72 h. The extract liquid was filter sterilized and supplemented with 10% (v/v) FBS prior to use in further tests. MC3T3-E1 cells were first cultured with basel α-MEM media and seeded on 96-well plate at 10^4 cells per well, and then left to grow in incubator for 24 h. Afterward, the media was removed and incubated with α-MEM media (control group) and extracts of hybrids for another 24 h. The media was then removed and replaced with ToX-8 dilution in α-MEM media and incubated for another 4 h. The cell viability and optical denstity (OD) are measured by the ToX8 method according to the manufacturer's instructions. The OD was measured spectrophotometrically at 600 and 690 nm using a microplate reader. The relative cell viability (%) was calculated as follows:

$$\text{cell viability}(\%) = \frac{[A]\text{test}}{[A]\text{control}} \times 100$$

Cell Proliferation. The hybrids were all sterilized with EtOH for over 30 min and washed three times with PBS solution. Then the hybrids were immersed in PBS solution and put under UV light overnight. After pretreatment, the cells were cultured on 24-well plates and hybrids with basel α-MEM media at 5000 cells per well. The media was changed every second day. After 3 and 7 days of incubation, media was removed and replaced with ToX-8 dilution in α-MEM media and incubated for another 4 h. The optical density was measured spectrophotometrically at 600 and 690 nm using a microplate reader.

MD Simulations. To understand the atomistic deformation and fracture mechanisms of the hybrid samples, MD simulations were carried out. All of the simulations were performed using LAMMPS software with the GPU-accelerated package, and visualization of the atomic snapshots was done using the OVITO package. During the simulation, periodic boundary conditions were applied in all directions. The atomic interactions of hybrids were described using the classical Consistent Valence Force-Field (CVFF) potential.[56] For comparison and validation, we also applied the reactive force field (ReaxFF)[57] at a smaller system size (fewer number of total atoms) to simulate the mechanical response. These two force fields have been widely applied in simulating structure and mechanical properties of polymers and inorganic materials.[58,59] The motion of atoms was integrated using the velocity-Verlet algorithm with a time step of 0.5 fs.

First, we prepared the basic unit of the hybrids, *i.e.*, one polymer chain linked to a SiO_2 nanoparticle through GPTMS. To enable qualitative comparison with the experiments, we selected THF and THP as the monomer unit (MU) to vary the chain length. Each polymer chain consisted of 56 MUs. The SiO_2-to-polymer molar ratio was set to 0, 2, 4, 8, and 16, respectively, corresponding to a growing size of the SiO_2 nanoparticle. Note that each basic unit of the hybrids consisted of >700 atoms (Figure S12). We then randomly placed 100 basic units (20 basic units for the ReaxFF system, which is more computationally expensive) into a cubic box using the PACKMOL package.[7] These systems were compressed into a densified matrix

https://doi.org/10.1021/acsnano.2c03440
ACS Nano XXXX, XXX, XXX−XXX

under *NPT* ensemble at 300 K and 1 GPa for 200 ps, which yielded a density close to the experimental value. Afterward, the system was equilibrated at 500 K in the *NVT* ensemble for 100 ps, and gradually cooled to 300 K at a cooling rate of 0.2 K ps^{-1} in the *NPT* ensemble at zero pressure. The resulting configurations were subsequently relaxed at 300 K for 120 ps to ensure the convergence of density and potential energy. The structure of hybrids was characterized using pair distribution function, describing the probability of a pair of atoms at a given distance.

The elastic properties of the hybrids were determined by stepwise deforming the atomic hybrid models for a strain step of 0.0005. This was applied for both uniaxial and shear deformation. After each deformation step, the structure was subjected to an energy minimization and the corresponding pressure in the deformation direction was extracted. Then the stiffness matrix was obtained through the slope of the linear part of the stress−strain curve. Based on the stiffness matrix, Young's modulus and shear modulus were determined as described elsewhere.[60] The deformation and fracture behavior of the hybrid systems were investigated through uniaxial tensile simulation. To this end, we first duplicated the orthorhombic configuration in the *x*-direction so that the deformation was applied to the longest direction. Before deformation, the resulting structures were dynamically equilibrated in the *NPT* ensemble at 300 K and zero pressure for 100 ps to remove internal stresses. Then a constant strain rate of 5×10^{10} s^{-1} was applied along the *x*-direction, while the system was maintained at 300 K in the *NVT* ensemble. During the deformation, all of the atoms were forced to move in an affine transformation way; *i.e.*, the coordinates of the atoms were scaled along with box deformation. The stress component in the *x*-direction and corresponding strain were recorded to construct the stress−strain curve until the system reached a maximum strain of 50%. During the tensile process, the motion of Si atoms in the hybrids was studied by calculating the mean squared displacement (MSD) of each Si atom

$$\mathrm{MSD}_i(t) = \Delta r_i^2(t) = \langle |r_i(t+\tau) - r_i(\tau)|^2 \rangle \quad (2)$$

where $r_i(t)$ is the position of the *i*th atom at time *t* and the brackets represent the averaging over multiple time origins (τ).

ASSOCIATED CONTENT

Supporting Information

The Supporting Information is available free of charge at https://pubs.acs.org/doi/10.1021/acsnano.2c03440.

Details of characterization, illustration of chemical structures, additional experimental results, additional characterization of silica NPs, compositions of the basic units of hybrids in MD simulation (PDF)

AUTHOR INFORMATION

Corresponding Authors

Donghong Yu − *Department of Chemistry and Bioscience, Aalborg University, 9220 Aalborg, Denmark;* orcid.org/0000-0002-3035-5035; Email: yu@bio.aau.dk

Morten M. Smedskjaer − *Department of Chemistry and Bioscience, Aalborg University, 9220 Aalborg, Denmark;* orcid.org/0000-0003-0476-2021; Email: mos@bio.aau.dk

Authors

Wei Fan − *Department of Chemistry and Bioscience, Aalborg University, 9220 Aalborg, Denmark*

Tao Du − *Department of Chemistry and Bioscience, Aalborg University, 9220 Aalborg, Denmark*

Aida Droce − *Department of Chemistry and Bioscience, Aalborg University, 9220 Aalborg, Denmark*

Lars R. Jensen − *Department of Materials and Production, Aalborg University, 9220 Aalborg, Denmark*

Randall E. Youngman − *Science and Technology Division, Corning Incorporated, Corning, New York 14831, United States;* orcid.org/0000-0002-6647-9865

Xiangting Ren − *Department of Chemistry and Bioscience, Aalborg University, 9220 Aalborg, Denmark*

Leonid Gurevich − *Department of Materials and Production, Aalborg University, 9220 Aalborg, Denmark*

Mathieu Bauchy − *Department of Civil and Environmental Engineering, University of California, Los Angeles, California 90095, United States;* orcid.org/0000-0003-4600-0631

Peter Kristensen − *Department of Chemistry and Bioscience, Aalborg University, 9220 Aalborg, Denmark*

Bengang Xing − *Division of Chemistry and Biological Chemistry, School of Physical and Mathematical Sciences, Nanyang Technological University, Singapore 637371, Singapore;* orcid.org/0000-0002-8391-1234

Complete contact information is available at: https://pubs.acs.org/10.1021/acsnano.2c03440

Notes

The authors declare no competing financial interest.

ACKNOWLEDGMENTS

This work was supported by grants from the China Scholarship Council (CSC No. 201904910782) awarded to W.F. and the Marie Skłodowska-Curie Individual Fellowship under the European Union's Horizon 2020 Programme (No. 101018156) awarded to T.D. and M.M.S. We also thank Aalborg University for providing the computational resources through CLAAUDIA. M.B. acknowledges funding provided by the National Science Foundation under grants DMREF-1922167 and CMMI-1826420.

REFERENCES

(1) Ritchie, R. O. The conflicts between strength and toughness. *Nat. Mater.* **2011**, *10*, 817−822.

(2) Schamel, M.; Barralet, J. E.; Gelinsky, M.; Groll, J.; Gbureck, U. Intrinsic 3D Prestressing: A New Route for Increasing Strength and Improving Toughness of Hybrid Inorganic Biocements. *Adv. Mater.* **2017**, *29*, 1701035.

(3) Launey, M. E.; Ritchie, R. O. On the Fracture Toughness of Advanced Materials. *Adv. Mater.* **2009**, *21*, 2103.

(4) Shi, F. K.; Wang, X. P.; Guo, R. H.; Zhong, M.; Xie, X. M. Highly stretchable and super tough nanocomposite physical hydrogels facilitated by the coupling of intermolecular hydrogen bonds and analogous chemical crosslinking of nanoparticles. *J. Mater. Chem. B* **2015**, *3*, 1187−1192.

(5) Sun, J. Y.; Zhao, X.; Illeperuma, W. R.; Chaudhuri, O.; Oh, K. H.; Mooney, D. J.; Vlassak, J. J.; Suo, Z. Highly stretchable and tough hydrogels. *Nature* **2012**, *489*, 133−136.

(6) Li, X.; Wang, H.; Li, D.; Long, S.; Zhang, G.; Wu, Z. Dual Ionically Cross-linked Double-Network Hydrogels with High Strength, Toughness, Swelling Resistance, and Improved 3D Printing Processability. *ACS Appl. Mater. interfaces* **2018**, *10*, 31198−31207.

(7) Fan, W.; Jensen, L. R.; Ceccato, M.; Quaade, T. S.; Gurevich, L.; Yu, D.; Smedskjaer, M. M. Flexible inorganic-organic hybrids with dual inorganic components. *Mater. Today Chem.* **2021**, *22*, 100584.

(8) Zhao, W.; Jin, X.; Cong, Y.; Liu, Y.; Fu, J. Degradable natural polymer hydrogels for articular cartilage tissue engineering. *J. Chem. Technol. Biotechnol.* **2013**, *88*, 327−339.

(9) Setton, L. A.; Elliott, D. M.; Mow, V. C. Altered mechanics of cartilage with os5teoarthritis: human osteoarthritis and an experimental model of joint degeneration. *Osteoarthritis and cartilage* **1999**, *7*, 2−14.

(10) Hooper, J. B.; Schweizer, K. S. Theory of Phase Separation in Polymer Nanocomposites. *Macromolecules* **2006**, *39*, 5133−5142.
(11) Ogoshi, T.; Chujo, Y. Organic-inorganic polymer hybrids prepared by the sol-gel method. *Compos. Interfaces* **2005**, *11*, 539−566.
(12) Imai, Y.; Naka, K.; Chujo, Y. Reversible Formation of Interpenetrating Polymer Network Structure in Organic-Inorganic Polymer Hybrids. *Polym. J.* **1998**, *30*, 990−995.
(13) Arumugam, S.; Ju, Y. Carbon nanotubes reinforced with natural/synthetic polymers to mimic the extracellular matrices of bone - a review. *Mater. Today Chem.* **2021**, *20*, 100420.
(14) Chung, J. J.; Li, S.; Stevens, M. M.; Georgiou, T. K.; Jones, J. R. Tailoring Mechanical Properties of Sol-Gel Hybrids for Bone Regeneration through Polymer Structure. *Chem. Mater.* **2016**, *28*, 6127−6135.
(15) Zhao, X. Designing toughness and strength for soft materials. *Proc. Natl. Acad. Sci. U. S. A* **2017**, *114*, 8138−8140.
(16) Munch, E.; Launey, M. E.; Alsem, D. H.; Saiz, E.; Tomsia, A. P.; Ritchie, R. O. Tough, bio-inspired hybrid materials. *Science* **2008**, *322*, 1516−1520.
(17) Ravarian, R.; Zhong, X.; Barbeck, M.; Ghanaati, S.; Kirkpatrick, C. J.; Murphy, C. M.; Schindeler, A.; Chrzanowski, W.; Dehghani, F. Nanoscale Chemical Interaction Enhances the Physical Properties of Bioglass Composites. *ACS Nano* **2013**, *7*, 8469−8483.
(18) Fan, W.; Zhang, X.; Li, C. Functional fibrous compositions: Applications and perspectives. *Compos. Commun.* **2019**, *15*, 68−75.
(19) Norris, E.; Ramos-Rivera, C.; Poologasundarampillai, G.; Clark, J. P.; Ju, Q.; Obata, A.; Hanna, J. V.; Kasuga, T.; Mitchell, C. A.; Jell, G.; Jones, J. R. Electrospinning 3D bioactive glasses for wound healing. *Biomed. Mater.* **2020**, *15*, 015014.
(20) Zakir, M.; Ashraf, U.; Tian, T.; Han, A.; Qiao, W.; Jin, X.; Zhang, M.; Tsoi, J. K.-H.; Matinlinna, J. P. The Role of Silane Coupling Agents and Universal Primers in Durable Adhesion to Dental Restorative Materials - a Review. *Current Oral Health Reports* **2016**, *3*, 244−253.
(21) Macon, A. L. B.; Li, S.; Chung, J. J.; Nommeots-Nomm, A.; Solanki, A. K.; Stevens, M. M.; Jones, J. R. Ductile silica/methacrylate hybrids for bone regeneration. *J. Mater. Chem. B* **2016**, *4*, 6032−6042.
(22) Mahony, O.; Tsigkou, O.; Ionescu, C.; Minelli, C.; Ling, L.; Hanly, R.; Smith, M. E.; Stevens, M. M.; Jones, J. R. Silica-Gelatin Hybrids with Tailorable Degradation and Mechanical Properties for Tissue Regeneration. *Adv. Funct. Mater.* **2010**, *20*, 3835−3845.
(23) Lee, D. W.; Yoo, B. R. Advanced silica/polymer composites: Materials and applications. *J. Ind. Eng. Chem.* **2016**, *38*, 1−12.
(24) Shi, F. K.; Wang, X. P.; Guo, R. H.; Zhong, M.; Xie, X. M. Highly stretchable and super tough nanocomposite physical hydrogels facilitated by the coupling of intermolecular hydrogen bonds and analogous chemical crosslinking of nanoparticles. *J. Mater. Chem. B* **2015**, *3*, 1187−1192.
(25) Zhong, M.; Liu, X. Y.; Shi, F. K.; Zhang, L. Q.; Wang, X. P.; Cheetham, A. G.; Cui, H.; Xie, X. M. Self-healable, tough and highly stretchable ionic nanocomposite physical hydrogels. *Soft Matter* **2015**, *11*, 4235−4241.
(26) Gabrielli, L.; Connell, L.; Russo, L.; Jiménez-Barbero, J.; Nicotra, F.; Cipolla, L.; Jones, J. R. Exploring GPTMS reactivity against simple nucleophiles: chemistry beyond hybrid materials fabrication. *RSC Adv.* **2014**, *4*, 1841−1848.
(27) Tallia, F.; Russo, L.; Li, S.; Orrin, A. L. H.; Shi, X.; Chen, S.; Steele, J. A. M.; Meille, S.; Chevalier, J.; Lee, P. D.; Stevens, M. M.; Cipolla, L.; Jones, J. R. Bouncing and 3D printable hybrids with self-healing properties. *Mater. Horiz.* **2018**, *5*, 849−860.
(28) Fan, W.; Youngman, R. E.; Ren, X.; Yu, D.; Smedskjaer, M. M. Structural control of self-healing silica-poly(tetrahydropyran)-poly-(epsilon-caprolactone) hybrids. *J. Mater. Chem. B* **2021**, *9*, 4400−4410.
(29) Vidil, T.; Tournilhac, F.; Leibler, L. Control of cationic epoxy polymerization by supramolecular initiation. *Polym. Chem.* **2013**, *4*, 1323.
(30) Guo, R.; Jacob, K. I. Effect of chain length distribution on thermal characteristics of model polytetrahydrofuran (PTHF) networks. *Polymer* **2014**, *55*, 4468−4477.
(31) Nébouy, M.; de Almeida, A.; Brottet, S.; Baeza, G. P. Process-Oriented Structure Tuning of PBT/PTHF Thermoplastic Elastomers. *Macromolecules* **2018**, *51*, 6291−6302.
(32) Owens, G. J.; Singh, R. K.; Foroutan, F.; Alqaysi, M.; Han, C.-M.; Mahapatra, C.; Kim, H.-W.; Knowles, J. C. Sol-gel based materials for biomedical applications. *Prog. Mater. Sci.* **2016**, *77*, 1−79.
(33) Liu, C.; Ning, W.; Tam, L. H.; Yu, Z. Understanding fracture behavior of epoxy-based polymer using molecular dynamics simulation. *J. Mol. GraphicsModell.* **2020**, *101*, 107757.
(34) To, T.; Sorensen, S. S.; Christensen, J. F. S.; Christensen, R.; Jensen, L. R.; Bockowski, M.; Bauchy, M.; Smedskjaer, M. M. Bond Switching in Densified Oxide Glass Enables Record-High Fracture Toughness. *ACS Appl. Mater. interfaces* **2021**, *13*, 17753−17765.
(35) Krishna, S.; Patel, C. M. Computational and experimental study of mechanical properties of Nylon 6 nanocomposites reinforced with nanomilled cellulose. *Mech. Mater.* **2020**, *143*, 103318.
(36) Hench, L. L.; West, J. K. The sol-gel process. *Chem. Revi.* **1990**, *90*, 33−72.
(37) Kotz, F.; Schneider, N.; Striegel, A.; Wolfschlager, A.; Keller, N.; Worgull, M.; Bauer, W.; Schild, D.; Milich, M.; Greiner, C.; Helmer, D.; Rapp, B. E. Glassomer-Processing Fused Silica Glass Like a Polymer. *Adv. Mater.* **2018**, *30*, No. e1707100.
(38) Rubio, F.; Rubio, J.; Oteo, J. L. A FT-IR Study of the Hydrolysis of Tetraethylorthosilicate (TEOS). *Spectrosc. Lett.* **1998**, *31*, 199−219.
(39) Matos, M. C.; Ilharco, L. M.; Almeida, R. M. The evolution of TEOS to silica gel and glass by vibrational spectroscopy. *J. Non-Cryst. Solids* **1992**, *147−148*, 232−237.
(40) Li, H.; Tripp, C. P. Infrared study of the interaction of charged silica particles with TiO2 particles containing adsorbed cationic and anionic polyelectrolytes. *Langmuir* **2005**, *21*, 2585−2590.
(41) Du, J.; She, X.; Zhu, W.; Yang, Q.; Zhang, H.; Tsou, C. Super-tough, anti-fatigue, self-healable, anti-fogging, and UV shielding hybrid hydrogel prepared via simultaneous dual in situ sol-gel technique and radical polymerization. *J. Mater. Chem. B* **2019**, *7*, 7162−7175.
(42) Glaser, R. H.; Wilkes, G. L.; Bronnimann, C. E. Solid-state 29Si NMR of TEOS-based multifunctional sol-gel materials. *J. Non-Cryst. Solids* **1989**, *113*, 73−87.
(43) Artaki, I.; Bradley, M.; Zerda, T. W.; Jonas, J. NMR and Raman study of the hydrolysis reaction in sol-gel processes. *J. Phys. Chem.* **1985**, *89*, 4399−4404.
(44) Schmidt, A.; Veeman, W. S.; Litvinov, V. M.; Gabriëlse, W. NMR Investigations of In-Situ Stretched Block Copolymers of Poly(butylene terephthalate) and Poly(tetramethylene oxide). *Macromolecules* **1998**, *31*, 1652−1660.
(45) Litvinov, V. M.; Bertmer, M.; Gasper, L.; Demco, D. E.; Blümich, B. Phase Composition of Block Copoly(ether ester) Thermoplastic Elastomers Studied by Solid-State NMR Techniques. *Macromolecules* **2003**, *36*, 7598−7606.
(46) Xu, Q.; Chen, J.; Huang, W.; Qu, T.; Li, X.; Li, Y.; Yang, X.; Tu, Y. One Pot, One Feeding Step, Two-Stage Polymerization Synthesis and Characterization of (PTT-b-PTMO-b-PTT)n Multiblock Copolymers. *Macromolecules* **2013**, *46*, 7274−7281.
(47) Liu, C.; Morimoto, N.; Jiang, L.; Kawahara, S.; Noritomi, T.; Yokoyama, H.; Mayumi, K.; Ito, K. Tough hydrogels with rapid self-reinforcement. *Science* **2021**, *372*, 1078−1081.
(48) Costa, C. S. M. F.; Fonseca, A. C.; Serra, A. C.; Coelho, J. F. J. Dynamic Mechanical Thermal Analysis of Polymer Composites Reinforced with Natural Fibers. *Polym. Rev.* **2016**, *56*, 362−383.
(49) Pillai, K. V.; Renneckar, S. Dynamic mechanical analysis of layer-by-layer cellulose nanocomposites. *Ind. Crops Prod.* **2016**, *93*, 267−275.
(50) Zandraa, O.; Jelínková, L.; Roy, N.; Sáha, T. s.; Kitano, T.; Saha, N.; Zatloukal, M. Viscoelastic Properties and Morphology of Mumio-based Medicated Hydrogels. *AIP Conf. Proc.* **2011**, *261*, 1375.

https://doi.org/10.1021/acsnano.2c03440
ACS Nano XXXX, XXX, XXX−XXX

(51) Yu, C.; Yang, L.; Chen, H.; Qin, Y.; Wang, T.; Sun, W.; Wang, C. Microscale investigations of mechanical responses of TKX-50 based polymer bonded explosives using MD simulations. *Comput. Mater. Sci.* **2020**, *172*, 109287.
(52) ISO 10993-5, Biological evaluation of medical devices. In *Part 5: Tests for in vitro cytotoxicity*; ISO: Geneva, 2009.
(53) Teng, L.; Chen, Y.; Jin, M.; Jia, Y.; Wang, Y.; Ren, L. Weak Hydrogen Bonds Lead to Self-Healable and Bioadhesive Hybrid Polymeric Hydrogels with Mineralization-Active Functions. *Biomacromolecules* **2018**, *19*, 1939−1949.
(54) Broitman, E. Indentation Hardness Measurements at Macro-, Micro-, and Nanoscale: A Critical Overview. *Tribol. Lett.* **2017**, *65*, 23.
(55) Oliver, W. C.; Pharr, G. M. An improved technique for determining hardness and elastic modulus using load and displacement sensing indentation experiments. *J. Mater. Res.* **1992**, *7*, 1564−1583.
(56) Dauber-Osguthorpe, P.; Roberts, V. A.; Osguthorpe, D. J.; Wolff, J.; Genest, M.; Hagler, A. T. Structure and energetics of ligand binding to proteins: Escherichia coli dihydrofolate reductase-trimethoprim, a drug-receptor system. *Proteins* **1988**, *4*, 31−47.
(57) Newsome, D. A.; Sengupta, D.; Foroutan, H.; Russo, M. F.; van Duin, A. C. T. Oxidation of Silicon Carbide by O2 and H2O: A ReaxFF Reactive Molecular Dynamics Study, Part I. *J. Phys. Chem. C* **2012**, *116*, 16111−16121.
(58) Liu, C.; Ning, W.; Tam, L. H.; Yu, Z. Understanding fracture behavior of epoxy-based polymer using molecular dynamics simulation. *J. Mol. Graphics Modell* **2020**, *101*, 107757.
(59) Krishna, S.; Patel, C. M. Computational and experimental study of mechanical properties of Nylon 6 nanocomposites reinforced with nanomilled cellulose. *Mech. Mater.* **2020**, *143*, 103318.
(60) Martinez, L.; Andrade, R.; Birgin, E. G.; Martinez, J. M. PACKMOL: a package for building initial configurations for molecular dynamics simulations. *J. Comput. Chem.* **2009**, *30*, 2157−64.

https://doi.org/10.1021/acsnano.2c03440
ACS Nano XXXX, XXX, XXX−XXX

SUPPORTING INFORMATION

Resolving the Conflict between Strength and Toughness in Bioactive Silica-Polymer Hybrid Materials

Wei Fan[1], Tao Du[1], Aida Droce[1], Lars R. Jensen[2], Randall E. Youngman[3], Xiangting Ren[1], Leonid Gurevich[2], Mathieu Bauchy[4], Peter Kristensen[1], Bengang Xing[5], Donghong Yu[1,], Morten M. Smedskjaer[1,*]*

[1] Department of Chemistry and Bioscience, Aalborg University, 9220 Aalborg, Denmark

[2] Department of Materials and Production, Aalborg University, 9220 Aalborg, Denmark

[3] Science and Technology Division, Corning Incorporated, Corning, New York 14831, United States

[4] Department of Civil and Environmental Engineering, University of California, Los Angeles, California 90095, United States

[5] Division of Chemistry and Biological Chemistry, School of Physical and Mathematical Sciences, Nanyang Technological University, 637371, Singapore

[*] Corresponding authors. e-mail: yu@bio.aau.dk, mos@bio.aau.dk

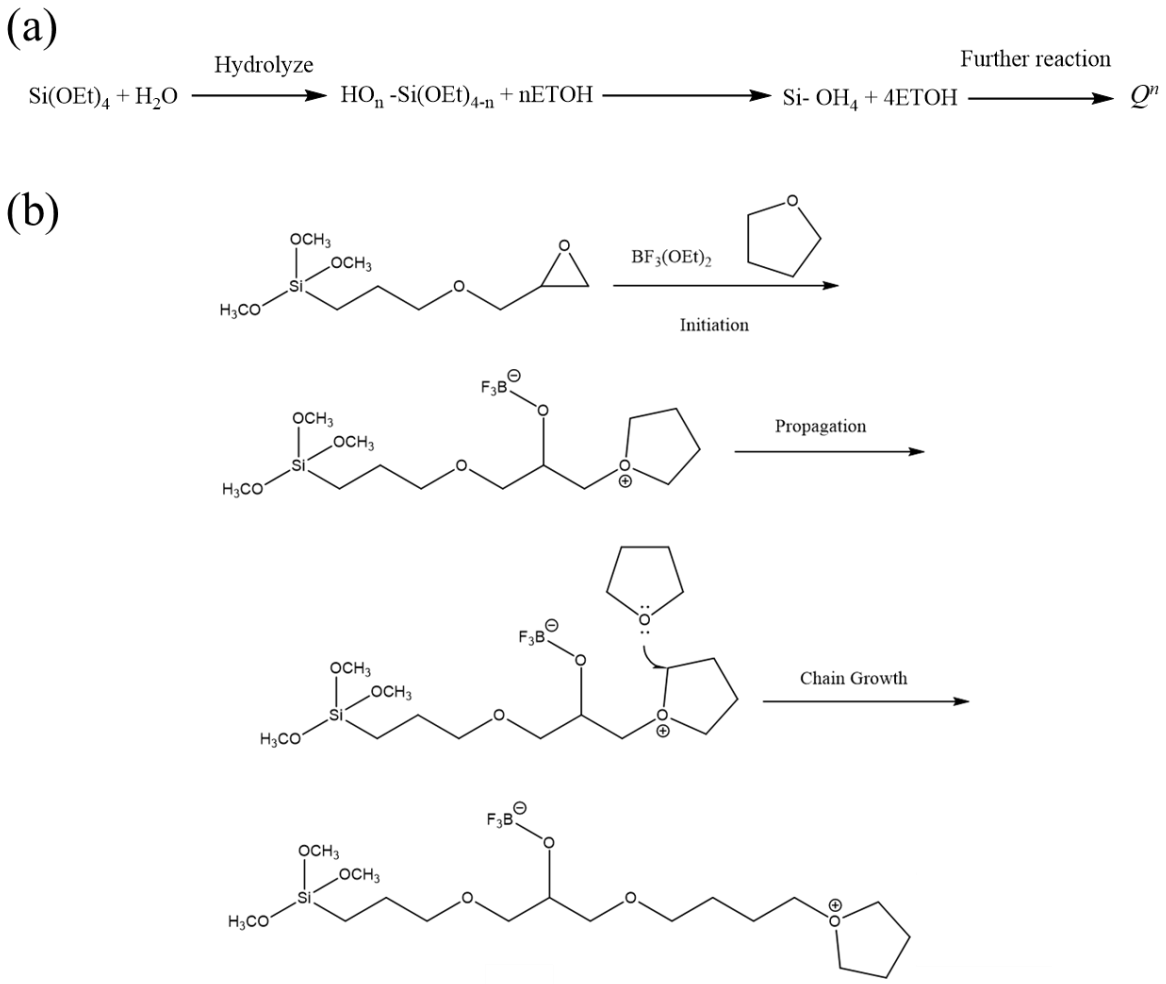

Figure S1. (a) Hydrolysis process of TEOS; (b) reaction mechanism and molecular structures of PTHF-SiO_2 hybrids.

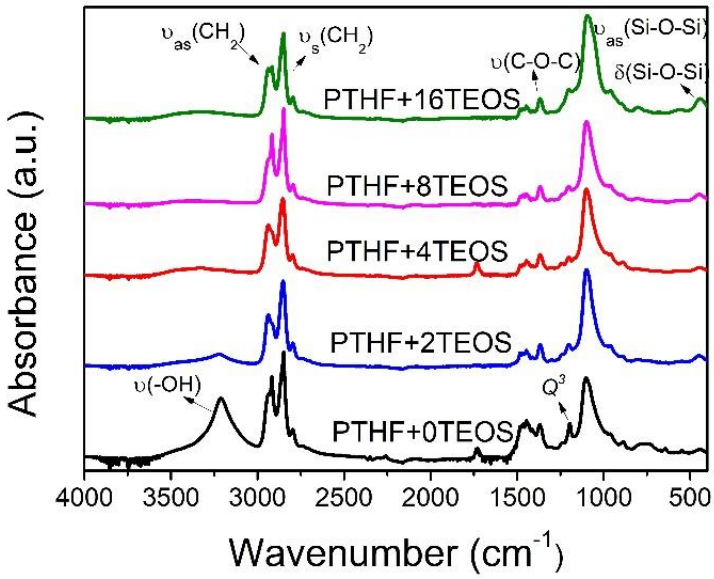

Figure S2. FT-IR spectra of experimental hybrids with varying I/O ratio, i.e., the series of PTHF·*x*TEOS hybrids.

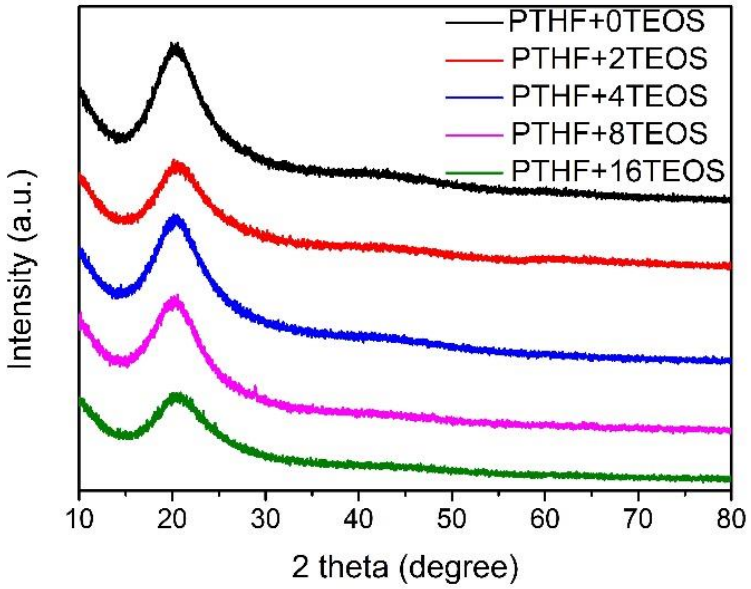

Figure S3. XRD patterns of hybrids with varying I/O ratio, i.e., the series of PTHF·*x*TEOS hybrids.

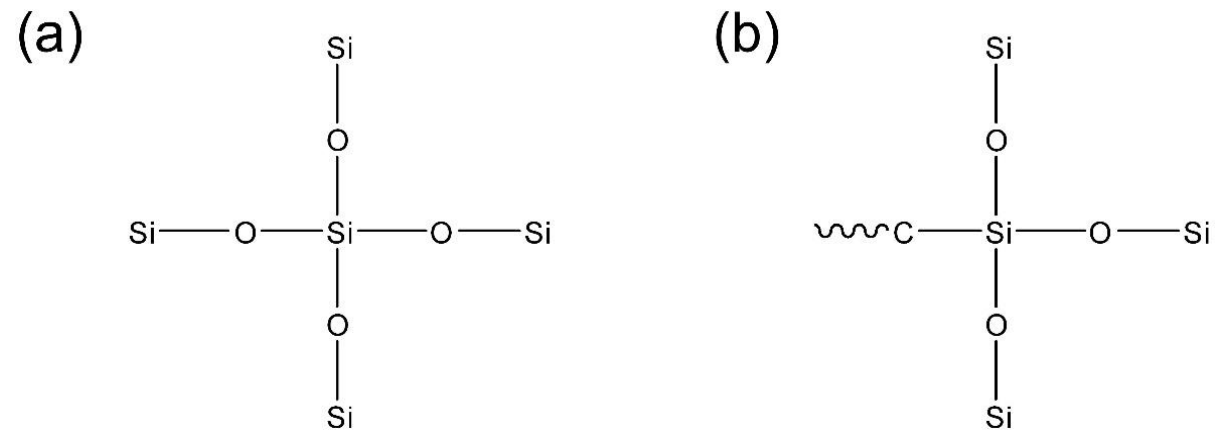

Figure S4. Illustration of chemical structures of silica (a) Q^4 and (b) T^3 species.

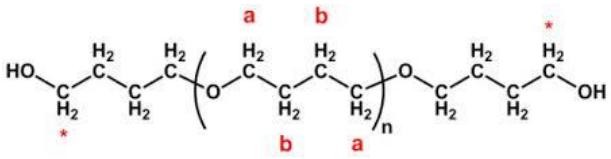

Figure S5. Molecular structure of PTHF and related H protons (named H_a and H_b).

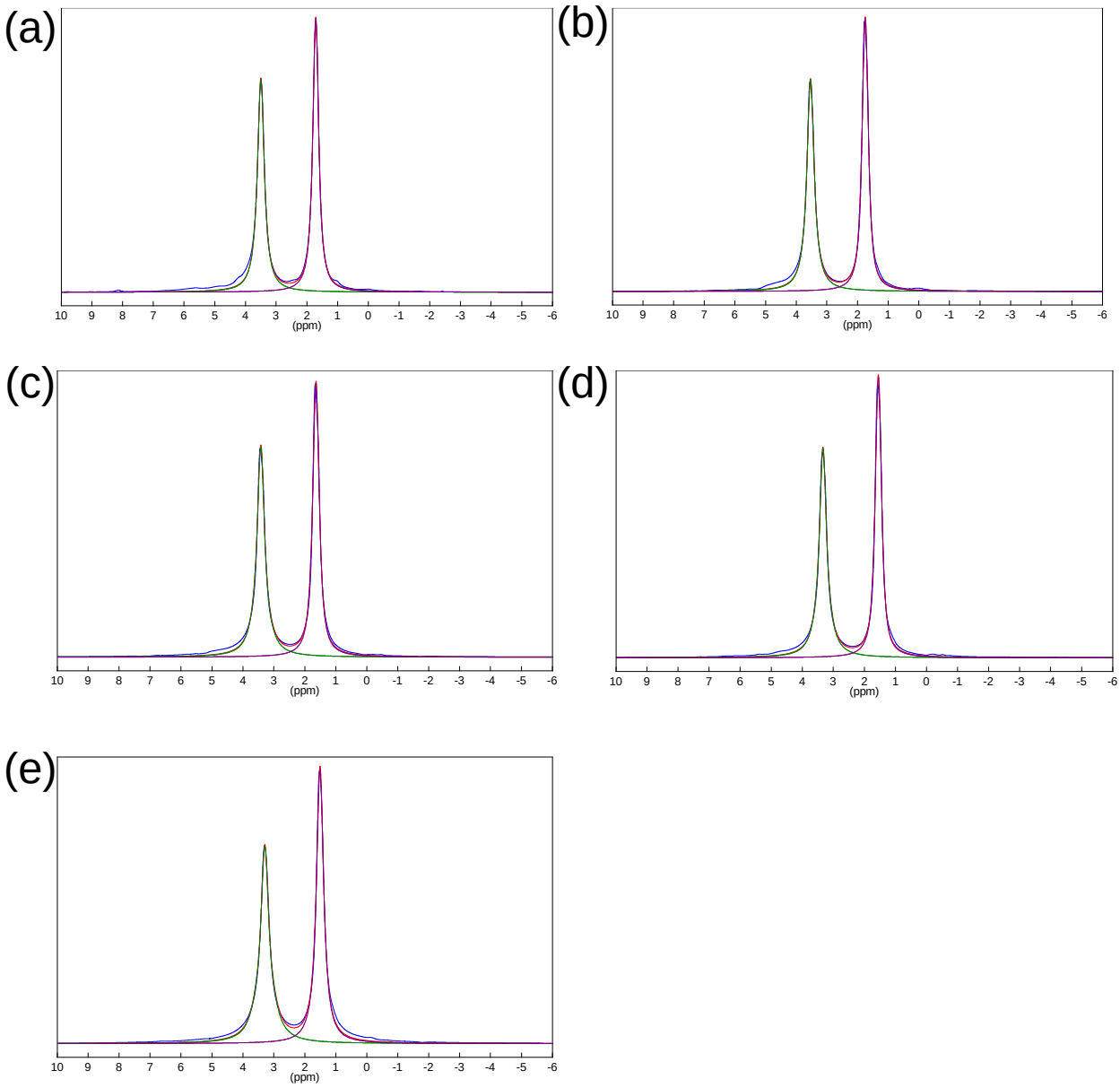

Figure S6. ^{1}H NMR spectra of the hybrids (a) PTHF·0TEOS; (b) PTHF·2TEOS; (c) PTHF·4TEOS; (d) PTHF·8TEOS; (e) PTHF·16TEOS.

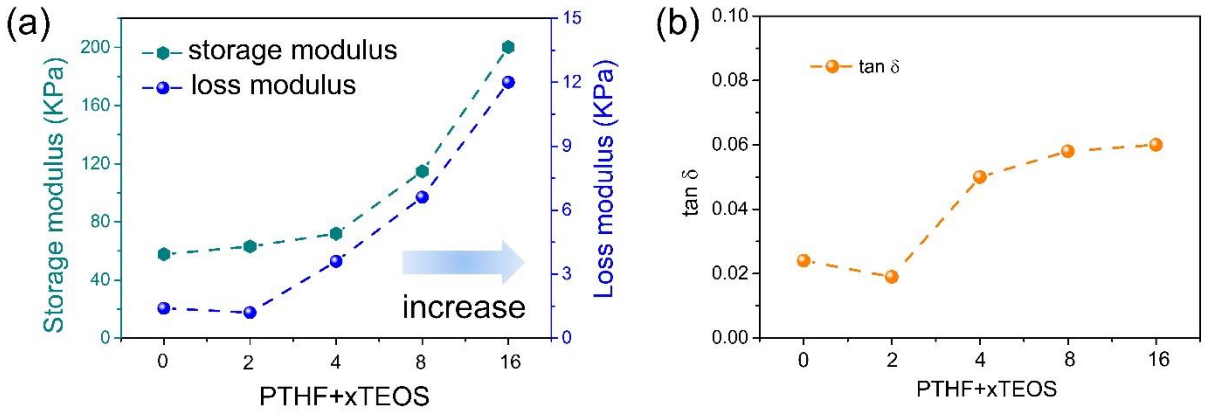

Figure S7. Composition dependence of (a) *E'* and *E''* and (b) tan (δ) of the hybrids with different I/O ratios, i.e., the series of PTHF·*x*TEOS hybrids. The values have been measured at 1 Hz.

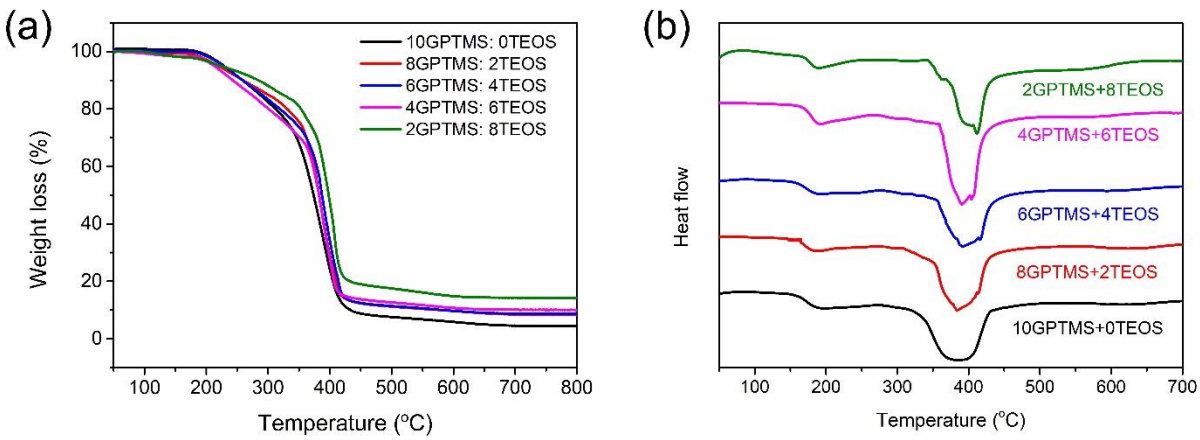

Figure S8. (a) TGA and (b) DSC results for *y*GPTMS:*z*TEOS hybrids.

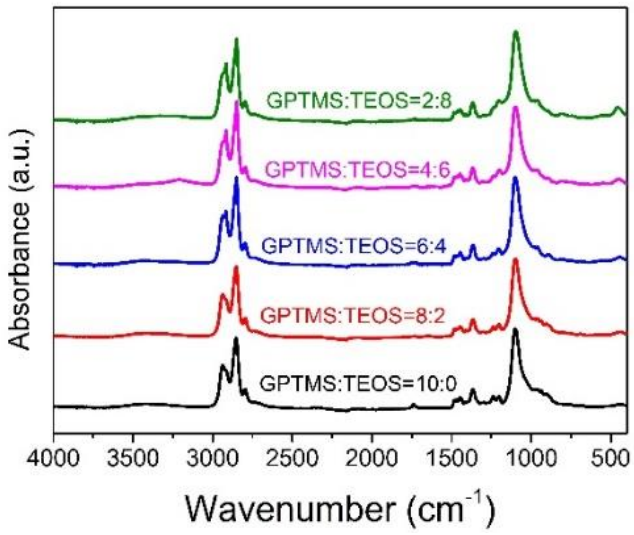

Figure S9. FT-IR spectra for *y*GPTMS:*z*TEOS hybrids.

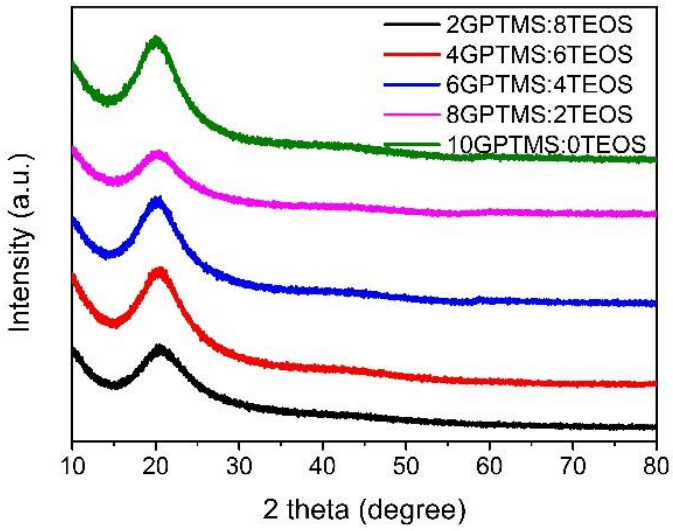

Figure S10. XRD patterns for *y*GPTMS:*z*TEOS hybrids.

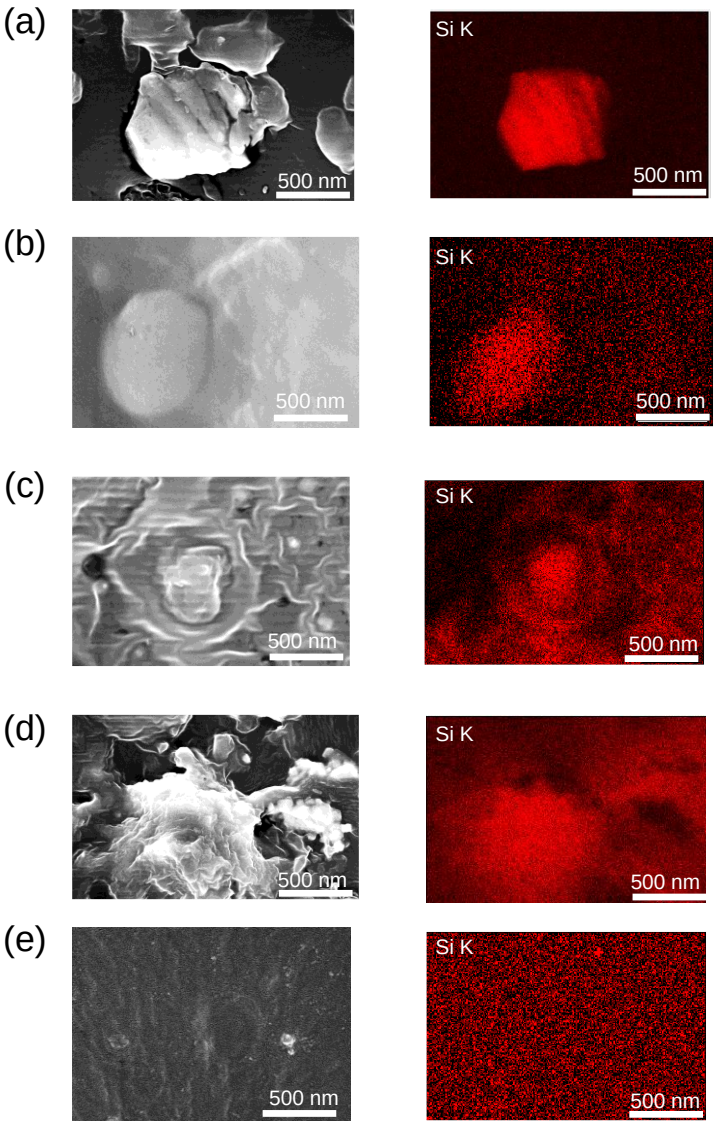

Figure S11. Morphology of hybrids as measured by scanning electron microscopy (SEM) and Si element distribution. (a) 2GPTMS:8TEOS; (b) 4GPTMS:6TEOS; (c) 6GPTMS:4TEOS; (d) 8GPTMS:2TEOS; (e) 10GPTMS:0TEOS.

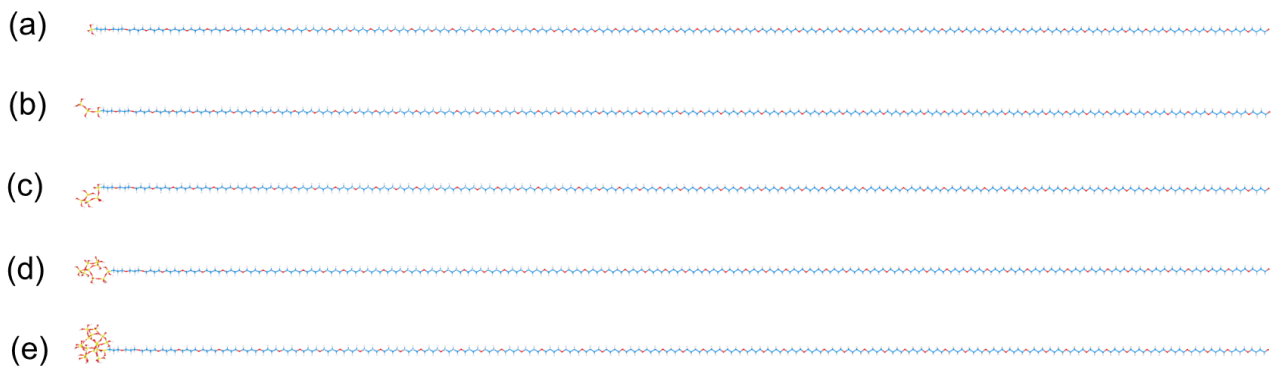

PTHF+xTEOS (x = 0, 2, 4, 8, 16)

Figure S12. Schematics of the basic unit of hybrids in the MD simulations with different I/O ratios.

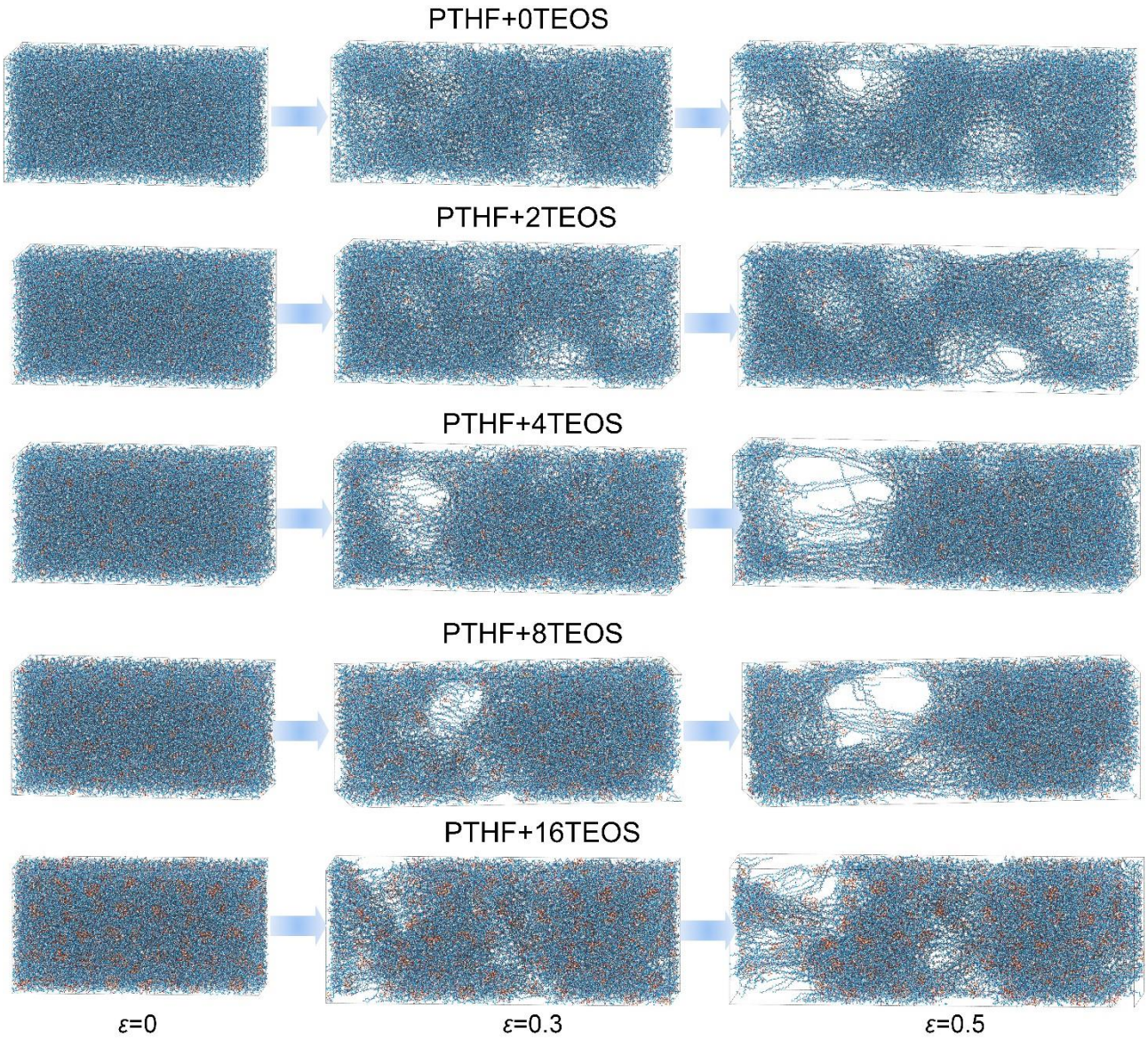

Figure S13. Simulated fracture evolution of hybrids with different I/O ratios under the elongation at the strains of ε=0, 0.3, and 0.5. The simulations were performed using the CVFF potential.

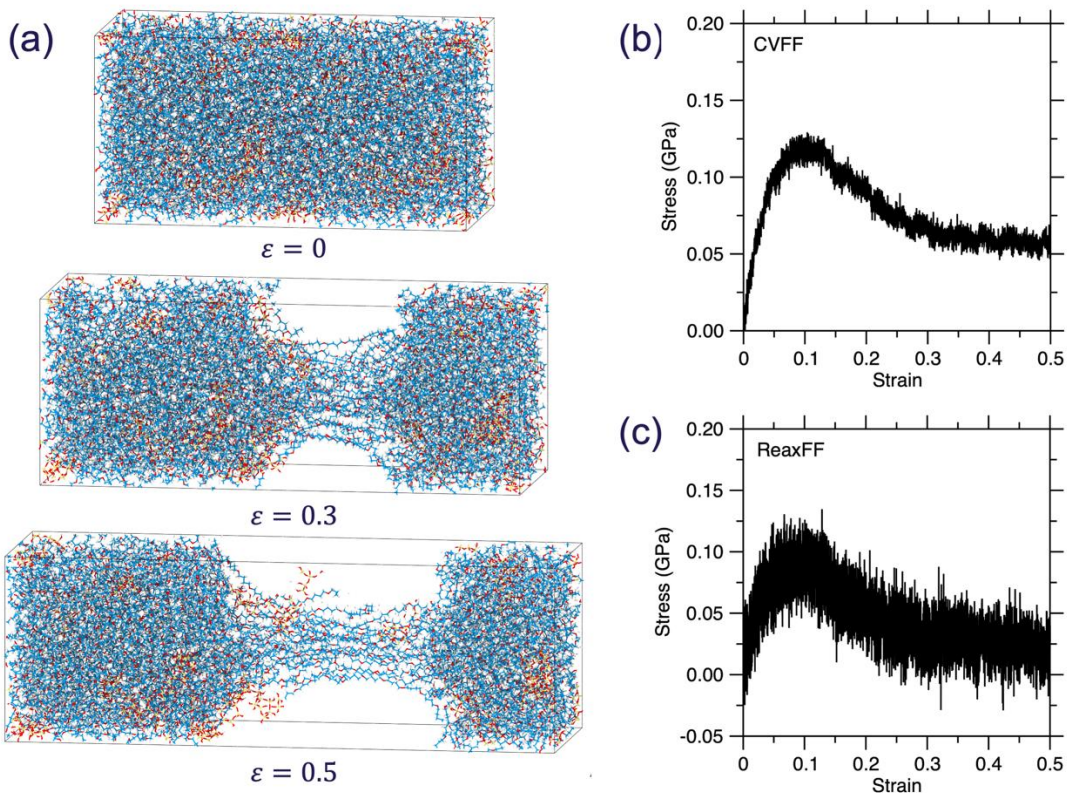

Figure S14. (a) Simulated fracture evolutions of hybrid under the elongation at the strains of ε=0, 0.3, and 0.5 using the ReaxFF potential. (b,c) Simulated stress-strain curve for PTHF·8TEOS hybrid using (b) CVFF potential or (c) ReaxFF potential.

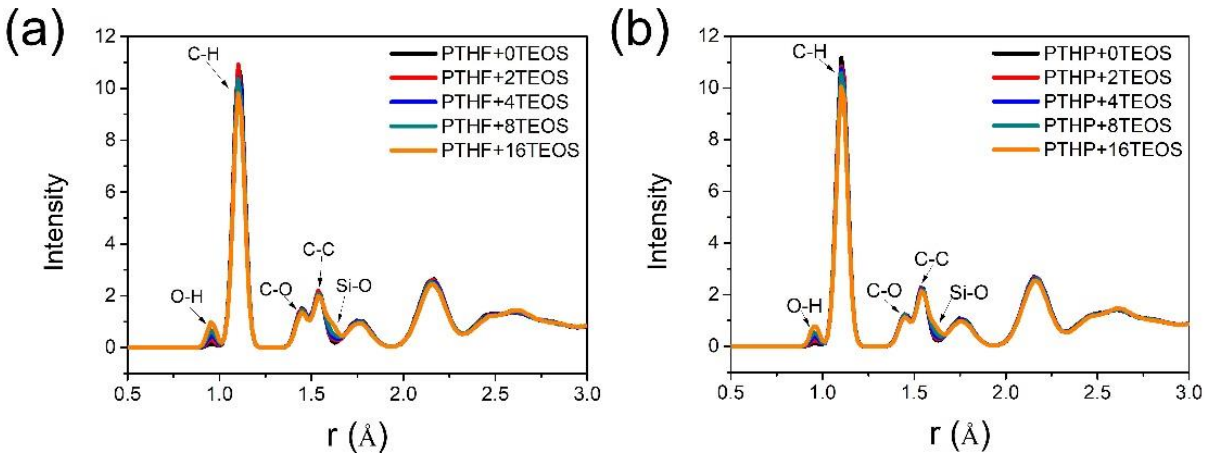

Figure S15. Simulated pair distribution functions of (a) PTHF-SiO_2 and (b) PTHP-SiO_2 based hybrids.

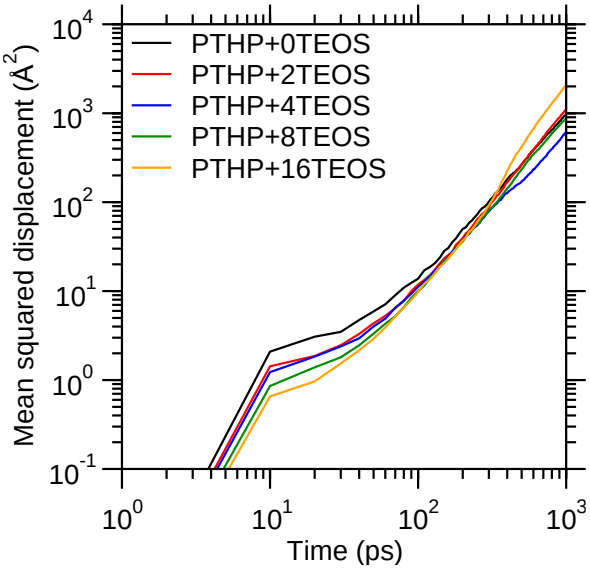

Figure S16. Time-dependence of the mean squared displacement (MSD) of Si atoms in PTHP·*x*TEOS based hybrids during the tensile process.

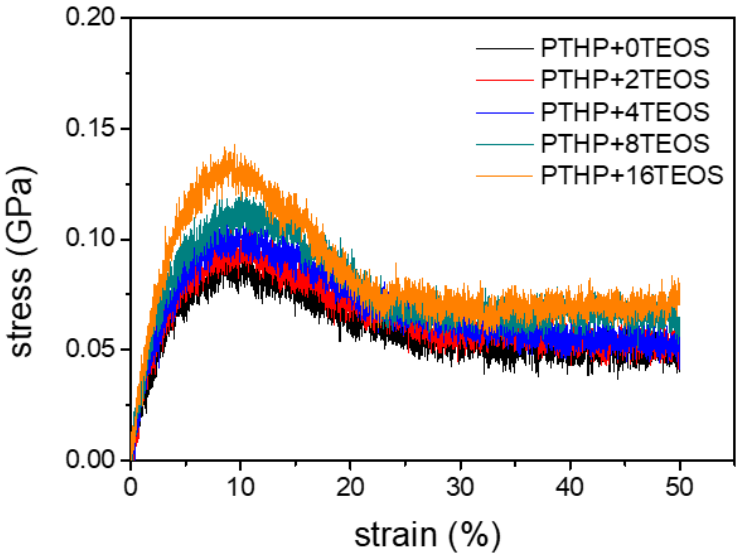

Figure S17. Simulated stress-strain curves of PTHP·*x*TEOS based hybrids.

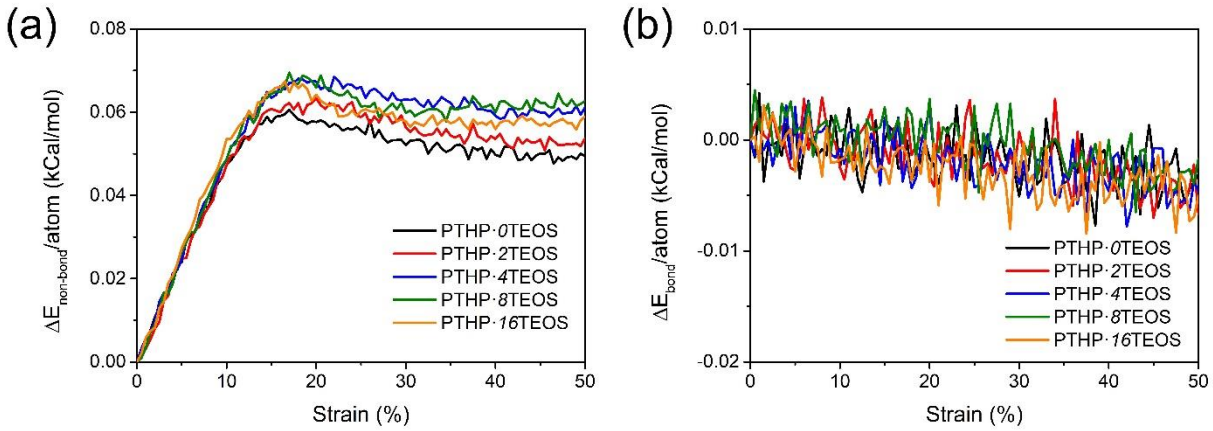

Figure S18. Simulated Potential energy terms evolution as a function of the applied strain. (a) Non-bonded energy of PTHP hybrids. (b) Bonded energy of PTHP hybrids.

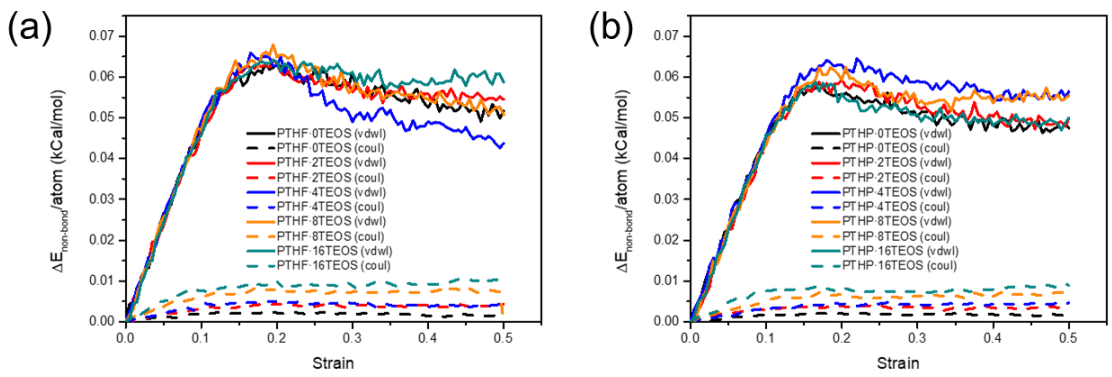

Figure S19. MD simulated contribution of van der Waals interactions (vdwl) and Coulombic forces (coul) as a function of strain in (a) PTHF·*x*TEOS and (b) PTHP·*x*TEOS hybrids.

SUPPORTING TABLE

Table S1. Compositions of the basic units of PTHF • *x*TEOS and PTHP • *x*TEOS hybrid systems in the MD simulations.

Sample	Polymer unit	GPTMS	SiO_2	Atom numbers
PTHF • 0TEOS	56	1	0	756
PTHF • 2TEOS	56	1	2	768
PTHF • 4TEOS	56	1	4	780
PTHF • 8TEOS	56	1	8	801
PTHF • 16TEOS	56	1	16	840
PTHP • 0TEOS	56	1	0	924
PTHP • 2TEOS	56	1	2	936
PTHP • 4TEOS	56	1	4	948
PTHP • 8TEOS	56	1	8	969
PTHP • 16TEOS	56	1	16	1008

Paper IV

Highly Stretchable, Anti-Swelling, Self-Healing, and Biocompatible Dual-Reinforced Double Polymer Network Hydrogels

Wei Fan[1], Lars R. Jensen[2], Yibing Dong[3], Abigail J. Deloria [4], Bengang Xing[5], Donghong Yu[1,*], Morten M. Smedskjaer[1,*]

[1]Department of Chemistry and Bioscience, Aalborg University, 9220 Aalborg, Denmark

[2]Department of Materials and Production, Aalborg University, 9220 Aalborg, Denmark

[3]School of Chemical and Biomedical Engineering, Nanyang Technological University, Singapore 637459, Singapore

[4]Center for Medical Physics and Biomedical Engineering, Medical University of Vienna, 1090 Vienna, Austria

[5]Division of Chemistry and Biological Chemistry, School of Physical and Mathematical Sciences, Nanyang Technological University, Singapore 637371, Singapore

[*] Corresponding authors. e-mail: yu@bio.aau.dk (D.Y.), mos@bio.aau.dk (M.M.S.)

Abstract: Superior flexibility and toughness can be achieved in bioactive hydrogels by the use of a double polymer network with complementary properties. Inspired by this design principle, we here combine polyacrylic acid (PAA) and sodium alginate (SA) to obtain a dual reinforced double interpenetrating network (d-DIPN) hydrogel. The dual reinforcement involves ionic crosslinking and introduction of SiO_2 nanoparticles, which leads to extraordinary improvements in strength and toughness. Compared with the standard PAA hydrogel that offers elongation of 240% and breakage stress of 0.03 MPa, the prepared SA(Ca^{2+})-PAA-SiO_2 hydrogel shows elongation above 1000% and breakage stress of 1.62 MPa. Moreover, the combination of strong covalent crosslinks and weak reversible interactions provide the d-DIPN hydrogel with anti-swelling and self-healing behavior, adhesive abilities and shape memory performance. Furthermore, we show that the biocompatibility and bone cell proliferation ability of the hydrogels can be improved through a mineralization process despite of a slight reduction in breakage strain and stress. Taken as a whole, our work paves the way for the design of strong and tough hydrogels, with potential applications within biomedicine and particularly tissue engineering.

Functional soft materials are increasingly demanded for tissue engineering,[1] drug delivery[2, 3] and soft robotics applications.[4-6]. Hydrogels, which are composed of three dimensional cross-linked polymer networks and large amount of water,[7-11] present superior mechanical flexibility and chemical properties. Such behavior of combining solid-like mechanical performances with liquid-like transport properties enable hydrogels with the ability to adapt to different shapes and deformation requirements,[12,13] adhesion to different surfaces[14] as well as self-healing ability.[10, 15-17] Normally, hydrophilic polymers such as polyacrylamide (PAM) and polyacrylic acid (PAA) are desirable materials for preparing hydrogels due to their amide and carboxyl groups as pendants[18] and their propensity to soak up water, which makes them suitable candidates for creating hydrated structures that resemble native soft tissues.[19, 20] Additionally, neutralized PAA could function as tissue scaffolds for wound and bone repair due to their excellent biocompatibility.[16, 21, 22] However, due to the low polymer content (high water content) ,[23, 24] single polymer based hydrogels inevitably lack the necessary toughness to absorb energy and deform without damage while undergoing large deformations. This is problematic for tissue engineering applications, where there is a need to sustain cyclic loading in the human body.

A variety of chemical and physical reinforcement methods have been attempted to improve the strength and toughness of hydrogels. A common approach is to use reversible crosslinks, e.g. hydrogen bonds, ionic bonds, reversible covalent bonds and metal coordination bonds.[16, 25] These reversible interactions can easily reform after breakage, thus enabling an effective energy dissipation, transfer of applied loads to neighboring networks and ability to undergo self-healing. The reversible interactions also offer hydrogels with desirable stiffness as well as extensibility. Additionally, as an alternative route, multi-network architectures such as double polymer network (DN) hydrogels with permanent covalent bonds can greatly adapt deformations resulting from so many reversible bonds. [26, 27] Normally, interpenetrating crosslinked networks are formed by polymers, one of which is densely cross-linked and relatively stiffer while the second one is sparsely cross-linked and more stretchable. The stiffer network will break first and dissipate energy due to reversible bonds for high toughness, while the stretchable network can maintain the integrity and shape of the hydrogel.[25] Thus, DN hydrogels regularly reveal much higher strength and toughness compared with single polymer based ones.

Alginate is a potential candidate for biomedical devices and is usually reinforced through ionically chelation with divalent cations (e.g. Ca^{2+}, Fe^{3+}) to form gels under mild synthetic conditions.[28-30] Suo *et al.* have investigated polyacrylamide (PAM) and alginate double network hydrogels, which revealed improved mechanical properties, including high fracture energy of ~9,000 J m^{-2} and ability to be stretched over 20 times their initial length.[12] In addition, nanoparticles (NPs) can act as crosslinkers or nanofillers, which is another common approach to significantly improve the strength and toughness of hydrogels. Inorganic NPs incorporation can function as analogous crosslinking points (ACPs) to enable the hydrogels to withstand relatively more external stress at a fixed strain and transfer the applied load to neighboring networks chains.[13, 16, 31, 32, 13, 33, 34] Moreover, such inorganic component can a larger number of cell recognition sites, which are especially important for skeletal tissue engineering. Xie *et al.* have prepared PAM hydrogels with size controllable SiO_2 nanoparticles that can be stretched to >1000% compared with their original length.[13] However, the tensile strength of the abovementioned hydrogels are only on the order of 10s of kPa and thus not sufficient for practical applications.[35-37]

Herein, we propose a novel strengthening and toughening approach by combining ionic and NPs reinforcement methods in a single DIPN hydrogel system to enable their biomedical applications. PAA and alginate are chosen as the components not only due to their previous incorporation into hydrogels, but also their extraordinary biocompatibility and possible skeletal tissue engineering applications. Compared with non-reinforced and single reinforced hydrogels, the prepared d-DIPN SA(Ca^{2+})-PAA(SiO_2) hydrogel with both weak and strong crosslinks shows significantly improved thermal stability, anti-swelling behavior, and most importantly, mechanical properties, with elongation up to 1000% compared with its original length and tensile failure stress of 1.62 MPa. Moreover, reversible interactions in the prepared hydrogels, e.g., hydrogen bonds and ionic interactions, are to continuously break and reform, which enable effective energy dissipation and further provide the ability to self-heal, rapid shape recovery and adhesive properties. As the next step, we also perform Ca/P mineralization of the DIPN hydrogel system, which improves its anti-swelling behavior in both distilled water and phosphate buffer saline (PBS) solution as well as its biocompatibility, however, with acceptable decrease of strain and stress. The design principles developed herein for strong, yet biocompatible

hydrogels could enable their future applications as biomedical scaffolds.

Results

Design and synthesis of DIPN hydrogels. The one-pot prepared DIPN hydrogel with the proposed dual-reinforcement approach is presented in Fig. 1. Silica NPs are prepared by hydrolyzing vinyl-silica precursors as shown schematically in Fig. 1a. Vinyltriethoxysilane (VTES) monomers are applied in this work for two reasons: first, silica NPs will be formed with the formation of Si-O-Si framework during conventional sol-gel process in self-assembled micelles of surfactant in nanometer scale, whose sizes could be controlled by adjusting the molar ratios, time of hydrolysis, and concentration of surfactant;[13, 38] and second, the vinyl group will become copolymerized with acrylic acid (AA) monomers to form random copolymer backbones (red bonds in Fig. 1b). Alginate monomers can effectively chelate Ca^{2+} ions, forming single gels under mild conditions as depicted in Fig. 1c. In this work, we constructed such PAA-alginate double polymer work in a single system depicted in Fig. 1d. NPs and ionic dual reinforcement methods are applied for improving intermolecular interactions in interpenetrating networks. Such strategy could lead to a much more compact and crosslinked structure formed in hydrogels, and further result in higher strength as well as toughness. Due to biocompatibilities of PAA and alginate in this work, such combined hydrogels are expected to be potentially applied into biomedical fields. Moreover, in view of strong intermolecular interactions, hydrogels possibly possess functional performances, e.g. high stretchability, anti-swelling behavior and self-healing abilities (Fig. 1e).

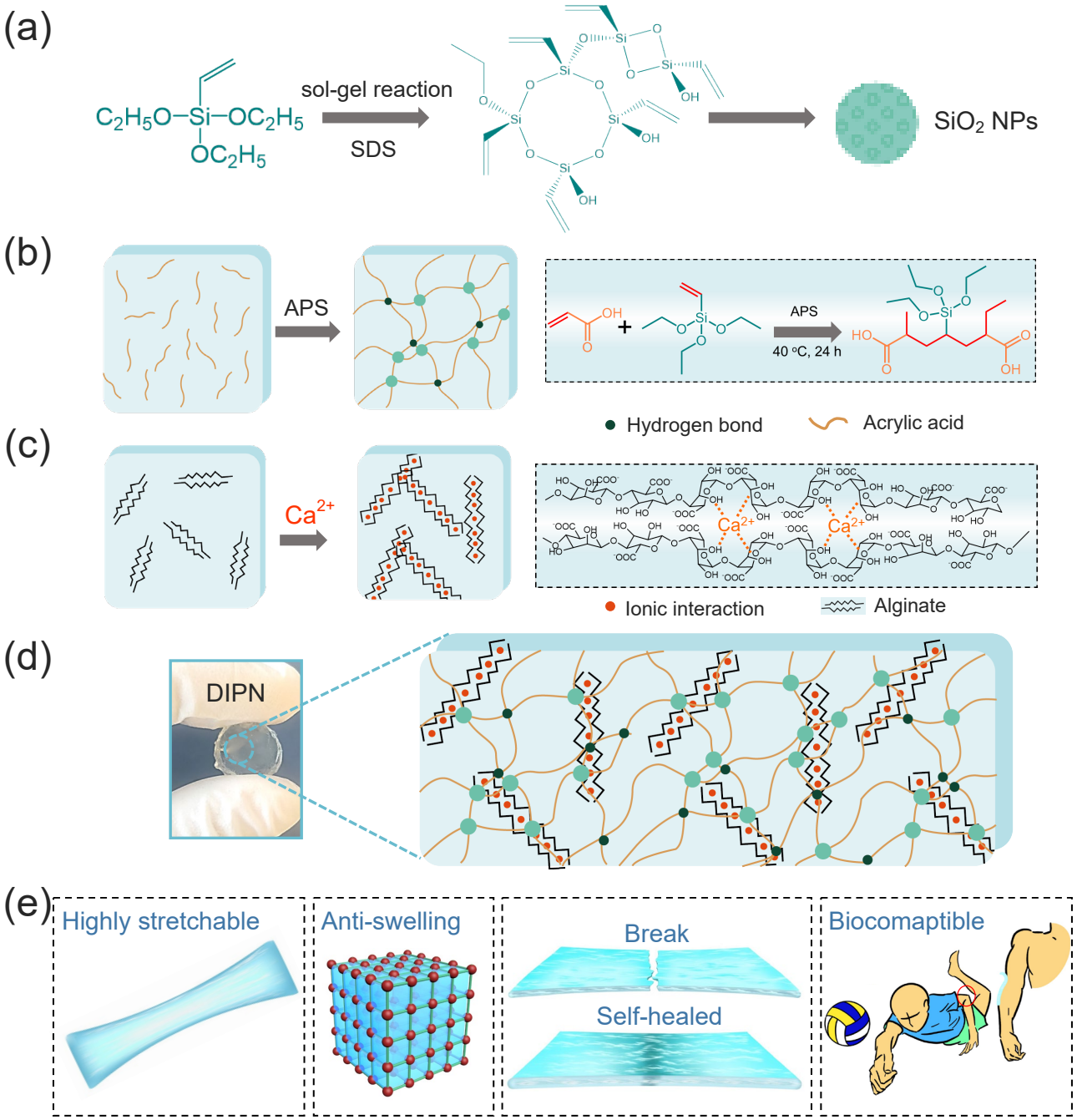

Figure 1. Design of double interpenetrating network (DIPN) hydrogels. (a) Reaction mechanism of preparing silica NPs with VTES precursor. (b) Free radical polymerization of AA and VTES (red bonds are vinyl groups for reaction). (c) Polymerization of alginate with Ca^{2+} ionic bonding. (d) Dual NPs and ionic reinforced PAA-Alginate double polymer network hydrogel. (e) Images show functionalities (highly stretchable, anti-swelling, self-healing and biocompatible) of DIPN hydrogel.

Structure characterization of DIPN hydrogels. In this work, we prepared PAA, SA-PAA, SA-PAA (SiO_2), SA (Ca^{2+})-PAA, and SA (Ca^{2+})-PAA (SiO_2) hydrogel materials to enable a systematic comparison of their structures, mechanical performances and other functions. In the DIPN networks, besides strong covalent bonds, weak reversible interactions also functions in hydrogel (Fig. 2a). That is, hydrogen bonds existed among (i) PAA chains, (ii) PAA and SA chains, (iii) silica NPs and PAA chains, and (iv) silica NPs and SA chains, as well as ionic crosslinks formed in alginate polymers. These reversible interactions, including hydrogen bonds and ionic interactions, could break and reform reversibly in a short time during loading and unloading of external forces (Fig. 2b), providing hydrogels with multi functions of improved strength and toughness, rapid shape recovery from deformation, improved anti-swelling performance, and self-healing ability.

Fourier transform infrared (FT-IR) spectroscopy is performed to characterize the polymerized hydrogel structures at the molecular level. As shown in Fig. S1, the peaks around 1100 cm^{-1} are ascribed to asymmetric stretching vibration of the Si-O bond,[38] representing the existence of silica structure in the hydrogels. There is a large fraction of carboxyl groups in the hydrogels, and the characteristic vibration of the -C=O group is thus present at 1710 cm^{-1} and that of -COOH at ~3000 cm^{-1}.[38, 39] The large amount of H_2O in the hydrogels is confirmed by the typical -OH group vibration peak at ~3400 cm^{-1}.[40] Fig. 2c shows an enlarged view of the absorbance in the region from 1600 to 1680 cm^{-1}, revealing the absence of typical -C=C vibrations in the hydrogels. This demonstrates the complete polymerization of AA and VTES monomers during the free radical polymerization process.[40]

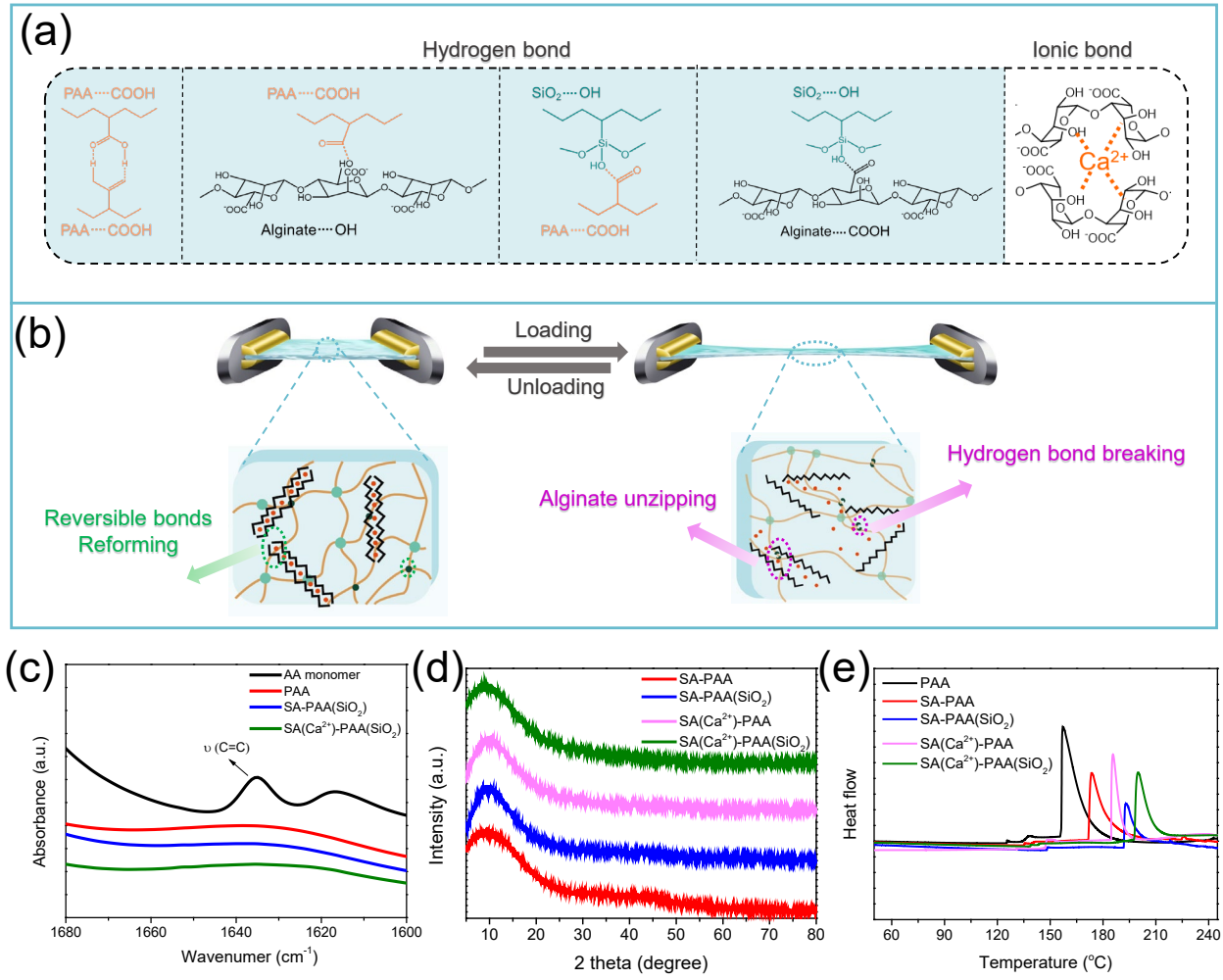

Figure 2. Structural features of DIPN hydrogels. (a) Reversible interactions, hydrogen bonds and ionic interactions in SA (Ca^{2+})-PAA-SiO_2 hydrogel. (b) Breaking and reforming of reversible bonds in SA (Ca^{2+})-PAA-SiO_2 hydrogel with loading and unloading. (c) FT-IR spectra of AA monomer and hydrogels. (d) X-ray diffractograms of different hydrogels. (e) DSC thermograms of different hydrogels (endothermal up).

The size of the silica NPs after hydrolysis was measured by means of the dynamic light scattering (DLS) method[41] (Fig. S2). The average size of the silica particles is around 9 nm, and such small size is beneficial for their uniform dispersion in the matrix and adequate active surface (vinyl groups) for further reactions with the AA monomers. X-ray diffraction (XRD) analysis was carried out for phase identification of the hydrogels (Fig. 2d). No sharp diffraction peaks are observed in the X-ray diffractograms, confirming that all hydrogels are

disordered amorphous materials. This is because the crystallization of silica was inhibited by the hydrolysis and condensation of VTES, and due to the covalent bonds formed with the polymers that enables silica to become uniformly dispersed in the hydrogels.[40] Differential scanning calorimetry (DSC) measurements were conducted to evaluate the thermal stability and possible phase transitions of the hydrogels. As shown in Fig. 2e, the reinforced hydrogels reveal improved thermal stability, with the dual-reinforced SA(Ca^{2+})-PAA(SiO_2) hydrogel offering the endothermic peak at the highest temperature of ~210 ℃ compared with the other hydrogels. Finally, morphology of the hydrogel SA(Ca^{2+})-PAA(SiO_2) was examined by scanning electron microscope (SEM). The hydrogel is found to be relatively porous, with many small but consecutive networks observed in the cross-section images in Fig. S3.

Functional properties of DIPN hydrogels. Based on the dual ionic and nanoparticle reinforcement methods, enhanced mechanical properties and functional performances are expected for the SA(Ca^{2+})-PAA(SiO_2) hydrogel compared to the others. Fig. 3a shows that this hydrogel could be stretched more than 10 times of its original length, and it can also be freely wrapped around a glass rod (Fig. S4). Such behavior suggests a strong potential for adapting the material to different shape and deformation requirements in its potential applications. Reversible interactions in the hydrogel further ensured quick shape-recovery upon compression-release tests. Strong adhesion of the hydrogel to different types of surfaces, including glass, plastic, metal, and human skin, has also been observed (Fig. 3a). We ascribe these findings to the incorporated functional groups, e.g. hydroxide, amide, and imine bonds that exist in the system, which effectively interact and bind with surrounding phases to enable the adhesive properties.[19] Moreover, the strong intermolecular interactions provide the hydrogel with a very good self-healing ability.[42, 43] That is, the broken hydrogel has been observed to rapidly self-heal without cracks after an applied damage without cracks under stretching.

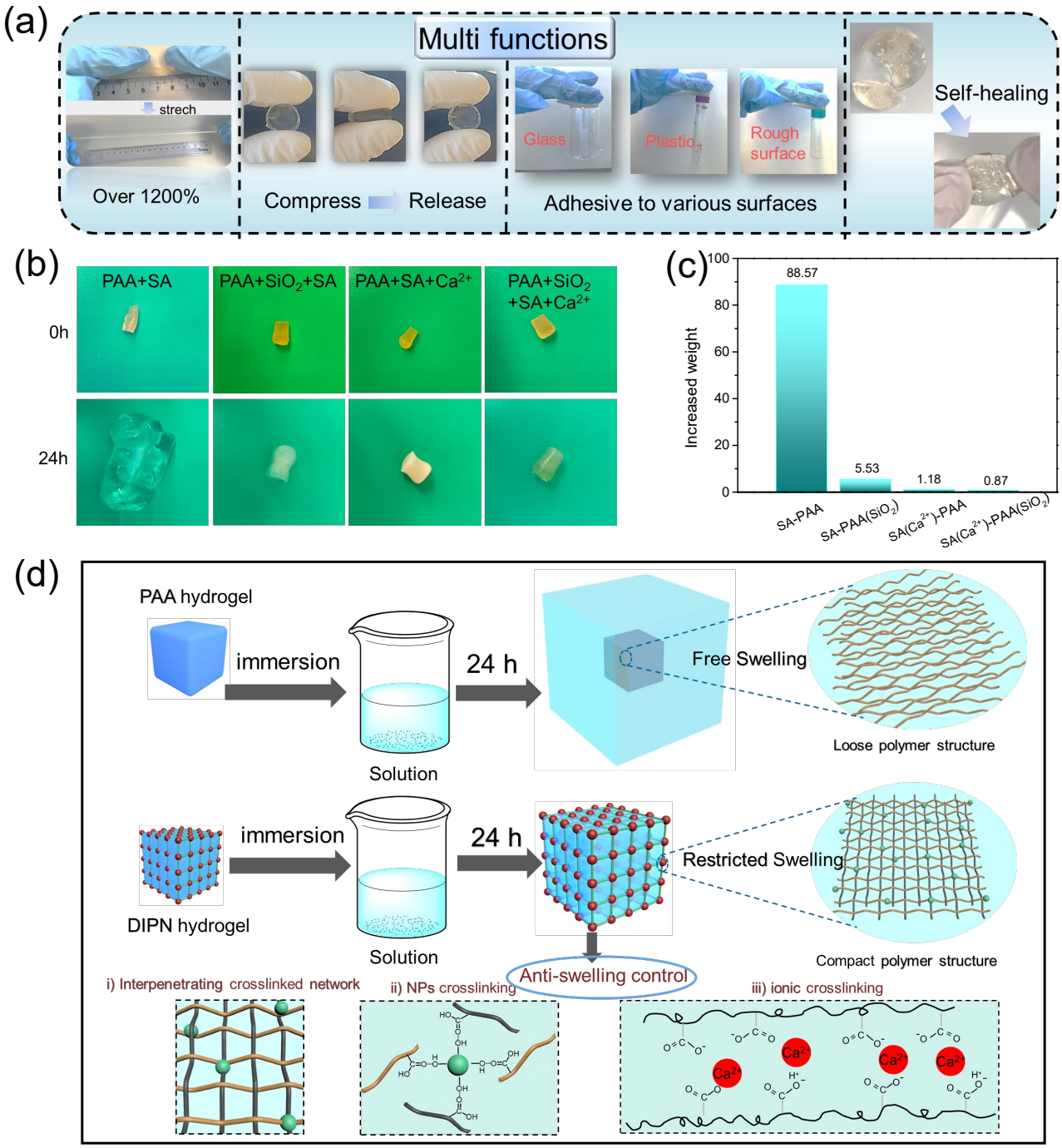

Figure 3. Functional properties of DIPN hydrogels. (a) High stretchability, quick shape-recovery, and adhesive and self-healing abilities of SA(Ca^{2+})-PAA(SiO_2) hydrogel. (b) Optical images of dry hydrogels and immersed ones in distilled water after 24 h. (c) Water up-take in hydrogels after 24 h. (d) Swelling mechanism of PAA hydrogel and reinforced DIPN hydrogels.

Anti-swelling behavior is another important factor for hydrogels as artificial cartilage materials. The low

swelling rate will avoid unnecessary extrusion of the material on the surrounding tissue and cause secondary damage, and such behavior is also improved as a result of the dual-reinforcement method.[7, 10, 44, 45] As seen in the images in Fig. 3b, the SA-PAA hydrogel without the applied reinforcement method swells to around ~89 times of its original weight after being immersed in distilled water for 24 h at room temperature. The single-reinforced SA-PAA(SiO_2) and SA(Ca^{2+})-PAA hydrogels exhibit only 5.5 and 1.2 times swelling under the same conditions (Fig. 3c). Impressively, the SA(Ca^{2+})-PAA(SiO_2) hydrogel reveals excellent anti-swelling behavior, with only 0.87 times more swelling relative to its original weight. The mechanism is vividly presented in Fig. 3d. Compared with PAA hydrogels with loose polymer network structures, whose shape and volume are quiet easy to change in solutions, double polymer crosslinked hydrogel with IPN are much more compact in comparison, and leads to it only minor changes in solutions. Moreover, silica NPs and ionic Ca^{2+} could form coordination bonds with carboxyl groups with polymer chains, which greatly improved the crosslinked sites in the system, and further result in denser network.[25] Thus, the more cross-linked structures and stronger intermolecular interactions formed after dual-reinforcement could effectively prevent chain disentanglement for hydrogels to swell.

There are many possible ionic groups pendent to the backbone of the PAA and SA components, which can accept or donate protons in response to the environmental pH change.[45, 46] We therefore immersed the SA(Ca^{2+})-PAA(SiO_2) hydrogel into different solutions with pH values ranging from 1 to 14 to explore the pH dependency of the swelling behavior. As shown in Fig. S5 and S6, pronounced swelling is prevented in lower pH solutions, likely because the carboxyl groups in the hydrogels remain in their acidic forms, and therefore intermolecular interactions like hydrogen bonds are well preserved in such conditions. However, when the pH increases, the carboxyl groups are gradually deprotonated, causing most of the hydrogen bonds to disassociate, and further resulting in disentanglement of polymer chains and promoting hydrogel swelling.

Mechanical properties of DIPN hydrogels. Hydrogels with high strength and toughness are demanded for applications in tissue engineering and soft robotics. Although having very good flexibility, the low strength and toughness of many hydrogel materials can severely restrain their practical applications and various

toughening strategies have thus been explored.[3, 4, 47] First, we compare the ability of the five different hydrogels of the same size to lift a 3 kg weight (cylindrical, ϕ =3.5 mm) in Fig. 4a. Pure PAA hydrogel is relatively weak and breaks before lifting the weight, while the DIPN SA-PAA and NPs reinforced SA-PAA-SiO_2 hydrogels behave similarly, i.e., the hydrogels are stretched to several times of their original length, but they are unable to lift the weight. Although the ionic reinforced hydrogel SA(Ca^{2+})-PAA can pull up the weight, it fractures after only several seconds. However, in comparison, d-DIPN hydrogel can lift the weight easily without breakage. Thus, the prepared d-DIPN hydrogel with dual-reinforcement methods appears to not only have high flexibility, but also improved strength and toughness compared with the non-reinforced or single-reinforced hydrogels. To this end, a series of mechanical tests were conducted to evaluate the related properties and understand the corresponding toughening and strengthening mechanisms.

The tensile test results are displayed in Fig. 4b, showing a comparison with a single PAA hydrogel with an elongation of 240% and maximum stress of 0.03 MPa. A great improvement of both stress and elongation at breakage is achieved for the PAA-SA DIPN hydrogel. The reason appears to be that external loads are shared by the entanglements created between the PAA and SA networks. Covalent crosslinks between PAA and SA chains (reacting with carboxyl groups) further strengthen the co-networks. Moreover, after introducing silica NPs and Ca^{2+} ions, we find that both stress and elongation of hydrogels get further improved. The hydrogel SA(Ca^{2+})-PAA(SiO_2) reveals an elongation up to 1000% compared with its original length and a stress of 1.62 MPa at breakage (Fig. S7). Based on the aforementioned results shown in Fig. 3a, the present hydrogel reveals good shape-recovery performance. Moreover, the incorporation of Ca^{2+} greatly affects the elastic/plastic deformation region of the hydrogels (Fig. 4b). That is, the alginate network without Ca^{2+} chelation could hardly reform after stretching, i.e., these hydrogels are relatively unrecoverable. However, upon introducing Ca^{2+}, the alginate networks are successfully connected and the ionic bonds are relatively reversible and could break/reform quickly. Thus, hydrogels SA (Ca^{2+})-PAA and SA (Ca^{2+})-PAA-SiO_2 reveal much more apparent elastic deformation in Fig. 4b

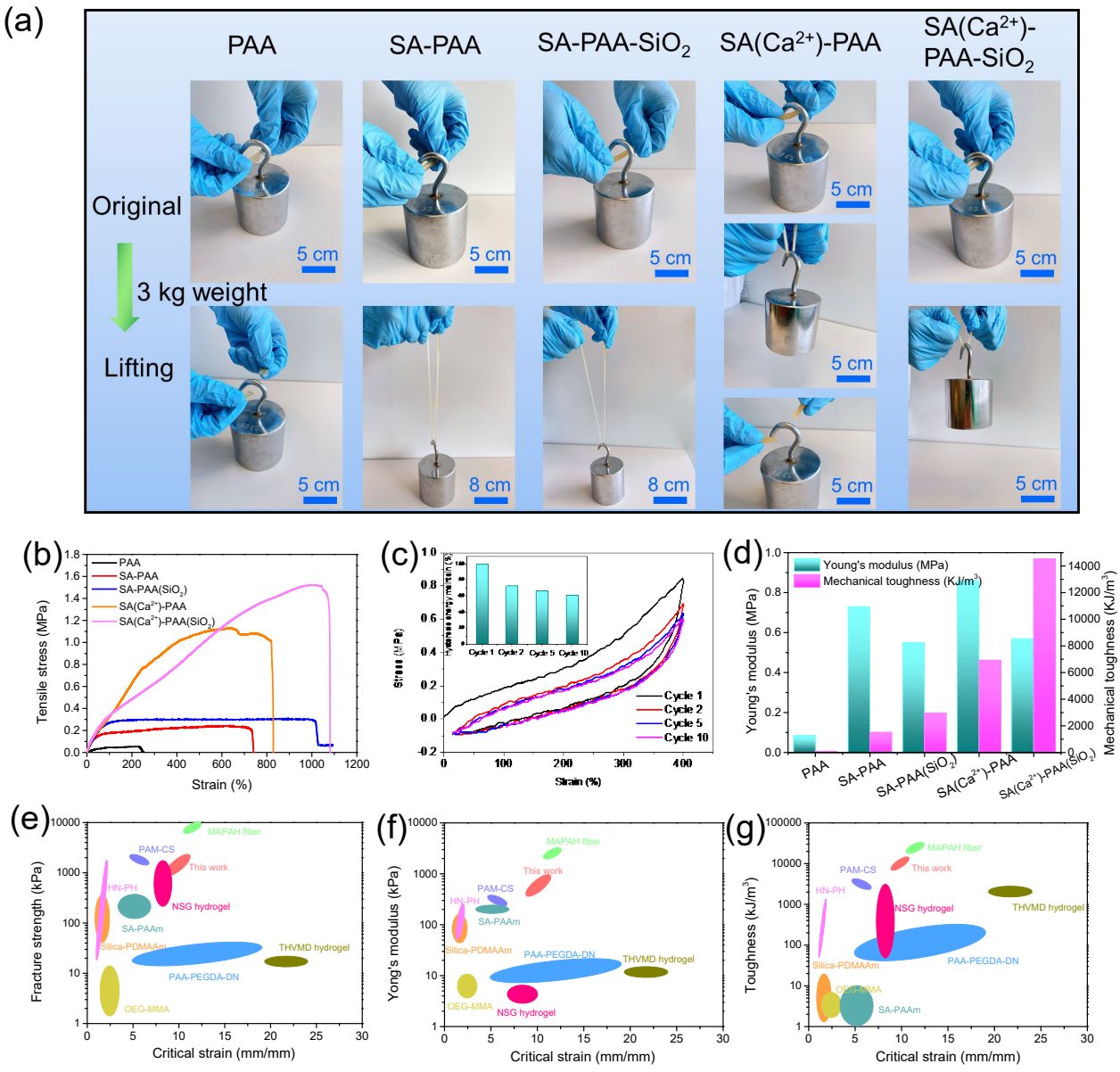

Figure 4. Mechanical testing of DIPN hydrogels. (a) Tensile stress-strain curves of hydrogels with different compositions. (b) Hysteresis loop of cyclic tensile curves of SA(Ca^{2+})-PAA(SiO_2) hydrogel for different cycles, with the inset showing the energy maintained after each cycle. (c) Young's modulus and mechanical toughness of hydrogels with different compositions. (d-f) Comparison of the present hydrogels with those from the literature [3, 6, 18, 21, 26, 27, 35, 37, 43, 48, 49] in terms of (d) fracture strength, (e) Young's modulus, and (f) toughness relative to the critical strain.

As the next step, a cyclic tensile test was conducted for the SA (Ca^{2+})-PAA-SiO_2 hydrogel to determine the recovery efficiency. As shown in Fig. 4c, hysteresis loops exist in every loading-unloading curve, with the area between the loading and unloading curves representing the energy dissipation per unit volume. The shape of the curves remains relatively constant, representing good self-recoverability of the SA(Ca^{2+})-PAA-SiO_2 hydrogel. Moreover, the dissipated energy that remains after the second cycle is ~73% compared with the first one, while the dissipated energy of the tenth cycle maintains at ~61% (see inset of Fig. 4c). The reason could be ascribed to the reversible interactions, e.g., hydrogen bonds and ionic interactions in the hydrogels (Fig. 1), as these reversible bonds can dissipate energy effectively during deformation.[12, 48, 50]

We then calculated the Young's modulus (E) and mechanical toughness (U) from the data in Fig. 4a based on the slopes of the initial linear elastic portion of the stress–strain curve and the area under the tensile stress-strain curves, respectively. The results are reported in Fig. 4d, showing that the Young's modulus and toughness of the PAA hydrogel are only 0.09 MPa and 50 kJ/m^3, respectively, while the designed SA(Ca^{2+})-PAA-SiO_2 hydrogel reveals significantly improved Young's modulus of 0.6 MPa and the highest toughness of 14,500 kJ/m^3. During the stretching process, hydrogen bonds are the primary breaking mechanism and follow with unzipping of SA chains according to previous studies.[12]

These findings provide insight into the reinforcement mechanism of the prepared hydrogels. The silica NPs in the hydrogel can function as macro-cross-linkers in hydrogels with many analogous crosslinking points (ATPs) and lead to increased frictions among the polymer chains during stretching. The load can easily transfer along the polymer networks due to these crosslinking points and guarantee hydrogels with improved mechanical properties.[13] Moreover, regarding the SA networks, which are composed of G- and M-blocks, among which G-blocks prefer to chelate with Ca^{2+} ions and form stiff crosslinks. During the stretching process, the toughness of the hydrogel largely depends on the unzipping of crosslinks (i.e., disentanglement of crosslinked SA) and pulling out of polymer chains. With stretching by external loads the G blocks unzipping process will quickly shift to the neighbor pair while other parts will remain intact.[12] As such, in the DIPN co-network, upon the breaking of hydrogen bonds, the SA networks first begin to unzip, while the much more widely spaced ionic crosslinks first unzip when the external load increases. The PAA networks contribute to provide crack bridging

and stabilizing deformation during this process, which in turn reduces the stress concentration and also contribute to high toughness according to the previous study.[13] Hydrogen bonds and ionic crosslinks are relatively reversible and could quickly reform after being broken, which further helps to heal the internal damage and leads to pronounced hysteresis resistance and limited permanent deformation.

The fracture stress, Young's modulus, and toughness of our prepared hydrogels are compared with other hydrogel materials from literature in Fig.s 4e, 4f, and 4g, respectively.[3, 6, 18, 21, 26, 27, 35, 37, 43, 48, 49] This comparison shows that our prepared d-DIPN hydrogel remarkably improved hydrogel's extensibility, strength and toughness. To sum up, such strategy inherit the advantage of constructing tough hydrogels with interpenetrating double polymer network. Moreover, with dual reinforcing measurement, reversible hydrogen bonds and ionic crosslinks widely exist in d-DIPN hydrogel. Besides strong covalent bonds formed in double polymer networks, such reversible interactions ensures a much more compact and crosslinked structure, providing hydrogels with much improved mechanical performances compared with other similar ones.

Mineralization of DIPN hydrogels. As shown previously, hydrogels can chelate alkali metal ions, providing active nanoparticle nucleating sites, and further inducing biomimetic mineralization due to strong interactions between carboxyl groups and metal ions.[43] As such, a mineralization process can potentially result in many functional changes, and we have therefore performed a biomimetic Ca/P mineralization of the SA(Ca^{2+})-PAA-SiO_2 hydrogel to test and confirm its possible biomedical applications based on the previous research.[43, 51, 52] To this end, the DIPN hydrogel was repeatedly immersed in $CaCl_2$ and Na_2HPO_4 aqueous solutions. The originally transparent DIPN hydrogel changed to an opaque white appearance after mineralization (Fig. 5a), indicating significant structural differences. Such immersion process helps to adjust the hydrogel with an appropriate pH value for further *in vitro* studies (see below). Compared with DIPN hydrogels with adhesive and self-healing ability, introducing inorganic compositions during mineralizing results in the removal of carboxyl bonds. Thus, strong adhesion ability as well as self-healing ability of original hydrogels inevitably becomes inhibited upon mineralization (Fig. S8).

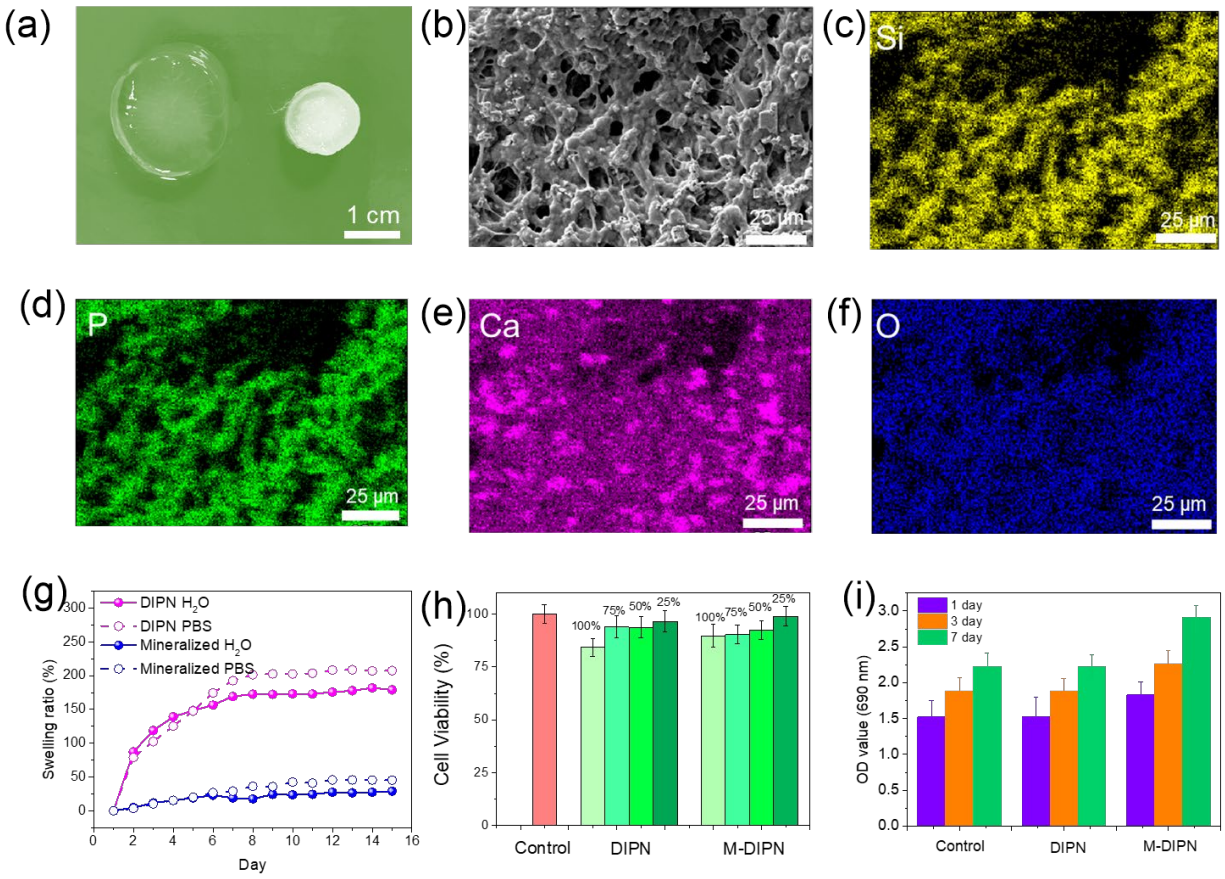

Figure 5. Mineralization and cell studies on DIPN hydrogels. (a) Optical images of transparent DIPN hydrogel and opaque white M-DIPN; (b) SEM image of M-DIPN hydrogel cross-section; (c-f) Element distribution of (c) Si, (d) P, (e) Ca, and (f) O atoms; (g) Swelling behavior of DIPN and M-DIPN hydrogels in H_2O and PBS solutions for up to 15 days; (h) Cytotoxicity test of DIPN and M-DIPN hydrogels; and (i) Cell proliferation of MC3T3-E1 cells on DIPN and M-DIPN hydrogels after culturing for 1, 3 and 7 days.

The cross section-morphology of the mineralized DIPN (M-DIPN) is investigated by SEM analysis as shown in Fig. 5b. Compared with the micro-structure of DIPN (Fig. S2), many inorganic particles are observed in the M-DIPN, together with small but consecutive networks through the cross-section morphology images. The EDX element mapping directly shows that these particles are composed of Si, Ca and P atoms (Figs. 5c-f). Thus, during the mineralizing process, Ca and P are more likely to cluster around SiO_2 NPs rather than being uniformly dispersed throughout the hydrogel. Interestingly, the anti-swelling behavior of the hydrogels is also

greatly improved upon such mineralizing process, as observed in both H_2O and PBS solutions (Fig. 5g). That is, even after 1 week, the mineralized hydrogels only swell ~19% and ~27% more in H_2O and PBS solutions, respectively, while the pristine DIPN hydrogel swells over 800% under the same conditions. This could be ascribed to the outer-layer inorganic particles that have consumed part of the -OH groups, which prevents the disentanglement of polymer chains and the swelling of hydrogels.

The mechanical performances of d-DIPN and M-DIPN hydrogels are compared in Fig. S9. After mineralization, the stress and strain at breakage of the hydrogel decrease. The reason could be ascribed to the following two aspects: (i) upon mineralization, most hydrogen bonds are consumed following the neutralization process, with the number of intermolecular interactions in the hydrogel thus decreasing; (ii) upon mineralization, the hydrogel surface changes from smooth to rough and the incorporated inorganic particles cause physical defects to appear in the hydrogels. Although the mechanical properties of the mineralized hydrogels are thus lower than the "pristine" ones, we find that the Young's modulus of M-DIPN reaches approximately 0.8 MPa. This remains to be significantly higher than that of native tissue environments (e.g., muscle with 8-17 kPa and osteoid matrix with 25-40 kPa[53, 54]), thus providing possibilities for biomedical applications of M-DIPN. More generally, the excellent mechanical behaviors, adaptation to various deformation requirements and anti-swelling performances suggest that the present hydrogels could be suitable candidates function as articular cartilage regeneration. For example, micro-fractures are induced in the underlying subchondral bone to release bone marrow containing stem cells, which is used to treat sports injuries.[23, 55, 56]

Before such clinical applications, cyto-compatibility and hemo-compatibility are important factors for hydrogel materials to be applied for tissue engineering or bone regeneration. Even though SA and PAA are both recognized as non-cytotoxic, biodegradable and bio-compatible materials, the hydrogels should be carefully checked before further applications. Here, the cytotoxicity test was measured through an indirect contact method with ToX-8 assay according to ISO 10993 standard. Materials are recognized as non-cytotoxicity when the cell viability is above 70%, and 50% dilution of extract should have the same or higher viability relative to the 100% extract solutions. Following this method, we cultured the MC3T3-E1 bone cells

with extracted media from DIPN and M-DIPN samples for 72 h and diluted the samples into different concentrations before testing them with the ToX-8 assay. As shown in Fig. 5h, compared with the control group, the DIPN or M-DIPN hydrogels show a high level of cell viability (>80%), confirming that the materials show non-cytotoxicity toward the MC3T3-E1 cells and are free from monomers and other unreacted components. This phenomenon reveals good cell biocompatibility of the hydrogel materials and inspires further proliferation studies. To this end, we cultured the MC3T3-E1 cells on both DIPN and M-DIPN hydrogels for 1, 3, and 7 days. We find that cells grow on M-DIPN to much larger extent than on the control group and DIPN hydrogels (Fig. 5i), showing that the mineralizing process is beneficial for cell growth. This is likely because the mineralization process induces the formation of calcium phosphate NPs,[22] which generate more biologically active surface sites, further enhancing the cell viability and functionality, and effectively improving the cell growth on hydrogels.

Discussion

In summary, we have designed and prepared a tough and bio-functional DIPN hydrogel through the use of ionic and nanoparticle reinforcement methods. Due to the crosslinked structures and strong molecular interactions, we achieve improved thermal stability, anti-swelling behavior, self-healing ability, and mechanical properties in the DIPN of SA (Ca^{2+})-PAA-SiO_2 hydrogel. This material could be stretched up to 1000% compared with its original length and its stress to failure is as high as 1.6 MPa. Reversible interactions in the hydrogels including hydrogen bonds and ionic interactions that break and reform provide an effective energy dissipation mechanism, resulting in self-healing ability, quick shape recovery and adhesive properties. We also investigated a Ca/P mineralization process of the DIPN hydrogel, finding that the mineralized DIPN hydrogel reveals improved anti-swelling behavior in both distilled water and PBS solution, with acceptable loss of stress and strain. Biocompatibility is also ensured through the mineralization process as more biologically active sites are formed, further leading to improved cell viability as well as cell proliferation. The mechanical and functional improvement by the abovementioned methods could potentially enable such hydrogels to be applied in biomedical fields such as bone regeneration.

Methods

Materials. All reagents, including acrylic acid (AA) (99%); sodium alginate (SA); vinyltriethoxysilane (VTES); calcium sulfate ($CaSO_4 \cdot 2H_2O$); calcium chloride dihydrate ($CaCl_2 \bullet 2H_2O$); Na_2HPO_4; N,N,N',N'-tetramethylenediamine (TEMED), N,N'-methylenebis(acrylamide) (MBAA); ammonium persulfate (APS) and sodium dodecyl sulfate (SDS), were commercially ordered and used without purification. Cell culture reagents were purchased from Invitrogen and Sigma-Aldrich UK. MC3T3-E1 preosteoblast cell line (ATCC, UK) was cultured in basal α-MEM supplemented with 10% (v/v) FCS (fetal calf serum) and 1% (v/v) penicillin. Cultures were maintained in an incubator at 37 °C, 5% CO_2, and 21% O_2. Cells were passaged upon confluence using 500 μg/mL trypsin-EDTA (ethylene diamine tetra-acetic acid).

Preparation of inorganic precursor (silica nanoparticles). 1.3 g vinyltriethoxysilane (VTES) and 10 g H_2O were mixed and vigorously stirred for 8 h until the oil droplets disappeared and a transparent solution was obtained.

Preparation of hydrogels. The PAA hydrogel and all the PAA-SA DIPN hydrogels were prepared through free radical polymerization process. First, 12 g AA monomer and 2 g SA powers were dissolved into 90 mL distilled water, stirring overnight to form a complete aqueous solution. Then, hydrolyzed VTES solution (1 wt % of AA monomer) was added into the mixture for another 2 h. After the re-dispersion process, TEMED, MBAA, APS, and $CaSO_4 \cdot 2H_2O$ in quantities of 0.0006, 0.0025, 0.01, and 0.05 compared with the weight of AA monomer were added to the solution in sequence. The solutions were then quickly transferred into plastic tubes after degassing. The samples were kept in furnace at 50 ℃ for 24 h to ensure the complete polymerization. Afterwards, the samples were removed from the mold and then washed by distilled water. For mineralized hydrogels, SA (Ca^{2+})-PAA-SiO_2 hydrogel was immersed in 0.5 M $CaCl_2$ and 0.3 M Na_2HPO_4 (pH = 9) solutions for three times. These were then washed with deionized water to remove the superfluous HPO_4^{2-}.

Structure characterization. FTIR was carried out to determine the molecular structure, functional groups, and verify the polymerization process of AA monomers. The measurements were done on a Bruker TENSOR II spectrometer along with Bruker Platinum attenuated total reflectance attachment, in the range of 4,000 to 400 cm^{-1}. All spectra were compiled from 64 consecutive scans and were baseline corrected using the vendor-

supplied software OPUS. To confirm the non-crystalline structure of the hybrid materials, X-ray diffraction (XRD) analysis was carried out on pulverized samples at 2θ angles from 5° to 80° using a Panalytical Empyrean diffractometer with Cu-Kα radiation source and Ni-filter. The thermal gravimetric analysis (TGA) was performed on a STA 449C (Netzsch) instrument. The samples were cut into small pieces and heated under air flow at a rate of 10 °C min^{-1}, from room temperature to 800 °C. The cross-section morphology and element distribution in hybrids were tested by scanning electron microscopy (SEM) using a Zeiss Gemini SEM 500 instrument at 5 kV/10 mA, equipped with energy dispersion X-ray (EDX) accessories. The hydrogels were freeze-dried and then fractured in the liquid CO_2. The average size of silica NPs was determined based on dynamic light scattering (DLS) measurements using a Zetasizer nano series (Malvern).

Swelling behavior. Hydrogels were placed in a furnace and dried at 40 ℃ overnight. The swelling ratio (*SR*) was calculated as,

$$SR = \frac{\mathrm{Ws}-\mathrm{Wd}}{\mathrm{Wd}} \times 100\% \quad (1)$$

The dried samples were immersed into different solutions firstly and weighed (Wd), then wiped the surface water gently using absorbent paper and weighed at regular time intervals (Ws).

Mechanical tests. The tensile tests were performed in room temperature on an Instron tensile testing machine with a 5 kN load cell and at a cross head speed of 5 mm/min. (The samples are prepared in shapes of cylindrical, Φ=3.5 mm).

Cytotoxicity tests. Potential *in vitro* cytotoxicity effects of the hydrogels on MC3T3-E1 cells were assessed in accordance to ISO 10993-536 and ISO 10993-12 standards. Dissolution products released by the samples (0.1 g/mL in α-MEM at 37 °C) over a 72 h period were collected. These were then filter sterilized, and dilution series (25%, 50%, 75%, and 100%) were prepared. In this assay, viable cells with active metabolism reduce resazurin (nonfluo-rescent dye, blue) to resorufin (pink fluores-cent dye). MC3T3-E1 cells were seeded on 96-well plates at 1×10^4 cells per well and left to grow in basal α-MEM (cell culture media) for 24 h until a subconfluent monolayer was formed. The culture media was removed, and MC3T3-E1 cells were then incubated with fresh basal α-MEM, the dissolution products of hybrid material or controls (100 μL/well) for a further 24 h. The culture media was removed, and then, Tox8 (dye for testing cell viability) was diluted ten

times in α-MEM media and then added (100 μL/well). Following an incubation period of 4 h, results could be measured spectrophotometrically at both 600 nm and 690 nm using a microplate reader (SpectraMax M5). The relative cell viability (%) was calculated as [(mean cell viability determined in sample)/ (mean cell viability determined in control)] × 100

Data availability

The authors declare that the main data supporting the findings of this study are available within the paper and the supplementary information. Any additional data that support the findings of this study are available from the corresponding authors upon request.

References

1. Chrisnandy, A., Blondel, D., Rezakhani, S., Broguiere, N. & Lutolf, M.P. Synthetic dynamic hydrogels promote degradation-independent in vitro organogenesis. *Nat. Mater.* **21**, 479-487 (2022).
2. Hu, X. et al. Preparation and characterization of a novel pH-sensitive Salecan-g-poly(acrylic acid) hydrogel for controlled release of doxorubicin. *Journal of materials chemistry. B* **3**, 2685-2697 (2015).
3. Sun, W. et al. Strong dual-crosslinked hydrogels for ultrasound-triggered drug delivery. *Nano Res.* **12**, 115-119 (2018).
4. Miao, Y., Xu, M. & Zhang, L. Electrochemistry-Induced Improvements of Mechanical Strength, Self-Healing, and Interfacial Adhesion of Hydrogels. *Adv. Mater.* **33**, e2102308 (2021).
5. Yuk, H., Zhang, T., Lin, S., Parada, G.A. & Zhao, X. Tough bonding of hydrogels to diverse non-porous surfaces. *Nat. Mater.* **15**, 190-196 (2016).
6. Wang, C. et al. Visible-light-assisted multimechanism design for one-step engineering tough hydrogels in seconds. *Nat. Commun.* **11**, 4694 (2020).
7. Zhao, T. et al. Macroscopic Layered Organogel-Hydrogel Hybrids with Controllable Wetting and Swelling Performance. *Adv. Funct. Mater.* **28**, 1800793 (2018).

8. Wang, L., Xu, H., Gao, J., Yao, J. & Zhang, Q. Recent progress in metal-organic frameworks-based hydrogels and aerogels and their applications. *Coord. Chem. Rev.* **398**, 213016 (2019).

9. Shi, H., Yang, J., You, M., Li, Z. & He, C. Polyhedral Oligomeric Silsesquioxanes (POSS)-Based Hybrid Soft Gels: Molecular Design, Material Advantages, and Emerging Applications. *ACS Mater. Lett.* **2**, 296-316 (2020).

10. Taylor, D.L. & In Het Panhuis, M. Self-Healing Hydrogels. *Adv. Mater.* **28**, 9060-9093 (2016).

11. Zhang, Y.S. & Khademhosseini, A. Advances in engineering hydrogels. *Science* **356** eaaf3627 (2017).

12. Sun, J.Y. et al. Highly stretchable and tough hydrogels. *Nature* **489**, 133-136 (2012).

13. Shi, F.K., Wang, X.P., Guo, R.H., Zhong, M. & Xie, X.M. Highly stretchable and super tough nanocomposite physical hydrogels facilitated by the coupling of intermolecular hydrogen bonds and analogous chemical crosslinking of nanoparticles. *J. Mater. Chem. B* **3**, 1187-1192 (2015).

14. Freedman, B.R. et al. Degradable and Removable Tough Adhesive Hydrogels. *Adv. Mater.* **33**, e2008553 (2021).

15. Si, Y. et al. Ultrahigh-Water-Content, Superelastic, and Shape-Memory Nanofiber-Assembled Hydrogels Exhibiting Pressure-Responsive Conductivity. *Adv. Mater.* **29,** 1700339 (2017).

16. Zhong, M. et al. Self-healable, tough and highly stretchable ionic nanocomposite physical hydrogels. *Soft Matter* **11**, 4235-4241 (2015).

17. Haraguchi, K., Uyama, K. & Tanimoto, H. Self-healing in nanocomposite hydrogels. *Macromol. Rapid Commun.* **32**, 1253-1258 (2011).

18. Xiao, D. et al. Seeking Answers from Tradition: Facile Preparation of Durable Adhesive Hydrogel Using Natural Quercetin. *iScience* **23**, 101342 (2020).

19. Qian, Y. et al. Direct Construction of Catechol Lignin for Engineering Long-Acting Conductive, Adhesive, and UV-Blocking Hydrogel Bioelectronics. *Small Methods* **5**, e2001311 (2021).

20. Li, M. et al. A self-healing hydrogel with pressure sensitive photoluminescence for remote force measurement and healing assessment. *Mater. Horiz.* **6**, 703-710 (2019).

21. Zhao, X. et al. Bioinspired ultra-stretchable and anti-freezing conductive hydrogel fibers with ordered and reversible polymer chain alignment. *Nat. Commun.* **9**, 3579 (2018).

22. Fiorini, F. et al. Nanocomposite Hydrogels as Platform for Cells Growth, Proliferation, and Chemotaxis. *Small* **12**, 4881-4893 (2016).

23. Xu, X., Jerca, V.V. & Hoogenboom, R. Bioinspired double network hydrogels: from covalent double network hydrogels via hybrid double network hydrogels to physical double network hydrogels. *Mater. Horiz.* **8**, 1173-1188 (2021).

24. Bin Imran, A. et al. Extremely stretchable thermosensitive hydrogels by introducing slide-ring polyrotaxane cross-linkers and ionic groups into the polymer network. *Nat. Commun*. **5**, 5124 (2014).

25. Li, X. et al. Dual Ionically Cross-linked Double-Network Hydrogels with High Strength, Toughness, Swelling Resistance, and Improved 3D Printing Processability. *ACS Appl. Mater. Interfaces* **10**, 31198-31207 (2018).

26. Ou, K., Dong, X., Qin, C., Ji, X. & He, J. Properties and toughening mechanisms of PVA/PAM double-network hydrogels prepared by freeze-thawing and anneal-swelling. *Mater. Sci. Eng. C.* **77**, 1017-1026 (2017).

27. Yang, Y., Wang, X., Yang, F., Shen, H. & Wu, D. A Universal Soaking Strategy to Convert Composite Hydrogels into Extremely Tough and Rapidly Recoverable Double-Network Hydrogels. *Adv. Mater.* **28**, 7178-7184 (2016).

28. Lee, K.Y. & Mooney, D.J. Alginate: properties and biomedical applications. *Prog. Polym. Sci.* **37**, 106-126 (2012).

29. Vueva, Y. et al. Silica/alginate hybrid biomaterials and assessment of their covalent coupling. *Appl. Mater. Today* **11**, 1-12 (2018).

30. Lueckgen, A. et al. Hydrolytically-degradable click-crosslinked alginate hydrogels. *Biomaterials* **181**, 189-198 (2018).

31. Zhang, D., Yang, J., Bao, S., Wu, Q. & Wang, Q. Semiconductor nanoparticle-based hydrogels prepared via self-initiated polymerization under sunlight, even visible light. *Sci. Rep.* **3**, 1399 (2013).

32. Wang, D. et al. Tuning morphology and mechanical property of polyacrylamide/Laponite/titania dual nanocomposite hydrogels by titania. *Polym. Compos.* **40**, E466-E475 (2019).

33. Zhao, Z., Fang, R., Rong, Q. & Liu, M. Bioinspired Nanocomposite Hydrogels with Highly Ordered Structures. *Adv. Mater.* **29** (2017).

34. Arno, M.C. et al. Exploiting the role of nanoparticle shape in enhancing hydrogel adhesive and mechanical properties. *Nat. Commun.* **11**, 1420 (2020).

35. Kamio, E., Yasui, T., Iida, Y., Gong, J.P. & Matsuyama, H. Inorganic/Organic Double-Network Gels Containing Ionic Liquids. *Adv. Mater.* **29** (2017).

36. Sun, G., Li, Z., Liang, R., Weng, L.T. & Zhang, L. Super stretchable hydrogel achieved by non-aggregated spherulites with diameters <5 nm. *Nat. Commun.* **7**, 12095 (2016).

37. Xia, L.W. et al. Nano-structured smart hydrogels with rapid response and high elasticity. *Nat. Commun.* **4**, 2226 (2013).

38. Matos, M.C., Ilharco, L.M. & Almeida, R.M. The evolution of TEOS to silica gel and glass by vibrational spectroscopy. *J. Non-Cryst. Solids* **147-148**, 232-237 (1992).

39. Rubio, F., Rubio, J. & Oteo, J.L. A FT-IR Study of the Hydrolysis of Tetraethylorthosilicate (TEOS). *Spectrosc. Lett.* **31**, 199-219 (1998).

40. Du, J. et al. Super-tough, anti-fatigue, self-healable, anti-fogging, and UV shielding hybrid hydrogel prepared via simultaneous dual in situ sol-gel technique and radical polymerization. *J. Mater. Chem. B* **7**, 7162-7175 (2019).

41. Bhattacharjee, S. DLS and zeta potential - What they are and what they are not? *J. Controlled release* **235**, 337-351 (2016).

42. Phadke, A. et al. Rapid self-healing hydrogels. *Proc. Natl. Acad. Sci. U. S. A.* **109**, 4383-4388 (2012).

43. Teng, L. et al. Weak Hydrogen Bonds Lead to Self-Healable and Bioadhesive Hybrid Polymeric Hydrogels with Mineralization-Active Functions. *Biomacromolecules* **19**, 1939-1949 (2018).

44. Zhan, Y., Fu, W., Xing, Y., Ma, X. & Chen, C. Advances in versatile anti-swelling polymer hydrogels. *Mater. Sci. Eng. C.* **127**, 112208 (2021).

45. Yesilyurt, V. et al. Injectable Self-Healing Glucose-Responsive Hydrogels with pH-Regulated Mechanical Properties. *Adv. Mater.* **28**, 86-91 (2016).

46. Bajomo, M., Robb, I., Steinke, J.H.G. & Bismarck, A. Fully Reversible pH-Triggered Network Formation of Amphoteric Polyelectrolyte Hydrogels. *Adv. Funct. Mater.* **21**, 172-176 (2011).

47. Su, X. & Chen, B. Tough, resilient and pH-sensitive interpenetrating polyacrylamide/alginate/montmorillonite nanocomposite hydrogels. *Carbohydr. Polym.* **197**, 497-507 (2018).

48. Sun, W. et al. Molecular engineering of metal coordination interactions for strong, tough, and fast-recovery hydrogels. *Sci. Adv.* **6**, eaaz9531 (2020).

49. Morelle, X.P. et al. Highly Stretchable and Tough Hydrogels below Water Freezing Temperature. *Adv. Mater.* **30**, e1801541 (2018).

50. Ducrot, E., Chen, Y., Bulters, M., Sijbesma, R.P. & Creton, C. Toughening elastomers with sacrificial bonds and watching them break. *Science* **344**, 186-189 (2014).

51. Mahony, O. et al. Silica-Gelatin Hybrids with Tailorable Degradation and Mechanical Properties for Tissue Regeneration. *Adv. Funct. Mater.* **20**, 3835-3845 (2010).

52. Huang, W. et al. Noncompressible Hemostasis and Bone Regeneration Induced by an Absorbable Bioadhesive Self-Healing Hydrogel. *Adv. Funct. Mater.* **31**, 2009189 (2021).

53. Wu, X. et al. Mineralized Hydrogels Induce Bone Regeneration in Critical Size Cranial Defects. *Adv. Healthc. Mater.* **10**, e2001101 (2021).

54. Zhou, L. et al. Biomimetic mineralization of anionic gelatin hydrogels: effect of degree of methacrylation. *RSC Adv.* **4**, 21997-22008 (2014).

55. Rahaman, M.N. et al. Bioactive glass in tissue engineering. *Acta Biomater.* **7**, 2355-2373 (2011).

56. Jones, J.R. Review of bioactive glass: from Hench to hybrids. *Acta Biomater.* **9**, 4457-4486 (2013).

Acknowledgements

This work was supported by the China Scholarship Council (CSC No. 201904910782).

Author contributions

W.F., M.M.S., and D.Y. conceived the study and designed the experiments. M.M.S. and D.Y. supervised the project. W.F. prepared the samples and performed the basic structure characterization. W.F. and L.R.J. performed the mechanical characterization. W.F., Y.D., and A.J.D. performed the cell *in vitro* experiments. W.F., M.M.S., and D.Y. wrote the manuscript with inputs from other co-authors. All authors contributed to analyzing and discussing the data.

Competing interests

The authors declare no competing interests.

Supporting Figures

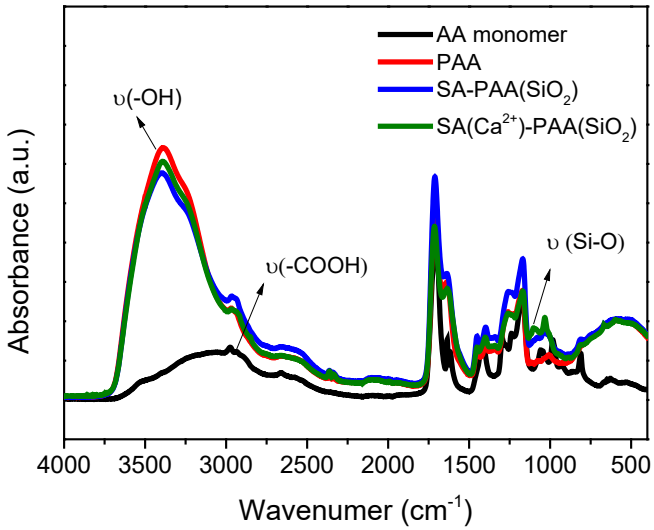

Figure S1. FT-IR spectra of AA monomer and hydrogels.

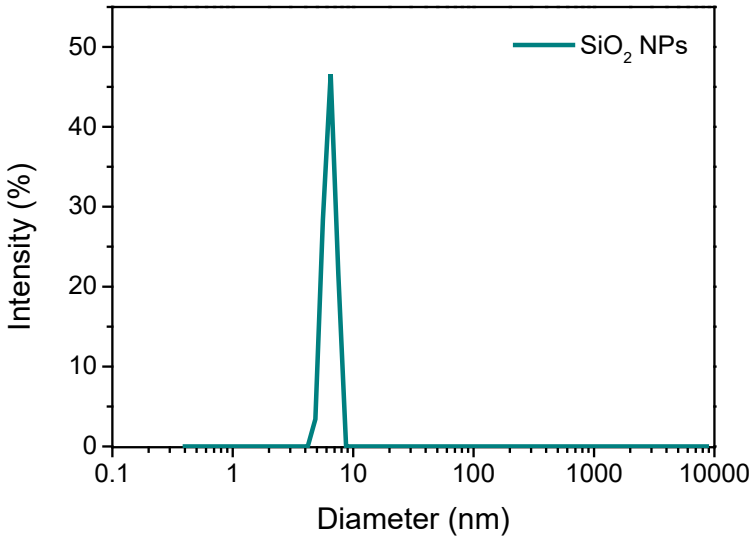

Figure S2. DLS data for silica nanoparticles hydrolyzed with VTES.

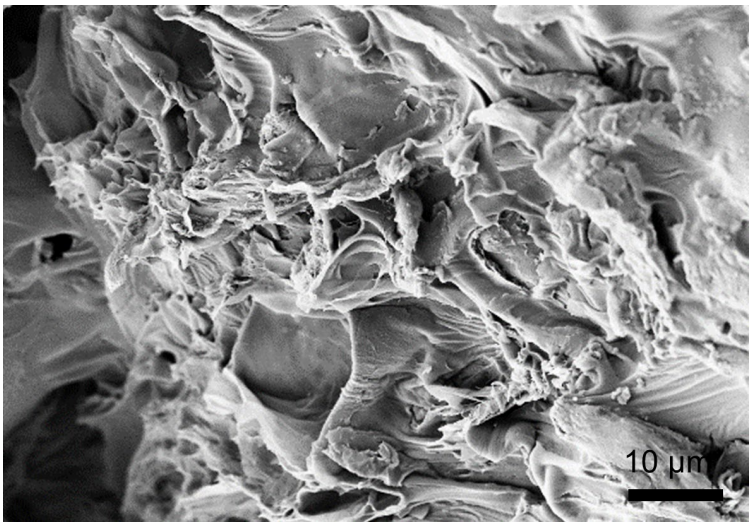

Figure S3. Cross-section morphology of d-DIPN hydrogel under SEM.

Figure S4. Wrapped d-DIPN hydrogel around a glass rod.

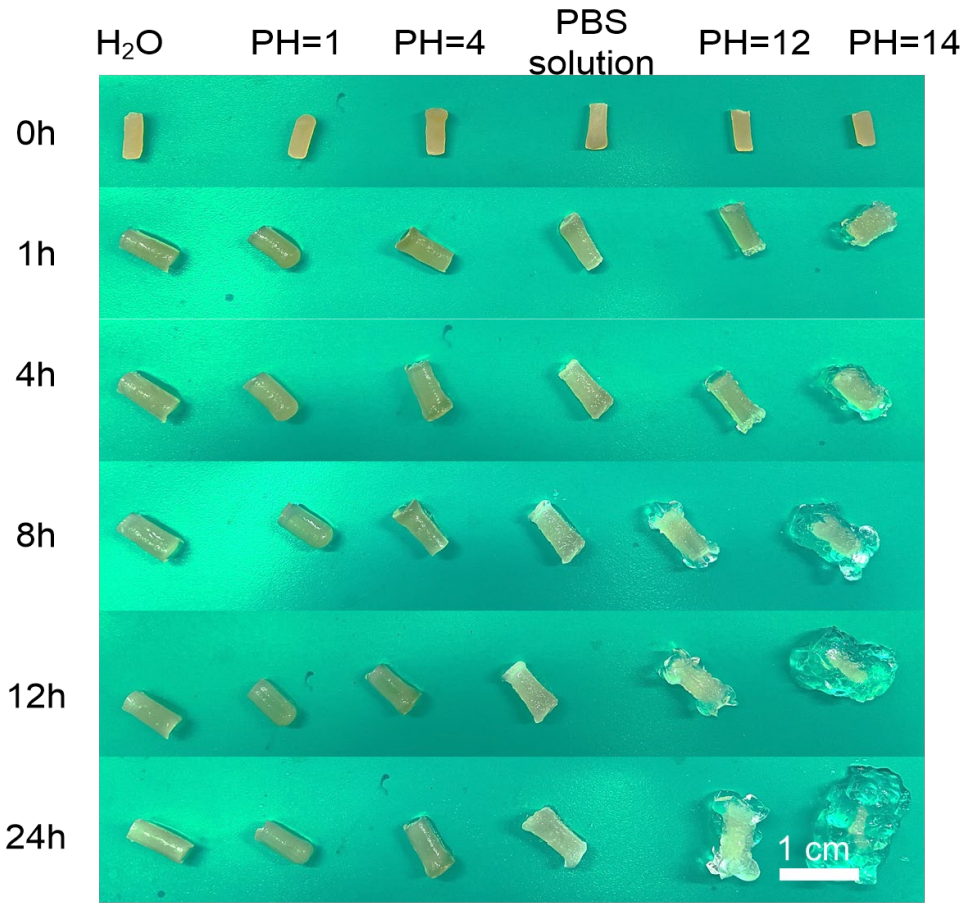

Figure S5. Optical images of different hydrogels immersed in different pH solutions for 24 h.

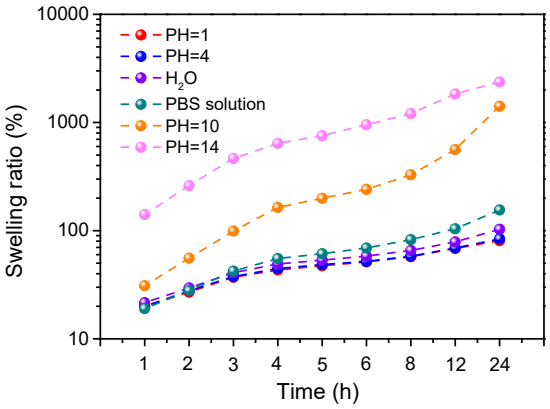

Figure S6. Swelling ratio of SA(Ca^{2+})-PAA(SiO_2) hydrogel in different pH solutions for up to 24 h.

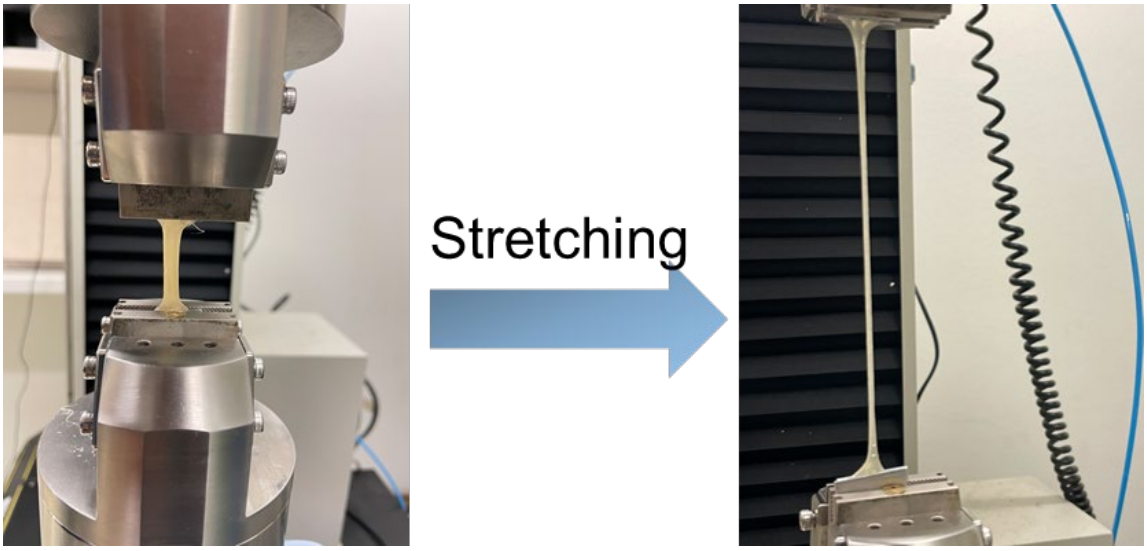

Figure S7. Tensile test of d-DIPN hydrogel.

Figure S8. M-DIPN hydrogel is unable to adhere to any surface.

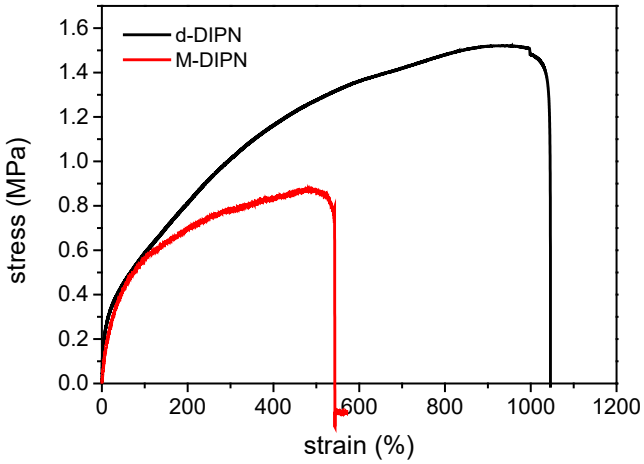

Figure S9. Tensile stress-strain curves of M-DIPN.

ISSN (online): 2446-1636
ISBN (online): 978-87-7573-880-9

AALBORG UNIVERSITY PRESS